Computational materials discovery : prediction of carbon dioxide and nitrogen-based compounds under pressure using density functional theory and evolutionary algorithm

Bowen Huang

To cite this version:

Bowen Huang. Computational materials discovery : prediction of carbon dioxide and nitrogen-based compounds under pressure using density functional theory and evolutionary algorithm. Other. Université de Poitiers, 2017. English. NNT : 2017POIT2301 . tel-01980787

HAL Id: tel-01980787
https://theses.hal.science/tel-01980787

Submitted on 14 Jan 2019

THESE

Pour l'obtention du Grade de

DOCTEUR DE L'UNIVERSITE DE POITIERS

(Faculté des Sciences Fondamentales et Appliquées)
(Diplôme National - Arrêté du 25 mai 2016)

Ecole Doctorale : Gay-Lussac n° 523

Secteur de Recherche : CHIMIE THÉORIQUE

Présentée par :

Bowen HUANG

****

COMPUTATIONAL MATERIALS DISCOVERY: PREDICTION OF CARBON DIOXIDE- AND NITROGEN-BASED COMPOUNDS UNDER PRESSURE USING DENSITY FUNCTIONAL THEORY AND EVOLUTIONARY ALGORITHM

****

Directeur de Thèse : Gilles FRAPPER

****

Soutenue le 11 décembre 2017
devant la Commission d'Examen

****

JURY

M. Jean-François HALET	Rapporteurs
M. Artem R. OGANOV	
M. Florent BOUCHER	Examinateurs
M. Gilles FRAPPER	
M. Laurent PIZZAGALLI	

THESE

Pour l'obtention du Grade de

DOCTEUR DE L'UNIVERSITE DE POITIERS

(Faculté des Sciences Fondamentales et Appliquées)
(Diplôme National - Arrêté du 25 mai 2016)

Ecole Doctorale : Gay-Lussac n° 523

Secteur de Recherche : CHIMIE THÉORIQUE

Présentée par :

Bowen HUANG

****

COMPUTATIONAL MATERIALS DISCOVERY: PREDICTION OF CARBON DIOXIDE- AND NITROGEN-BASED COMPOUNDS UNDER PRESSURE USING DENSITY FUNCTIONAL THEORY AND EVOLUTIONARY ALGORITHM

****

Directeur de Thèse : Gilles FRAPPER

****

Soutenue le 11 décembre 2017
devant la Commission d'Examen

****

JURY

M. Jean-François HALET	Rapporteurs
M. Artem R. OGANOV	
M. Florent BOUCHER	Examinateurs
M. Gilles FRAPPER	
M. Laurent PIZZAGALLI	

Acknowledgments

Calculations were performed on the THOR supercomputer at the Mesocentre SPIN (Poitiers University) and at HPC GENCI (TGCC Curie and CINES; grant 2016087539 ; 2 millions cpu).

The work was supported by Région Poitou-Charentes (PhD fellowship 2014-2017), CNRS and Poitiers University, GDRI RFCCT CNRS (DNM-evol program), and Hubert Curien Partnerships PHC XU GUANGQI 2015 (No. 34455PE) program of the French Ministry of Foreign Affairs.

Our Institute, « Institut de Chimie des Matériaux et Milieux de Poitiers » UMR 7285, and our research team E4 “Catalyse et Milieux Non Conventionnels” are also acknowledged for their financial support (operating & HPC equipment, CPER 2017).

I would like to thank, first and foremost, my supervisor Dr. Gilles Frapper, to whom I am deeply grateful for all of his help and guidance in my Ph.D. student's lifetime. He has taught me how good theoretical chemistry is done. More important thing is the rigorous attitude toward to research. I appreciate all his contributions of time, ideas, and computing resources to make my experience productive. Beyond the science, Gilles introduced how marvelous and delicious the French cuisine is to me. And I appreciate his hospitality for the unforgettable journey in Saint-Cado.

I would like to thank my family for all their love. For my loving, encouraging, and understanding wife Keyi whose faithful support is so appreciated. For my parents who raised me up and supported me in all my pursuits.

Thank you.

List of publications

The text of this thesis contains material which has already been published, under review or in submission. These articles, oral and poster communications are listed thereafter.

Articles

B. Huang and G. Frapper "Pressure-induced polymerization of CO_2 in lithium-carbon dioxide phases" *J. Am. Chem. Soc.*, vol. 140, no. 1, p. 413, 2018

E. Angot, **B. Huang**, C. Levelut, R. Le Parc, P. Hermet, A. S. Pereira, G. Aquilanti, G. Frapper, O. Cambon, and J. Haines, "Experimental and first-principles calculation study of the pressure-induced transitions to ametastable phase in $GaPO_4$ and in the solid solution $AlPO_4$-$GaPO_4$" *Phys. Rev. Mater.*, vol. 1, no. 3, p. 33607, 2017.

S. Yu, **B. Huang**, Q. Zeng, A. R. Oganov, L. Zhang, and G. Frapper, "Emergence of novel polynitrogen molecule-like species, covalent chains, and layers in magnesium–nitrogen Mg_xN_y phases under high pressure," *J. Phys. Chem. C*, vol. 121, no. 21, p. 11037, 2017.

S. Yu, Q. Zeng, A. R. Oganov, G. Frapper, **B. Huang**, H. Niu, and L. Zhang, "First-principles study of Zr–N crystalline phases: phase stability, electronic and mechanical properties," *RSC Adv.*, vol. 7, no. 8, p. 4697, 2017.

S. Yu, **B. Huang**, X. Jia, Q. Zeng, A. R. Oganov, L. Zhang, and G. Frapper, "Exploring the real ground-state structures of molybdenum dinitride," *J. Phys. Chem. C*, vol. 120, no. 20, p 11060, 2016.

B. Huang and G. Frapper, "Binary phase diagrams of Ba-N under pressure: a pressure-induced electride to insulator transition and others", ACS, 2017, submitted.

B. Huang and G. Frapper , "Up to 10 nitrogen per alkaline earth metal: prediction of dipentazolate $Ae(N_5)_2$ salts (Ae=Be, Mg, Ca, Sr, Ba) ", 2017, in preparation

B. Huang and G. Frapper, "8-coordinated silicon in high-pressure silicon disulfide phases", 2017, in preparation

Oral and poster communications

11. 2017 French theoretical chemistry network meeting in Nantes

"Promising high-energy-density material: prediction of *bis*-pentazolate Ba(N_5)$_2$ and novel high-pressure Ba-N phases." **B. Huang** and G. Frapper (Oral presentation)

01. 2017 TCCM winter school LTTC in Luchon

"Pressure-induced polymerization of CO_2 in lithium-carbon dioxide phases" **B. Huang** and G. Frapper (Oral presentation)

01. 2017 12th USPEX workshop in Poitiers

"Pressure-induced polymerization of CO_2 in lithium-carbon dioxide phases" **B. Huang** and G. Frapper (Oral presentation & Poster)

10. 2016 The 8th multiscale materials modeling international conference in Dijon

"Exploring the Real Ground-State Structures of Molybdenum Dinitride" S. Yu, **B. Huang**, X. Jia, Q. Zeng, A. R. Oganov, and G. Frapper (Poster)

03. 2016 Day of the center-west of France chemistry society in Poitiers

"Exploring the real ground-state structures of molybdenum dinitride" **B. Huang** and G. Frapper (Oral presentation)

11. 2015 Scientific day of IC2MP, University of Poitiers

08. 2015 10th USPEX workshop in Beijing, China

08. 2015 9th USPEX workshop in Poitiers

"Emergence of novel nitrogen covalent networks in magnesium-nitrogen under high pressure"
S. Yu, **B. Huang** , Q. Zeng, A. R. Oganov, G. Frapper (Poster)

List of symbols

Ae	Alkaline earth cations
AIMD	*Ab Initio* Molecular Dynamic simulations
BH	Born-Huang approximation
BO	Born-Oppenheimer approximation
cg	Cubic gauche
COOP	Crystal Orbital Overlap Population
COHP	Crystal Overlap Hamilton Populations
CSP	Crystal Structure Prediction
DFT	Density Functional Theory
DOS	Densities of States
EA	Evolutionary Algorithm
Eg	Band gap
EHT	Extended Hückel theory
ELF	Electron Localization Function
EXAFS	Extended X-ray Absorption Fine Structure
FWHM	Full Width at Half Maximum
GGA	Generalized-Gradient Approximation
HEDM	High-Energy Density Materials
HK	Hohenberg-Kohn (HK) theories
HOMO	Highest Occupied Molecular Orbital
HSE06	The Heyd-Scuseria-Ernzerhof exchange-correlation functional
KS	Kohn-Sham (KS) method
LDA	Local Density Approximation
LUMO	Lowest Unoccupied Molecular Orbital
MD	Molecular Dynamics

MIF	Metal-Inorganic Framework
MM	Molecular Mechanics
MO	Molecular Orbital
PAW	Projector Augmented Wave
PBE	Perdew, Burke and Enzerhof
PES	Potential Energy Surface
RDF	Radial Distribution Functions
SCF	Self-Consistent Field
SG	Space Group
VASP	Vienna Ab-initio Simulation Package
VC-EA	Variable Composition – Evoluationary Algorithm
VEC	Valence Electron Concentration
VOD	Velocity of Detonation
VRH	Voigt-Reuss-Hill approximation
VSEPR	Valence-Shell Electron-Pair Repulsion Theory
XAS	X-ray Absorption Spectroscopy
XRD	X-ray Powder Diffraction
ZKC	Zintl-Klemm Concept
ZPE	Zero-Point Energy

Présentation en français du manuscrit

Traduit par Dr Gilles Frapper, Directeur de thèse

MC HdR Chimie théorique 31° section CNU

Groupe Chimie Théorique, équipe E4, IC2MP UMR 7285 Université de Poitiers-CNRS

gilles.frapper@univ-poitiers.fr

Prédiction *in silico* de phases cristallines $Li_x(CO_2)_y$ ou nitrures par algorithme évolutionnaire et calculs en chimie quantique

La découverte de nouveaux composés cristallins par simulation numérique est un défi majeur en Science des Matériaux. Ce travail de thèse s'inscrit dans ce champ de recherche et aborde trois familles de composés : (1) les composés constitués de lithium et de dioxyde de carbone, $Li_x(CO_2)_y$; (2) les phases de composés binaires M-azote avec M = Mg, Ba, Mo et Zr ; (3) les systèmes $GaPO_4$ et SiS_2 isoélectroniques à la silice. Leurs structures cristallines sous contrainte de pression sont prédites à partir de l'unique connaissance de leur composition chimique. Nos analyses basées sur une approche propre à la chimie quantique permettent de répondre entre autres à la question suivante : la polymérisation de molécules insaturées tels que CO_2 et N_2 est-elle favorisée par l'ajout d'un élément chimique, lequel, en quelle quantité et dans quelles conditions de pression ?

Nous avons identifié une grande diversité de composition chimique lors de l'étude des diagrammes de phases binaires Li-CO_2 et M-N à pression atmosphérique et/ou extrême. La stabilité thermodynamique et dynamique de plusieurs dizaines de phases cristallines a été étudiée tels que les systèmes cristallins $Li_2(CO_2)$, MgN_4, $Ba(N_5)_2$ et MoN_2. Nous émettons l'hypothèse que certaines phases devraient pouvoir être synthétisées, et ceci dans des conditions de pression variées.

Les structures cristallographiques sont déterminées *in silico* à l'aide d'un algorithme évolutionnaire basé sur les concepts de la théorie Darwinienne de l'évolution couplé à une méthode de calcul en chimie quantique. Les principes généraux qui gouvernent l'algorithme évolutionnaire USPEX sont exposés au chapitre I abordant la méthodologie générale. L'optimisation structurale et électronique d'un composé de l'état solide est réalisée par des calculs quantiques basés sur la théorie de la fonctionnelle de la densité dont une brève présentation est donnée. L'analyse des arrangements structuraux et de la structure électronique est réalisée à l'aide de plusieurs approches méthodologiques issues de la chimie quantique tels que la densité d'état DOS, la population de Hamilton des orbitales cristallines COHP, la fonction de localisation des électrons ELF, la densité de charge et la théorie des orbitales moléculaires et cristallines. Cette boite à outils « analyse de la liaison chimique » est détaillée et une présentation de chaque méthode conclut le premier chapitre.

Ce manuscrit est divisé en trois parties. La première aborde l'étude de la structure électronique et géométrique des composés $Li_x(CO_2)_y$ sous pression. Elle est développée au chapitre II. Le diagramme de phase Li-CO_2 est établi entre 0 et 100 GPa et trois compositions sont localisées : Li_2CO_2, $Li_3(CO_2)_2$ et $LiCO_2$ (cf **1**). En particulier, nous étudions la polymérisation théorique des entités CO_2 au sein de l'oxalate de lithium $Li_2(C_2O_4)$ **2**. Il est montré que la phase poly-1,4-dioxane constitue l'arrangement structural le plus stable thermodynamiquement au-dessus de 33 GPa pour la stoichiométrie 1:1 $LiCO_2$. A pression atmosphérique, cette structure comprenant du « dioxyde de carbone polymérisé » est thermodynamiquement métastable et, selon nos simulations de dynamique moléculaire *ab initio*, cinétiquement stable.

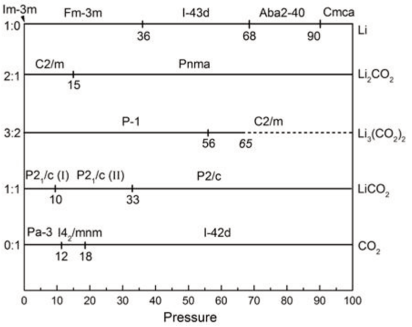

1, phases $Li_x(CO_2)_y$ prédites

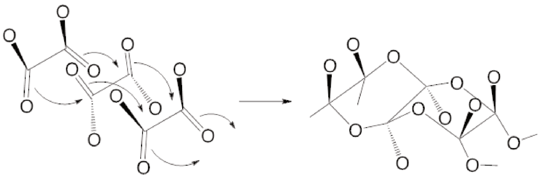

2, oxalate $C_2O_4^{2-}$ et **3**, poly-dioxane $[(^-O\text{-}C\text{-}O\text{-})_2]_n$

Deux autres compositions sont obtenues, $Li_3(CO_2)_2$ and Li_2CO_2 ; cette dernière phase **3** présente un motif de type éthène $(^{-}O)_2C{=}C(O^{-})_2$, association formelle de deux groupes carbonites CO_2^{2-}. Sur la base de calculs DFT, ces oxalates $Li_{2+x}(C_2O_4)$ sont proposés comme électrode positive d'une batterie lithium organique (cf. **4**).

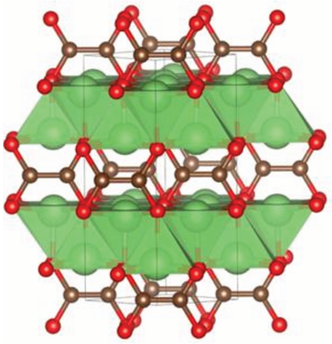

3, phase *C2/m* de $Li_4C_2O_4$

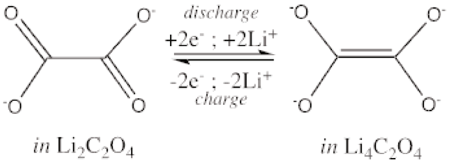

4, mécanisme redox

La deuxième partie de ce manuscrit a trait à la recherche de composés de l'état solide riches en azote potentiellement candidats dans le domaine des explosifs et du stockage de l'énergie.

L'étude théorique de nitrures d'alcalino-terreux de formule Ae_xN_y avec Ae = Mg et Ba est abordée et la discussion des résultats exposée au chapitre III. Les deux diagrammes de phases binaires ont été établis à T = 0 K et pour plusieurs pressions externes (0-300 GPa pour Mg-N **5** et 0-100 GPa pour Ba-N **6**). L'émergence de compositions inattendues présentant des motifs covalents N_y moléculaires, voire uni- et bidimensionnels constitue l'originalité de ces travaux théoriques (voir **7**). Neuf compositions chimiques sont thermodynamiquement stables dans le système Mg-N (16 phases) entre 0 et 300 GPa, et 12 dans le système Ba-N (22 phases) entre 0 et 100 GPa.

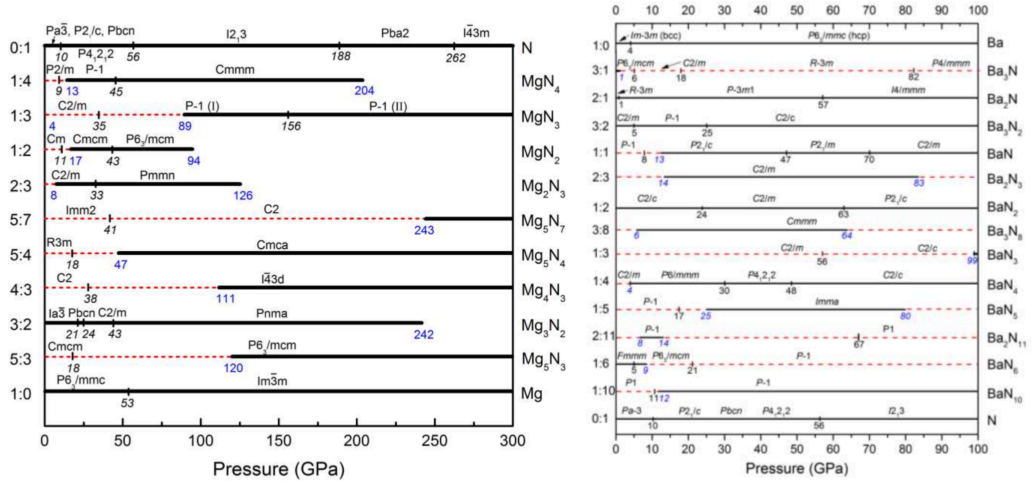

5 **6**

Composition chimique *vs* pression dans les diagrammes de phase Mg-N et Ba-N.

Des chaînons N_2, N_3 et N_4, des anions pentazolates N_5^- et des cycles type benzène N_6 sont rencontrés (voir ci-après **7**) ; leurs structures électroniques et géométriques ont été étudiées et rationnalisées. De même, des systèmes polymériques d'azote ont été observés, chaines covalentes infinies (1D) et feuillets (2D) stabilisées par les cations alcalino-terreux. Certains de ces matériaux ont des propriétés de conduction métallique sous pression extrême.

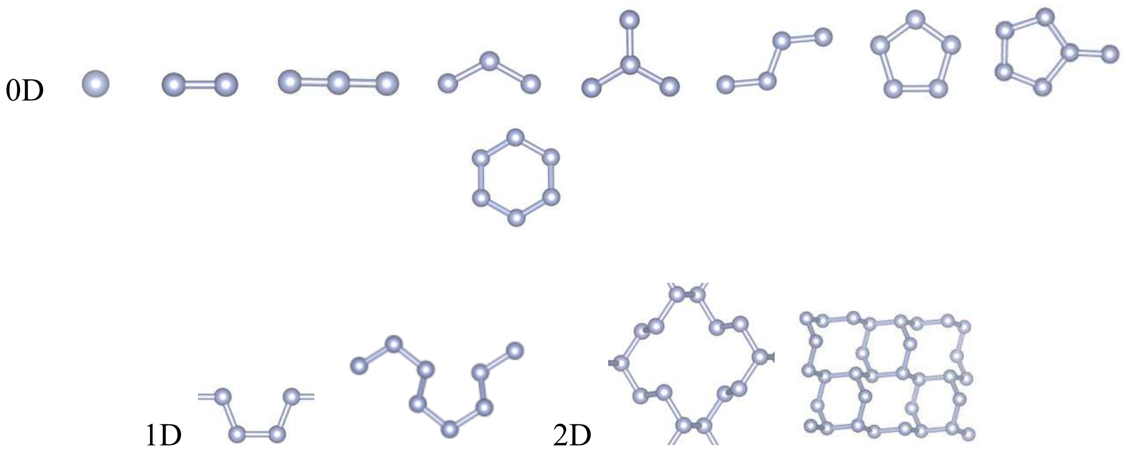

7, motifs N_y rencontrés dans les structures Ae_xN_y (Ae=Mg, Ba) sous pression

Tandis que Mg_3N_2 est un composé ionique isolant de type Zintl ($3Mg^{2+}$, $2N^{3-}$) à pression ambiante, Ba_3N_2 présente une surprenante structure *C2/m* en feuillet dans sa phase la plus stable thermodynamiquement. Dans *C2/m*, des entités N_2^{4-} et des ions N^{3-} sont encapsulées dans le sous-réseau barium. A pression ambiente, *C2/m* Ba_3N_2 **8** est un conducteur électrique, un *électride* bidimensionnel, une propriété observée dans les composés riches en barium Ba_3N et Ba_2N. De plus, sous pression, deux transformations de phase sont prédites pour Ba_3N_2 : *C2/m (5 GPa)→P-*1 *(25 GPa)→C2/c*, avec la séquence *électride conducteur* (*C2/m*) *→isolant* (*P*-1) *→métal* (*C2/c*). La localisation d'électrons dans l'espace inter-feuillets explique les propriétés de conduction métallique de *C2/m* Ba_3N_2, voir l'illustration en **8**, tandis que la phase *P*-1 stable comprend des nitrures N^{3-} encapsulés dans un réseau cationique, caractéristique structurale d'un composé Zintl qui lui confère un caractère d'isolant électrique. Ba_3N_2 constitue une exception structurale et électronique parmi ses composés isoélectroniques Ae_3N_2 à pression ambiante (Ae=Be, Mg, Ca).

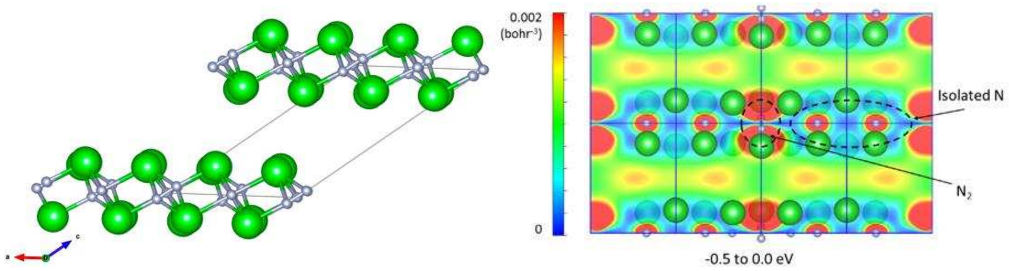

8

Structure cristalline Ba_3N_2 *C2/m* et densité de charge (à droite) :

une localisation d'électrons est observée dans l'espace inter-feuillet

Finalement, et pour la première fois à notre connaissance, des composés de l'état solide de type $Ae(N_5)_2$ sont proposés dans la série des alcalino-terreux Ae = Be, Mg, Ca, Sr et Ba. Chaque structure cristalline comprend deux cycles N_5^- pentazolates, soit 10 atomes d'azote par métal. Pour le beryllium dipentazolate BeN_{10} **9**, une structure à charpente ouverte de type *Metal Inorganic Framework MIF* autorise le stockage de 1,5 molécules de diazote par formule unitaire ; sur la base d'une simulation dynamique (AIMD), il est montré que la charpente pentazolate-Be^{2+}

du composé hypothétique $Be(N_5)_2(N_2)_{1,5}$ est stable au moins jusqu'à 600 K. Ces sels de pentazolates peuvent libérer une quantité d'énergie et de moles gazeuses lors de la réaction de décomposition hypothétique $Ae(N_5)_2 = \frac{1}{3}Ae_3N_2 + \frac{28}{3}N_2$, et à ce titre, s'invitent dans la famille des matériaux à haute densité d'énergie et des explosifs.

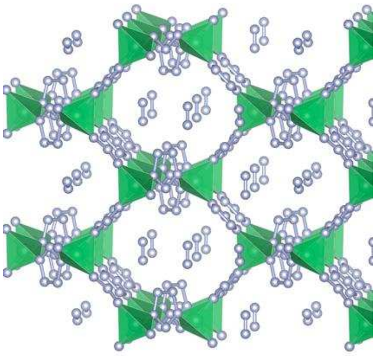

9, phase $Be(N_5)_2(N_2)_{1,5}$

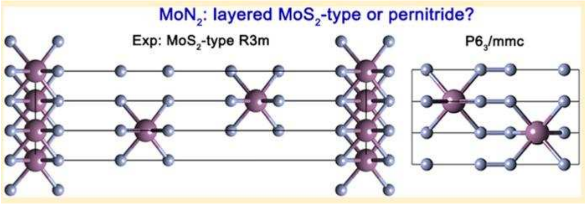

10, phase MoN_2 : *P6₃/mmc* est la plus stable

La dernière classe de composés nitrurés abordée dans cette deuxième partie concerne les matériaux Mo_xN_y et Zr_xN_y. Au quatrième chapitre est traité un sujet en réponse à des travaux expérimentaux qui conduisaient en 2015 à la proposition d'une structure en feuillet de type MoS_2 pour le composé dinitrure de molybdène MoN_2 **10**. Notre recherche de la structure cristalline de MoN_2 par approche évolutionnaire couplée à des calculs DFT bat en brèche les conclusions des expérimentateurs : la phase stable thermodynamiquement de MoN_2 présente une structure cristalline où des entités N_2 sont encapsulées dans des cages prismatiques d'atomes de Molybdène. La phase « expérimentale » de structure-type MoS_2 est instable dynamiquement du fait de la présence de branches de phonons imaginaires dans son spectre de phonons. De plus, elle est instable thermodynamiquement. Il est montré que l'optimisation géométrique de MoN_2 type-MoS_2 conduit au couplage des atomes d'azote donc à l'existence d'unités N_2 encapsulées dans le réseau métallique, du fait du caractère radicalaire de l'azote dans la phase de type MoS_2. Ces résultats invitent à une nouvelle démarche expérimentale pour la détermination de la composition chimique et la structure cristallographique du matériau catalytique MoN_2.

Puis une étude théorique des liaisons chimiques et des arrangements structuraux présents au sein de nitrures de zirconium Zr_xN_y à pression ambiante est menée en collaboration avec une équipe de l'université NPU de Xi'an. Un modèle théorique basée sur une analyse orbitalaire est proposé pour l'analyse de la perturbation électronique liée à la création de défaut en azote ou en zirconium au sein de phases Zr_xN_y de type NaCl.

La troisième partie de ce manuscrit traite deux thèmes relatifs à la prédiction de la structure cristalline de composé de composition fixé, l'un $GaPO_4$ **11** et l'autre SiS_2 **12**, tous deux isoélectroniques à la silice SiO_2. Le premier est le fruit d'une collaboration avec une équipe d'expérimentateurs en Sciences des matériaux sous haute pression. Les travaux expérimentaux et théoriques portent sur l'élucidation de la structure cristallographique d'une phase métastable de $GaPO_4$ obtenue à haute pression. Notre étude évolutionnaire/DFT conduit à la proposition d'une transformation de phase de la forme α-quartz vers une forme métastable orthorhombique de groupe d'espace $Pmn2_1$, en très bon accord avec les données expérimentales (DRX & IR). Le deuxième thème envisage les différentes transformations de phase du disulfure de silicium SiS_2 induites par la pression (0 à 500 GPa).

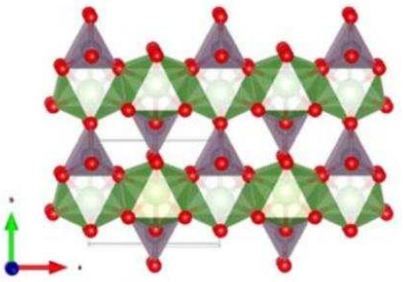

11, $GaPO_4$ à 20 GPa

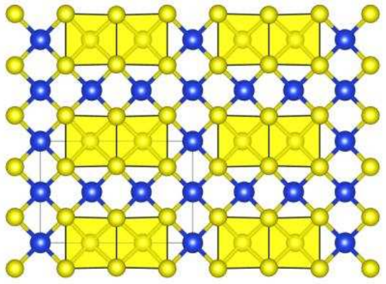

12, SiS_2 à 500 GPa ; Si et S sont en coordinence 8

Finalement, nous présentons une conclusion générale.

Ces travaux de thèse ont fait l'objet de 4 articles publiés dans des revues internationales à comité de lecture et de plusieurs communications orales (3) et par voie d'affiche (4). Deux autres publications sont soumises pour publication et deux sont en cours de rédaction.

Mots-clés : alcalino-terreux, algorithme évolutionnaire, analyse orbitalaire, calculs théoriques, CO_2, DFT, dioxyde de carbone, $GaPO_4$, haute pression, *in silico*, liaison chimique, matériaux nitrurés, MoN_2, pentazolate, prédiction de phases cristallines, structure électronique, SiS_2, USPEX, ZrN_2

CONTENT

General introduction

The discovery of new crystalline compounds by numerical simulation is a significant challenge in materials science. My Ph.D. work has contributed to this research and focused on three families of compounds: (i) compounds consisting of lithium and carbon dioxide; (ii) the M-nitrogen binary compounds with M = Mg, Ba, Mo, and Zr; and (iii) $GaPO_4$ and SiS_2 systems.

The crystalline structures under compression were predicted from the knowledge of their chemical composition. Our analysis based on quantum chemistry makes it possible to answer, among others, the following questions: is the polymerization of unsaturated molecules, such as CO_2 and N_2, favored by the addition of an element? Which element and in what quantity? What are the pressure conditions?

The crystallographic structures are determined *in silico* using an evolutionary algorithm based on the concepts of the Darwinian theory, coupled with density functional theory. The general principles of the evolutionary algorithm are discussed in Chapter I. In addition, a brief presentation of the structural and electronic optimization for the solid-state compound is illustrated. The analysis of the structural arrangements and the electronic structure has been carried out using several methodological approaches, such as density of states, the crystal orbital Hamilton population, and the molecular and crystalline orbital theory.

In the field of CO_2 capture and storage, condensed extended CO_2-based net crystals present interesting properties. Unsaturated CO_2 species possess lone pairs and/or multiple bonds that may interact with atoms with low coordination numbers in neighboring units, leading to novel covalent C/O oligomers and extended nets. Nevertheless, three-dimensional poly-CO_2 are not quenchable at ambient conditions. Therefore, alternative conceptual strategies of CO_2 polymerization need to be explored. One approach involves the activation of CO_2 under high pressure, by mixing CO_2 with an electropositive s-block element. In this study, the phase diagram Li-CO_2 is established between 0 and 100 GPa, and three stable compositions are located: Li_2CO_2, $Li_3(CO_2)_2$ and $LiCO_2$. The geometrical and electronic structure of $Li_x(CO_2)_y$ is developed in Chapter II. In particular, we study the polymerization of CO_2 entities in lithium oxalate $Li_2(C_2O_4)$. It is shown that the poly-1,4-dioxane phase is the most stable structural arrangement, and is thermodynamical stable beyond 33 GPa. Two other compositions ($Li_3(CO_2)_2$ and Li_2CO_2) are obtained, the later phase has a unit of ethene type $(^{-}O)_2C=C(O^{-})_2$. By DFT calculations, these oxalates $Li_{2+x}(C_2O_4)$ are proposed as an electrode of the organic lithium battery.

The discovery and synthesis of environmental friendly, high energy-density materials is now more critical than at any time in the past. Polynitrogen compounds are of significant interest due to their particularly high specific energy. One practical approach to stabilize such polymeric nitrogen phases is to form nitrogen-rich alloys with other elements; such “chemical precompression” may significantly reduce the pressure of polymerization. Therefore, we studied the alkaline earth nitrides of Ae_xN_y formula with Ae = Mg and Ba at specific pressures.

Chapter III deals with the search for potential candidates of nitrogen-rich compounds in the field of high energy density materials. The two binary phase diagrams were established at zero Kelvin, and for various pressures (0-300 GPa for Mg-N and 0-100 GPa for Ba-N). Nine chemical compositions in the Mg-N system (16 phases), and twelve in the Ba-N system (22 phases) are thermodynamically stable. The emergence of unexpected compositions with N_2, N_3, and N_4 units, pentazolate N_5^- anions and benzene N_6 rings, even one- and two-dimensional covalent N_y-motifs, constitutes the originality of these theoretical works.

In this study, Ba_3N_2 is a structural and electronic exception among its isoelectronic Ae_3N_2 compounds at ambient pressure. Mg_3N_2 is an insulating compound of Zintl phase ($3Mg^{2+}$, $2N^{3-}$) at ambient pressure, while Ba_3N_2 has a surprising *C2/m* layered structure and is a conductive electride, a similar property observed in barium-rich compounds (Ba_3N and Ba_2N). Two pressure-induced phase transformations of Ba_3N_2 are observed combining with conductive electride → semiconductor → metal transitions.

For the first time, to our knowledge, $Ae(N_5)_2$ solid-state compounds are proposed in the alkaline earth series. Moreover, a metal-organic-framework type structure allows at least 1.5 molecules of dinitrogen per unit formula in beryllium pentazolate BeN_{10}. The *ab initio* molecular dynamics simulation indicated that the Be^{2+}-pentazolate framework of $Be(N_5)_2(N_2)_{1.5}$ is stable up to 600 K. These pentazolate salts can release a quantity of energy and are included in the family of high-energy density materials.

Transition metal nitrides have been widely used in cutting tools, and as wear-resistant coatings, because of their excellent properties, such as superior hardness and strength. The understanding of their peculiar mechanical and chemical properties needs the characterization of these materials from a crystallographic point of view. Also, Wang *et al.*[1] synthesized a MoN_2 structure which adopts a rhombohedral $R3m$ structure, and was proposed to be isotypical with MoS_2. However, nitrogen atoms do not fulfill the octet rule in the proposed $R3m$ phase. We hypothesized that this electronic situation should be unstable from thermodynamic and mechanical points of view. Motivated by these factors, we worked in close collaboration with the team (Dr. Yu and Prof. Oganov *et al.*) from the Northwestern Polytechnic University (NPU Xi'an, China). The zirconium-nitrogen and molybdenum-nitrogen binary compounds have been demonstrated. In Chapter IV, a theoretical study of the chemical bonds, and the structural arrangements based on the orbital analysis, were conducted by our side. Our search for the crystalline structure of MoN_2 defeated the conclusions of the researchers. The ground-stable phase of MoN_2 has a structure where N_2 entities are encapsulated in prismatic cages of molybdenum atoms. Whereas, from our DFT calculations, the "experimental" phase of structure-type is thermodynamical and dynamical unstable. These results invite a new experimental approach for the determination of the chemical composition and the crystallographic structure. In the following part, we analyzed the electronic and structural properties of several *ab initio* predicted zirconium nitrides, concentrating on their chemical bonding.

The Chapter V of this manuscript deals with two topics relating to the prediction of the crystalline structure of the 16-valence electron compounds $GaPO_4$ and SiS_2. The first one is the result of a collaboration with a team researching materials science under pressure. This work concerns the elucidation of the crystallographic structure of a metastable phase of $GaPO_4$ obtained at high pressure. Our theoretical study leads to a phase transformation of the quartz form to a metastable orthorhombic form with $Pmn2_1$ space group, in agreement with the experimental data (XRD & IR). The second theme considers the different phase transformations of silicon disulfide induced by pressure from 0 to 500 GPa. Above 200 GPa, 8-coordinated Si phases are proposed as stable structures.

Part of the Ba-N and SiS_2 topics have been partially developed by two co-supervised students from Northwestern Polytechnic University, during their international research exchange program in 2016, Mr. Le Wang and Mr. Shipeng Gong, respectively (6 months in Dr. Gilles Frapper's Lab).

We finish off with a general conclusion.

1. Methods

1.1 Crystal structure prediction methods

"If you want to understand function, study structure!"

Francis H. Crick, 1988.[2]

"One of the continuing scandals in the physical sciences is that it remains impossible to predict the structure of even the simplest crystalline solids from a knowledge of their composition."

John Maddox, 1988[3]

Various researchers, coming from diverse fields of Sciences - physics, chemistry, mathematics, …, have tried hard to overcome this scandal denunciated by John Maddox 30 years ago. In 1994, physicist Angelo Gavezzotti tried to answer the question "*are crystal structures predictable?*" by just writing down "NO!".[4] In 2003, Jack D. Dunitz summarized the state of affairs *'The one word answer to the title is still "No", although, at certain levels of discussion, a "Maybe", or even a conditional "Yes", may be entertained as possible responses'*.[5]

Prediction is always a difficult task if one wants to predict a crystal structure from knowing only its chemical composition. Let's illustrate the complexity of such a goal. Imagine a cube of 10*10*10 Å^3, a crude model of a unit cell. Just put one atom in it, and let's consider that 1 second of computing time is needed to calculate the total energy of the associated ground-state system (*i.e.*, MM, force fields, DFT calculations). However, a typical chemical crystal structure has at least 10 atoms per unit cell. Now, it will take 10^{11} seconds to compute all structural configurations of such a system;[5] from this data, one may determine, from the computed potential energy surface (PES), the localization of the global minimum, *i.e.* the lowest point of energy, corresponding to the, so-called, global optimized structure. If we increase the size of the system: with 20 atoms per unit cell, the CPU time would increase to 10^{25} seconds, larger than the age of the universe! We are in trouble. One can see the need for an automatic and efficient crystal structure prediction

(CSP) method. In the last ten years, the situation has changed dramatically: several CSP methods have appeared which give successful predictions in materials science.[5–7]

Before we start a brief presentation of actual CSP methods, we need to underline that the CSP is mainly the combination of two procedures: the local optimization and the global optimization. The first step concerns the structural and energy optimization of a given crystal structure to reach the equilibrium state, by using appropriate interatomic potentials, electronic structure techniques, and an energy minimization algorithm. This procedure means that we already have a rough idea about the structure: the primary chemical topology should be known. For example, the initial guess state of H_2O is located at the red point in *Figure 1.1*, while the black point represents the equilibrium state.

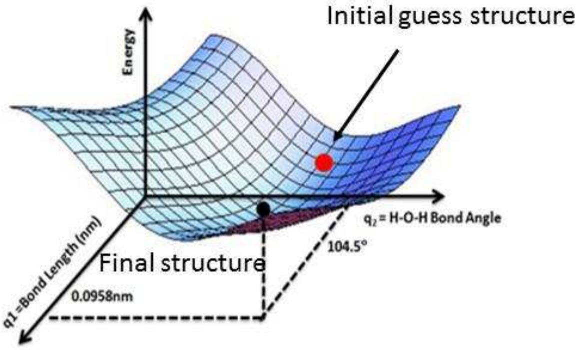

Figure 1.1 Local potential energy surface of H_2O molecule (From Wikipedia).

In other words, an approximate structure guess should be given as a starting point, and also not to far from the stationary point. Many crystal structures have been proposed using this heuristic approach, for example, taking a well-identified and characterized structure, one may predict a new one by changing the nature of the atoms - the isostructural and isoelectronic phase would then be optimized. We see that this step does not correspond to a full prediction of a crystal structure by knowing only its chemical formulae, because of all possible local minima of the PES are not explored, thus the lowest energy is not determined. One needs to use an efficient CSP technique to explore the energy landscape of a given chemical composition, and to locate with efficiency the lowest energy structure. Due to the tremendous number of potentially atomic arrangements (roughly ~10^N seconds for an N-atoms system), one has to solve this global optimization problem mathematically. Several global optimization algorithms have been devised, and used with some success for CSP. We will present these technics in the following section.

1.1.1 Global optimization

Exploring the energy landscape

When a crystal contains multiple atoms, the generation of structures requires an efficient algorithm in order to explore the structural configuration space and to identify the low-energy structures. In general, these procedures will involve exploring the, so-called, 'energy landscape' (See *Figure 1.2*).

Free energy landscapes, in chemical systems, have an overwhelming number of local minima separated by high barriers, but only a tiny fraction of the landscape is of any chemical interest. The deepest minimum usually has the greatest surface area, and is thus easier to obtain than any single local minimum. Most of the low-energy minima are located in the same region of the landscape, which gives an overall shape to the landscape, and stems from the fact that most of the good structures have similar bond lengths and coordination environments of the atoms. What's more, low-lying free energy minima are usually separated by low energy barriers.

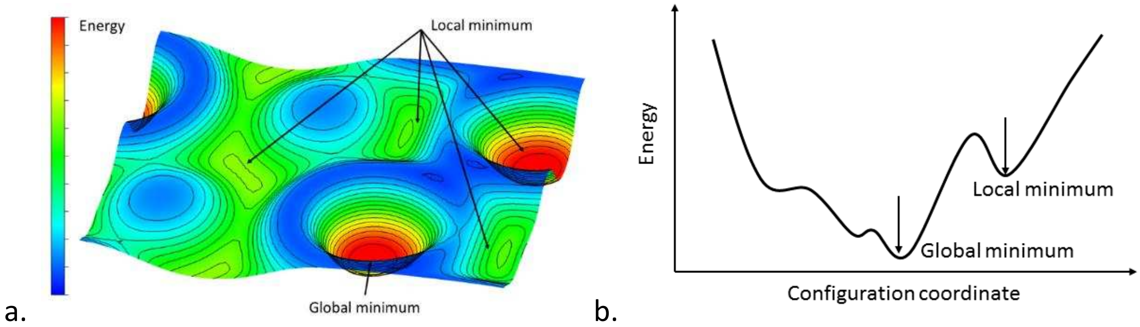

Figure 1.2 (a) Two-dimensional, (b) one-dimensional potential energy surface.

Therefore, different types of crystal structure prediction methods, with inherently different ways of approaching this difficult task, are proposed.[8–15] Most methods designed for crystal structure prediction, such as simulated annealing, metadynamics, minima hopping, and genetic algorithms, have focused on overcoming the free energy barriers. Usually, in these methods, one starts within a suitable region of configuration space, then explores its neighborhood by moving across a barrier into a nearby local minimum, hoping to discover a new good minimum. Below is an overview of several successful CSP algorithms.

a. Random search

From its name, we can easily understand the idea behind the random search algorithm: randomly generate some structures; locally relax this structure; and repeat the first two steps until the lowest-energy structure remains unchanged. This method has been around for decades, and has found applications in different kinds of optimization issues. Recently, it has been applied, with great success, in crystal structure prediction, as well as for molecular systems.[14,15] For example, Pickard *et al.* predicted structures of calcium and magnesium carbonate at high pressures using Ab initio Random Structure Searching (AIRSS),[16] and Pulido *et al.* identified a highly porous solid with the lowest density reported for a molecular crystal.[6]

Apparently, the crucial advantage of this method is its simplicity and ease of implementation. Few variation operators are required during the structural generation. Its achievement is based on the assumption that the energies of local minima correlate strongly with the size of their catchment basins, *i.e.*, low-lying minima are surrounded by a large basin of attraction. The superiority of random search is unbias. Random search has been found to correctly and reliably predict structures with low energies, for small systems, to a somewhat moderate number of degrees of freedom. However, larger systems have more complex energy. Thus, random search is less efficient in time and does not guarantee that the ground state will ever be found.

b. Simulated annealing

The theory behind simulated annealing[9,17,18] is based on the application of annealing in metallurgy, where people apply it to reduce defects and obtain larger single crystals. Annealing, in metallurgy and materials science, is a heat treatment that alters the physical, and sometimes chemical, properties of a material. It involves heating a material to above its recrystallization temperature, maintaining a suitable temperature, and then cooling. The average kinetic energy of the atoms is increased after heating, thus enabling them to diffuse quickly. The system can cross over high energy barriers, towards preferably lower energy structures. The controlled cooling process allows the atoms to rearrange themselves into their ground state structure.

Simulated annealing is a thermodynamic approach which mimicks this physical process. The simulation starts from an initial configuration; then the atoms are equilibrated at a high constant temperature through the Monte Carlo method, or molecular dynamics, where periodic local quenching is performed. After that, by gradually cooling the system, the structure moves towards lower energy phases. Finally, if thermodynamical equilibrium is preserved throughout the cooling process, the system will crystallize at the ground state. However, in practice, this method is only applicable for simple energy landscapes, since the system can easily get trapped in a local minimum, *i.e.*, metastable structure, especially if this structure is cycled through a very high energy barrier. Therefore, the selection for the initial structures has significant influence to the whole simulation. The simulated annealing approach has been applied to predictive studies of inorganic solids.[10] Mellot-Draznieks *et al.* predicted the inorganic-organic hybrid structure, which was synthesized in the experiment.[19]

c. Minima hopping

The minima hopping method[20] is an efficient algorithm that finds the global minimum structure by minimizing the potential energy of a complex system. In other words, this algorithm is designed to reduce the energy barrier to avoid being trapped in local minima. This method is not based on the thermodynamic principles that simulated annealing algorithms are, but on the fact that, by exploring the low energy part of the PES as fast as possible, the global minimum will be revealed at some point.

Among the low energy configurations, many local minima separated by potential barriers have to be examined. The minima hopping simulation starts with an arbitrary configuration in a specific funnel on the PES. Due to high barriers surrounding the funnel, the system will be trapped within the lowest minima within the funnel. The minima hopping algorithm is based on two primary principles to avoid trapping by a built-in feedback. It recognizes the regions that have previously been visited. In this case, the program makes more violent moves which will force it to explore different regions of the configurational space. Secondly, it exploits the Bell-Evans-Polanyi principle[21] for the moves from one catchment basin into another one. Minima hopping has, up to now, mainly been applied to the structural determination of non-periodic systems, such as silicon clusters,[20,22] doped silicon fullerenes,[23] and large gold clusters,[24] but it could be equally as well applied to periodic systems.

d. Evolutionary algorithm

The evolutionary algorithm (EA) is inspired by Darwin's natural evolutionary theory by taking advantage of slight successive variations. Genetic algorithm is a class of EA, whereby a populations of the best (fittest) individuals are most likely to survive. They have been successfully applied to different ranges of optimization, including global optimization in materials science.

To mimic the multiplication of nature, the EA is usually encoded in binary form but could be ternary, or even higher. Initially, a set of individuals is randomly generated as the population of the first generation, and each one is evaluated according to its fitness. By variation operations, such as random mutation or by the recombination of two individuals based on their fitness, a new offspring of solutions is created. By iterating this algorithm, the overall fitness of each generation is improved, thus leading towards the optimal solution of the problem. Even though the fitness of the individual solutions is usually given by the free energy or enthalpy of the structures in EA, structures can also be optimized concerning other variables, such as volume and hardness.

In 1995, Bush *et el.* reported the first attempt in EA for the Li_3RuO_4 ternary using a general purpose structure prediction program with rather limited success rates.[25] Since then, progress on EA crystal structure prediction has been made, through the adoption ofimproved representation schemes. Successful implementations are available including USPEX[8,13,28–30], XtalOpt[26] and Calypso[7,27]. In particular, the evolutionary algorithm, developed by Oganov *et al.* in 2006, is one of the successful methods of crystal structure prediction, and will be discussed in the following section.

Up to now, several global optimization algorithms have been devised to explore the global minimum of the free energy surface. The simulated annealing, basin hopping, and minima hopping approaches start within a good region of configuration space. Only evolutionary algorithms locate, step by step, the best structures. Among all these groups of methods, the advantage of evolutionary simulations is that they do not necessarily require any specific knowledge, apart from chemical composition, and are self-improving.

1.1.2 USPEX algorithm

In contrary to the EA,[31–33] USPEX represents lattice vectors and atomic coordinates by real numbers, which enhance the learning power of the algorithm. For structural optimization, they use conjugate-gradients, or steepest-descent methods, which are available in many *ab initio* and molecular dynamics codes. Currently, USPEX can interface with VASP and SIESTA, GULP, LAMMPS, as well as some other programs.

Few minimal inputs are required to initiate a USPEX calculation:

a. The number of atoms of each element

b. Pressure-temperature conditions

c. The size of the population in one generation

d. Constraints (Inter-atomic distance, cell angle)

e. The percentage of structures are reproduced by variation operators

Initialization of the first generation, a set of fair points in the search space that satisfy the constraints. Then determine the quality for each member of the population using the fitness function (Interface with DFT or MD codes). The program selects the fine structures from the current generation as parents, from which the algorithm creates new offspring in the search space, by applying specially designed variation operators to them. After that, an evaluation of the quality for each new member of the population is undertaken. It selects the excellent offspring to build the new generation of the population. Finally, repeat the last three steps until the halting criteria is achieved.

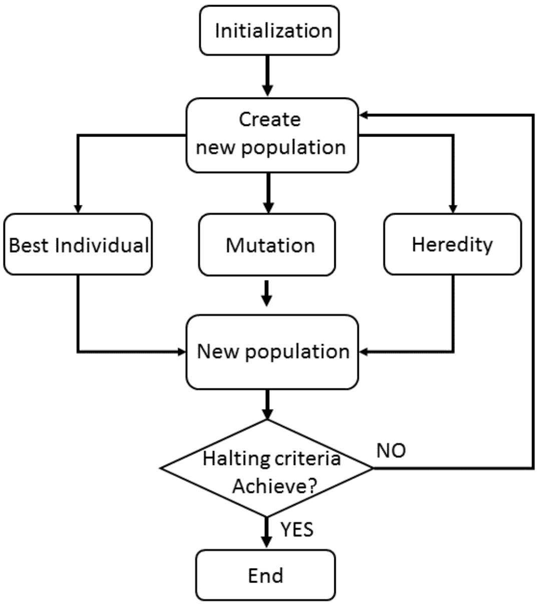

Figure 1.3 Block scheme of USPEX.

1.1.2.1 Variation operators

According to the law developed by Darwin, only the superior quality offspring can survive. An important section of the EA is to carry the good gene to the next population. In USPEX, such transportation is done by, so-called, variation operators. Most of the time, the choice of variation operators follows naturally from the representation and the nature of the fitness landscape, while the others may not be inspired by physical processes. Here several variation operators are presented in brief.

a.Heredity

Heredity is an essential part of the EA approach. The algorithm randomly chooses the lattice vector and a point on that vector. Then the unit cells of the parent structures are cut by the plane, parallel to other vectors that go through this point. Finally, match the planar slices and adjust the number of atoms consistent with previous structures.

b. Lattice mutation

The fixed position of atoms remains unchanged. Applies a strain matrix, with zero-mean Gaussian random strains, to the lattice vectors. This operator allows the algorithm to investigate the neighborhood of competent individuals.

c. Permutation

Fixes the lattice and swaps chemical identities of atoms in randomly selected pairs. Such swaps provide the algorithm with steps in the search space that are very far away, and difficult, in the Euclidean distance. This operator is especially useful for systems with chemically similar atoms.

d. Rotational mutation

Because a large rotation can have a marked effect on global optimization, it helps the system to jump out of the present local minimum. Rotational mutation rotates a certain number of randomly selected molecules by random angles. This operator is useful for molecular crystal systems or clusters.

e. Soft mutation

Displace atoms along the softest mode eigenvectors, or a random linear combination of softest eigenvectors. To calculate the softest modes, they construct the dynamical matrix from bond hardness coefficients.[34,35]

1.1.2.2 Variable composition searches

Another important feature distinguished with other code is the variable composition searches technique. Take the Calypso[7,27] as an example; users have to specify the individual stoichiometry manually. However, people prefer to use stoichiometries that they are familiar with. Thus, omitting of some 'strange' composition is unavoidable, *e.g.*, BaN_{10} discussed in chapter 3.4. Variable composition searches enable simultaneous prediction of all stable stoichiometries and structures. A pioneering study was performed by Jóhannesson *et al.*[36], who succeeded in predicting stable alloys within a given structure type. However, a simultaneous search for stable structures and compositions is much more challenging when dealing with a complicated landscape consisting of compositional and structural coordinates. Therefore, a proper fitness should be devised to evaluate the quality of structures that have different compositions, *i.e.*, convex hull.

1.1.2.3 Fitness: representation as a convex hull

In 2008, Oganov *et al.*[265] implemented the variable composition function in USPEX code. This new function requires a series of modification of the standard EA approaches. The enthalpy is not the only criterion in the variable composition prediction. We cannot determine the thermostability of two different stoichiometries by merely comparing their enthalpies. For a system with a given chemical formula, the optimizing target only involves energy per formula unit. When people want to search the whole area of the binary or ternary phase diagrams, the stability can be evaluated by the formation of energy towards the decomposition into mixtures of other compounds. For binary system, the energy of formation of A_xB_y can be expressed as

$$E_f = E_{AB} - xE_A - (1-x)E_B \qquad Eq\ 1.1$$

where E_A and E_B correspond to the energy of the elemental A and B. Cleary E_f is a function of the compositional ratio x, and its calculation requires the knowledge of E_A, E_B, and E_{AB}. Stable compounds have the negative energy of formation. If we draw the plot of $E_f(x)$ for a series of stoichiometries, any structure with negative E_f is stable towards decomposition to its elements.

As structure A_xB_y, stable against decomposition into A and B, is below the line drawn from A to B. Connection of all the thermodynamically stable compounds form a convex hull as shown in *Figure 1.4*. Thus, the fitness in variable composition searches can be defined as the minimum vertical distance from the convex hull.

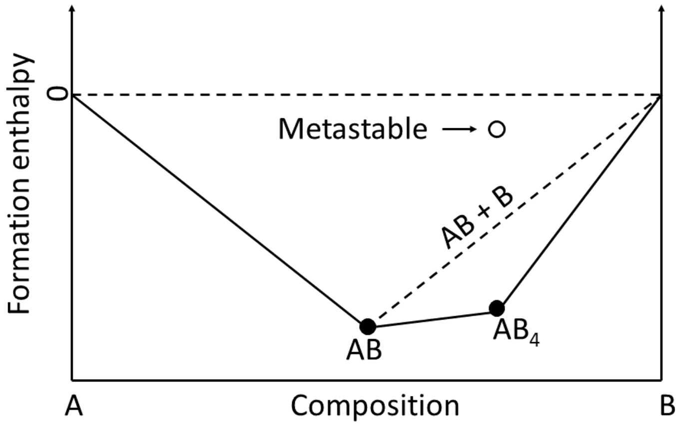

Figure 1.4 Binary convex hull.

1.2 First principles calculations

We have seen that, in CSP, a local optimization step is needed. Local optimization drives the initial configuration, - atomic arrangement - to the state of local energy minimum (see *Figure 1.2*). Thus, one has to evaluate precisely the net-atomic force on each atom, and then a numerical energy minimization technic finds an arrangement in the space of the atoms, where the position on the PES is a stationary point (net-atomic forces close to zero). Here we chose to use a DFT approach to evaluate the forces and total energies. This section will introduce the first principles foundation and DFT based methods used in our researches.

The many-body Schrödinger equation

In the *ab initio* calculation, the ultimate goal is the solution of the time-independent non-relativistic Schrödinger equation,

$$\hat{\mathrm{H}}\Psi = E\Psi \tag{Eq 1.2}$$

where $\hat{H}$ is the many-body quantum mechanical Hamiltonian operator, E is the total energy and Ψ is the many-body wavefunction. The wavefunction is a complex mathematical object that, neglecting spin, depends on all of the spatial coordinates of the electrons (r_i) and nuclei (R_i) in the system, $\Psi(r_1, \ldots, r_n, R_1, \ldots, R_N)$. The Hamiltonian operator is presented as *Eq 1.3*.

$$\hat{\mathrm{H}} = T_N + T_e + V_{Ne} + V_{NN} + V_{ee} \tag{Eq 1.3}$$

T_N and T_e, are the kinetic energy operators for the electrons and nuclei respectively. The last three operators represent the nuclear-electron (V_{Ne}), nuclear-nuclear (V_{NN}) and electron-electron (V_{ee}) interactions. Therefore, we can express the many-body Hamiltonian as:

$$\hat{\mathrm{H}} = -\frac{\hbar^2}{2}\sum_{I=1}^{N}\frac{1}{M_I}\nabla_i^2 - \frac{\hbar^2}{2m_e}\sum_{i=1}^{n}\nabla_i^2$$

$$+\frac{e^2}{4\pi\varepsilon_0}\left[-\sum_{i=1}^{n}\sum_{I=1}^{N}\frac{Z_I}{|r_i - R_I|} + \sum_{I=1}^{N}\sum_{I>J}^{N}\frac{Z_I Z_J}{|R_i - R_j|} + \sum_{i=1}^{n}\sum_{i>j}^{n}\frac{1}{|r_i - r_j|}\right] \tag{Eq 1.4}$$

where n and N are the number of electrons and nuclei in the system, respectively. The electron mass is m_e and e is the elementary charge, the mass and charge of nucleus I are M_I and Z_I respectively, and ε_0 is the vacuum permittivity.

Born-Oppenheimer Approximation

In principle, everything about the system is known if we can solve the Schrödinger equation. However, due to the complexity of an atomic system, it is not possible to solve the equation in practice. In 1927 Born and Oppenheimer developed a so-called Born-Oppenheimer (BO) approximation[37] which separates the movement of nuclei and electrons. Since the nuclei are much heavier than electrons, the nuclei move much slower than the electrons; it is reasonable to consider the positions of nuclei are fixed. Thus the total wavefunction can be expressed as:

$$\Psi(\{R_I\},\{r_i\}) = \Theta(\{R_I\})\phi(\{r_i\},\{R_I\}) \qquad Eq\ 1.5$$

where $\Psi(\{R_I\},\{r_i\})$ is the total wavefunction of the system, $\Theta(\{R_I\})$ and $\phi(\{r_i\};\{R_I\})$ describe the nuclei and the electrons separately.

$$\hat{\mathrm{H}}_{tot}\Psi(\{R_I\},\{r_i\}) = E(\{R_I\},\{r_i\}) \qquad Eq\ 1.\ 6$$

According to the BO approximation, the time-independent Schrödinger equation can be divided into two separate Schrödinger equations *Eq 1.7* and *Eq 1.9*:

$$\hat{\mathrm{H}}_e\phi(\{r_i\};\{R_I\}) = V(\{R_I\})\phi(\{r_i\};\{R_I\}) \qquad Eq\ 1.7$$

where

$$\hat{\mathrm{H}}_e = -\sum_i \frac{\hbar^2}{2m_e}\nabla_r^2 + \frac{1}{2}\sum_{\substack{I,J\\ I\neq J}} \frac{Z_I Z_J e^2}{|R_I - R_J|} + \frac{1}{2}\sum_{\substack{i,j\\ i\neq j}} \frac{e^2}{|r_i - r_j|} - \frac{1}{2}\sum_{I,i} \frac{Z_I e^2}{|R_I - r_i|} \qquad Eq\ 1.8$$

and

$$\left[-\sum_I \frac{\hbar^2}{2M_I}\nabla_{R_I}^2 + V(\{R_I\})\right]\Theta(\{R_I\}) = E'\Theta(\{R_i\}) \qquad Eq\ 1.9$$

Eq 1.7 is the equation for the electronic problem where the nuclei positions are fixed. After solving *Eq 1.7*, $V(\{R_I\})$ is known and by applying it to *Eq 1.9* which has no electronic degrees of freedom, the motion of the nuclei is obtained. *Eq 1.9* is sometimes replaced by a Newton equation.

The BO approximation separates the movement of electrons and nuclei, so that we can consider that the electrons move in a static external potential $V_{ext}(r)$ formed by the nuclei. Born and Huang then extended the BO approximation, known as Born-Huang (BH) approximation[38], to take into account more nonadiabatic effects in the electronic Hamiltonian than in the BO approximation.

1.2.2. Density functional theory

The core idea of DFT is to make use of an exact reformulation of the problem that features the many interacting electronic charge density as the fundamental variable instead of the wavefunction. According to the theory, all the properties of the system can be thought of as a function of the ground state density (*i.e.*, any property is a function of the density). To put it another way, knowing the ground state density is equivalent to knowing the wavefunction for the ground state, and all excited states as well. As we build to the Kohn-Sham formalism, we no longer require the Hamiltonian operating on a 3N-dimensional wavefunction. We can work with independent particle wavefunctions and can derive all the attributes of our system from scalar functions of density in three dimensions.

As suggested by the BO approximation, it is typical to consider the electrons separately from the nuclei. The nuclei are often abstracted as an external potential V_{ext}, in which the electrons relax into their ground state. The ionic kinetic and self-interaction potential energy are considered separately. The Hamiltonian for the electrons, therefore, becomes:

$$\hat{H}_e = -\frac{\hbar^2}{2m_e}\sum_i \nabla_i^2 + \sum_i v_{ext}(r_i) + \frac{1}{2}\sum_{i\neq j}\frac{e^2}{|r_i - r_j|} \qquad Eq\ 1.10$$

This complex, multi-body problem cannot be broken up into simpler single-body equations due to the electron culombic self-interaction term.

Hohenberg-Kohn theorems

The Hohenberg-Kohn (HK) theories[39] provide an initial step toward a solution to this problem by assigning a particular significance to the ground state particle density. The modern density-functional theory was born in 1964, with the work of Hohenberg and Kohn. The approach of HK is to formulate DFT as an exact theory of many-electron systems. The HK approach is based on two theorems:

Theorem I: For any system of interacting particles in an external potential $v_{ext}(r)$*, the total energy is determined uniquely (up to an additive constant) by the ground-state particle density* $n_0(r)$*.*

Theorem II: A universal functional for the energy in terms of the density n(r) can be defined, valid for any external potential $v_{ext}(r)$*. For any particular potential, the exact ground-state energy* *of the system is the global minimum of this functional, and the density n(r) that minimizes the functional is the exact ground-state density $n_0(r)$.*

As a result, the energy functional has the following form:

$$E[n(r)] = F_{HK}[n(r)] + \int v_{ext}(r)n(r)dr \qquad Eq\ 1.11$$

and the universal HK function is represented as:

$$F_{HK} = T[n(r)] + V_{ee}[n(r)] \qquad Eq\ 1.12$$

where $T[n(r)]$ is the kinetic-energy functional, and $V_{ee}[n(r)]$ is the electron-electron interaction functional. The HK theorems is a one-to-one correspondence between the external potential and the ground-state density. Therefore, we can have a universal functional which is defined for any density. Besides, by minimizing this functional, we could find the exact density and energy of the true interacting many-body system. Then, if F_{HK} was known, the task of evaluating all of the properties of a system with a given external potential should be reduced to minimizing the energy functional of the 3-dimensional electron density. This provides the fundamental concept upon which all practical DFT calculations are built up. The most practical scheme is known as the Kohn-Sham (KS) method, proposed by Kohn and Sham in 1965.[40]

Kohn-Sham formalism

We understand that HK theorems allow us to use a straightforward ground-state electronic density, instead of the complicated many-body wavefunction and the associated Schrödinger equation. However, the Hohenberg-Kohn theorem only proves the existence of F_{HK}, and does not provide a way to determine its form. The problem now lies in finding a suitable computational scheme that allows us to determine the ground state density, as well as all the other physical properties of the system in question.

Kohn and Sham[40] developed a computational scheme in which the interacting electron system is embedded into a system of non-interacting independent particles. Therefore, we consider the electrons move within an effective Kohn-Sham single-particle potential $V_{KS}(r)$.

Moreover, assume that the original, many-body system, and this independent-particle system, have precisely the same ground state density. The density is then constructed as the sum of the individual particle densities of the Kohn-Sham eigenfunctions. For the auxiliary independent-particle system, the Hamiltonian is:

$$\hat{\mathrm{H}}_{KS} = -\frac{1}{2}\nabla^2 + V_{KS}(r) \qquad Eq\ 1.13$$

For a system with *N* independent electrons, the ground state is obtained by solving the *N* one-electron Schrödinger equations:

$$\left(\frac{1}{2}\nabla^2 + V_{KS}(r)\right)\Psi_i(r) = \varepsilon_i\Psi_i(r) \qquad Eq\ 1.14$$

where there is one electron in each of the *N* orbitals $\Psi_i(r)$ with the lowest eigenvalues ε_i. Then the density of the auxiliary system is constructed from:

$$n(r) = \sum_{i=1}^{N}|\Psi_i(r)|^2 \qquad Eq\ 1.15$$

The non-interacting independent-particle kinetic energy $T_S[n(r)]$ is given by:

$$T_s[n(r)] = -\frac{1}{2}\sum_{i=1}^{N}\int \Psi_i^*(r)\,\nabla^2\Psi_i(r)dr \qquad Eq\ 1.16$$

Then the universal functional $F[n(r)]$ was rewritten as:

$$F[n(r)] = T_s[n(r)] + E_H[n(r)] + E_{XC}[n(r)] \qquad Eq\ 1.17$$

where $E_H[n(r)]$ is the classic electrostatic energy of the electrons:

$$E_H[n(r)] = \frac{1}{2}\iint \frac{n(r)n(r\prime)}{|r-r\prime|}drdr' \qquad Eq\ 1.18$$

and $E_{XC}[n(r)]$ is the exchange-correlation functional energy, which contains the difference between the exact and non-interacting kinetic energies, and also the non-classical contribution to the electron-electron interactions. The KS one-particle potential is:

$$V_{KS}(r) = V_{ext}(r) + V_H(r) + V_{XC}(r) \qquad Eq\ 1.19$$

The Hartree potential $V_H(r)$ is represented as:

$$V_H(r) = \frac{\delta E_H[n(r)]}{\delta n(r)} = \int \frac{n(r')}{|r-r'|} dr' \qquad Eq\ 1.20$$

and the XC potential is:

$$V_{XC} = \frac{\delta E_{XC}[n(r)]}{\delta n(r)} \qquad Eq\ 1.21$$

Equations *Eq 1.14, Eq 1.15* and *Eq 1.19* together are the well-known KS equations, which must be solved self-consistently, because $V_{KS}(r)$ depends on the density through the exchange-correlation potential. To calculate the density, the *N* equations in *Eq 1.15* have to be solved in KS theory, as opposed to one equation in the TF approach. However, an advantage of the KS method is that as the complexity of system increases, due to *N* increasing, the problem becomes no more difficult, only the number of single-particle equations to be solved increases.

1.2.3 The exchange-correlation functional

Although, in principle, the KS theory is approximate in practice because of the unknown exchange-correlation energy functional $E_{XC}[n(r)]$, an implicit definition of $E_{XC}[n(r)]$ can be given as:

$$E_{XC}[n(r)] = T[n(r)] - T_S[N(r)] + E_{int}[n(r)] - E_H[n(r)] \qquad Eq\ 1.22$$

where $T[n(r)]$ and $E_{int}[n(r)]$ are the exact kinetic and electron-electron interaction energies of the interacting system respectively. It is crucial to have an accurate exchange-correlation energy functional $E_{XC}[n(r)]$ or potential $V_{XC}(r)$ to give a satisfactory description of a realistic condensed-matter system. Currently, the most widely used approximations for the exchange-correlation potential are the local density approximation (LDA) and the generalized-gradient approximation (GGA).

Generalized gradient approximation (GGA)

Due to the limitation of LDA, another advanced way to progress is to include, not only the local density, but also the local density gradient, in what is called the generalized gradient approximation (GGA). The gradient of the density at a point as well:

$$E_{XC}^{GGA}[n] = \int n(r)\varepsilon_{xc}(n(r), \nabla n)dr \qquad Eq\ 1.23$$

Exchange and correlation are now semi-local functions; the degree of non-locality depending on the electron density. For high densities, exchange dominates correlation, which is true in a physical system, but not in LDA. For a fixed density, as the gradient of the density increases, exchange interactions give a more significant energy benefit. For most common densities, the non-locality of the exchange becomes so beneficial that GGA favors density in-homogeneity more than LDA. Only for low densities does correlation start to compare with exchange effects; as the density goes to zero, the GGA exchange-correlation hole eventually becomes as local as LDA.

GGA functionals tend to improve total energies and structural energy differences over LDA. They are more accurate in determining the binding energy of in-homogeneous systems, like molecules, which historically lead to the widespread acceptance of DFT in the chemistry community. They tend to favor non-uniform density more than LDA, which tends to soften bonds, an effect that sometimes corrects and sometimes overcorrects the LDA prediction.

One of the major drawbacks of the LDA and GGA is the self-interaction error. Because in LDA and GGA each electron interacts with the density through the Hartree and exchange-correlation potentials, but each electron also contributes to the density. This self-interaction is strictly unphysical. The self-interaction error is apparently far worse for localized states, and DFT often fails in describing systems with open-shell d and f orbitals. However, they are still among the most influential computational tools of modern condensed matter physics. The GGA functional that is used within this paper was developed by Perdew, Burke and Enzerhof. [41,42]

Hybrid functionals

The problem with local and semi-local functionals is that they are too restrictive to reproduce all the effects of the exchange-correlation functional. A local (or semi-local) exchange operator cannot completely wipe out self-interaction error. Becke first proposed another attractive approach in 1993[43], known as the hybrid functional method, in which the exchange-correlation potential (V_{XC}) is calculated by mixing V_{XC} from a DFT calculation with a fraction of exact Hartree-Fock exchange.

In principle, any exchange functional can be combined with any correlation functional. A fraction of exact exchange can be added to conventional GGA. A general form for hybrid GGAs can be written as:

$$E_{XC}^{Hybrid} = \alpha E_X^{EXX} + (1-\alpha)E_X^{GGA} + E_C^{GGA} \qquad Eq\ 1.24$$

where E_X^{EXX} represents the exact exchange, and the coefficient α reflects the amount of the exact-exchange mixing, which can be defined semi-empirically or using perturbative arguments from the adiabatic connection formalism. Hybrid functionals have gained wide popularity in quantum chemistry, due to their improved predictions for many molecular properties relative to local and semi-local functionals.

However, the application of hybrid schemes to extended systems is computationally challenging because of the consideration of HF exchange. Recently, a set of screened hybrid functionals, obtained by the use of a screened Fock exchange operator, such as HSE06[44,45], addressed this problem by separating the exchange interaction into a short-range and a long-range part. To date, these developments have allowed hybrid functionals to become popular in solid-state physics.

1.2.4 Pseudopotentials

As the chemical properties of most atoms are determined by their valence electrons, it is desirable to replace the core electrons together with the strong ionic potential. The pseudopotential is identical to the actual potential outside the core radius. The nodes of the actual wavefunction are removed inside the core radius, but at the same time, the norm of the wavefunction, and with it all scattering properties of the full system, is preserved. The pseudo wavefunctions should be identical to the all-electron wavefunctions outside the cut-off radius, as shown in *Figure 1.5*.

The accuracy of the pseudopotential calculations is only determined by the energy convergence of the valence electrons, since core electrons are not directly considered. Hellmann originally introduced the pseudopotential approximation in 1934.[266] During the 70s, Hamann and others developed the norm-conserving pseudopotential formalism.[267] The Troullier-Martins and the Rappe-type pseudopotentials are the most widely used in solid-state and surface-science applications.[46,47] With the help of pseudopotential we can achieve a significant reduction of the computational cost, and also maintain an accurate description of most systems at the same time. Furthermore, by giving up the norm conservation, one can reduce the computational effort.

In this thesis, calculations are predominantly carried out using the Vienna Ab-initio Simulation Package (VASP)[48], which is a plane wave DFT code.VASP makes use of the projector augmented wave (PAW) method[49]. The principal advantage of the PAW approach is that it allows for the pseudized valence wavefunctions to retain their complex structure near the atomic cores, while still allowing for them to be expanded regarding a plane wave basis set. It has to be mentioned that the pseudopotential is constructed from an exact, all electron calculation of the free atom. The chosen core radius influences the transferability of the pseudopotential to molecular or bulk systems, and has to be verified. Furthermore, in order to avoid significant errors, the exchange-correlation functional has to be the same when constructing and applying the pseudopotential approximation.

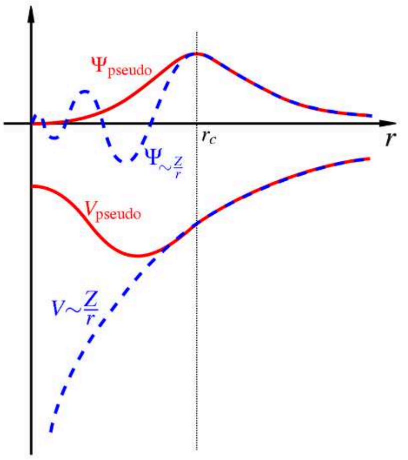

Figure 1.5 Comparison of a wavefunction in the Coulomb potential of the nucleus (blue), to the one in the pseudopotential (red). The real, and the pseudo wavefunction and potentials match above a certain cutoff radius. (From Wikipedia)

1.2.5 Periodicity and Brillouin zone sampling

To reduce the computation, it is necessary to use periodic boundary conditions as the implementation of DFT. Due to the periodicity of the crystal, the molecular orbitals can be expressed as Bloch waves, which are the product of a lattice periodic function and a plane wave:

$$\phi_{i,k}(r) = e^{ik\cdot r}u_i(r) \qquad Eq\ 1.25$$

where k is the crystallographic wave vector. A key property of the Bloch function is that for any reciprocal lattice vector G:

$$\phi_{i,k+G} = \phi_{i,k} \qquad Eq\ 1.26$$

This equivalence, or non-uniqueness, of k and $(k+G)$ implies that, in a practical DFT calculation, one can restrict k to the first Brillouin zone. All values of k outside of the first Brillouin zone can be shown to be non-unique. The size of the k-point set is further reduced by noticing that some points are equivalent by symmetry. In this work, the scheme of Monkhorst-Pack[50] is implemented to minimize the number of special k-points in the irreducible Brillouin zone.

1.3 Chemical bonding analysis in crystals

When a crystalline structure is identified by CSP, a detailed chemical bonding analysis is needed to understand and rationalize its structural arrangement and electronic properties. To do so, different approaches are envisaged: analysis of band structures; total and projected density of states (DOS); Crystal overlap and Hamilton populations (COHP, COOP); electron local functions (ELF); AIM Bader charges, etc. Moreover, extended Hückel (eHT) calculations have been done on various molecular and solid-state systems to get a clearer picture of the chemical bonding via the use of molecular and crystal orbital theory-based language. Some of these well-known tools are now briefly described.

1.3.1 Band structure and density of states

The electronic band structure of a crystalline phase of a solid describes the range of energies that an electron within the solid may have (called band), or not, thus band gaps may occur. Band structure calculations use the periodic nature of a crystal lattice, exploiting its symmetry. The single electron Schrödinger equation is solved for an electron in a lattice-periodic potential, giving the Bloch waves. The wavevector k takes on any value inside the Brillouin zone, which is a polyhedron in wavevector space that is related to the crystal's lattice (See *Figure 1.6*).

The density of states (DOS) of a crystal structure represents the number of states per interval of energy, at each energy level available to be occupied. It is represented by a density distribution of the various states occupied by the system. The DOS $n(e)$ in an extended system is the number of allowed band orbital levels having an energy e. For the one-dimensional case, $n(e)$ is known to be inversely proportional to the slope of the e as shown in *Figure 1.7*. A great DOS, at a specific energy level, means that there are many states available for occupation. Otherwise, fewer states can be occupied at that energy level.

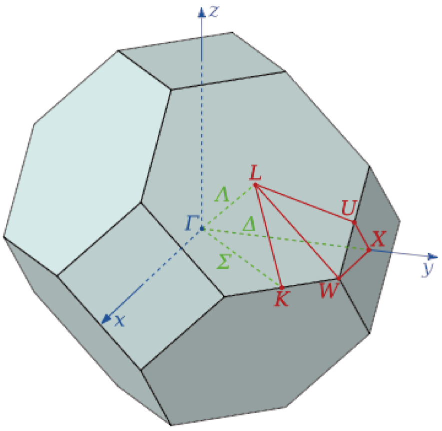

Figure 1.6 Brillouin zone of a face-centered cubic lattice of calcium showing labels for special symmetry points. (From Wikipedia)

The method described in the VASP manual has been employed to plot a band structure and a DOS. A very fine k-meshes is used, up to 12x12x12 grid points for small unit cells, and up to 6x6x6 for large unit cells (at least 10 k-points are required for reasonable values). The vasprun.xml file is visualized using pymatgen (*http://pymatgen.org*). Wigner Seitz radii (RWIGS) may be adapted when atomic and orbital projected DOS is required. Below are the usual steps that we follow using VASP code. (See INCARs in Appendix)

1. Relax the crystal structure to its converged geometry (directory 1)

2. Copy the CHGCAR file in directory 2. Do an SCF calculation with the converged geometry from the previous step; employ a special K-points set for a band structure (an online code to generate the k points of a given Brillouin zoon *http://materials.duke.edu*); increase the number of k-points in KPOINTS file for a DOS

3. Do a non self-consistent calculation using the CHGCAR and WAVECAR of the previous step

1.3.2 Crystal orbital Hamilton population

The crystal orbital Hamilton population, (COHP), analysis was introduced in 1993,[51] a DFT successor of the familiar COOP concept which is based on extended Hückel theory.[52] COHP is a partitioning of the band-structure energy regarding orbital-pair contributions, and it is therefore based on a local basis, *i.e.*, the tight-binding approach, as is commonly used in chemistry and parts of physics as well.

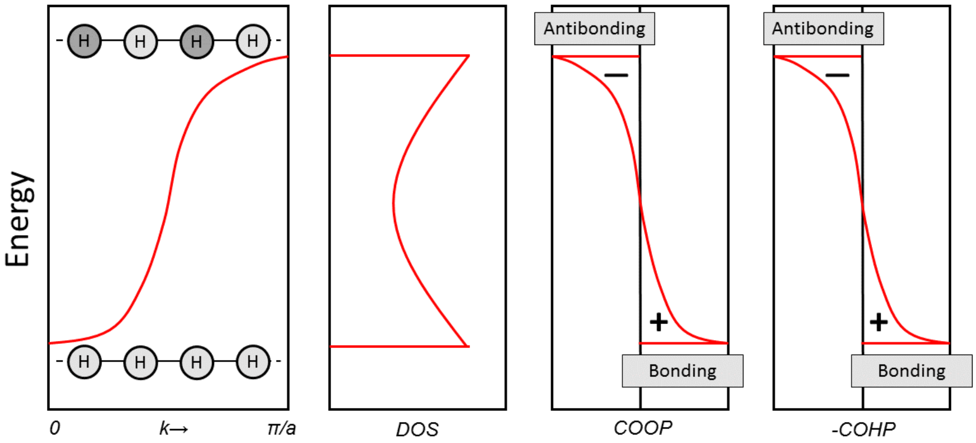

Figure 1.7 Schematic representation of a conceptual bonding analysis.

Given that the interaction between two orbitals, centered at neighboring atoms, is described by their Hamiltonian matrix, the multiplication with the corresponding densities of states matrix then easily serves as a quantitative measure of bonding strength because the product either lowers (bonding), or raises (antibonding), the band-structure energy. Thus, energy-resolved COHP plots make bonding, nonbonding (no energetic effect), and antibonding contributions discernible at first glance, just like the earlier *COOP(E)* plots. There is also a difference in the +/- signs: we recall the bonding is characterized by a positive overlap population; the corresponding Hamiltonian off-site element will be negative. Consequently, antibonding is characterized by a negative overlap population exhibiting positive off-site Hamiltonian elements. In this thesis, the COHP curves are calculated by using the LOBSTER package.[51,53,54]

1.3.3 Bader charge analysis

To accurately describe these complex interactions, and rationalize the calculated energetics, Bader discovered a method using the charge density to divide space within molecular systems into atomic volumes.[55] Each atomic volume, or so-called Bader volume, contains a single charge density maximum, and is separated from other volumes by surfaces on which the charge density is a minimum normal to the surface. The dividing zero-flux surfaces separating these volumes lie in the bonding regions between atoms. Usually, there is one Bader volume for each atom. However, there are cases in which Bader volumes do not contain a nucleus, *e.g.,* electride.

Bader partitioning is more robust than other partitioning schemes (*e.g.*, Mulliken population analysis). There are several different approaches to calculating Bader volumes. Most current implementations of Bader's analysis are based upon a grid of charge density values, which is particularly important for plane-wave-based DFT calculations.[56–59]

1.3.4 Electron localization function

The ELF was introduced by Becke and Edgecombe[60] as a simple measure of electron localization in atomic and molecular systems. It went on to be applied to a great range of systems, from atoms to solids, by Savin *et al.*[61] The original formula was based on the Taylor expansion of the spherically averaged conditional same spin pair probability density to find an electron close to a same-spin reference electron. In DFT, the pair density is not explicitly defined. Savin *et al.* utilized the observation that the Kohn-Sham orbital representation of the Pauli kinetic energy. They defined ELF as a property based on the diagonal elements of the one-particle density matrix, *i.e.*, the electron density.

ELF is a relative measure of the electron localization used to analyze the pair electron localization in the spirit of Lewis structures. High ELF values show that the electrons are more localized than in a homogeneous electron gas, of the same density, at the examined position. The upper limit 1 corresponds to perfect localization, while ELF = 0.5 represents the effect as in a homogeneous electron gas of the same density. *Figure 1.8* represents the ELF of BaN_2 at 0 GPa.

The ELF indicates that the electrons are localized near the atom forming, ironic system. The strong covalent bonding between nitrogen atoms and the lone pair electrons is revealed clearly by the ELF value of 0.8.

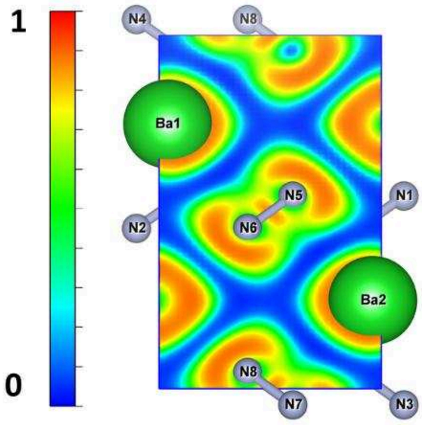

Figure 1.8 ELF of BaN_2 at 0 GPa.

Chemical information can be obtained from ELF attractors, taking the other topological elements into account as well. The attractors can be attributed to bonds, lone pairs, atomic shells and other elements of chemical bonding. However, the attribution is done empirically, which means no direct proof that relates ELF with these conceptual aspects of chemistry. There is no quantum mechanical motivation yet for the definition of a surface of zero flux in the gradient vectors of ELF. The integrated electron density in an ELF basin does not correlate in an obvious manner with the energetic aspects of the bonding. In this work, ELF was calculated using VASP.

1.3.5 Extended Hückel theory

The extended Hückel theory (eHT) was first developed by Hoffmann,[52] It takes account of all valence electrons, including σ and π orbital, and the overlaps between all the atomic orbitals. According to this, it allows the method to remove the unknown Coulomb integral and resonance integral.

In EHT, the Coulomb integral is taken to be the negative of the ionization potential from each electron within the molecule, which is obtained from experiments. Using this value, and the overlap integrals between the atomic orbitals, it is possible to define all the elements of the Hamiltonian numerically:

$$H_{ij} = KS_{ij}\frac{H_{ii}+H_{jj}}{2} \qquad Eq\ 1.27$$

where, S_{ij} is the overlap between the i and j atomic orbital, and K is the Wolfsberg-Helmholtz constant. It is then straightforward to construct and diagonalize the Hamiltonian in order to obtain numerical expressions for the energy levels and eigenvectors of the system.

The crystal orbital overlap population (COOP) serves as the differential version of the bond order concept. It can be used in bonding analysis. The integrated COOP curve up to the Fermi level represents the total overlap population of the specified bond in a solid, whereas the integrated COOP represents the contribution to the total overlap population of those crystal orbitals whose energy levels lie in the range from E to $E + dE$. COOP has positive values (bonding, because of the positive overlap population), and negative values (which identify antibonding interactions).

The calculations are carried out using the tight-binding method within the extended Hückel frameworks implemented in the YAeHMOP package.[62] The number of k-points and overlap used in our calculations has been verified and did not affect the results. The eHT analysis confirmed the results obtained from our DFT calculations. Therefore, we did not detail it in this thesis.

2. Pressure-induced polymerization of CO_2 in lithium-carbon dioxide phases

2.1 Introduction

In the field of CO_2 capture and storage, phase transformation of molecular CO_2 crystals to condensed extended CO_2-based net crystals represents an elegant but industrially irrelevant process. This phase transformation makes sense chemically, at least conceptually. Unsaturated CO_2 species possess lone pairs and/or multiple bonds that may interact with atoms with low coordination numbers in neighboring units, leading to novel covalent C/O oligomers, such as the hypothetical reactive molecular C_2O_4 and C_3O_6 species,[63,64] or even extended 1D and 3D networks.[65–67]

In the late 90's, Frapper and Saillard studied the polymerization of CO_2 using *ab initio* molecular modeling. From a chemist's perspective, they proposed the existence of polymeric CO_2-based chain with 3-coordinated carbon atoms, named poly-$COO_{2/2}$, and of CO_2-based 3D materials with tetrahedral CO_4-based units.[64] In the meantime, several silica-like phases, with tetrahedral CO_4 units sharing common oxygen atoms, were proposed from first-principles and high-pressure investigations.[66,68–70] After which, a plethora of extended covalent CO_2 phases appeared from the condensed-state community. Let's describe these molecular and extended CO_2 phases (See *Figure 2.1*).

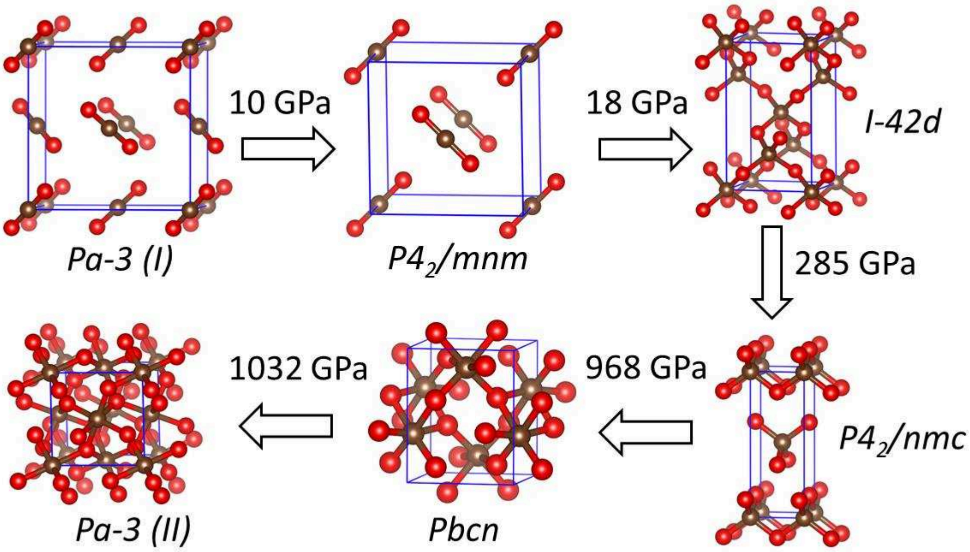

Figure 2.1 Predicted CO_2 pressure-induced phase transitions at 0 K.[66]

The experimental solid-state CO_2 phase has a cubic *Pa*-3 structure at ambient pressure and room temperature, and consists of packed molecular CO_2 (commonly known as dry ice). This phase has been predicted by CSP searches using USPEX (in 2008)[71] and Calypso (in 2013)[66] codes, in perfect agreement with experiments.[72–74] Around 10 GPa, this molecular crystalline structure transforms to a pseudo-tetragonal $P4_2/mnm$ CO_2 molecular crystal phase.[75] Yoo *et al.* characterized this phase, so-called CO_2-II, and discussed tetragonal to orthorhombic (*Pnnm*) distortion by angle-resolved XRD, under pressures up to 100 GPa, and at elevated temperatures.[76] The formation of an extended C-O network is observed in a β-cristobalite like phase with space group *I*-42*d*. In this phase, C and O atoms form CO_4 tetrahedral units with sp^3 hybridized carbon atoms linked by O atoms at the corners. This structure was first proposed by Dong *et al.* in 2000.[268] Oganov *et al.* predicted a $P4_2/mnm \rightarrow I\text{-}42d$ transition pressure at 18.6 GPa.[71] At 285 GPa, the *I*-42*d* structure undergoes a transition into $P4_2/nmc$, as predicted by Lu *et al.*[66] Finally, two 6-coordinated structures, with *Pbcn* and *Pa*-3 space group, are theoretically identified at 968 and 1032 GPa. All of these phases are not quenchable, therefore, alternative approaches should be applied to trap CO_2 in its solid-state.

The mineral carbon dioxide (CO_2) sequestration process on Earth is the “Nature” answer to this CO_2 capture and storage goal. This process involves CO_2 reacting with abundantly available metal oxides, either magnesium oxide (MgO) or calcium oxide (CaO), to form stable carbonates. Magnesite goes together with calcite and dolomite ($CaMg(CO_3)_2$) during the stable phases at ambient conditions. Crystal chemical changes that happen in carbonates under pressure, for example, the increase of coordination numbers and polymerization of carbonates, have been extensively investigated.[77–79] With an enthalpy of formation of -1207 kJ/mol,[80] calcium carbonate/$CaCO_3$(s) is a major thermodynamic sink for CO_2.[81]

Beside this carbonates chemistry, many solid-state compounds based on CO_2 units and s-block elements exist, *i.e.,* an A-CO_2 phase in the oxygen-poor environment? To the best of our knowledge, alkaline oxalates are the only compounds that have been experimentally characterized and synthesized in the s-block element - CO_2 family (See *Scheme 2.1*).

Nevertheless, no experimental or theoretical studies have investigated the structural arrangement of oxalates under high pressure, whereas we have at least this question in mind: does oxalate may polymerize to give infinite chains in A-CO_2 phases under pressure?

Moreover, besides oxalate, could other finite CO_2-based moieties be predicted in binary A-CO_2 phase diagrams? And finally, besides the experimentally known 1:1 composition, such as in $Na_2C_2O_4$, are other composition stable? This is the aim of the present study: to attempt to answer these questions through the help of CSP and DFT calculations.

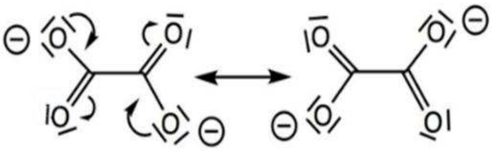

Scheme 2.1 Oxalate dianion is topologically based on two bent CO_2^- units.

The only known natural alkaline oxalate is $Na_2(C_2O_4)$, found together with pyrite, sphalerite, albite, and other minerals.[82] Natroxalate (mineral name of $Na_2(C_2O_4)$) was obtained by the crystallization of the reactive product of Na_2CO_3 with oxalic acid solutions. Jeffrey and Parry first reported the structure of $Na_2(C_2O_4)$, which belongs to the monoclinic crystal system, space group $P2_1/c$, with two formulas in the unit cell. Sodium cation connects to planar oxalates with a distorted octahedral coordination to form a typical ionic compound.

In 1964, Beagley *et al.* reported the crystal structure of lithium oxalate which adopted a similar monoclinic $P2_1/n$ space group.[83] Recently, $K_2(C_2O_4)$, $Cs_2(C_2O_4)$ and $Rb_2(C_2O_4)$, have been reported under ambient conditions using X-ray powder diffraction. $K_2(C_2O_4)$ has an orthorhombic *Pbma* space group, whereas $Cs_2(C_2O_4)$ adopts a monoclinic, $P2_1/c$ space group. Two polymorphic forms were found in rubidium oxalate. The α-$Rb_2(C_2O_4)$ is isotypic to $P2_1/c$ $Cs_2(C_2O_4)$ and β-$Rb_2(C_2O_4)$ is isotypic to *Pbma* $K_2(C_2O_4)$.[82,84]

We have shown that pure extended CO_2 nets are unstable at ambient conditions, and that mixed s-block element-CO_2 phases present only a dimeric motif, oxalate. Thus, alternative conceptual strategies of CO_2 polymerization need to be explored. One approach involves the activation of CO_2 under high pressure, by mixing CO_2 with an electropositive s-block element A, instead of an A_nO metal oxide which may give A_nCO_3 carbonate materials (A, alkaline and earth alkaline metals; $n = 2$ and 1, respectively).

Firstly, following the Zintl-Klemm concept (ZKC) applied to $A_x(CO_2)_y$ solids, the electropositive A atom is expected to give its valence electron(s) to the linear triatomic unit, with each CO_2 formally having a negative charge of $-q$ ($q = nx/y$), thus the degenerated CO_2^{q-} π_u* antibonding levels are occupied. This Jahn-Teller instability is alleviated through bending of the CO_2 molecule.

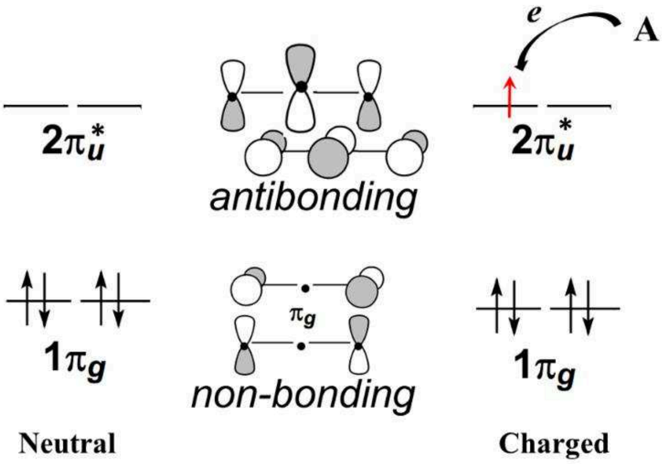

Scheme 2.2 Molecular orbital diagram of the neutral CO_2 and $(CO_2)^-$.

Under high pressure, these activated bent CO_2^{q-} building blocks (illustrated in *Scheme 2.3*) may interact to form novel stabilized molecular-like anions, or even infinite extended CO_2-based nets encapsulated in a cation A^{n+} sublattice. The reverse concept would be to consider electropositive element A as a scissor of C-O bonds in a high-pressure silicate-like CO_2 phase: antibonding σ^*_{CO} becomes occupied, decreasing the dimensionality of the covalent tridimensional

C-O network. These descriptions oversimplify the kinetic and thermodynamic mechanisms that may be in place, but help to rationalize the covalent C/O net dimensionality of the proposed $A_x(CO_2)_y$ crystal structures. Secondly, the s-block element may decrease the pressure required to enable the coupling of the CO_2 units in a compressed volume, as observed in N_2[85] and other unsaturated molecules (CO;[86,87] A-N_2 phases where, for example, A = Na,[88] Mg,[89] N_2O,[90] …). Such A-CO_2 mixing under pressure may lead to original, aesthetic covalent CO_2-based networks. Finally, Madelung electrostatic forces between the $(CO_2)_y^{nx-}$ nets and s-block cations may prevent the escape of CO_2 when pressure is released, *i.e.*, the high kinetic barrier may hinder C-O/C-C bond cleavage in $A_x(CO_2)_y$. Note that this conceptual scheme is reinforced by the existence of oxalate salts.

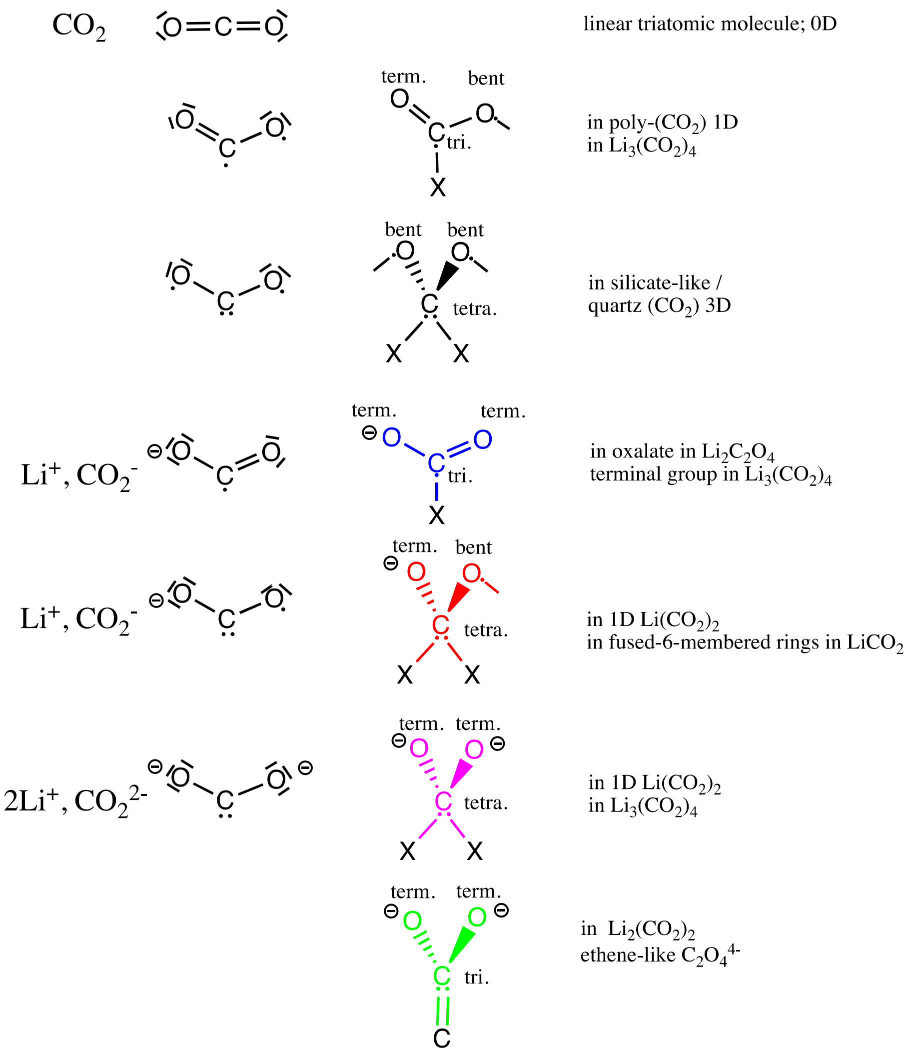

Scheme 2.3 CO_2^{q-} building blocks encountered in solid $Li_x(CO_2)_y$ phases. The corresponding Lewis structures are shown.

Within the family of s-block A-CO_2 solid-state compounds, we sought to investigate the Li-CO_2 phase diagram at finite temperature and pressures up to 100 GPa. Our choice of this system was motivated by the potential applications of our predicted $Li_x(CO_2)_y$ structures in the fields of CO_2 storage and organic materials for lithium-ion batteries. We expect to discover advanced electrode materials which are based on alkaline-oxocarbon. Those organic electrode materials have revealed powerful competence, owing to their intrinsic designability, high abundance, and sustainability. Liu *et al.*[91] indicated that oxocarbon compounds with salted substituents have superiorities of high theoretic capacity and low dissolution. Chen *et al.*[92] reported a renewable $Li_XC_6O_6$ organic electrode displaying a high capacity of 580 mA h g^{-1} in the first cycle. Moreover, $Na_2C_5O_5$ and $Na_2C_6O_6$ were also reported as rechargeable lithium and sodium batteries.[93] The $K_2C_6O_6$ electrode enables ultrafast potassium-ion insertion/extraction.[94] These previous studies have verified the potential interest of oxocarbon salts for energy storage, while the comprehensive investigation of oxocarbon salts with various substituents is required for further research.

Moreover, the effect of high pressure on the experimentally characterized lithium oxalate $Li_2(C_2O_4)$ - the only known composition in the Li-CO_2 phase diagram - is interesting, as it could be expected that the unsaturated oxalate $^-O_2C\text{-}CO_2^-$ anions will create polymeric CO_2-based networks more easily than triatomic carbon dioxide. The present work sought to identify which topological CO_2-based net would lead to this polymerization process.

To predict (meta)stable $Li_x(CO_2)_y$ phases, we performed an extensive structural search on $Li_x(CO_2)_y$ up to 100 GPa. We used *ab initio* techniques to map the high-pressure phase diagram of the Li-CO_2 binary system, by exploring the compositional and configurational space of $Li_x(CO_2)_{y,}$ using an evolutionary structure prediction method in combination with density functional theory (DFT; see Computational details). With the help of molecular orbital bonding analysis, the valuable ZKC and VSEPR rules were used to rationalize the observed formulas, shapes and chemical bonding of the anionic C/O nets in the solid-state $Li_x(CO_2)_y$ phases.

In this study, we suggest several novel ambient and high-pressure Li-CO_2 phases that combine 3- and 4-connected carbon atoms, constructed using the CO_2 building blocks displayed in *Scheme 2.3*, and examine their structural and electronic properties. These thermodynamically and dynamically stable structures contain molecular-like covalent anionic units, such as the experimentally known oxalate $^{-}O_2C\text{-}CO_2^{-}$ in solid $Li_2(CO_2)_2$, ethene-like units $(^{-}O)_2C{=}C(O^{-})_2$ in Li_2CO_2, finite $^{-}O_2C\text{-}C(O^{-})_2\text{-}C(O^{-})_2\text{-}CO_2^{-}$ oligomers in $Li_3(CO_2)_2$, and extended one-dimensional networks in $LiCO_2$ and Li_2CO_2. One of the proposed phases is quenchable to atmospheric pressure and thermally stable up to 600 K, as demonstrated by *ab initio* molecular dynamic simulations (AIMD). Moreover, two-dimensional covalent carbon-oxygen nets are encountered in the metastable high-pressure *P*-1 $Li(CO_2)_2$ and *C*2, *P*1 $Li_3(CO_2)_4$ phases.

2.2 Computational details

The goal of this work was to find and study ambient and high pressure (meta)stable $Li_x(CO_2)_y$ phases based on CO_2 building blocks. Application of an evolutionary algorithm (EA) structure search method designed to locate the global energy minimum structures may lead to chemical decomposition, *i.e.,* cleavage of carbon-oxygen bonds and formation of more stable Li-O and Li-C based structures. Therefore, only structures with CO_2 units were kept during the EA search, while the others were rejected (no n C neighbors for a n-coordinated C atom with $n = 3, 4$ and no peroxide O-O bonds). Therefore, constraining the EA search prevented decomposition to avoid formation of graphene-like, diamond-like and Li-O networks. Under these conditions, a structural search approach based on the variable-composition evolutionary algorithm (VC-EA) implemented in USPEX was employed to scan the configurational, structural and compositional spaces of $Li_x(CO_2)_y$ (where x and y are positive integers) and seek the local minima on the enthalpy landscape. Thus, the VC-EA enabled identification of specific compositions in the pseudo-binary Li-CO_2 system at a given pressure, in this case, atmospheric pressure and 10, 50 and 100 GPa (see *Figure 2.3*). Finally, fixed-composition EA structural searches were undertaken for given (x, y) compositions and pressures to check the lowest energetic phase on the potential energy surface (PES) had been found.

Note that at each pressure, the reaction enthalpy was calculated by considering the most stable form of the reactants and products, including structures reported in the literature. The EA method implemented in the USPEX code has been successfully applied to a large number of different systems and provided a variety of relevant findings.[71,95]

The technical details of the USPEX evolutionary structural searches are given in the were presented in chapter 1, as well as a brief description of the variable- and fixed-composition EA, which have previously been described in detail.[8,13,30] Structure relaxations (shape, volume, atomic positions) were performed within DFT in the framework of the all-electron projector augmented wave (PAW) method,[49] as implemented in the VASP code.[48] We adopted the Perdew-Burke-Ernzerhof (PBE) functional[41] at the generalized gradient approximation (GGA)[42] level of theory, with PAW potentials for lithium, carbon and oxygen atoms with radii of 1.70 a.u. for Li (no core electron), 1.50 a.u. for C ([He] core) and 1.52 a.u. for O ([He] core), a plane wave kinetic energy cutoff of 600 eV, and a uniform, Γ-centered grid with $2\pi * 0.04$ Å^{-1} spacing for reciprocal space sampling. All of the (meta)stable structures were optimized at pressures from 1 atm up to 100 GPa until the net forces on atoms were below 1 meV Å^{-1} and the total stress tensor deviated from the target pressure by ≤ 0.01 GPa, resulting in enthalpies that converged to better than 1 meV per atom (lower than a chemical accuracy of 1 kcal/mol, *i.e.,* 0.04 eV/atom).[96] Phonon dispersion curves and phonon contribution to the free energy of formation were calculated using the finite displacement method implemented in the PHONOPY code.[97]

Ab initio molecular dynamics (AIMD) simulations based on DFT were carried out to examine the thermal stability of the $Li_x(CO_2)_y$ phases using supercells of 300 K, 600 K, 900 K and 1200 K with time steps of 1 fs; the total simulation time was ten ps for each temperature. In the AIMD simulations, the canonical NVT (N, constant number of particles; V, constant volume; T, constant temperature) ensemble was adopted, as implemented in the VASP code. The AIMD computational details, radial distribution functions (RDF) and snapshots of the structures are provided in the Appendix.

To perform the chemical bonding analysis, we carried out single-point calculations (with the geometry obtained from VASP) based on the extended Hückel theory (eHT) Yaehmop code[62] (DOS, COOP) and LOBSTER[51,53,54] (DOS, COHP). Images of the structures were produced using VESTA software.[98]

2.3 Results and discussion

All of the proposed solid-state $Li_x(CO_2)_y$ compounds are stationary points on the potential energy surface, located on or above the Li-CO_2 convex hull. We verified that each phase meets two stability criteria. Firstly, a dynamic criterion was applied to identify dynamically stable structure, as indicated by an absence of imaginary frequencies in all phonon dispersion curves. The corresponding stationary point on the PES is a local enthalpy minimum. Secondly, a thermodynamic criterion was employed. Strictly speaking, all $Li_x(CO_2)_y$ structures are metastable in the ternary Li-C-O phase diagram with respect to the global minimum lithium carbonate Li_2CO_3, but may appear experimentally for kinetic reasons, such as experimental squarate $Li_2C_4O_4$[99] and oxalate $Li_2C_2O_4$ (see the computed ternary phase diagram in *Figure 2.2*). Metastable structures are highly significant and can often be synthesized in practice by selecting the appropriate precursors and controlling the experimental conditions (pressure, temperature, quench rate, etc.). Bearing in mind that we aimed to identify (meta)stable phases in the binary Li-CO_2 phase diagram, a $Li_x(CO_2)_y$ compound was considered thermodynamically stable when (i) its free energy of formation (at $T = 0$ K, enthalpy) is negative, (ii) it cannot decompose to other $Li_x(CO_2)_y$ compounds and (iii) its components are Li and CO_2, *i.e.,* located on the convex hull. If not located on the convex hull, the phase is unstable and will decompose into other $Li_x(CO_2)_y$ stoichiometries and/or elements and/or CO_2, unless the kinetic barrier is sufficiently high.

Moreover, the kinetic stability of selected quenchable candidates was confirmed by performing AIMD simulations up to 1 200 K. The crystalline structure was definitively termed *quenchable* if no structural transformations*, i.e.,* C/O bond breaking, were observed after a long simulation (10 ps), indicating the existence of a large kinetic barrier which facilities the formation and trapping of viable (meta)stable structures.

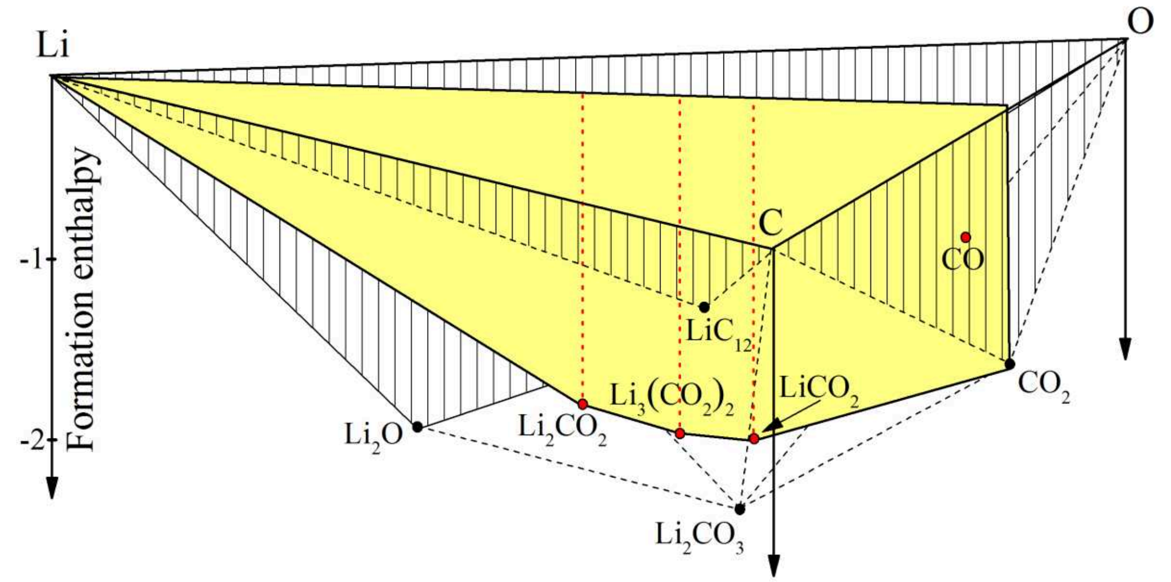

Figure 2.2 Computed ternary convex hulls of the Li-C-O system at ambient pressure.

The extensive EA searches produced a set of known (1:1) and two novel (2:1, 3:2) Li-CO_2 stable compositions. Seven stable phases were predicted; their covalent carbon-oxygen nets are displayed in *Table 2.1*, then the energetics of these phases are presented, followed by their structural and bonding properties. Moreover, four metastable CO_2-rich phases were located, namely $Li(CO_2)_2$ and $Li_3(CO_2)_4$ compositions.

Table 2.1 Chemical features of the predicted stable lithium-dioxide $Li_x(CO_2)_y$ compounds.

Compound	Phase	Stability domain^a	Structure information	Covalent carbon-oxygen net
$Li_2(CO_2)$ (2:1; *z* = 2)^b	*C2/m*	0-15	finite C_2O_4 chain ethene-like anion 3-coordinate C, terminal O^-	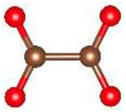
	Pnma	>15	infinite poly-$C(O)_2$ chain 4-coordinate C, terminal O^-	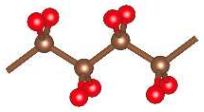
$Li_3(CO_2)_2$ (3:2; *z* = 1.5)	*P*-1	0-56	finite C_4O_8 chain 3- and 4-coordinate C, terminal O	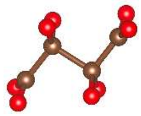
	C2/m	>56	infinite poly-$C(O)_2$ chain 4-coordinate C, terminal O^-	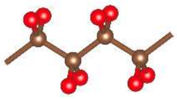
$LiCO_2$ (1:1; *z* = 1)	$P2_1/c$ (I)	0-10	finite C_2O_4 chain oxalate anion 3-coordinate C, terminal O	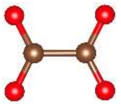
	$P2_1/c$ (II)	10-33	finite C_2O_4 chain oxalate anion 3-coordinate C, terminal O	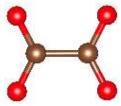
	P2/c	>33	infinite 1,4-dioxane-based chain fused 6-rings 4-coordinate C, 2-coordinate O, terminal O^-,	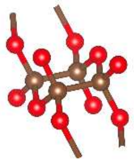

^{a}Pressure is in GPa. ^{b}The *x* and *y* values in $Li_x(CO_2)_y$ are given in parentheses; *z* = *x*/*y*.

2.3.1 Thermodynamic stability

The thermodynamic stability of the $Li_x(CO_2)_y$ system was examined using the enthalpies of formation over the pressure range of 0-100 GPa.

At 0 K, the ground-state enthalpy of formation ΔH_f is defined as:

$$\Delta H_f(\mathrm{Li_x(CO_2)_y}) = H(\mathrm{Li_x(CO_2)_y}) - x\mathrm{H(Li)} - y(\mathrm{H(C)} - \mathrm{H(O_2)})$$

where $H = E_e + PV$ and H, E_e, P, and V are enthalpy, total electronic energy, pressure, and volume, respectively.

As references, the graphite and diamond structures for C[100,101]; the α phase (*C*2/*m*-*I*) and ϵ phase (*C*2/*m*-*II*) of O_2[102,103]; the two molecular crystal structures (*Pa*-3 and $I4_2/mnm$) and silica-like structure *I*-42*d* of CO_2[66]; and the body-centered cubic (*bcc, Im*-3*m*), face-centered cubic (*fcc, Fm*-3*m),* and *I*-43*d* and *Cmca* of Li[104,105] at their respective stability ranges were used. The structure and phase transition findings were in good agreement with the experimental and theoretical results.

Compounds located on the convex hull are thermodynamically stable against decomposition into any other $Li_x(CO_2)_y$ or Li and CO_2, while compounds above the convex hull are unstable. The convex hull of all known ΔH_f values at a given pressure connects the enthalpically stable phases. in *Figure 2.2* we show the relative ground-state enthalpies of formation (ΔH_f) of the selected phases at ambient and high pressures. The solid lines in *Figure 2.3* indicate that in addition to the well-characterized 1:1 composition found in experimentally synthesized lithium oxalate $Li_2C_2O_4$[83], two stable compositions, 2:1 and 3:2, emerge at atmospheric pressure. Interestingly, composition diversity does not increase with pressure up to 100 GPa; only the 2:1, 1:1 and 3:2 compositions are located on the convex hull at 10 and 50 GPa, while the 3:2 phase lies slightly above the convex hull at 100 GPa. Although other compositions are not on the convex hull but are dynamically stable and have negative enthalpies of formation, see the CO_2-rich phases with 3:4 and 1:2 stoichiometry in *Figure 2.3*.

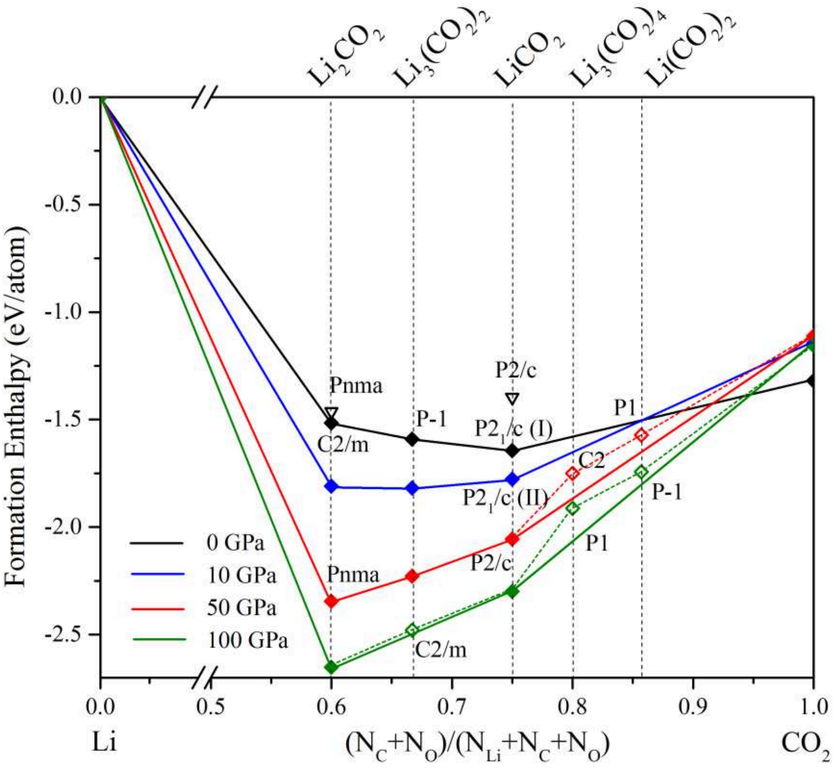

Figure 2.3 Convex hulls for the Li-CO_2 system at selected pressures. Empty squares represent metastable structures, solid squares denote stable structures.

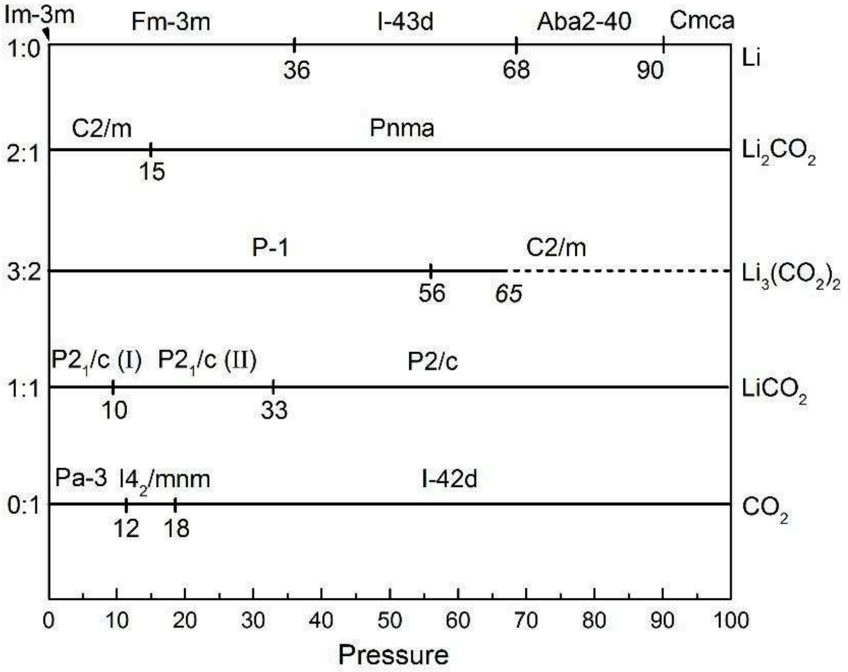

Figure 2.4 Pressure-composition phase diagram for the Li-CO_2 system from 0 to 100 GPa. The stable phases are indicated by bold lines and metastable phases are depicted by thin dashed lines. The italic numbers represent the thermodynamic stability ranges, while black numbers denote the phase transition pressures.

We found that the enthalpies of formation for all $Li_x(CO_2)_y$ stoichiometries are negative at 0 K, indicating elemental Li, C and O_2 should react, for example, Li and CO_2 could be used as starting reactants. As the pressure increases, the enthalpy of formation of each $Li_x(CO_2)_y$ phase becomes more negative. Interestingly, above 1 atm, the phases of the experimentally known oxalate-derived 1:1 composition, $Li_2C_2O_4$, have the highest enthalpies of formation of the proposed stable phases. Above ambient pressure, the more lithium-rich $Li_3(CO_2)_2$ phase is predicted to have the lowest enthalpy of formation in the Li-CO_2 phase diagram.

The relative thermodynamic stability of each phase obtained in the EA searches was determined from 0 to 100 GPa and the transition phase pressure was computed to define the stability ranges. This data was used to build the pressure-composition phase diagram for Li-CO_2 depicted in *Figure 2.4*. Seven different $Li_x(CO_2)_y$ phases are proposed, and their geometrical and electronic structures are subsequently discussed.

2.3.2 Structure and bonding in $Li_x(CO_2)_y$ phases

Next, we examined the electronic and geometrical structures of the proposed $Li_x(CO_2)_y$ phases to better understand the bonding within these structures. The covalent carbon-oxygen nets encountered within the predicted phases are summarized in *Table 2.1*. Carbon-carbon bonds are roughly 1.54 Å long for the single bond and 1.34 Å for the double bond at ambient conditions (while the C-O bond is 1.40 Å and C=O bond is 1.18 Å; see *Figure 2.5*). For calibration, the C-C single bond distance in diamond C (*Fd*-3*m*) is 1.46 Å at 100 GPa (C-O = 1.34 Å at 100 GPa in high-pressure quartz-like solid CO_2). These crude structural parameters were used to guide our assignment of C-C and C-O bond order to rationalize the local structural environments using VSEPR theory and the Zintl-Klemm concept.

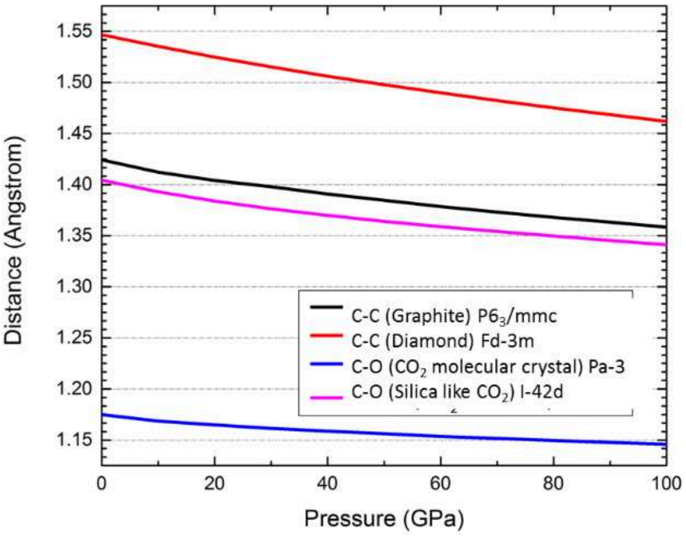

Figure 2.5 Interatomic distance as a function of pressure.

a. Lithium oxalate at atmospheric and high pressures

Encouragingly, the only known experimental 1:1 composition was found on the convex hull in the variable-composition EA structural search at atmospheric pressure, illustrating the relevance of our methodology.

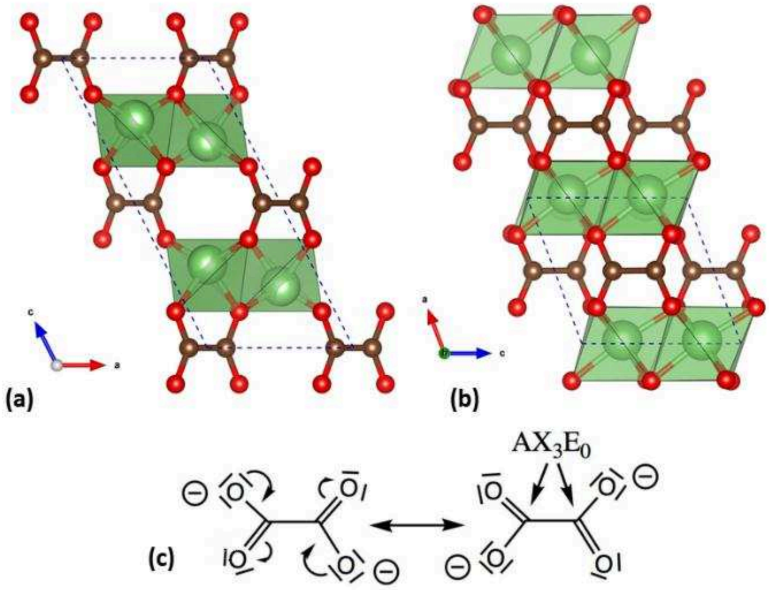

Figure 2.6 Crystal structures of $Li_2C_2O_4$ (a) *P*2$_1$*/c-I* at 0 GPa and (b) *P*2$_1$*/c-II* at 10 GPa. (c) Lewis structures of the planar $C_2O_4^{2-}$ anion and VSEPR annotation.

For the 1:1 system, the most stable phase found at atmospheric pressure is the oxalate crystal, which is dynamically stable. This is the only known polymorph of $LiCO_2$ and crystallizes in the monoclinic type (space group $P2_1/c$, $Z = 4$). The structural parameters calculated using the GGA approach for $Li_2C_2O_4$ $P2_1/c$-*I* are in excellent agreement with experimental observations (*Table 2.2*), as well as previous GGA calculations of atomic positions[106,84], with only a typical, but small, GGA overestimation of the lattice parameters.

Table 2.2 Crystal structures of $LiCO_2$ $P2_1/c$ phases at 0 GPa and 10 GPa.

Phase	Lattice parameters	Volume (Å^3/atom)	Bond length (Å)	
			C-C	C-O
Experimental[105] 0 GPa, $Z = 4$	a=3.965, b=4.849, c=10.019 α=90.0, β=114.9, γ=90.0	10.921	1.568	1.266
$P2_1/c$-I 0 GPa, $Z = 4$	a=4.202, b=4.651, c=10.044 α=90.0, β=115.5, γ=90.0	11.074	1.570	1.266
$P2_1/c$-II 10 GPa, $Z = 4$	a=4.840, b=5.833, c=4.950 α= 90.0, β=110.6, γ=90.0	8.176	1.551	1.257 1.264

$P2_1/c$-I is the most stable phase calculated for $LiCO_2$ in the 0-10 GPa pressure range (*Figure 2.4*). As shown in *Figure 2.6*, this structure is a molecular solid formed by isolated $C_2O_4^{2-}$ oxalate anions embedded in a sublattice of Li^+ cations. Each oxygen atom of the oxalate is coordinated to two Li atoms and each lithium atom is coordinated via ionic interactions to four oxygens at 1.95-2.00 Å, forming a tetrahedral environment. Therefore, the structure of lithium oxalate consists of planes of corner-shared LiO_4 tetrahedra connected by planes of oxalate anions. Within the carboxylate CO_2^- group, a unique C-O distance of 1.27 Å was computed, comparable to the experimental C-O separation of ~1.27 Å observed in oxalate salts.[105] Four π electrons are delocalized over each -C(=O)(O$^-$) group, leading to a formal CO bond order of 1.5, as illustrated by the resonant structures presented in *Figure 2.6b*. The C-C bond length (1.57 Å at ambient pressure) is approximately 0.03 Å too long for two 3-coordinate C atoms (~1.54 Å). Slightly elongated C-C bonds are also encountered in experimental oxalates structures,[105] indicating an associated single bond order, or lower. Therefore, the extent of π conjugation between two CO_2 groups is minimal, as previously established.[107] This peculiar structural feature rationalizes the flexible conformation of the oxalate moiety, *i.e.,* planar in Li, Na and K oxalates, and staggered in $Cs_2C_2O_4$.[106] In $P2_1/c$-I $Li_2C_2O_4$, the oxalate anion was experimentally found to be planar due to the strong ionic interactions between Li^+ and $C_2O_4^{2-}$, which lead to a packed structure. Moreover, the $C_2O_4^{2-}$ anions located between two lithium layers exhibit a parallel arrangement at 1 atm; this feature is characteristic of all stable oxalate structures, as well as ground-state carbonate structures. A parallel arrangement may be favored due to its higher packing density and/or minimization of repulsion between carboxylate groups. The calculated band gap (Eg) for the $P2_1/c$-I phase at 0 GPa is around 3.9 eV, indicating oxalate-containing $LiCO_2$ should be transparent. This is not surprising, as this Zintl $P2_1/c$ phase fulfills the octet rule.

A phase transition occurs at 10 GPa, and the novel $P2_1/c$-I phase adopts the same space group $P2_1/c$-II. The oxalate C_2O_4 unit is maintained, but the change in relative position between units leads to a more highly packed ionic crystal. At 10 GPa, the volume was computed to decrease from 33.840 Å^3/f.u ($P2_1/c$-I at 10 GPa) to 32.719 Å^3/f.u ($P2_1/c$-II). As shown in *Figure 2.6b*, the coordination number of the lithium cation increases from 4 in the low-pressure $P2_1/c$-I phase (LiO_4 tetrahedra) to 6 in the high-pressure oxalate phase (LiO_6 octahedra), in which fused LiO_6 octahedra form packed 2D lithium-oxygen slabs.

Note that the oxalate motif in $P2_1/c$-II remains intact up to higher pressures, and the Zintl $P2_1/c$-II phase is thermodynamically stable up to 33 GPa (see *Figure 2.4*). $P2_1/c$ remains an insulator at 33 GPa, with a calculated E_g of 3.0 eV.

Above 33 GPa, the $P2/c$ phase becomes the most stable structure. A drastic phase transformation occurs, as the $P2/c$ CO_2-based covalent net topology is quite different to that of $P2_1/c$ oxalate. Nevertheless, breaking and creation of bonds during the $P2_1/c \rightarrow P2/c$ phase transformation may be prevented due to the high kinetic barriers between these structures. Next, we discuss the $P2/c$ phase.

b. High pressure *P*2/*c* $LiCO_2$ with infinite 1,4-dioxane chains

The monoclinic *P*2/*c* structure ($Z = 4$, *Figure 2.7*) was calculated to be the most stable $LiCO_2$ phase above 33 GPa. This Zintl phase is particularly interesting; 6-membered rings can be identified, consisting of four C and two O atoms, as illustrated in *Figure 2.8*. Each 1,4-C_4O_2 ring adopts a chair conformation, typical of related structures in 1,4-dioxane and cyclohexane. These 1,4-C_4O_2 rings form chain-like arrangements along an axis, where each repeating unit (ring) is fused to its neighbor via a common C-C edge. Each ring junction contains two stereocenters (*Figure 2.8a*), with terminal O atoms in a *cis* arrangement, whereas the terminal O pairs along the chain are in *trans* with one 'up' and the next 'down' (*Figure 2.8b*). Thus, this ionic $LiCO_2$ crystal contains chiral CO_2-based anionic chains without chiral centers. This unusual stereo configuration minimizes repulsive interactions between the charged terminal O atoms and maximizes the ionic forces between the chains and the Li^+ sublattice. Together, these effects lead to the overall packed-shape of the poly-$COO_{2/2}^-$ chain shown in *Figure 2.7* and *Figure 2.8*.

All of the bond angles within the infinite CO_2-based chain are close that of a tetrahedral arrangement (106.2-113.1° at 50 GPa), as expected for bent oxygen and tetrahedral carbon atoms. The calculated C-O and C-C bond lengths within the rings at 50 GPa are 1.42 Å and 1.51 Å, respectively, indicating classical single bonds at this pressure. A shorter terminal C-O separation of 1.30 Å is observed, as expected for $C(sp^3)$-$O(sp)^-$. Bird's-eye views of the crystal structure along the *b* and *ac* directions are presented in *Figure 2.7a* and *b*, respectively. The ionic bond length for Li-O is approximately 1.84-1.97 Å, and connects the separated chains into layers along the crystal direction [101]. In *P*2/*c* $LiCO_2$, each Li is coordinated to six O atoms from four neighboring chains, and fused LiO_6 octahedra form packed 2D lithium-oxygen slabs.

The calculated DOS indicates *P*2/*c* is an insulator at 50 GPa (E_g ~6.5 eV). The *P*2/*c* $LiCO_2$ structure has potential as a high-pressure polymorph and should be obtained at pressures above 33 GPa. A chemical mechanism can be proposed to connect the molecular oxalates and infinite poly-dioxane chain found in $LiCO_2$, as displayed in *Scheme 2.4*. In this model, pressure favorizes the formation of new C-C and C-O single bonds, which thermodynamically stabilize the $LiCO_2$ *P*2/*c* phase at high pressure.

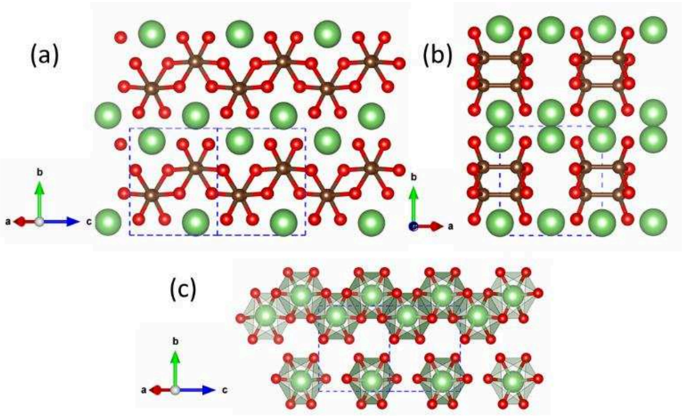

Figure 2.7 High-pressure *P*2/*c* $LiCO_2$ phase at 50 GPa. (a) View perpendicular to the one-dimensional CO_2-based chains, (b) view along the [001] direction and (c) corrugated fused octahedra LiO_6 layers stacking along the b axis (carbon atoms have been removed for clarity).

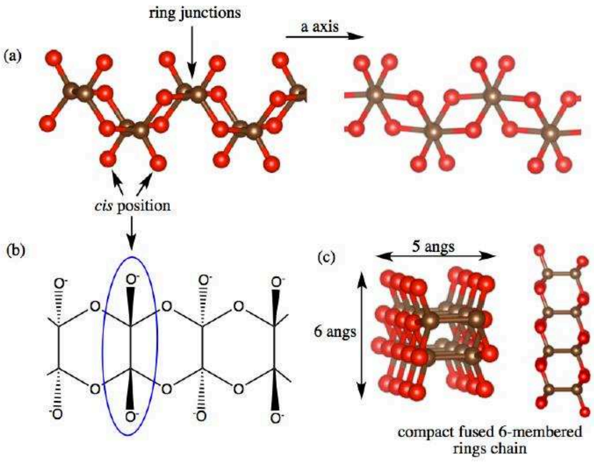

Figure 2.8 Representations of the C-O covalent net in the high-pressure *P*2/*c* $LiCO_2$ phase at 50 GPa. In (a) and (b), the extended fused 6-membered ring chain is highlighted in red. The 1,4-dioxane C_4O_2 rings form a boat conformation with all terminal O atoms in a cis arrangement. In (c), the compact conformational arrangement is shown.

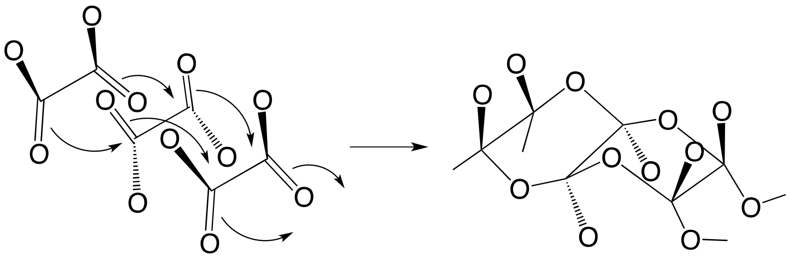

Scheme 2.4 Proposed chemical pathway for the phase transition of $LiCO_2$ from oxalate units to an infinite poly-dioxane chain.

c. *C2/m* Li_2CO_2 with ethene-like C_2O_4 units.

A novel thermodynamically stable lithium-rich composition, 2:1, appeared on the convex hull in the crystal structure searches at 0 and 10 GPa (*Figure 2.3*). This Li_2CO_2 crystalline compound adopts the *C2/m* space group and remains thermodynamically stable up to 15 GPa (*Figure 2.4*). The computed ionic Li-O bond lengths for the *C2/m* phase are in the range of 1.99-2.28 Å at ambient pressure. Each Li is coordinated to five O atoms from four neighboring C_2O_4 units, which are located above and below the Li-O slab, as shown in *Figure 2.9a*. These fused LiO_5 square planar pyramids form packed 2D lithium-oxygen slabs, composed of two connected, square-like Li-O monolayers in an AB stacking configuration. Each planar C_2O_4 unit contains two 3-bonded carbon atoms and four terminal oxygen atoms, exhibiting an oxalate-type topology. The shortest CC and CO distances are computed at 1.40 Å (characteristic of double C=C bonds) and 1.37 Å (characteristic of single C-O bonds), respectively. Remember that four electropositive lithium atoms formally transfer their four valence electrons to the observed C_2O_4 unit in Li_2CO_2. Therefore, all of the computed structural parameters for the C_2O_4 unit can be understood if one considers $C_2O_4^{4-}$ as an ethene-like structure, as illustrated in *Figure 2.9b*.

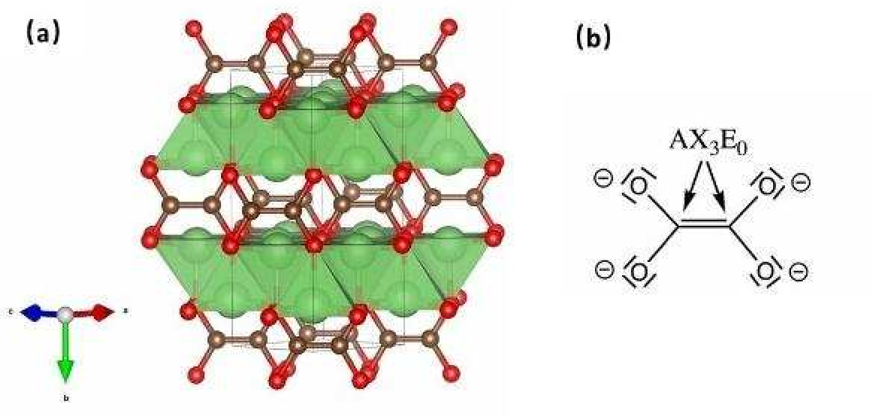

Figure 2.9 (a) Crystal structure of the *C2/m* phase of $Li_4C_2O_4$. (b) Lewis structure of the planar $C_2O_4^{4-}$ anion (ethene-like) and VSEPR annotation.

When oxalate $C_2O_4^{2-}$ converts to ethene-like $C_2O_4^{4-}$ units, two electrons are added to a CC bonding (C-O antibonding) π molecular orbital, which explains the contraction of the CC bond

(1.57 to 1.40 Å) and elongation of the C-O bonds (1.27 to 1.37 Å) at 0 GPa. During the phase transition from experimental $LiCO_2$ to predicted Li_2CO_2, formal chemical reduction of the C_2O_4 motifs occurs without CC/CO bond breaking (*Scheme 2.5*).

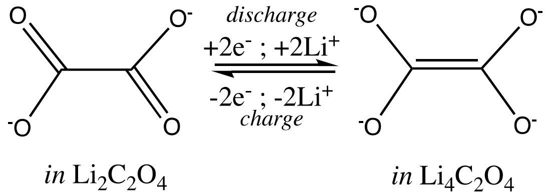

Scheme 2.5 Schematic redox mechanism for $Li_x(C_2O_4)$ where x = 2, 4.

The structural feature of a phase transition that does not require bond breaking is potentially appealing when one envisages the use of *C2/m* Li_2CO_2 as a positive electrode (cathode) material in lithium-ion rechargeable and renewable batteries. Lithium insertion and extraction could be described by the following reaction:

$LiCO_2$ [cathode] + Li [anode] = Li_2CO_2 [cathode]

The computed cell voltage (*vs* Li+/Li) is 1.01 V, which is relatively high for oxocarbon Li-ion electrodes[94,108,109]. Theoretical capacitance is 463 V mAh g^{-1}, which is comparable with the experimental value of 590 V mAh g^{-1} for $Li_2C_6O_6$. A deeper theoretical investigation is beyond the scope of this study, but is required to evaluate the potential of Li_2CO_2 as a Li-ion electrode, and should include an assessment of parameters such as electrochemical properties, ion transport and defect chemistry.

Finally, one may hypothesize a polymerization process occurs for the ethene-like $C_2O_4^{4-}$ units in Li_2CO_2 when pressure increases, as observed in ethene under high pressure.[110] Indeed, the numerical simulations indicate polymerization occurs; the following sections describe the predicted structures.

d. *Pnma* Li_2CO_2 with infinite poly-$C(O^-)_2$ chains

The CSP searches at 50 GPa identified a novel 2:1 phase on the convex hull. This phase has a *Pnma* space group ($Z = 2$) and the *C2/m-Pnma* transition phase pressure is evaluated at 15 GPa (see *Figure 2.4*). As shown in *Figure 2.10*, all C atoms are tetracoordinated (sp^3), each to two terminal O atoms and two C atoms. The calculated C-C and C-O bond lengths at 50 GPa are 1.54 Å and 1.36/1.38 Å, respectively, comparable to the interactomic separations (single bonds) in cubic diamond carbon (C-C = 1.50 Å) and the silica-like CO_2 phase (C-O = 1.36 Å). The covalent carbon-oxygen net forms unidimensional chains, whereas the infinite carbon chain has an all-*trans* skeleton running along the *b* axis. The closest computed Li--O separations ranged from 1.75 to 2.10 Å, characteristic of ionic bonding (computed Li-O = 1.75~2.07 Å in Li_2O at 50 GPa). In the condensed state, poly-$(C(O^-)_2)_n$- forms a 2_1 helix stabilized by ionic interactions and chain packing. Based on these structural parameters, we confidently conclude that poly-$(C(O^-)_2)_n$- is an isoelectronic analogue of poly(tetrafluoroethylene) -$(CF_2)_n$-. The *Pnma* Li_2CO_2 phase is an insulator at both 15 and 50 GPa (computed E_g of 3.5 eV and 3.6 eV, respectively).

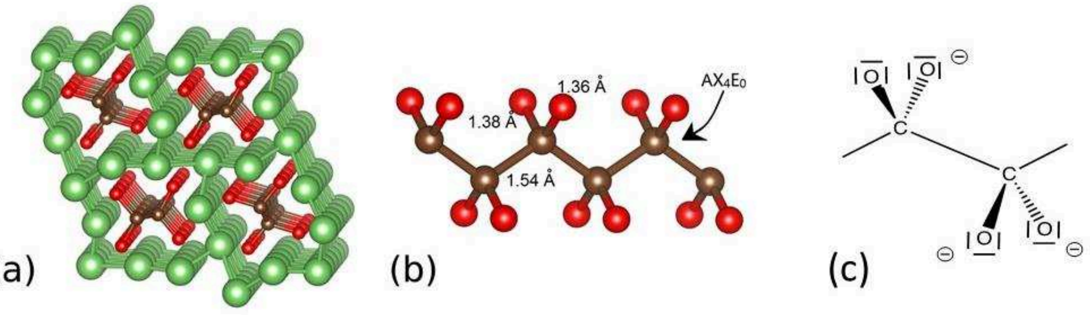

Figure 2.10 *Pnma* Li_2CO_2 phase at 50 GPa. (a) Projection along the (010) direction. Extended infinite CO_2-based chains running in the Li channels. (b) Representation of a fragment of the poly-$C(O^-)_2$- chain. Distances are indicated in angstroms and the VSEPR AX_nE_m annotation is given. (c) Lewis resonant structure for a repeat unit of the poly-$C(O^-)_2$- chain.

This infinite poly-$C(O^-)_2$ chain possesses a unique $C(O^-)_2$ building block, while oxalate exhibits the carboxylate $C(=O)(O^-)$ conformation. Thus, by varying the Li/CO_2 ratio, one may imagine finite chains based on these two motifs, *e.g.*, $^-O_2C\text{-}C(O^-)_n\text{-}CO_2^-$ in $Li_{2(n+1)}(CO_2)_{n+2}$ solids. Encouragingly, this was observed in the numerical investigation. In the following sections, we describe a new composition, $Li_3(CO_2)_2$ with *n* = 2, which exhibits two stable phases at the pressure range studied: one phase contains finite $C_4O_8^{6-}$ motifs and the other infinite extended -$(C(O)_2)_n$- chains.

e. $Li_3(CO_2)_2$ with the finite $C_4O_8^{6-}$ motif and infinite -$(C(O)_2)_n$- chains

A 3:2 composition emerged on the convex hull at 1 atm and is thermodynamically stable up to 65 GPa (*Figure 2.3* and *Figure 2.4*). Two phases were identified, with a *P*-1 to *C2/m* transition phase pressure of 56 GPa. At low pressure, $Li_3(CO_2)_2$ crystallizes in a triclinic structure, with the space group *P*-1 and *Z* = 2 (*Figure 2.11*). In this structure, carbon and oxygen atoms form molecular-like C_4O_8 units which occupy cavities in the channels running along the *c* axis. In C_4O_8, two C atoms are 3-coordinated and the other two are 4-coordinated, while all oxygen atoms are terminal. This C_4-anion possesses an inversion center and two planar terminal carboxylate groups. The calculated C-C and C-O separations around the tetrahedral carbon atoms are 1.47/1.57 Å and 1.33/1.38 Å at 50 GPa, respectively. The anion possesses a peculiar structural characteristic, namely the slightly elongated central C-C bonds along the C_4-unit due to steric repulsion between oxygen lone pairs, a phenomenon also observed in oxalate anions. The C-C bond strength should be weaker than that of other C_4 alkanes. Shorter C-O bond lengths of ~1.26 Å were predicted for the terminal CO_2 groups, a signature of the delocalized double bond character in carboxylate units. Thus, the encapsulated $C_4O_8^{6-}$ anion may be formulated as $^-O_2C\text{-}C(O^-)_2\text{-}C(O^-)_2\text{-}CO_2^-$. All atoms fulfill the octet rule, as depicted in the Lewis structure (*Figure 2.11c*), which explains the insulator property of the *P*-1 $Li_3(CO_2)_2$ phase at 50 GPa (see the DOS in *Figure 2.11*).

Above 56 GPa, the *C2/m* space group phase has the lowest enthalpy. This novel $Li_3(CO_2)_2$ phase is thermodynamically stable in the narrow pressure range of 56-65 GPa. Interestingly, the carbon-oxygen covalent net of this phase forms unidimensional chains with a chemical topology analogous to *Pnma* Li_2CO_2. The infinite carbon chains contain an all-*trans* skeleton running in a lithium channel (*Figure 2.11d, e*) and can be viewed as the result of polymerization of the $C_4O_8^{6-}$ species found in the low-pressure *P-1* $Li_3(CO_2)_2$ phase. At 60 GPa, the C-C bond length is 1.61 Å, longer than in *Pnma* Li_2CO_2 (1.48 Å), while the C-O distance was computed at 1.27-1.29 Å, smaller than in *Pnma* Li_2CO_2 (1.33-1.36 Å). These structural differences are understandable if one considers that each poly-CO_2 chain in *C2/m* $Li_3(CO_2)_2$ contains one less electron per $(CO_2)_2$ unit than *Pnma* $Li_4(CO_2)_2$, which results in weaker C-C bonds and stronger C-O bonds. Due to this non electron-precise and delocalized picture, one expects *C2/m* $Li_3(CO_2)_2$ to be metallic; this prediction was confirmed by the DOS.

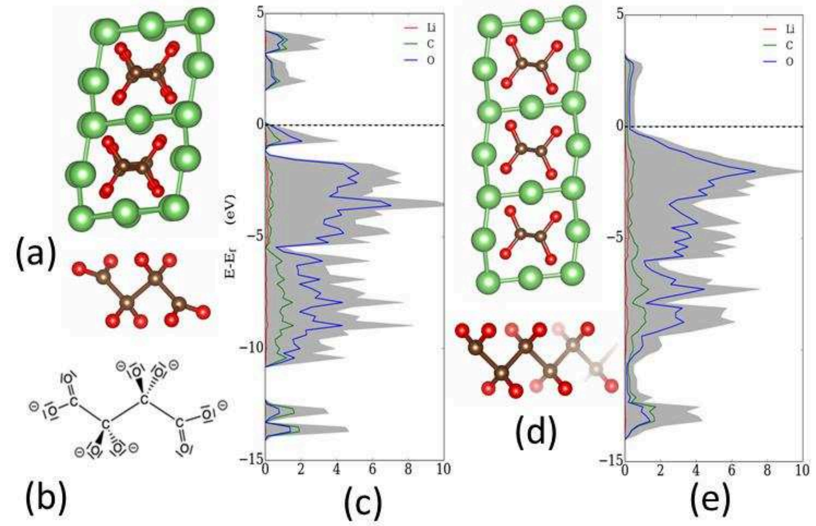

Figure 2.11 (a) *P*-1 $Li_3(CO_2)_2$ phase at 50 GPa with (b) encapsulated $C_4O_8^{6-}$ anions and (c) the associated Lewis structure. (d) *C2/m* $Li_3(CO_2)_2$ phase at 100 GPa with (e) infinite poly-$C(O)_2$ chains.

2.3.3 Quenchable high-pressure $Li_x(CO_2)_y$ phases?

To check the stability of the CO_2-based networks found in the proposed high-pressure $Li_x(CO_2)_y$ phases when pressure is released—namely *P2/c* $LiCO_2$, *Pnma* Li_2CO_2 and *C2/m* $Li_3(CO_2)_2$—their structures and associated phonon spectra were calculated at 1 atm and are given in the Supporting Information. The computed phonon band structures in *Figure 2.12* did not exhibit imaginary frequencies over the entire Brillouin zone, indicating these structures are dynamically stable at 1 atm and 0 K. The computed structures for the corresponding CO_2-based nets at ambient pressure are displayed in *Figure 2.13*.

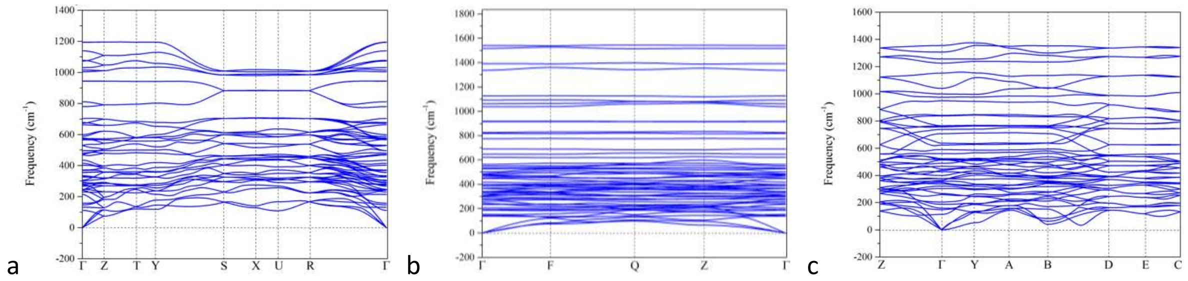

Figure 2.12 Phonon frequencies (a) *Pnma* Li_2CO_2, (b) *C2/m* $Li_3(CO_2)_2$, (c) *P2/c* $LiCO_2$ at 0 GPa.

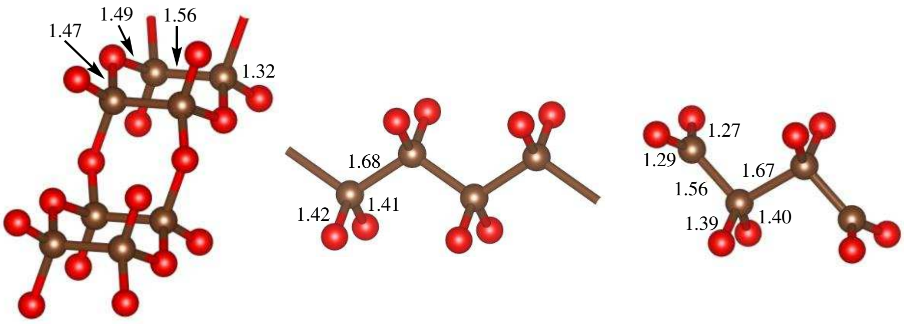

(a) (b) (c)

Figure 2.13 CO_2-based nets encountered in (a) *P2/c* $LiCO_2$-poly-1,4-dioxane-, (b) *Pnma* Li_2CO_2-poly-$C(O^-)_2$ and (c) *C2/m* $Li_3(CO_2)_2$-finite $C_4O_8^{6-}$- crystal structures at ambient pressure. Distances are indicated in angstroms.

At 1 atm, *P*2/*c* poly-1,4-dioxane $LiCO_2$ lies 0.243 V/atom above $P2_1/c$ oxalate $Li_2C_2O_4$. It is noteworthy that, with respect to elemental $Li_{(s)}$ and molecular CO_2, the decomposition enthalpy of *P*2/*c* $LiCO_2$ at 1 atm is still negative (approximately -0.411 eV/atom) and its enthalpy of formation from elemental Li(s), C(graphite) and molecular O_2 is negative, up to -1.401 eV/atom. We supposed that if the barrier to isomerization of stable oxalate $P2_1/c$ $Li_2C_2O_4$ or decomposition to the elements can protect *P*2/*c* poly-1,4-dioxane $LiCO_2$, then perhaps this barrier could be detected. Thus, to investigate the viability of the $LiCO_2$ *P*2/*c* polymeric structure at finite temperature and low pressure, we performed AIMD calculations using a supercell model at 1 atm and different temperatures (see Computational Details). Although small chain shifts and Li^+ cation displacements were observed during the entire ten ps AIMD simulations at temperatures of 300 K and 600 K, the covalent C-C and C-O bonds were not broken. In confirmation of this finding, the C-C and C-O distances varied from 1.45 to 1.65 Å (1.26 to 1.65 Å, respectively) at

600 K. At 900 K, the intra-ring C-O bonds break (*Figure 2.14*). Interestingly, the AIMD analysis revealed that the encapsulated polymeric anionic carbon-oxygen chains in *P*2*/c* $LiCO_2$ can be successfully preserved at ambient conditions. Furthermore, the chains exhibit robust thermal stability and strong kinetic trapping, at least at temperatures up to 600 K.

In our numerical simulation, polymerized oxalate *P*2*/c* $LiCO_2$ appears above 33 GPa at 0 K, a pressure range that is accessible in modern high-pressure experiments. These results invite experimentalists to investigate the polymerization of lithium oxalate at high pressure.

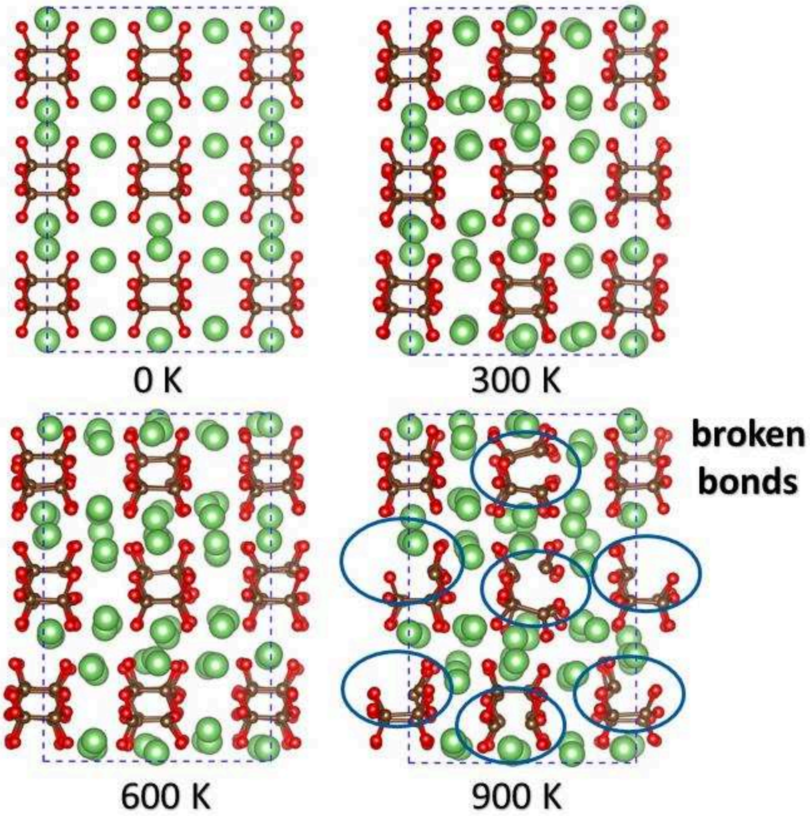

Figure 2.14 Snapshots of the $LiCO_2$ supercells at the end of the AIMD simulations for *P*2*/c* $LiCO_2$-based supercells at ambient pressure and 0, 300, 600 and 900 K.

Now, we turn our attention to the extended 1D poly-$C(O^-)_2$- chain found in the high-pressure *Pnma* Li_2CO_2 phase and finite $C_4O_8^{6-}$ observed in *C*2*/m* $Li_3(CO_2)_2$ illustrated in *Figure 2.13b* and *Figure 2.13c*. At ambient pressure, the carbon backbones of these phases remain intact, though elongated CC bonds are observed along the zig-zag carbon net (~1.7 Å), which weaken structural stability. The *Pnma* structure possesses an enthalpy of decomposition to solid lithium and carbon dioxide of 0.671 eV/atom, slightly higher that that of oxalate (0.654 eV/atom). However, the enthalpy of 0.053 eV/atom is greater than that of the lowest metastable Li_2CO_2 phase at 1 atm, the *C2/m* space group that contains ethene-like C_2O_4 units (see *Figure 2.9*). If the barrier to isomerization of *C2/m* Li_2CO_2 (or decomposition to elements or other $Li_{x(}CO_2)_y$ compounds) can protect *Pnma*, then perhaps the barrier could be detected at low temperatures. Our AIMD calculations show that the polymeric units are broken above 600 K, but their carbon net is maintained at 300 K (See *Appendix*).

Finally, we finish by discussing the quenchability of the finite C_4O_8 chains in $Li_3(CO_2)_2$. At ambient pressure, the enthalpy of formation is exothermic (-1.596 eV/atom). The elongated central CC bond of 1.67 Å observed at 0 K and 1 atm weakens the molecular $C_4O_8^{6-}$ anion. Nevertheless, no carbon-carbon bond cleavage or other decomposition was observed during a AIMD simulation at 600 K and 1 atm. The C_4O_8 motif within *P*-1 $Li_3(CO_2)_2$ is maintained. At 900 K, structural instability is observed as C-C bonds are broken.

To conclude, in addition to the experimentally proven oxalate 1:1 phase, we propose three novel phases in the pseudo-binary Li-CO_2 phase diagram are viable solid-state structures at ambient pressure based on our numerical CSP searches, namely *C2/m P-1* $Li_2(CO_2)_2$, *P*-1 $Li_3(CO_2)_2$ and *P2/c* poly-1,4-dioxane $LiCO_2$. These structure predictions should generate interest in the synthesis of these crystals.

2.3.4 A metastable CO_2-rich $Li(CO_2)_2$ phase containing two-dimensional CO_2 nets

In our EA searches, we identified several stationary structures that are local minima on the potential energy surfaces of the $Li_x(CO_2)_y$ phases at a given pressure. We selected four metastable phases above but close to the convex hull, all located in the CO_2-rich region (see *Figure 2.3*). All of these structures have one- or two-dimensional CO_2-based nets. Here, we focus our discussion on the structural and electronic properties of the high-pressure *P*-1 $Li(CO_2)_2$ phase, which possesses highly symmetrical and aesthetical 2D covalent CO_2 layers.

At 100 GPa, our evolutionary crystal structure search identified a low-energy stationary point on the PES of the 1:2 composition. *P*-1 $Li(CO_2)_2$ is a local minimum ($Z = 4$) with an enthalpy of formation of -1.744 eV/atom. Its structure contains a covalent CO_2-based slab sandwiched between Li layers. The C-O layer is built from repeated $C_4O_8^{2-}$ units, as illustrated in *Figure 2.15*. Each unit possesses a non-planar seven-membered C_4O_3 ring. Typical interatomic separations are observed, and a tentative Lewis structure is depicted in *Figure 2.15c*; all local structural environments can be rationalized with the help of simple VSEPR theory. As expected for an electron-precise count in the Zintl phase, *P*-1 is an insulator at 100 GPa. Note that the C-O bonds which connect two chains are broken when pressure reduces to 1 atm. Hence *P*-1 is not a quenchable phase.

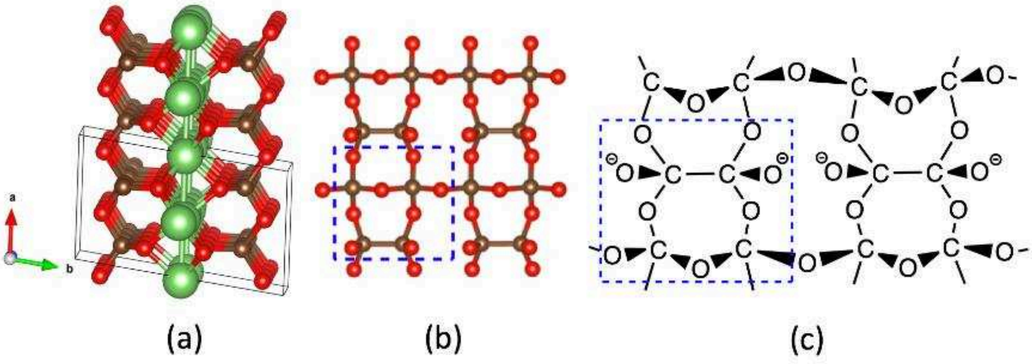

(a) (b) (c)

Figure 2.15 (a) *P*-1 $Li(CO_2)_2$ at 100 GPa. View along the c axis. (b) Representation of the 2D CO_2-based net. (c) $C_4O_8^{2-}$ repeating unit.

2.4 Conclusion and perspectives

In this work, we performed evolutionary crystal structure searches on the Li-CO_2 system, at ambient and high pressures, using the evolutionary principles implemented in the USPEX code in combination with first-principle electronic structure calculations. In addition to the well-known oxalate anions experimentally found in $Li_2C_2O_4$, our numerical investigation identified novel polymeric carbon-oxygen nets in high-pressure $Li_x(CO_2)_y$ phases, such as finite ethane-like $(O^-)_2C=C(O^-)_2$ and C_4O_8 units, poly-1,4-dioxane-based chains, and 1D poly-$C(O)_2$ planar zig-zag chains.

The valuable Zintl-Klemm concept and VSEPR rules could be invoked to rationalize the shape and connectivity of these phases. With the exception of *C2/m* $Li_3(CO_2)_2$, all of the phases identified are insulators, even at high pressures, up to 100 GPa. Three $Li_x(CO_2)_y$ phases are viable at ambient conditions, being thermodynamically, dynamically and mechanically stable. In particular, $Li_2(CO_2)$ contains reduced oxalate units, - $Li_4C_2O_4 = 2Li + Li_2C_2O_4$ -, thus one could envisage this phase has potential for use in Li-batteries. Overall, these results indicate that pressure may induce the polymerization of carbon dioxide in binary Li-CO_2 phases, and merit experimental confirmation.

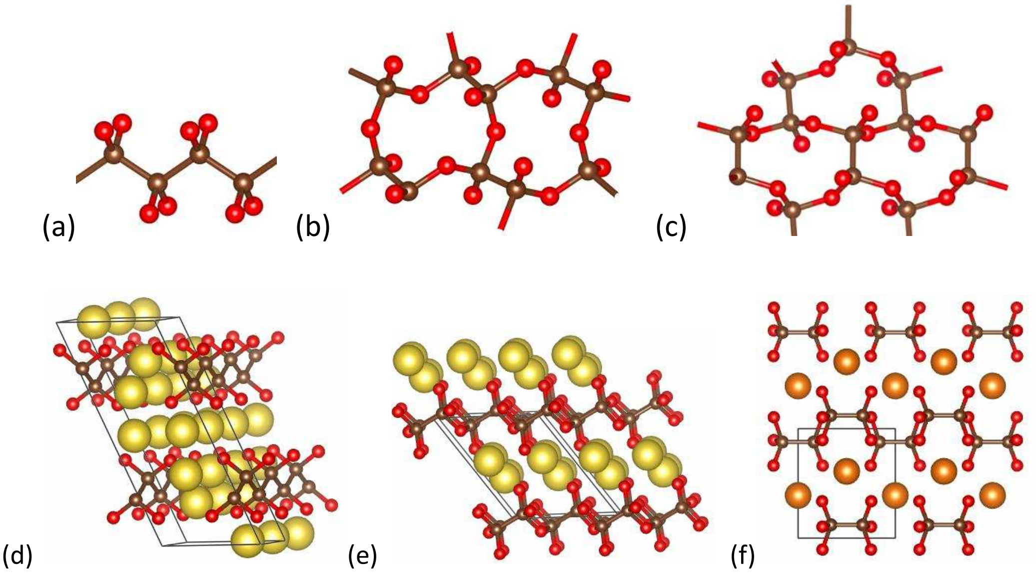

Figure 2.16 Predicted (a,d) *C2/m* Na_2CO_2, (b,e) *P*2_1*/c* $NaCO_2$, and (c,f) *P*2_12_12 $Mg(CO_2)_2$ phases at 100 GPa.

We have presented the results of the Li-CO_2 binary phase diagram under pressure. As we mentioned in the beginning of this chapter, our goal is to explore the s-block elements-CO_2 binary phases in order to predict novel CO_2-based materials with finite and infinite CO_2 nets.

Therefore, we started to investigate the Na-CO_2 and Mg-CO_2 systems under pressure. The first family we chose to look at was the cation size effect -Na^+ is bigger than Li^+-, and the second family we looked at was the electron concentration effect on A:CO_2 composition, as here $2e^-$ rather than $1e^-$ are given by Mg to the CO_2 net. We have almost finished the CSP step.

Numerous interesting structures emerged as stable or metastable phases at high pressure. To illustrate these preliminary results, and to wet the appetite of the reader, let's present three of these predicted phases. They are shown in *Figure 2.16*: a one-dimensional chain is encountered in *C2/m* Na_2CO_2, isostructural to poly-$C(O^-)_2$ found in *Pnma* Li_2CO_2, while a two-dimensional layered CO_2 net appears in $P2_1/c$ $NaCO_2$; $P2_12_12$ $Mg(CO_2)_2$ presenting layered CO_2-nets, whereas each slab is made of 10-membered C_6O_4 rings.

Further structural and electronic analysis is underway.

3. Alkaline earth metal nitrides

3.1 Introduction

Nitrogen forms about 78% of the Earth's atmosphere, making it the most abundant, uncombined element accessible to man, and a potential natural resource in chemistry. The characterization of nitrogen is credited to Scottish physicist Daniel Rutherford in 1772,[111] but at the same time, it has also been studied by several scientists such as Carl Wilhelm Scheele, Henry Cavendish, and Joseph Priestley.[112] Its name was given by the French scientist Jean-Antoine-Claude Chaptal, comte de Chanteloup, in 1790 (in French, nitrogène, from Greek roots *νἰτρον*, nitre ; *γεννᾶν*, to form). Nevertheless, Antoine Lavoisier gave this inert gas another name, azote -mephitic air-, from the Greek word άζωτικός (azotikos), "no life".

At standard conditions, two nitrogen atoms bind to form a dinitrogen molecule, a tasteless, colorless and odorless diatomic gas. At 1 atm, molecular nitrogen liquefies at 77 K (-195.8°C), and freezes at 63 K (-210 °C) into the beta hexagonal close-packed crystal allotropic form. Diatomic N_2 is mostly unreactive at atmospheric pressure and room temperature due mainly to its bonding; it has a strong triple N≡N bond, with a short bond length of 1.10 A and a high dissociation energy of 945 kJ/mol. N≡N triple bond is much stronger than those of the N=N double bond (418 kJ/mol) or the N–N single bond (160 kJ/mol).[269,270] These energy properties have lead the scientific community to search for nitrogen oligomers and polymers, so-called polynitrogen. In the following, we consider polynitrogen N_n with $n > 2$.

It has been proposed that molecules and ionic species containing nitrogen atoms connected by unstable single or double bonds decompose to give very stable N_2 molecules, along with the release of large amounts of energy. Therefore, their potential applications as propellants, explosives, and pyrotechnics have been envisaged.[113–115] The quest for high nitrogen content materials is still considered to be a Holy Grail in the science world, due to their chemical interest and their potential as high-energy density materials (HEDMs) that are environmentally friendly. From a theoretical point of view, our current research tentatively works towards the challenging and attractive objective of the development of polynitrogen-based compounds.

Unfortunately, neutral polynitrogen compounds are metastable and are expected to have a small energy barrier towards decomposition, such as the long-sought but still unknown tetrahedrane.[116]

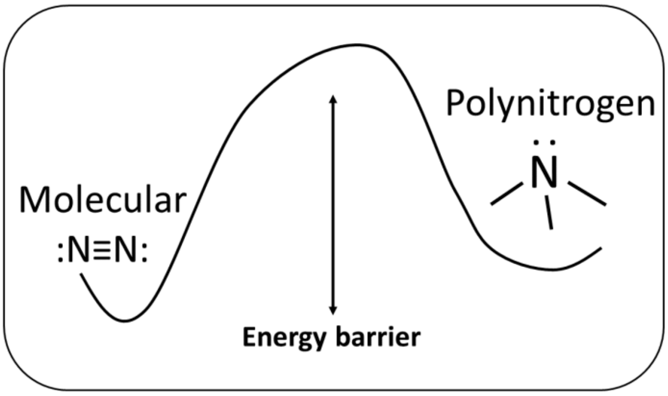

Figure 3.1 Schematic energy profile of molecular N_2 to polynitrogen compound reaction.

To alleviate this kinetic issue, chemists and physicists have proposed different strategies to synthesize viable polynitrogen-containing compounds. Here, we present the different experimental and predicted allotropes of nitrogen which contain covalently nitrogen extended nets, then we describe ionic structures which contain polynitrogen units.

Allotropes of nitrogen with extended covalent nets

In a tiny and constrained space, for instance N_2 under pressure, N≡N triple bonds break, and new nitrogen-nitrogen bonds are created. Thus, under pressure, one can expect the emergence of (meta)stable oligomers or polymeric nitrogen nets. This is what is observed in nitrogen. Under extremely high pressure (1.1 million atm, 110 GPa) and high temperature (2000 K), elemental nitrogen polymerizes experimentally into the single-bonded cubic gauche crystal structure, *cg*-N, which is displayed in *Figure 3.2*.

This *cg*-N phase has been experimentally determined in 2004 by Eremets *et al.* by laser-heated diamond anvil cell experiments.[88,117,118] In Chemical and Engineering news, Stephen

Ritter wrote “Polynitrogen should have an energy capacity more than five times that of the most powerful nonnuclear energetic materials” and Klapötke said “[polynitrogen] would seem to be the ideal high-energy-density material”.[119] This high-pressure allotrope of nitrogen has been reported in 1985 by MacMahan *et al.*,[85,120] and later on, in 1992, a DFT study of this *cg*-N phase was developed.

Since this seminal work, a number of different nitrogen allotropes have been predicted from first-principles calculations: cubic gauche (*cg*-N) $I2_13$,[121] chaired web (CW),[122] poly-N (pN),[28] arsenic-like (A7),[122] layered boat (LB),[122] phosphorus-like (BP),[85] metallic chain (CH),[108] zigzag chain (ZZ),[109] simple cubic (SC) allotropes,[122] a diamondoid (N_{10}-cage)[124] allotropes and phases of the space groups $Pba2$,[122] $P2_12_12_1$,[122] $P1$,[122] $C2/c$,[122] $Cmcm$.[122] The latest one has been proposed by Bondarchuk and Minaev in 2017, “*a new ambient-pressure metastable single-bonded 3D nitrogen allotrope (TrigN) of trigonal symmetry (space group R*-3*)*”.[125]

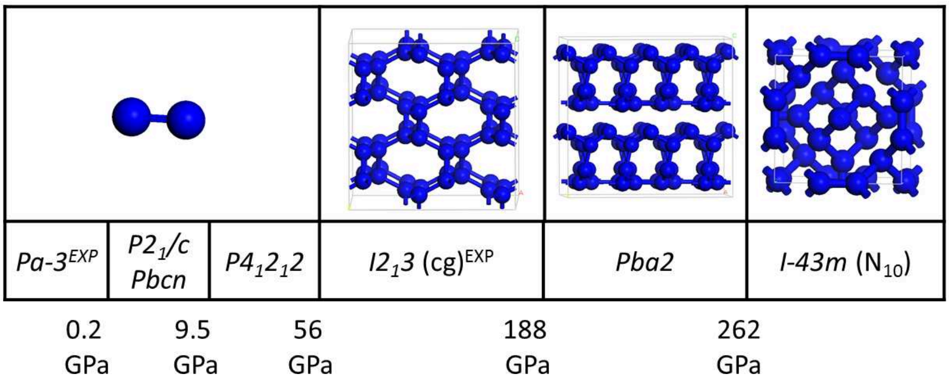

Figure 3.2 N_n nets found in solid-state nitrogen allotropes. Experimentally characterized phases are indicated (EXP) while theoretical ones correspond to the lowest ground-states.

Molecular polynitrogen units

Besides the predicted, and experimentally characterized, extended nitrogen nets encountered in solid-state high-pressure phases, several neutral and charged molecular species N_n (n>2) have been proposed in a variety of forms, such as cyclic, acyclic, or caged conformations. The imagination of researchers in the field of energetic materials produces novel, predicted neutral and charged N_n structures year after year.[127–130]

We've selected three of them as representative candidates, and display their structures in *Figure 3.3*, *i.e.*, octaazacubane N_8 derived from cubane C_8H_8, dipentazole $(N_5)_2$ analog to dicyclopentadienyl $(C_5H_5)_2$, and nitrogen fullerene N_{60} from C_{60}, which has been proposed for the first time by Indian chemist Riad Mana of Livermore lab.[131]

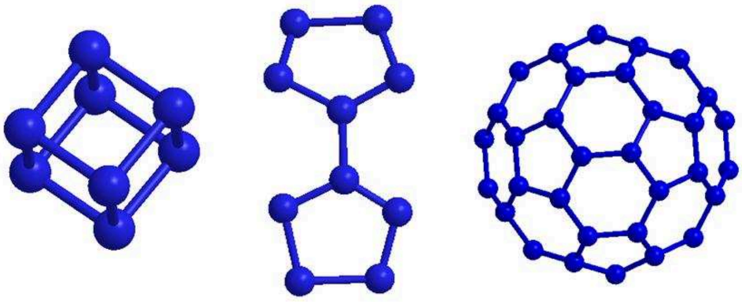

Figure 3.3 Hypothetical octaazacubane, dipentazole $(N_5)_2$ and N_{60} polynitrogen molecules.

Our bibliographic search shows that the latest article on this topic was published in May 2017, and deals with octaazacubane N_8 species,[132] the so-called nitrogen cubane (see *Figure 3.3*). This species was theoretically explored 26 years ago by Engelke and Stine at the Hartree-Fock level of theory but, due to the emergence of more accurate quantum methods, and nowadays access to powerful computers, the exploration of their electronic properties is still on-going!

Dozens of N_n^q structures have been suggested from *ab initio* calculations, all of them are metastable thermodynamically but dynamically stable (local minima on the nitrogen potential energy surface). Remember that these molecular forms of nitrogen suffer from a lack of stability. Therefore they can hardly be applied as mere explosives or propellants, thus, most of the predicted species remain hypothetical at the time of writing.

Besides dinitrogen, only a few neutral or ionic molecular species are detected experimentally in gas phase, but are not viable (*i.e.,* short-lived N_4 with a lifetime exceeding 1 ms at 298 K).[133] However, the high endothermic heats of formation make the safe synthesis and handling of these molecules the major challenges for experimental chemists.

Polynitrogen units in covalent compounds

Different N_n motifs are observed experimentally in molecular $R[N_n]R$ compounds, in which an R group acts as a “stabilizer” due to its size (a bulky substituent) and its ability to form a (partial) covalent bond with the unsaturated nitrogen atom of the N_n moieties. *Figure 3.4* gives an illustration of this family of compounds, focusing on the encountered N_n topologies.

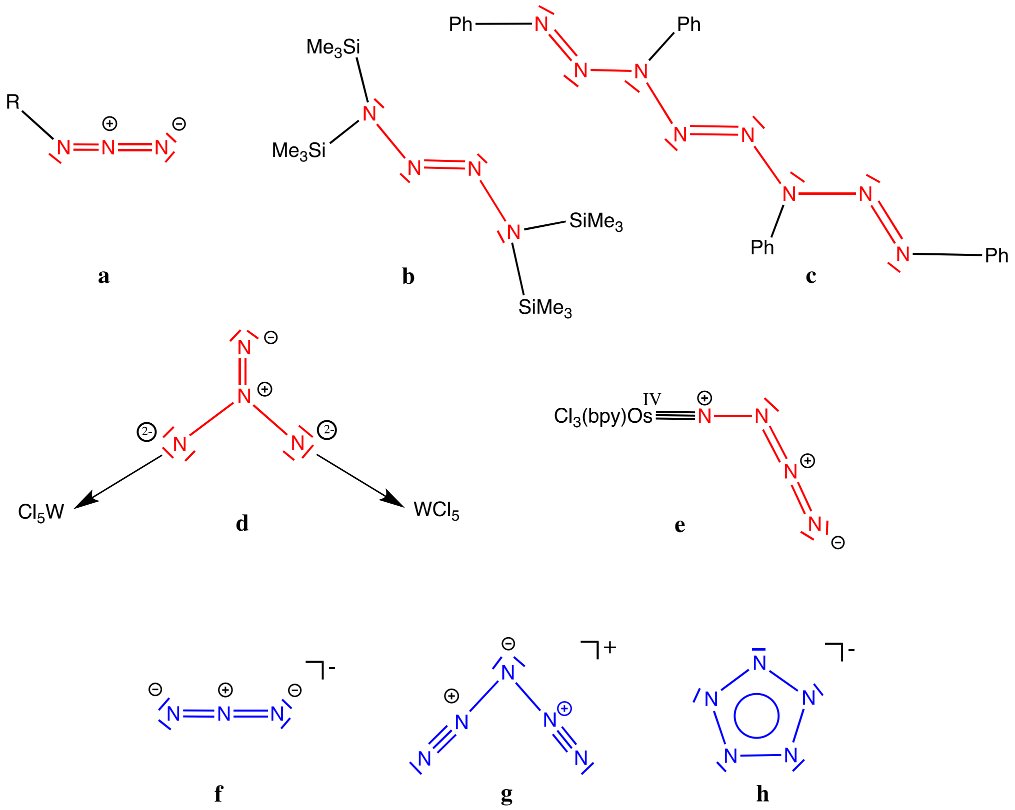

Figure 3.4 Examples of experimental N_n motifs found in molecular species (**a-e**) and solid-state salts (**f-h**). Azido RN_3 molecules **a** (R=H, CF_3, organometallic fragment,…), $(Me_3Si)_2N\text{-}N\text{=}N\text{-}N(SiMe_3)_2$ **b**, the longest nitrogen chain in Ph-N=N-N(Ph)-N=N-N(Ph)-N=N-Ph **c**, organometallic $[(Cl_5W)\text{-}N(N)_3\text{-}WCl_5]^+$ **d** and amidoazido $[Os(bpy)(Cl)_3(N_4)]^-$ **e** compounds.[126] In blue are represented the three experimentally characterized N_n ions in crystalline salts; N_3^- azide **f**, pentazenium N_5^+ **g** and *cyclo*-pentazole anion N_5^- **h**.

Linear triatomic unit NNN is found in numerous azido RN_3 molecules **a** (R=H, CF_3, …), whereas concatenation larger than N_3 are rare, and is more limited than for carbon; bent N_4 chain is present in $(Me_3Si)_2{>}N\text{-}N\text{=}N\text{-}N{<}(SiMe_3)$ **b** and, as far as we know, the longest chain so far reported being the N_8 unit in PhN=N-N(Ph)-N=N-N(Ph)-N=NPh; **c** These oligomers are reminiscent of the infinite form of poly-nitrogen $–(–N=N–)_x–$, isoelectronic to polyacetylene, which has been proposed, from theoretical calculations, as a stationary point on the PES.[134]

Others motifs have been described experimentally, such as the three-pointed-star NN_3 motif found in organometallic $[(Cl_5W)\text{-}N(N)_3\text{-}WCl_5]^+$ **d** isoelectronic to CO_3^{2-} carbonate, and the amidoazido $[Os(bpy)(Cl)_3(N_4)]^-$ complex **e** with bent finite N_4 chain (see *Figure 3.4*).

This brings us to the end of this brief paragraph on molecular N_n-based species, and we switch to polynitrogen N_n moieties present in binary ionic salts, the scope of our present study.

Polynitrogen units in salts

To get “stabilized” polynitrogen N_n units, a fruitful way might consist of the mixing of nitrogen and an electron-donor (*i.e.,* electropositive element), or -acceptor (*i.e.,* electronegative element) species to get anionic and cationic N_n^q entities, respectively, stabilized by strong ionic interactions in solid-state minerals or ionic liquids. To the best of our knowledge, only three charged nitrogen-based species have been experimentally characterized: the well-established azide N_3^- **f** which has a moderate stability; the reported pentazenium N_5^+ cation **g**, which can exist only with large counter anions; and the *cyclo*-pentazole anion N_5^- **h** (see *Figure 3.4*).[135–143]

Note that the latest ion, N_5^-, has been characterized very recently in solid-state phases: CsN_5,[144,145] $(N_5)_6(H_3O)_3(NH_4)_4Cl$ salt[146], and in carbon-free inorganic–metal complex $[M(H_2O)_n(cyclo\text{-}N_5)_2]\cdot 4H_2O$ (M=Mn, Fe, Co, n=4; Mg, n=6).[147,148] These results demonstrate that all-nitrogen units can be synthesized and stabilized in a crystal field and belong to an active field of research.

A number of theoretical studies have appeared in recent years on the crystal structure prediction of novel structures in binary s-block nitrogen phase diagrams, and we “compete” in this research area. Presented in *Table 3.1* is an up-to-date list of A_xN_y, where A is an s block element, alkaline or alkaline earth metal. *Figure 3.4* summarizes the topology of N_n units observed in experimentally characterized and theoretically predicted A_xN_y phases:

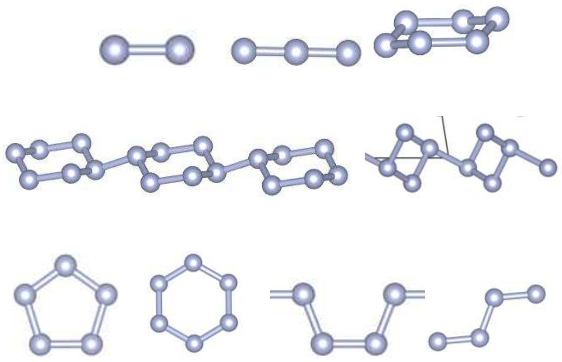

Figure 3.5 N_n motifs encountered in A_xN_y ionic salts listed in *Table 3.1*.

Prasad *et al.*[149] explored lithium azides LiN_3 phases from ambient pressure up to 500 GPa using the DFT method. They successfully reproduced the experimentally known monoclinic *C2/m* LiN_3 phase, and predicted two other competing metallic phases containing N_2 units at low pressure. The N_6 member rings, infinite chain and wave like nitrogen-rich layer in LiN_3 structures then emerge as the stable phases at a pressure larger than 36 GPa. Peng *et al.*[150] predicted a new crystal pentazolate LiN_5, which is thermodynamically stable above 9.9 GPa, and metastable at ambient conditions. Recently, Shen *et al.*[151] explored the Li-N binary phase diagram at different pressures and up to 100 GPa. They predicted the existence of five compositions, namely $Li_{13}N$, Li_5N, Li_3N_2, LiN_2, and LiN_5. Isolated nitrogen N^{3-} ions, N_2 dimers, polyacetylene-like chains and *cyclo*-N_5 rings are identified (see *Figure 3.6*).

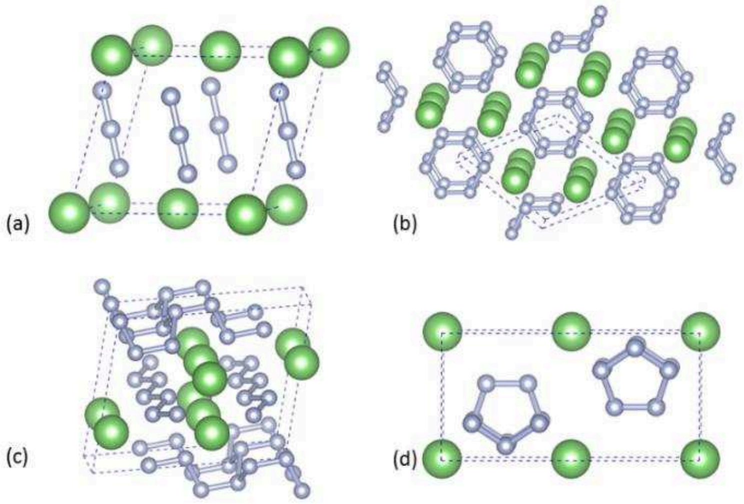

Figure 3.6 (a) Monoclinic lithium azide *C2/m*-LiN_3 at 1 atm, (b) *P6/m*-LiN_3 at 60 GPa, (c) *C2/m*-LiN_3 at 200 GPa, (d) Lithium pentazolate $P2_1/m$-LiN_5 at 20 GPa.

The sodium azide is predicted to undergo a chemical transformation above 50 GPa into two sodium pentazolates, namely *Cm* NaN_5 and *Pbam* Na_2N_5. Steele *et al.*[152] predicted sodium pentazolates which are stabilized in the solid phase by Na^+ cations at pressures exceeding 20 GPa, and quenchable to ambient pressure.

Meanwhile, five new stoichiometric Cs-N compounds have been predicted and could be experimentally synthesizable at modest pressures[144,153], including polynitrogen chains in the *C*2/*c* phase of CsN_2 and the newly identified CsN crystal with a novel N_4^{4-} anion.

Let's switch to alkaline earth metal nitrogen phases, Ae-N (Ae=Be, Mg, Ca, Sr, Ba). Experimentally, beryllium and magnesium form only salt-like nitrides (isolated N^{3-} in Be_3N_2 and Mg_3N_2). Eckerlin *et al.*[154] report a polymorph Be_3N_2 phase transition around 1400°C. Chang *et al.* investigated the structural stability and mechanical properties of Be_3N_2 crystallizing in α and *β* phases.[155] These two phases are strongly pressure dependent in the pressure range 0 to 80 GPa. The superior mechanical properties show that the two phases of Be_3N_2 could be a potential candidate for hard material. Wei *et al.*[156] predicted that *P*-1 and *P*2$_1$/*c* BeN_4 become energetically stable at high pressure. Interestingly, *P*2$_1$/*c* BeN_4 has a novel 3-dimensional N_{10} member rings network, in which the nitrogen atoms are in the sp^3 hybridization.

Mg_3N_2 nitride is prepared in similar ways as Be_3N_2, by reaction of finely divided magnesium metal with gaseous nitrogen or ammonia.[157] The cubic *anti*-bixbyite Mg_3N_2 has been confirmed isostructural to *β*-Be_3N_2. From *ab initio* calculations, Mg_3N_2 is a semiconductor with a band gap of 1.1 eV. Liu *et al.*[158] predicted a novel metastable Mg_3N_2 monolayer with a hexagonal lattice. It displays an intrinsic direct band gap of 1.86 eV. While we were studying the Mg-N phase diagram, Wei *et al.* predicted similar results using another structure prediction method.[159] They predicted a series of stable chemical stoichiometries at high pressures with a rich variety of polynitrogen forms. We will compare their results with ours in the following section.

Heavy alkaline earth metals (Ca, Sr, Ba), however, seemingly form no such ionic nitride, but more than one partially metallic nitride with unexpected stoichiometries. Compared with beryllium and magnesium, the number of binary compounds formed in the Ca-N system is larger.

Experimentally, compositions have been characterized, namely Ca_2N, Ca_3N_2 and CaN_2.[160–162163] From a theoretical point of view, other compositions emerged. In 2016, Zhu *et al.*[164] explored the whole stoichiometries of Ca-N binary compounds. A rich variety of polynitrogen forms is presented. Besides the experimental compositions, they also found Ca_2N_3, CaN, CaN_3, CaN_4, and CaN_5, which are stable under high pressure. Notably, the CaN phase is predicted to be quenchable.

In experimental Sr-N and Ba-N phase diagrams, are located 1:6 phases which feature symmetrical linear N_3- groups. $Sr(N_3)_2$ and $Ba(N_3)_2$ are metastable azides. The true nature of the "charge-balanced" Sr_3N_2 and Ba_3N_2 compounds are yet unclear, even though these compounds were first mentioned in 1892 by Maquenne.[165] In 1980 Künzel proposed a defect NaCl-type structure for Ba_3N_2, but no further mentionof this structure can be found in the literature.[166] Early studies identified the product of the nitridation of barium metal only by chemical analysis.[167,168] The compound was observed to be obtained from the decomposition of the azide, $Ba(N_3)_2$, but no solid characterization was performed.

Ba_3N_2 is the only alkaline earth nitride for which we find an alternative ground-state structure. The α-Ba_3N_2 comes out lowest in energy with *anti*-A-sesquioxide type. β-Ba_3N_2 will adopt an *anti*-Rh_2O_3-II structure becoming the ground state at 2 GPa. Another structure, termed γ-Ba_3N_2, exhibits an *anti*-$CaIrO_3$ structure starting at 34 GPa. At 51 GPa, δ-Ba_3N_2 may be found with a hexagonal *P*6_3*/mmc* structure becoming stable. A comprehensive list of the s-block element nitrides is detailed in *Table 3.1.*

Table 3.1 Literature report on A_xN_y binary phases (A, s-block elements; alkaline and alkaline earth metals). These structures are classified into four families relating to the dimensionality of the nitrogen sublattices: (1) extended 2D nitrogen layers, (2) infinite 1D nitrogen chains, (3) encapsulated molecule-like 0D anionic units, and (4) isolated nuclei N^{3-} ions. Experimentally characterized structures are explicitly indicated (EXP); if not, this is a strictly hypothetical phase.

Phases	**P (GPa)**	**VEC[a]/ACN[b]**	**Nitrogen framework, electrical property**
Two-dimensional (2D) network			
LiN_3 (*C2/m*) Prasad[149]	190-500	5.33/2.6+2	layers of fused puckered 10-embered decagon rings + 1D zigzag chains, metallic
One-dimensional (1D) network			
LiN_2 (*P*-1) Shen[151]	>56	5.5/2	polyacetylene-like armchair chains poly-N_4^{2-}, semiconductor
LiN_3 (*P*-1) Prasad[149]	metastable	5.33/2.33	linked chair six-membered rings poly-N_6^{2-}, metallic
LiN_3 ($P2_1$) Wang[169]	>375	5.33/2.67	puckered fused 5-membered rings poly-N_6^{2-}, insulator
NaN_2 (*Cmmm*) Steele[152]	50-100	5.5/2	polyacetylene-like zigzag chains poly-N_2^-, metallic
NaN_3 (*C2/m*) Zhang[170]	152-200	5.33/2.5+2	puckered fused six-membered rings poly-N_4^- and zigzag chains poly-N_2^-, metallic
KN_3 (*P6/mmm*) Zhang[171]	40-100	5.33/2.67	Fused chair-like six-membered rings poly-N_6^{2-}, metallic
KN_3 (*C2/m*) Zhang[171]	>298.6	5.33/2.5+2	puckered fused six-membered rings poly-N_4^- and zigzag chains poly-N_2^-, metallic
KN_3 (*C2/m*) Zhang[171]	>274	5.33/2.67	Fused chair-like six-membered rings poly-N_6^{2-}, insulator
RbN_3 (*P*-1) Wang[172]	30-50	5.33/2	polyacetylene-like trans-cis chains poly-N_{12}^{4-} , metallic
RbN_3 (*C2/m*) Wang[172]	>200	5.33/2.67	Fused chair-like six-membered rings poly-N_6^{2-}, metallic
CsN_3 (*P*-1) Wang[173]	51-200	5.33/2	polyacetylene-like trans-cis chains poly-N_{12}^{4-}, metallic
CsN_2 (*C2/c*) Peng[145]	>40	5.5/2	infinite spiral chains poly-N_8^{4-}, insulator
CaN_4 ($P4_12_12$) Zhu[164]	19-67	5.5/2	armchair chains poly-N_4^{2-}, metallic

Molecular anions			
Phases	**P (GPa)**	**VEC[a]/ACN[b]**	**Nitrogen framework, electrical property**
Li_3N_2 (*P4/mbm*) Shen[151]	30-39	6.5/1	dumbbell N_2^{3-}, metallic
Li_3N_2 (*C2/c*) Shen[151]	39-89	6.5/1	dumbbell N_2^{3-}, metallic
Li_2N_2 (*Pmmm*) Shen[151], Zhang[174]	0-8.2	6/1	dumbbell N_2^{2-}, metallic
Li_2N_2 (*Immm*) Shen[151]	8.2-8.9	6/1	dumbbell N_2^{2-}, metallic
Li_2N_2 (*Pnma*) Shen[151]	8.9-66.4	6/1	dumbbell N_2^{2-}, metallic
Li_2N_2 (*Cmcm*) Shen[151]	>66.4	6/1	dumbbell N_2^{2-}, metallic
Li_2N_2 ($P6_3/mmc$) Shen[151]	0-56	5.5/1	dumbbell N_2^{2-}, metallic
LiN_3 (*P*-62*m*) Shen[151]	0-0.9	5.33/1	dumbbells N_2^{-}, metastable
LiN_3 (*C2/m*) Shen[151]	0-36	5.33/1.33	linear N_3^{-} azide, metastable below 49 GPa
LiN_3 (*P6/m*) Shen[151], Wang[169]	>49 36-375	5.33/2	benzene-like N_6^{2-}, metallic
KN_3 (*I4/mcm*) Zhang[171]	0-22	5.33/2	linear molecular N_3^{-} anions
KN_3 (*C2/m*) Zhang[171]	22-40	5.33/2.5+2	linear molecular N_3^{-} anions
LiN_5 ($P2_1/c$) Shen[151]	15-65	5.2/2	5-membered ring N_5^{-} pentazolate, insulator
LiN_5 (*C2/c*) Shen[151]	>65	5.2/2	5-membered ring N_5^{-} pentazolate, insulator
NaN (*Pmmm*) Zhang[175]	0	6/1	dumbells N_2^{2-}, metallic
NaN (*Cmcm*) Steele[152]	10-30	6/1	dumbells N_2^{2-}, metallic
NaN (*Cmmm*) Steele[152]	28-100	5.33/1	dumbells N_2^{2-}, metallic
NaN_2 (*Cmmm*) Steele[152]	30-100	5.5/1	dumbells N_2^{2-}, metallic
Na_2N_5 (*Pbam*) Steele[152]	30-100	5.4/1	Five-membered ring N_5^{2-}, pentazolate, metallic
NaN_3 (*C2/m*) Steele[152]	<0.85	5.33/1.33	linear N_3^{-} azide, insulator
NaN_3 (*R*-3*m*) Zhang[170]	0.85-6.5	5.33/1.33	linear N_3^{-} azide, insulator
NaN_3 (*I4/mcm*) Zhang[170]	6.5-58	5.33/1.33	linear N_3^{-} azide, insulator
NaN_3 (*P6/m*) Zhang[170]	58-152	5.33/2	benzene-like N_6^{2-}, metallic
NaN_5 (*P2/c*) Steele[152]	16.5	5.2/2	five-membered ring N_5^{-} pentazolate, insulator
NaN_5 (*Cm*) Steele[152]	20-100	5.2/2	five-membered ring N_5^{-} pentazolate, insulator
KN_3 (*I4/mcm*) Babu[176]	0-20	5.33/1.33	linear N_3^{-} azide insulator
KN_3 (*C2/m*) Zhang[171]	15.7-20	5.33/1.33	linear N_3^{-} azide, insulator
KN_3 ($Cm2_1$) Zhang[171]	20-41	5.33/1.33	linear N_3^{-}, azide; metastable
KN_3 (*P6/mmm*) Zhang[171]	>41	5.33/1.33	benzene-like N_6^{2-}, metallic
RbN_3 (*I4/mcm*) Wang[172]	0-30	5.33/1.33	linear N_3^{-} azide, insulator
RbN_3 (*P6/mmm*) Wang[172]	50-200	5.33/2	benzene-like N_6^{2-}, metallic

Cs_2N (*C2/m*) Peng[145]	>18	7/1	dumbbell N_2^{4-} pernitride
CsN (*C2/m*) Peng[145]	7.5-44	6/1	dumbbell N_2^{2-} diazenide
CsN (*P*-1) Peng[145]	>44	6/1	open-chain N_4^{4-} tetrazadiene, semiconductor
CsN_2 (*C2/m*) Peng[145]	4-40	5.5/1	dumbbell N_2^{-}
CsN_3 (*I4/mcm*) Peng[145]	<6	5.33/1.33	linear N_3^{-} azide, insulator
CsN_3 (*C2/m*) Peng[145]	6-13	5.33/1.33	linear N_3^{-} azide
CsN_3 ($P2_1/m$) Peng[145]	16-26	5.33/1.33	linear N_3^{-} azide
CsN_3 (*C2/m*) Peng[145]	>81	5.33/2	benzene-like N_6^{2-}, metallic
CsN_3 ($P2_1$) Wang[173]	13-51	5.33/1.33	linear N_3^{-} azide
CsN_5 ($Cmc2_1$) EXP Peng,Steele[140,141]	>14	5.2/2	cyclopentadiene-like N_5^{-} pentazolate, metallic
CaN (*C2/m*) Zhu[164]	0-14	7/1	dumbbell N_2, metallic
CaN ($Cmc2_1$) Zhu[164]	14-40	7/1	dumbbell N_2, metallic
CaN (*C2/m*) Zhu[164]	40-76	7/1	dumbbell N_2, metallic
CaN (*Pbam*) Zhu[164]	76-100	7/1	dumbbell N_2, metallic
Ca_2N_3 (*P*-62*m*) Zhu[164]	18-44	6.33/	dumbbell N_2, metallic
CaN_2 (*Pnma*) Zhu[164]	0-3	6/1	dumbbell N_2^{2-}
CaN_2 (*I4/mmm*) Zhu[164]	3-18	6/1	dumbbell N_2^{2-}
CaN_2 ($P2_1/c$) Zhu[164]	18-92	6/1.5	N_4^{4-}, metallic
CaN_2 (*Pbam*) Zhu[164]	92-100	6/1.5	N_4^{4-}, metallic
CaN_3 (*Pmma*) Zhu[164]	8-36	5.67/1	dumbbell N_2, metallic
CaN_4 (*P4/mbm*) Zhu[164]	5-19	5.5/1	dumbbell N_2, metallic
CaN_3 (*C2/c*) Zhu[164]	36-100	5.67/2	N_6^{4-}, metallic
CaN_5 (*Pm*) Zhu[164]	33-100	5.4/2	N_5^{2-}, metallic
CaN_6 (*Fddd*) Zhu[164] EXP	ambient	5.33/1.33	linear N_3^{-} azide
SrN_6 (*Fddd*) Zhu[177]	ambient	5.33/1.33	linear N_3^{-} azide, insulator
BaN_6 (*Fddd*) Zhu[177]	ambient	5.33/1.33	linear N_3^{-} azide, insulator

Isolated nitrides N^{3-}			
Phases	**P (GPa)**	**VEC[a]/ACN[b]**	**Nitrogen framework, electrical property**
$Li_{13}N$ (*Immm*) Shen[151]	43-76	18/0	metallic
$Li_{13}N$ (*C*2/*m*) Shen[151]	>76	18/0	metallic
Li_5N (*P*6/*mmm*) Shen[151]	>80	10/0	metallic
Li_3N (*Pm*-3*m*) Shen[151]	0-0.2	8/0	insulator
Li_3N (*P*6/*mmm*) Shen[151]	0.2-	8/0	insulator
Li_3N (*P*6$_3$/*mmc*) Shen[151]	0.2-	8/0	insulator
Li_3N (*Fm*-3*m*) Shen[151]	0.2-	8/0	insulator
Na_3N (*Pm*-3*m*) Vajenine[178]	0-1	8/0	insulator
Na_3N (*P*6/*mmm*) Vajenine[178]	1-2.3	8/0	insulator
Na_3N (*P*6$_3$*cm*) Vajenine[178]	2.3-25	8/0	insulator
Na_3N (*P*6$_3$*cm*) Vajenine[178]	>25	8/0	insulator
Na_3N (*Fm*-3*m*) Steele[152]	>10	8/0	insulator
K_3N (*P*6$_3$/*mmc*) Fischer[179]	metastable	8/0	insulator
Cs_3N (*Cmcm*) Peng[145]	18-64	8/0	insulator
Be_3N_2 (*Ia*-3) Xia[175]	0-118	8/0	insulator
Be_3N_2 (*P*-3*m*1) Xia[175]	118-150	8/0	insulator
Be_3N_2 (*P*6$_3$/*mmc*) Xia[175]	metastable	8/0	insulator
Be_3N_2 (*Pn*-3*m*) Xia[175]	metastable	8/0	insulator
Be_3N_2 (*R*3*m*) Xia[175]	metastable	8/0	insulator
Ca_2N (*R*-3*m*) Zhu[164]	0-10	9/0	insulator
Ca_2N (*Fm*-3*m*) Zhu[164]	10-84	9/0	metallic
Ca_2N (*I*4/*mmm*) Zhu[164]	84-100	9/0	metallic
Ca_3N_2 (*Ia*-3) Römer[180]	0-0.5	8/0	insulator
Ca_3N_2 (*R*-3*c*) Römer[180]	metastable	8/0	insulator
Ca_3N_2 (*Pbcn*) Römer[180]	0.5-10	8/0	insulator
Ca_3N_2 (*C*2/*m*) Römer[180]	10-27	8/0	insulator
Ca_3N_2 (*P*-3*m*1) Römer[180]	27-38	8/0	insulator
Ca_3N_2 (*C*2/*m*) Römer[180]	38-90	8/0	insulator

[a] In A_xN_y, VEC is the valence electron concentration; VEC= (cx+5y)/y with c: number of electrons given by A; x: number of A atoms; y: number of nitrogen atoms.

[b] ACN is the averaged coordination number of the nitrogen atoms in A_xN_y structures.

Goals

As a crucial thermodynamic parameter, pressure has emerged as a powerful tool to investigate the physical and chemical behaviors of materials, and this has lead to new and unexpected products.

In this study, we investigate the possible formation and stability of polymeric nitrogen compounds in the binary Mg-N system, and the Ba-N system, at high pressure. Structure searches for stable Mg/Ba-N compounds were performed using an unbiased evolutionary structure prediction algorithm in conjunction with density-functional calculations. After which, electronic properties and chemical bonding of the identified compounds were systematically investigated, with the aim of exploring the properties and potential applications of Mg/Ba-N compounds as high energy-density materials.

3.2 Computational details

To identify stable ground-state structures and compositions of binary Mg/Ba-N system, a variable-composition evolutionary algorithm implemented in the USPEX code[8,13,30] was employed. The total number of atoms in the primitive cell was up to 30. The first generation had 100 randomly produced candidate structures; all subsequent generations contained 80 structures. Evolutionary variation operators were applied to produce new structures; 60% of the new structures were produced by heredity with the remaining structures produced by softmutation (15%), transmutation (15%), and random generation (10%).

Density-functional energy calculations and geometry optimizations were performed using the VASP package[48] with the Perdew-Burke-Ernzerhof (PBE) parametrization of the generalized gradient approximation[41,42]. Projector-augmented wave (PAW) potentials[49] were used for magnesium, barium and nitrogen atoms with radii of 2.0 a.u. for Mg ([Ne] core), 2.8 a.u. for Ba ([Kr] core) and 1.5 a.u. for N ([He] core). A plane-wave basis set with a kinetic energy cutoff of 600 eV was employed. Uniform Γ-centered meshes with a reciprocal space resolution of $2\pi \times 0.03$ Å^{-1} were used for Brillouin zone sampling to ensure the error bars of the total energies were less than 1 meV/atom. Structure relaxations proceeded until all forces on atoms were less than 1 meV/Å, and total stress tensor deviated from target pressure by ≤0.01 GPa.

The dynamical stability of the statically relaxed structures was established by the absence of imaginary phonon frequencies, which were computed using the finite-displacement approach as implemented in the PHONOPY code[97]. Moreover, the effect of zero-point energy (ZPE) on the stability of Mg/Ba-N compounds was studied. The inclusion of ZPE only shifted moderately the fields of stability but did not change the topology of the phase diagram. Thus the following energies are non-ZPE corrected. Compounds located on the convex hull are thermodynamically stable against decomposition into any other binaries or the elements, while compounds above the convex hull are not stable. The most stable forms of pure Mg and N depend on the applied pressure, *i.e.,* the hcp, bcc structures for Mg/Ba and $Pa\text{-}3$, $Pbcn$, $P2_1/c$, $P4_12_12$, $I2_13$, $Pba2$, and $I\text{-}43m$ structures for nitrogen.

3.3 Magnesium nitrides

3.3.1 Phase stability of the Mg-N system under pressure

Stable compounds, which form the thermodynamic convex hull (*Figure 3.7*), were identified at selected pressures and their stability fields are shown in the pressure-composition phase diagram (*Figure 3.8*). It is noteworthy that our evolutionary searches successfully reproduced experimentally known Mg_3N_2 structures. Moreover, the searches revealed that Mg_3N_2 transforms from the *Ia*-3 to *Pbcn* phase at 21 GPa, to the *C*2/*m* phase at 24 GPa and the *Pnma* phase at 43 GPa. The high-pressure *Pnma* phase has been proposed by Wei *et al*. based on first-principles particle swarm methodology implemented in Calypso code.[7,27] Besides Mg_3N_2, eight hitherto unknown stoichiometries emerged to be stable under pressure, including five N-rich stoichiometries, namely, Mg_5N_7, Mg_2N_3, MgN_2, MgN_3, and MgN_4, and three Mg-rich compositions, Mg_5N_3, Mg_4N_3, and Mg_5N_4. As shown in *Figure 3.8,* Mg_3N_2, Mg_2N_3, MgN_2, MgN_3, and MgN_4 undergo a series of phase transitions in their stability domains, while other stoichiometries only possess a single phase.

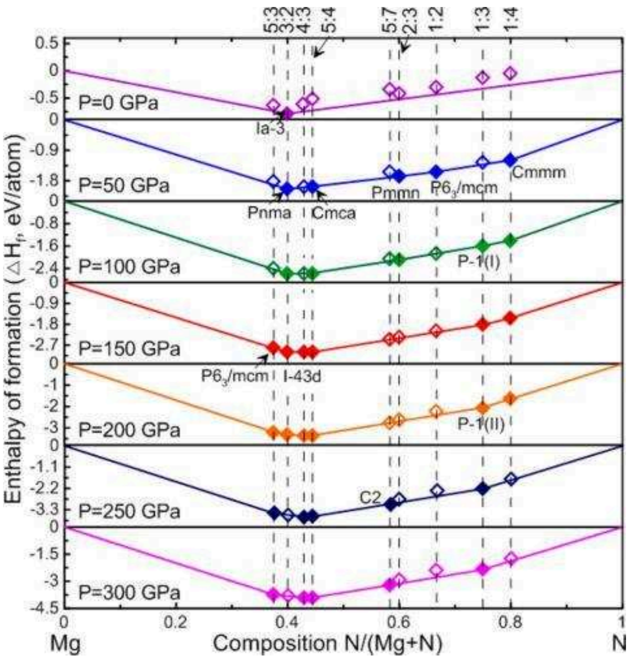

Figure 3.7 Convex hulls of the Mg-N system at selected pressures. Solid squares denote stable structures, while empty ones represent metastable structures.

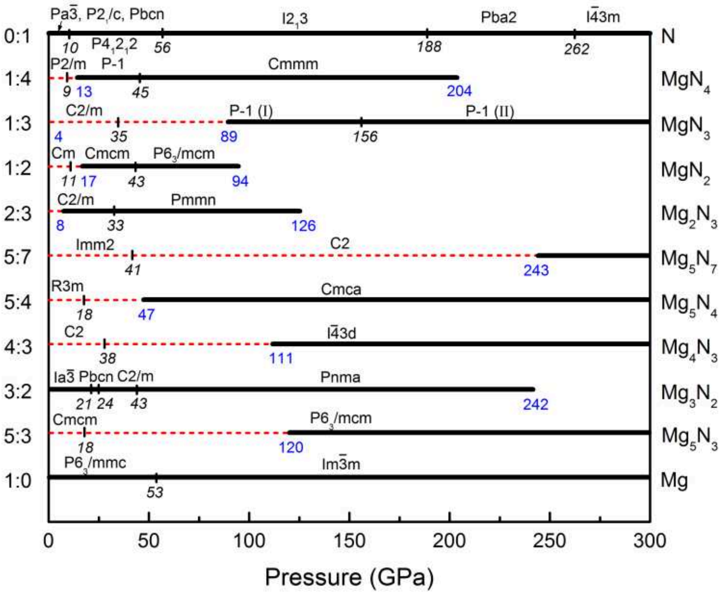

Figure 3.8 Pressure-composition phase diagram of Mg-N system from 0 to 300 GPa. The stable phases are indicated by bold lines, and metastable phases are depicted by thin dashed lines. The blue numbers represent compound stability ranges, while black italic numbers denote phase transition pressures.

According to the structural arrangement and dimensionality of the covalent nitrogen network, the great variety of crystal structures was classified into four different categories (*Table 3.2*): structures with (1) 1D infinite nitrogen chains (MgN_4); (2) 2D covalent nitrogen layers alternating with magnesium sheets (MgN_3); (3) encapsulated molecule-like covalent anionic units such as N_2 dumbbells, bent triatomic N_3 units and planar $N(N_3)$ motifs, as found in Mg_5N_4, Mg_5N_7, Mg_2N_3, or MgN_2; and (4) isolated nitrogen atoms, as found in Mg_5N_3, Mg_3N_2, Mg_4N_3, and Mg_5N_4. This structural classification can be applied to other alkali and alkali earth nitrides A_xN_y compounds, such as N_2 dumbbells, linear N_3 units, five-membered N_5 rings, cyclic N_6 rings, and 1D linear N_x.

The electronic and geometric structures of the Mg_xN_y phases were examined in order to better understand their chemical bonding. Throughout this article, electron transfer is considered to occur from electropositive magnesium atoms into the polynitrogen sublattice. Thus a N_y network bears 2× valence electrons (ve) per formula unit. Except for isolated N_3 based structures, covalent N-N bonds are encountered in the nitrogen sublattice. We recall the lengths of N-N bonds are roughly 1.10 Å for the triple bond, 1.25 Å for the double bond, and 1.45 Å for the single bond at ambient conditions. For calibration, the N-N single bond distance in *cg*-N is 1.31 Å at 200 GPa. These values were used to guide assignment of nitrogen-nitrogen bonds to rationalize the local structural environments using VSEPR theory and the Zintl-Klemm concept (ZKC).

Table 3.2 Chemical features of stable magnesium-nitrogen Mg_xN_y compounds.

Compounds	Phases	Stability domain (GPa)	Structure type	Nitrogen net
MgN_4	*P-1*[1] *Cmmm*	13~45 45~204	1D armchair chains 2-coordinated N	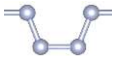
MgN_3	*P-1* (I)[1]	89~156	benzene-like N_6 rings	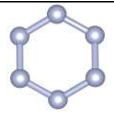
	P-1 (II)	156~300	2D layers 2- and 3-coordinated N	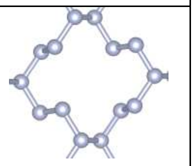
MgN_2	*Cmcm*	17~43	N_2 dumbbells	
	P6₃/mcm	43~94	$N(N)_3$ three-pointed stars	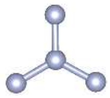
Mg_2N_3	*C2/m*	8~33	isolated nuclei N_2 dumbbells	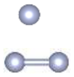
Mg_2N_3	*Pmmn*	33~126	bent N_3 units	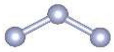
Mg_5N_7	*C2*	243~300	N_2 dumbbells bent N_3 units	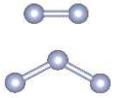
Mg_5N_4	*Cmca*	47~300	isolated nuclei N_2 dumbbells	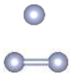
Mg_4N_3	*I-43d*	111~300	isolated nuclei	
Mg_3N_2	*Ia-3*	0~21	isolated nuclei	
	Pbcn	21~24	isolated nuclei	
	C2/m	24~43	isolated nuclei	
	Pnma[1]	43~242	isolated nuclei	
Mg_5N_3	P6₃/mcm	120~300	isolated nuclei	

3.3.2 Compounds containing 1D polynitrogen armchair chains and corrugated 2D layers

a. MgN_4

Our evolutionary searches uncovered N-rich MgN_4 stoichiometry as a thermodynamic ground state at a pressure as low as 13 GPa, easily achievable in high-pressure synthesis. The *P*-1 → *Cmmm* phase transition occurs at 45 GPa while their energy difference is as low as 0.05 eV/atom in the pressure range of 13-45 GPa. *P*-1 and *Cmmm* structures feature infinite planar 1D armchair-shaped nitrogen chains intercalated by magnesium atoms. The structural difference of these two phases mainly comes from the poly-N_4 chain-stacking sequences. Therefore, we focus our structural and electronic analysis on the higher-symmetry *Cmmm* phase. Its crystal structure is shown in *Figure 3.9a*. Each N atom of the poly$(N_4)_x$ chain is coordinated with two nearest Mg atoms, which are above and below the nitrogen chain plane, and each Mg atom is eight-coordinated by nearby N atoms forming an MgN_8 cube (Mg-N = 2.26 Å at 15 GPa). The shortest interchain separations are 2.77 Å along the c axis (π stacking interactions) and 2.70 Å along the b axis. The N-N separation along the chains are around 1.35 Å at 15 GPa, while the N-N-N bond angles are roughly 112°.

In the ionic picture, each Mg atom gives its two valence electrons to the N_4 building block; thus, the N_4^{2-} unit has 22 valence electrons, four σ bonding pairs, four in-plane lone pairs and six π delocalized electrons. The poly-N_4^{2-} chain is isotopological and isoelectronic to polythiazyl -$(S_2N_2)_x$-, an inorganic metallic polymer. Standard application of VSEPR theory to this planar chain enabled rationalization of the structural and bonding properties of poly-N_4^{2-} chains: each nitrogen atom is bent (*Figure 3.9b*). The planarity of the whole armchair chain is the result of delocalization, but also of the firm ionic interactions between Mg^{2+} ions and poly-N_4^{2-} chains. Recall that all N-N bonds in N_4^{2-} are of nearly same length, *i.e.,* 1.35 Å, which is longer than a double bond (1.25 Å) but shorter than a single bond (1.45 Å). This intermediate distance is consistent with the bonding picture in which six π electrons are distributed along the $-(N_4^{2-})_x-$ chain.

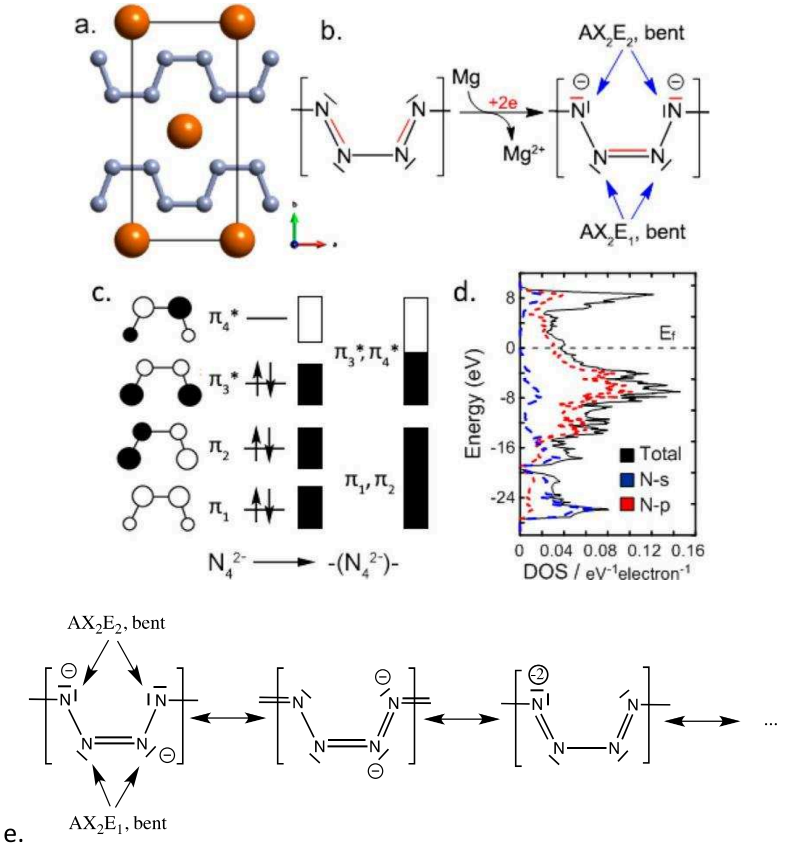

Figure 3.9 (a) Crystal structure of *Cmmm* MgN_4. The large orange circles represent Mg atoms, while small blue ones denote N atoms. (b) Scheme illustrating electron transfer from electropositive Mg atoms to the 1D $poly(N_4)_x$ chain and VSEPR AX_nE_m notation (A, central atom; X, ligand and n, its number; E, lone pairs and m its numbers; n + m is the steric number). (c) Molecular orbital diagram of the open N_4^{2-} π system. The right side shows the schematic band structure of the $-(N_4^{2-})x-$ chain without (left) and with (right) band overlap. (d) Calculated density of states of *Cmmm* MgN_4 at 100 GPa. (e) Resonant structures.

To confirm this analysis from the perspective of the simplified yet useful ZKC and Lewis theory, the electron localization function (ELF) was calculated. Topological analysis of ELF reveals the presence of two kinds of attractors (*Figure 3.10*). Each nitrogen atom has three valence basins: two disynaptic valence basins (N-N bonds) and one monosypnatic basin (a lone electron pair). This confirms the sp^2-like nature of the N-N bonding in the *Cmmm* structure. To assess if this poly nitrogen anionic chain is metallic like polythiazyl $-(S_2N_2)_x-$, we chose to start with the planar *cis*-N_4^{2-} molecular unit then built the extended armchair chain. The open *cis*-N_4^{2-} unit has four π molecular orbitals (1 AO π per nitrogen atom) and six π electrons. Two bonding π_1 and π_2 and one antibonding HOMO π_3^* exist and are occupied, while the highest in energy, antibonding π_4^*, remains vacant. The molecular orbital diagrams are displayed in *Figure 3.9c.* When converting from the molecular planar *cis*-N_4^{2-} unit to the extended poly-N_4^{2-} system, each π orbital generates a dispersive π band in the entire Brillouin zone (*Γ-X* line). If no band overlap occurs, one may expect semiconductor behavior for the -(N_4^{2-})x- chain. If band overlap occurs, joint valence and conduction (π_3^*, π_4^*) bands exist; in this case, the armchair polynitrogen anionic chain would be a metallic conductor.

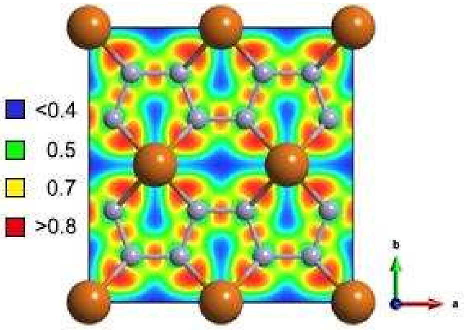

Figure 3.10 The calculated electron localization function (ELF) of the (001) plane of *Cmmm* MgN_4 at 100 GPa.

The densities of states (DOS) of *Cmmm* MgN_4 were computed, shown in *Figure 3.9d*. This phase is calculated to be metallic; the bands crossing the Fermi level are π-like, *i.e.,* joint (π_3^*, π_4^*) bands with some lone pair characteristics. Note that a Peierls distortion should occur in the -(N_4^{2-})x- chain as the Fermi level crosses π bands, though the strong ionic interactions between Mg^{2+} cations and -$(N_4^{2-})_x$- chains should prevent substantial Peierls distortion of the polymeric chain. As a result, the alternating N-N bond length differences along the covalent nitrogen chain are small, less than 0.01 Å. To conclude, MgN_4 contains planar nitrogen-based -$(N_4^{2-})_x$- chains and is an analog of the inorganic -$(S_2N_2)_x$- polythiazyl polymer. MgN_4 should behave as a highly anisotropic conductor at room temperature. The isoelectronic and isotopological polynitrogen chain was also discovered by Zhu *et al*. in the *P*4_12_12 CaN_4 phase.

b. MgN_3

In the nitrogen-rich side of the phase diagram, the structure search also yielded the composition MgN_3 with a phase transition sequence of *C2/m* (0 GPa, isolated N_2 dumbells) → *P*-1 (I) (35 GPa, isolated N_6 rings) → *P*-1 (II) (156 GPa, covalent nitrogen layers). However, the low-pressure *C2/m* phase, $(2Mg^{2+})(3N_2)^{4-}$ appears as metastable, as it is above the convex hull. MgN_3 presents only two thermodynamically stable phases, *P*-1 (I) from 89 to 156 GPa and *P*-1 (II) above 156 GPa. Our results are in agreement with Wei *et al.* ones who proposed a stable *P*-1 (I) phase above 80 GPa. Moreover, from a theoretical point of view, *P*-1 (I) phase can be recovered at atmospheric pressure while high-pressure *P*-1 (II) phase can not.

In *P*-1 (I) phase, nitrogen atoms form six-membered N_6 rings as shown in *Figure 3.12a*. At 100 GPa, a chair conformation is observed with a calculated dihedral angle of 150°. When pressure is released to 1 atm (the Mg-N Madelung energy and the packing forces decrease), covalent hexazine-N_6 anion remains intact and becomes planar with six nearly identical N-N bonds of 1.39 Å, which are slightly shorter than a single N-N bond (1.45 Å) but longer than a double one (1.25 Å). Formally, magnesium atoms transfer all of their valence electrons to N_6 rings, leading to N_6^{4-} unit. This ten π-electron 6-membered ring follows the 4n + 2 Hückel rule (aromatic), and it is isoelectronic to the well-known inorganic cyclic $S_3N_3^-$ and P_6^{4-} species. A molecular orbital diagram of the benzene-like N_6^{4-} anion is displayed in *Figure 3.11*. Among the six π levels of the planar N_6 ring, the three bonding π molecular orbitals (MO) and the two degenerated antibonding π^* ones are fully occupied, leading to only one π-bond delocalized over the six nitrogen atoms. This electronic situation explains well the structural feature encountered in N_6^{4-}, *e.g.,* N-N bonds slightly stronger than usual single N-N bond. An energy gap separates the degenerate occupied π_4^* and π_5^* MO (top of the valence band) and the empty π_6^* MO (bottom of the conduction band); MgN_3 is a semiconductor (see *Figure 3.12c*).

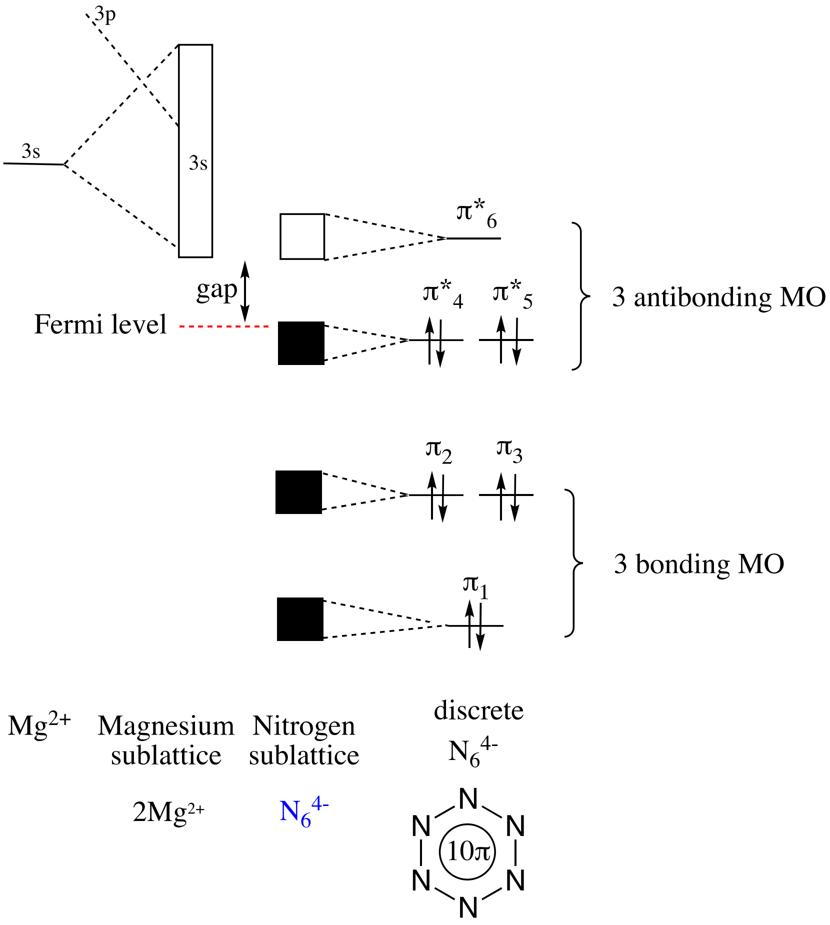

Figure 3.11 At right, molecular orbital levels of planar D_{6h} N_6^{4-} ring. Each level leads to localized π band (black boxes, occupied levels; empty boxes, unoccupied levels). At left, empty 3s level of Mg^{2+} atoms will lead to an empty 3s band. A band gap separates the valence and the conductions bands.

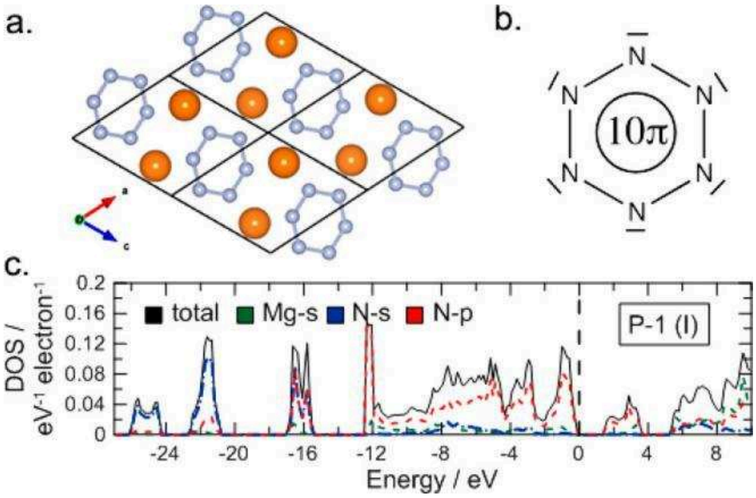

Figure 3.12 (a) Crystal structure of *P*-1 (I) MgN_3. (b) Lewis structure of cyclic N_6^{4-} anion. (c) Calculated density of states for *P*-1 (I) MgN_3 at 100 GPa.

As mentioned previously, *P*-1 (I) has no imaginary phonons from its range of stability down to P=1 atm, and presents persistent six-membered N_6^{4-} ring motif. If the barrier to decomposition to elements or others Mg_xN_y phases can protect *P*-1 (I) phase, then perhaps this original aromatic hexazine-N_6 dianion could be detected.

Above 156 GPa, a novel stable phase emerges on the energy surface as a static ground-state structure (space group: *P*-1). Its crystal structure is shown in *Figure 3.13a*. This high-pressure *P*-1 (II) phase contains extended 2D nitrogen sheets separated by isolated magnesium atoms. The 2D nitrogen sublattice is closely related to the orthorhombic layered black phosphorus structure (*α*-P, space group: *Cmca*), which is composed of condensed P_6 rings in a chair conformation and can be derived from *α*-P by removing one-quarter of the phosphorus atoms. This covalent nitrogen sublattice is also isostructural to the network found in the isoelectronic *α*-SrP_3 phase.

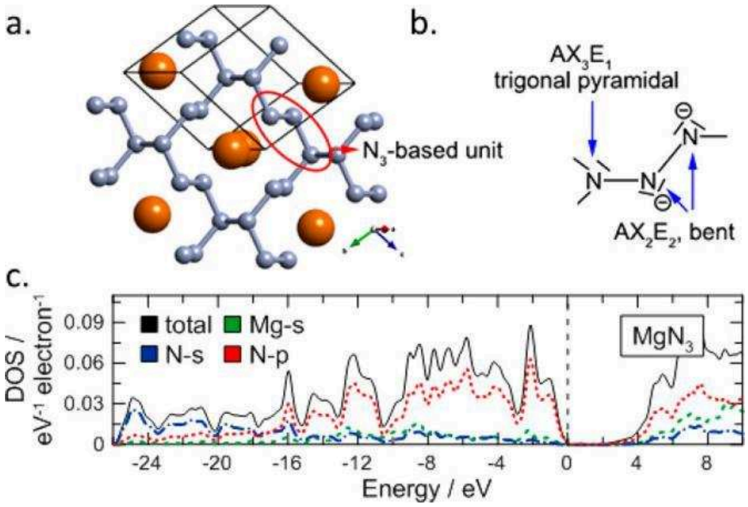

Figure 3.13 (a) Crystal structure of *P*-1 (II) MgN_3. (b) Lewis structure of the N_3-based unit N_3^{2-} with VSEPR AX_nE_m notation (A, central atom; X, ligand and n, its number; E, lone pairs and m its numbers; n + m is the steric number). (c) Calculated density of states at 200 GPa.

In MgN_3, each nitrogen slab is based on puckered 14-membered nitrogen ring which contains four N_3 units with two different types of nitrogen (>N-N-N-). This N_3 building block is illustrated in *Figure 3.13b*. One atom has a trigonal pyramidal conformation, and the others have a bent conformation with N-N separations in the range of 1.33-1.40 Å at 200 GPa (single bond character). The N-N-N bond angles vary from 88 to 113°, within the allowable range for sp^3 hybrid bond angles. The geometric structure of the >N-N-N- unit is well explained by VSEPR theory if one assigns a formal charge of -1 to each two-coordinated nitrogen atom (*Figure 3.13b*). Thus, MgN_3 belongs to the family of Zintl phases; all of the nitrogen atoms can fulfill the octet rule, and all valence electrons are in localized states; therefore, *P*-1 MgN_3 should be an insulator or a semiconductor with a band gap between the occupied bonding and nonbonding nitrogen-based orbitals and the vacant orbitals, *i.e.,* the antibonding nitrogen-based levels and Mg(3s) levels. Based on the computed DOS, MgN_3 is a semiconductor with a DFT band gap of 2.2 eV at 200 GPa (*Figure 3.13c*). Note that the band gap increases to 3.3 eV when a screened hybrid functional HSE06 is used (see *Figure 3.14*).

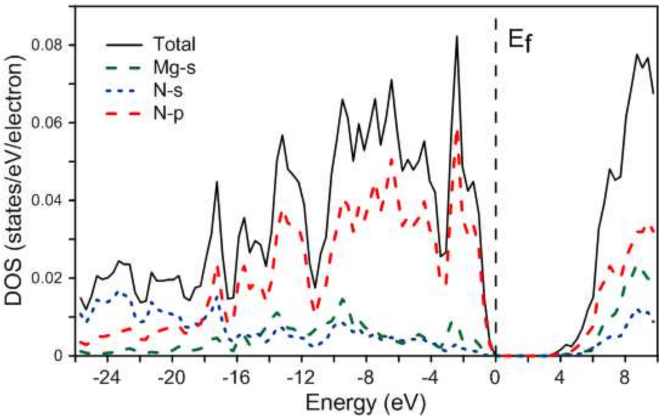

Figure 3.14 Calculated density of states (DOS) of *P*-1 MgN_3 at 200 GPa at HSE06 hybrid functional level.

3.3.3 Compounds containing molecule-like covalent anionic units

a. MgN_2

As shown in *Figure 3.8*, MgN_2 is stable between 17 and 94 GPa, and has two phases, with the transition *Cmcm* to *P*6$_3$*/mcm* pressure of 43 GPa. The *Cmcm* structure consists of N_2 dimers sitting in the channels of a 3D magnesium network (*Figure 3.15a*). At 40 GPa, the N-N distance is 1.25 Å, indicating N-N double bond character. According to the ZKC, MgN_2 can be described as $Mg^{2+}N_2^{2-}$. Thus, diazenide N_2^{2-} has 12 valence electrons and its electronic ground-state configuration is $1\sigma_g^2\ 2\sigma_u^{*2}1\pi_u^4 2\sigma_g^2 1\pi_g^{*2}$. The N_2^{2-} dumbbell possesses a bond order of 2 and the N_2^{2-} unit is a solid-state equivalent of molecular triplet O_2. As shown in the calculated DOS (*Figure 3.15d*), $1\pi_g^*$ degeneracy is broken by the static electric field created by the surrounding Mg^{2+} ions. Therefore, a small gap is created between these two antibonding HOMO-LUMO $1\pi_g^*$ levels. *Cmcm* MgN_2 is a very narrow-gap semiconductor with a band gap of 0.25 eV at 40 GPa.

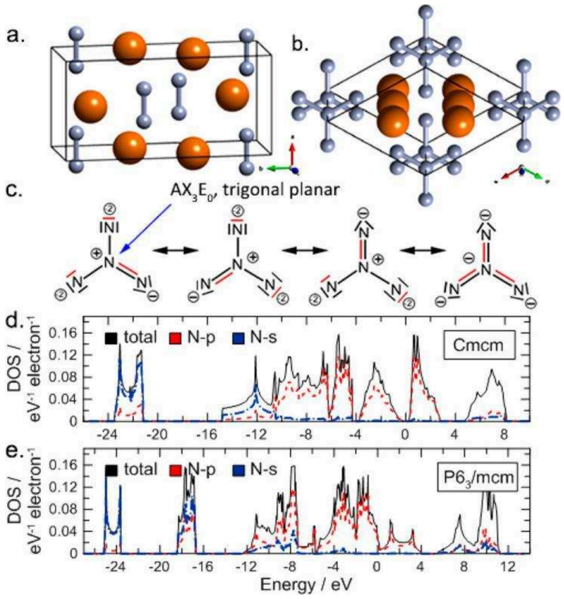

Figure 3.15 (a, b) Crystal structures of *Cmcm* and *P6₃/mcm* MgN_2. (c) Resonant Lewis structure of the planar $N(N)_3^{4-}$ unit with VSEPR notation. (d, e) Calculated density of states for the *Cmcm* phase at 40 GPa and *P6₃/mcm* phase at 100 GPa.

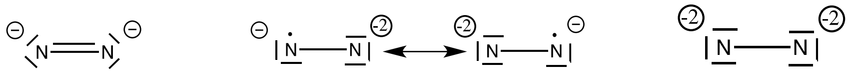

(a) (b) (c)

Scheme 3.1 Lewis structures of (a) N_2^{2-} (in *Cmcm* MgN_2, and *C*2 Mg_5N_7), (b) N_2^{3-} (in *C*2 Mg_5N_7), and (c) N_2^{4-} (in *Cmca* Mg_5N_4).

Above 43 GPa, the most stable MgN_2 phase has *P*6₃*/mcm* symmetry; its structure is displayed in *Figure 3.15b* and can be thought of as being composed of isolated flat triangular $N(N)_3$ units sitting in hexagonal prisms formed by 12 Mg atoms. Each planar $N(N)_3$ moiety possesses D3h symmetry with N-N bond lengths of 1.28 Å at 100 GPa. Based on our current knowledge, this three-pointed star motif is proposed here and in our recent work for the first time in nitrides. The metal atoms bear a +2 positive charge, whereas each polynitrogen anion has a -4 negative charge, *i.e.,* $N(N)_3^{4-}$; thus, the $N(N)_3^{4-}$ unit has 24 valence electrons (*Figure 3.15c*) and is an all-nitrogen analogue that is isoelectronic to the carbonate CO_3^{2-} and nitrate NO_3^- anions, and neutral gaseous sulfur trioxide SO_3. At 100 GPa, band gap closure appears as the pressure becomes higher due to increased π-π interactions between stacked $N(N)_3$ units (*Figure 3.15e*).

b. Mg_2N_3

Mg_2N_3 becomes thermodynamically stable between 8 and 126 GPa. A *C*2*/m* → *Pmmn* phase transition occurs at 33 GPa. In the *C*2*/m* structure, we can see layering at ambient pressure as displayed in *Figure 3.16a*. Each Mg_2N slab is built from 2D hexagonal double layers of Mg atoms, with nitrogen atoms centering Mg_6 octahedra within the layers. These slabs are isostructural to layered subnitride A_2N slabs (A = Ca, Sr, Ba; *anti*-$CdCl_2$-type structure, space group *R*-3*m*), with N_2 dimers filling the voids between Mg_2N layers. Formally, *C*2*/m* Mg_2N_3 can be described as $(Mg^{2+})2(N^{3-})(N_2^-)$. As expected from simple molecular orbital consideration, an elongated triple N-N bond is expected in N_2- dimer as the antibonding $1\pi_g^*$ level of this 11-electron diatomic unit is formally singly occupied. This is what happens in *C*2*/m* Mg_2N_3; a N-N distance of 1.18 Å is computed at 1 atm, a value setting between a triple bond (1.10 Å) and a double bond (1.25 Å). To summarize, the *C*2*/m* structure may be viewed as an A_2N-type layered Mg_2N structure with intercalated N_2 dumbells.

Let us now focus on the high-pressure *Pmmn* structure of Mg_2N_3. Its crystal structure is shown in *Figure 3.16b*. To the best of our knowledge, this is the first binary nitride of an s-block element in which a bent triatomic N_3 motif is observed rather than the classical linear motif, *i.e.,* azide N_3^- with 16 valence electrons. Note that this unprecedented discrete bent triatomic

N_3 species is also encountered in Mg_5N_7 (*Figure 3.16c*). The calculated N-N interatomic distances for *Pmmn* Mg_2N_3 at 50 GPa are 1.37 Å with a N-N-N bond angle of 122°. The electropositive Mg atoms can provide four electrons per formula unit, thus forming a 19 valence electron species N_3^{4-}, which is isoelectronic to molecular open-shell O-Cl-O. Starting from the well-known azide N_3^-, the three extra electrons found in N_3^{4-} would occupy the degenerate antibonding π_u^* orbitals of a linear triatomic species (*Figure 3.17*). This situation leads to Jahn-Teller instability. The two π_u^* levels split by distortion to an angular structure due to s-p orbital mixing. The two a_1 molecular orbitals can mix in bent N_3 (ex-π_{uz}^* and σ^*), then the π_{uz}^* level (antibonding at 180°) is strongly stabilized and becomes nonbonding (formally, a lone pair orbital localized on the central atom, see the Lewis structures in *Figure 3.16d*).

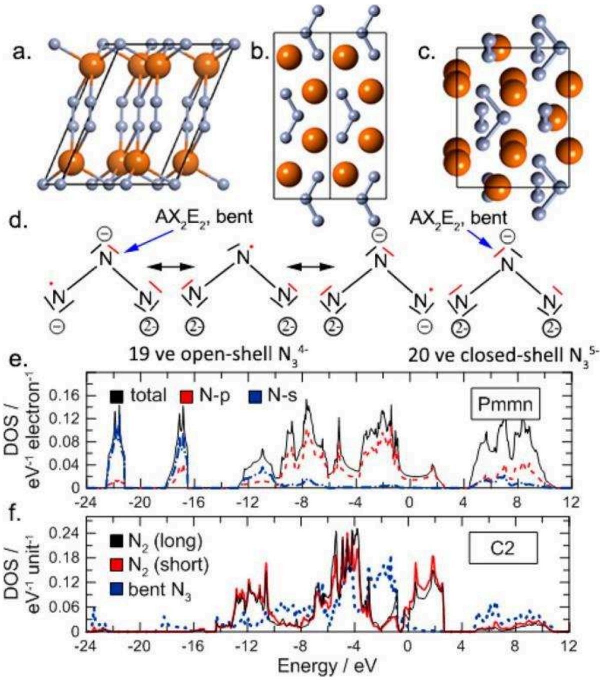

Figure 3.16 (a-c) Crystal structures of *C*2/*m* and *Pmmn* Mg_2N_3, and *C*2 Mg_5N_7. (d) Lewis structures of the bent 19 ve N_3^{4-} and 20 ve N_3^{5-} anions. Delocalized π electrons or pairs are shown in red. (e, f) Calculated density of states for *Pmmn* Mg_2N_3 at 50 GPa and *C2* Mg_5N_7 at 250 GPa.

For an electron count of 19 valence electrons in N_3^{4-}, a radical species is identified; its HOMO is singly occupied and π antibonding in character, as depicted in *Figure 3.17*. Orbital interaction analysis explains why the main group, specifically polynitrogen triatomic species with 17 to 20 valence electrons would be bent (O-N-O, 17 ve, 134°; O-N-O, 18 ve, 118°; O-S-O, 18 ve, 119°; O-Cl-O, 19 ve, 117°). This is consistent with the VSEPR theory, as the 16 ve AB_2 systems have steric number 2, giving linear molecule geometry, while the 17-20 ve AB_2 systems have steric number 3 or 4, which will give bent molecule geometry with one or two lone pairs on the central atom. The calculated electronic DOS also corroborates our findings (*Figure 3.16e*): the Fermi level crosses a region mainly based on nitrogen π antibonding states, *i.e.,* the π_x^* of molecule-like N_3^{4-}. Half of the π_x^* band is filled. Thus Mg_2N_3 is metallic.

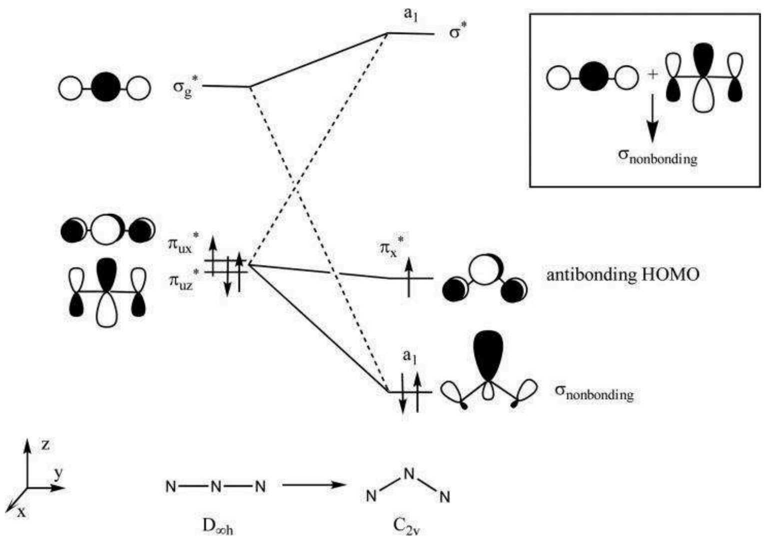

Figure 3.17 Simplified correlation diagram of the main orbitals of the linear and bent N_3^{4-} molecular system.

c. Mg_5N_7

This 5:7 composition is thermodynamically stable at very high pressures (above 243 GPa) and adopts the *C*2 structure (*Figure 3.16c*). N_2 dumbbells and bent N_3 units in the nitrogen sublattice are embedded in the magnesium framework. First, we focused on bonding analysis of the bent N_3 unit. In Mg_5N_7, C2v N_3 has a N-N distance of 1.36 Å and bond angle of 103° at 250 GPa. Note this N-N bond length is larger than in Mg_2N_3 (1.28 Å at 250 GPa), indicating a bond order of 1. Therefore, one may assign a formal charge of -5 to the N_3 group, leading to the 20 ve triatomic species isoelectronic to bent closed-shell Cl-O-Cl. This bent geometry for

N_3^{5-} conforms to the VSEPR prediction: AX_2E_2 deriving from a tetrahedron (*Figure 3.16d*). Molecular orbital analysis of linear and bent triatomic N_3 species revealed the antibonding π_x^* level (HOMO) is occupied by two electrons in N_3^{5-}; thus, the associated band would be filled (see the Walsh diagram in *Figure 3.17*).

Besides bent N_3 units, two nonequivalent N_2 dumbbells are observed in Mg_5N_7. The shortest interatomic N-N distance is 1.25 Å at 250 GPa, indicating a double bond character, thus a formal charge of -2 may be attributed. The other nonequivalent N_2 dimer has an elongated bond length of 1.32 Å, between that of single (1.36 Å) and double (1.25 Å) bonds. Thus, one may attribute a formal charge of -3 to this dimer, which is isoelectronic to the superoxide O_2^- species encountered in the known from experiment paramagnetic KO_2 salt (O-O distance of 1.28 Å). To summarize, open-shell N_2^{2-}, N_2^{3-} and diamagnetic bent N_3^{5-} species are encountered in Mg_5N_7, and these anions are stabilized via ionic interactions with Mg^{2+} cations. Mg_5N_7 may be viewed as the formal ionic limit formula $(Mg^{2+})5(N_3)^{5-}(N_2)^{3-}(N_2)^{2-}$. As the highest occupied molecular orbital, *i.e.,* the degenerate antibonding π^* levels of N_2^{2-} and N_2^{3-} are partially occupied by two and three electrons, respectively, one may expect that Mg_5N_7 is a metal. Indeed, this compound is metallic in character according to the DOS calculations (*Figure 3.16f*).

d. Mg_5N_4

This 5:4 composition is the first member of the Mg-rich family of stable high-pressure Mg_xN_y phases that is stable above 47 GPa. In this structure (*Figure 3.18*), magnesium atoms lie in the center of a slightly compressed octahedron formed by nitrogen atoms, while isolated nitrogen atoms lie in a distorted pentagonal bipyramid. This structure has N_2 dumbbells, with N-N distances equal to 1.44, 1.50, and 1.63 Å at 300, 200, and 50 GPa, respectively, indicative of a weakened single bond in the N_2 dimer. This behavior is more easily understood when one looks at the valence electron concentration (VEC = 7.66). A VEC close to 8 (octet rule) or higher leads to phases with isolated nitrogen atoms (*Table 3.2*). Mg_5N_4 sits at the border between phases with covalent molecule-like species and isolated N^{3-} particles. To explain the bonding mode in Mg_5N_4, this compound could be described as $(Mg^{2+})_5(N^{3-})_2(N_2)^{4-}$. With a charge of -4 per N_2 unit, the two antibonding π_g^* orbitals of N_2^{4-} are filled. Thus, a bond order of one is expected in N_2^{4-}, a 14 ve species isoelectronic to F_2. As magnesium completely transfers its valence electrons to the nitrogen framework, and if the N^{3-} and N_2^{4-} units follow the octet rule, this compound is expected to be an insulator or a semiconductor, in perfect agreement with the DOS calculation. A gap separates the valence and conduction bands (*Figure 3.18*), in perfect agreement with ZKC.

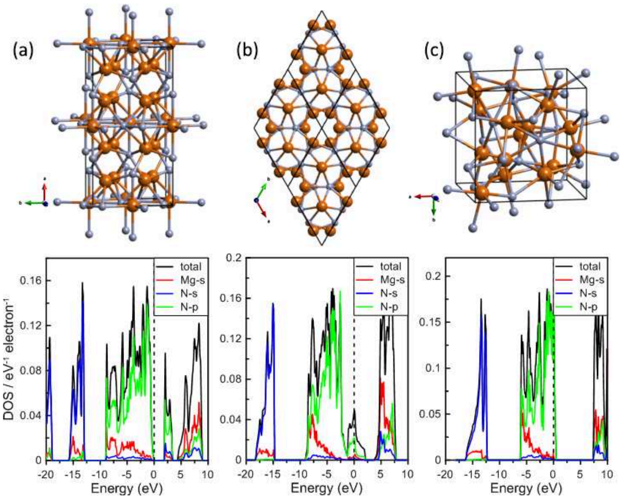

Figure 3.18 Crystal structures and electronic density of states of (a) *Cmca*-Mg_5N_4 at 100 GPa, (b) *P*6₃*/mcm*-Mg_5N_3 at 100 GPa and (c) *I*-43*d*-Mg_4N_3 at 100 GPa.

3.3.4 Compounds containing only isolated nitrogen atoms

Besides Mg_3N_2, two new compounds, Mg_5N_3 and Mg_4N_3, feature isolated nitrogen atoms. They occupy cavities inside magnesium sublattice, as depicted in *Scheme 3.1*. These compounds have VEC values ranging from 7.66 to 8.33 (close to 8, octet rule), in which isolated N^{3-} anions are found. With VEC values of 7.66 and 8.33, one extra hole h^+ or electron e^- is expected over the whole structure. Thus, p- and n-type materials are predicted for the Mg_4N_3 and Mg_5N_3 phases, respectively.

Mg_5N_3 adopts a hexagonal Mn_5Si_3-type structure with the space group *P*6₃*/mcm* and is stable above 120 GPa. This structure consists of infinite chains of empty face-sharing Mg_6-antiprisms and isolated atoms. The formula Mg_5N_3 can be rationalized as $(Mg^{2+})_5$ $(N^{3-})_3$ $(1e^-)$. With respect to this "extra" electron, a small half-filled band composed mostly of Mg-Mg bonding is found centered on the Fermi level, as shown in *Scheme 3.1*. Thus, Mg_5N_3 has a metallic behavior. Note that many Mn_5Si_3-type A_5B_3 phases well known to bind diverse atoms in the interstitial cavities within a chain of face-sharing trigonal antiprisms formed by A atoms. In Mg_5N_3, these interstitial sites are empty. We predict this Mg-Mg bonding will disappear due to insertion of hydrogen or fluorine, as observed in Ca_5Bi_3H.

Mg_4N_3 crystallizes in an *anti*-Th_3P_4 type structure with the space group *I*-43*d*, and becomes stable near 111 GPa. In this structural arrangement, the nitrogen atoms are eight-coordinated by magnesium atoms, while Mg atoms are octahedrally coordinated by nitrogens. A recent study also suggested an isoelectronic analogue of Mg_4N_3, the hypothetical Ca_4N_3, adopts this complex structure. Such alkali earth metal nitrides can be described as Zintl phases, where magnesium atoms donate their two valence electrons to the nitrogen atoms to form closed-shell configurations. The formula of Mg_4N_3 can be written using the ionic limit $(Mg^{2+})4(N^{3-})3(1h^{+})$ with electroneutrality being achieved by the presence of one extra hole h^{+}, leading to a p-type conductor. Therefore, from this simple electron count, the N-2p levels are not expected to be fully occupied; this was confirmed by analysis of the DOS plot (*Figure 3.18*) in which the Fermi level crossed the top of the N-2p bands, reflecting the metallicity of this high-pressure *I*-43*d* Mg_4N_3phase.

3.3.5 Quenchable high-pressure MgN_4? A route towards HEDM

To further confirm the stability of the polymeric chain found in high-pressure *Cmmm* MgN_4 phase after pressure release, its associated phonon spectrum was calculated at 1 atm. After relaxation, the extended 1D nitrogen net remained intact. Moreover, the absence of any imaginary modes throughout the entire 3D reciprocal space indicates this *Cmmm* poly-N_4 containing phase is dynamically stable at 1 atm and 0 K. However, its enthalpy is 0.191 eV/atom above the lowest metastable MgN_4 phase at 1 atm, *i.e., P2/m*, which contains two isolated N_2 molecular units per formula unit. If the barrier of transformation to *P2/m* (or decomposition to elements or other Mg_xN_y compounds) can protect *Cmmm*, then perhaps it could exist at normal conditions. Therefore, to further probe the structural stability of the covalent armchair-shaped polynitrogen chains, ab initio molecular dynamic (AIMD) simulations based on DFT were performed at different temperatures based on a 3 × 2 × 4 supercell. During the entire 10 ps AIMD simulations at temperatures of 300 K, 600 and 900 K, the covalent N-N bonds in poly-N_4^{2-} nets were not broken, and only small poly-N_4^{2-} chains shifts and Mg^{2+} cations displacements were observed (*Figure 3.19*).

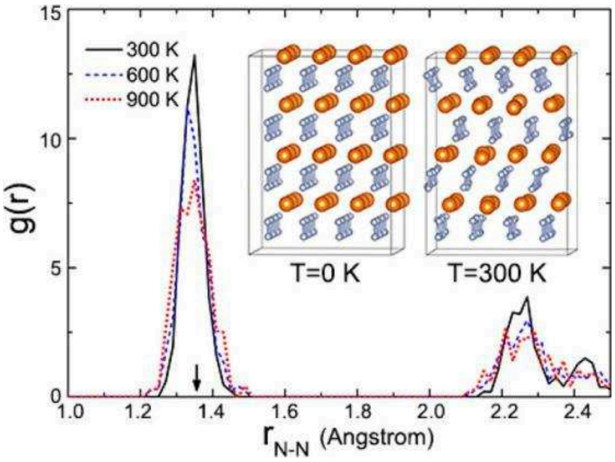

Figure 3.19 Radial distribution functions (RDF) for the N-N separations observed during AIMD simulations for a *Cmmm* MgN_4-based supercell at ambient pressure and temperatures of 300, 600, and 900 K. The black arrow indicates the average N-N distance in poly-N_4^{2-}.

To illustrate the findings, the closest N-N bond lengths fluctuate from 1.25 to1.45 Å at 900 K, suggesting bond order ranges between 1 and 2 within the covalent poly-N_4^{2-} chains. The AIMD simulations clearly suggest that the nitrogen net in *Cmmm* MgN_4 maintains integrity of the infinite planar 1D armchair-shaped chains from 0 K up to 900 K with robust thermal stability and strong kinetic trapping (at least up to 900 K). Interestingly, compared to the instability of pure nitrogen polymers, this analysis reveals the encapsulated polymeric anionic nitrogen chain in MgN_4 can be successfully preserved at ambient conditions.

Velocity of detonation (VOD), an important parameter used to evaluate the detonation properties of energetic compounds, was calculated with the Kamlet-Jacobs empirical equation. The energy density is 2.08 kJ·g^{-1} and 2.44 kJ·g^{-1} for *P-1* and *Cmmm*, respectively, assuming that the final products are $Mg_3N_{2(s)}$ and $N_{2(g)}$. Thus, the detonation velocity of *Cmmm* MgN_4 was found to be 11.5 km/s, which is comparable to the secondary explosive cyclotetramethylene tetranitramine $(CH_2)_4(NNO_2)_4$ HMX (VOD ~ 9.1 km/s), but much higher than 2,4,6-trinitrotoluene-TNT explosive (VOD ~ 6.9 km/s) and the primary explosive lead azide $Pb(N_3)_2$ (VOD ~ 3.8 km/s). Moreover, the stabilization pressure for *P*-1 MgN_4 is only 13 GPa, much lower than the pressure required to synthesize polymeric *cg*-N_2 (>100 GPa). High energy density, low stabilization pressure and quenchability make *P*-1 MgN_4 a candidate high energy-density material. Finally, to extend this analysis on nitrogen-rich Mg_xN_y-based HEDM compounds, we computed the energy density of all predicted Mg_xN_y phases (see *Appendix*). The high-pressure phase *P*-1 (I) MgN_3 with covalent N_6 rings is the most promising HEDM candidate with an energy density of 2.87 $kJ \cdot g^{-1}$, followed by *P*-1 MgN_4 (2.08 $kJ \cdot g^{-1}$), *P*6₃*/mcm* MgN_2 (1.95 $kJ \cdot g^{-1}$) and *Pmmm* Mg_2N_3 (1.90 $kJ \cdot g^{-1}$).

3.3.6 Conclusion

In summary, we present the first complete phase diagram for the Mg-N system at pressures up to 300 GPa. High pressure may be an effective route to stable Mg nitrides with unusual stoichiometries and original, yet aesthetic, structures. Besides Mg_3N_2, eight new compositions at Mg:N ratios of 1:4, 1:3, 1:2, 2:3, 5:7, 5:3, 4:3, and 5:4 were identified. Their structures contain molecule-like covalent nitrogen units, such as N_2 dumbbells, bent N_3 motifs, planar SO_3-like $N(N_3)$ units, and benzene-like N_6 species. In addition to well-known Mg_3N_2, newly predicted Mg_5N_3 an Mg_4N_3 feature isolated N^{3-} anions. ZKC, molecular orbital analysis and VSEPR theory proved useful for rationalizing the structural, bonding and electronic properties of these Mg_xN_y compounds. Notably, the dimensionality of the nitrogen network decreases as the amount of magnesium increases, with magnesium atoms acting as a scissor by transferring their valence electrons to the antibonding states of the nitrogen sublattice. More interestingly, the polymeric nitrogen network found in MgN_4 is preserved from 0 K up to 900 K. This analysis reveals that magnesium atom plays an important role in stabilization of polymeric nitrogen networks, and that MgN_3 and MgN_4 are potential high energy-density materials. The present study contributes to understand the unusual crystal features and exploitable physical properties of nitrogen compounds under extreme conditions.

3.4 Barium nitrides

In this study, we have investigated the possible formation and stability of molecular and polymeric nitrogen motifs in the Ba-N binary system upon pressure. In comparison with Mg^{2+}, the increase of the Ba^{2+} size should allow more nitrogen atoms around the cation. We have focused on the pressure range from 0 up to 100 GPa, as these pressures can nowadays be easily reached in diamond anvil cells. Structure searches for (meta)stable Ba-N compounds were performed using an unbiased structure prediction method, based on the evolutionary algorithm, in conjunction with first principles density-functional approaches, to evaluate total energies and forces. We predicted, upon compression, the emergence of several (meta)stable nitrogen networks in different compositions, such as 3:1, 2:1, 1:1, 3:2.

Our calculation indicated that nitrogen atoms would form, besides isolated nitride, N_2 dumbbells, linear N_3 azides, N_4 zigzag units, pentazolate N_5 rings, 5-membered rings with terminal nitrogen N_6 motifs, benzene-like N_6 rings, infinite nitrogen-based chains, and nitrogen layers at high pressure. We rationalized the nitrogen shapes through chemical bonding analysis, and thus explained the electronic properties of the identified compounds. Finally, we explored the properties and potential applications of Ba-N compounds as high energy-density materials.

3.4.1 Phase stability of Ba-N system under pressure

All proposed solid-state Ba_xN_y compounds are stationary points on the potential energy surface, located on the Ba-N convex hull or above. We verified that each phase meets two criteria of stability:

(1). Dynamical criterion: a structure is dynamically stable, as indicated by the absence of imaginary frequencies, in all of the phonon dispersion curves. The corresponding stationary point on the PES is a local enthalpy minimum.

(2). Thermodynamic criterion: a Ba_xN_y compound is thermodynamically stable when its free energy (at $T = 0$ K, enthalpy) of formation, from the component elements and any other Ba_xN_y

compound, is negative, *i.e.*, they are located on the convex hull. Other metastable phases, with different covalent nitrogen nets, are also detected on the PES above the convex hull, but we selected the ones which have exothermic formation reactions ($\Delta H_f < 0$), and are close to the convex hull ($\Delta H_f < 0$), or experimentally synthesized.

These latest structures are metastable in the binary Ba-N phase diagram, but there might appear, experimentally for a kinetic reason, so-called, viable structures,[181] such as experimental $Ba(N_3)_2$ azide.[182] The metastable structures are of great significance, and in practice can often be synthesized by choosing appropriate precursors and controlling conditions of the experiment (pressure, temperature, quench rate, etc.).

Moreover, for selected high-pressure nitrogen-rich structures, *e.g.,* BaN_4 and BaN_{10}, we checked their quenchability by looking at their kinetic and thermal properties. We performed *ab initio* molecular dynamics simulations up to 900 K. A crystalline structure is definitively called viable if there are no structural transformations of the nitrogen network, *i.e.,* nitrogen bond breaking, were observed after a long simulation (10 ps), indicating the existence of a substantial kinetic barrier which facilitates the formation and trapping of viable, (meta)stable structures.

Stable compounds, which form the thermodynamic convex hull (*Figure 3.20*), were identified at selected pressures, and their stability fields were shown in the pressure-composition phase diagram (*Figure 3.21*). It is noteworthy that our evolutionary searches successfully reproduced the experimentally known Ba_3N,[183] Ba_2N,[184] BaN_2[185] and BaN_6[182,186] structures. However, the expected charge-balanced 3:2 composition for an alkaline earth nitride salt has not yet been characterized.

Twelve stoichiometries emerged to be stable, including nine N-rich stoichiometries, namely BaN, Ba_2N_3, BaN_2, Ba_3N_8, BaN_4, BaN_5, Ba_2N_{11}, BaN_6 and BaN_{10}, and three Ba-rich compositions, Ba_3N_2, Ba_2N and Ba_3N, when pressure increased up to 100 GPa. Within the same pressure range, the binary Ae-N stable stoichiometries have been predicted for Be,[156] Mg,[89,159] Ca,[164], respectively. The diversity of stable stoichiometries in Ae-N phases increases when $Z_{(Ae)}$ increases. The increase of the cation size (Be < Mg < Ca < Sr < Ba) allows more nitrogen atoms around each cation center. As shown in *Figure 3.21*, these Ba_xN_y compounds undergo a series of phase transitions in their stability domains.

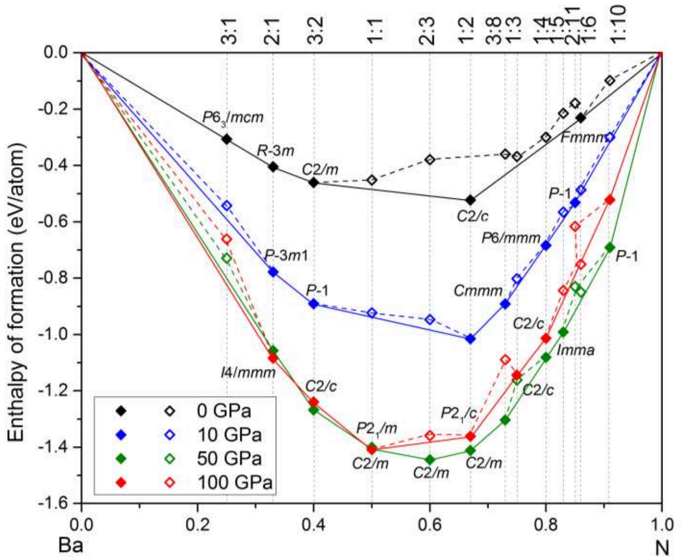

Figure 3.20 Convex hulls of the Ba-N system at selected pressures. Solid squares denote stable structures, while empty ones represent metastable structures. The space group is indicated for each novel stable structure.

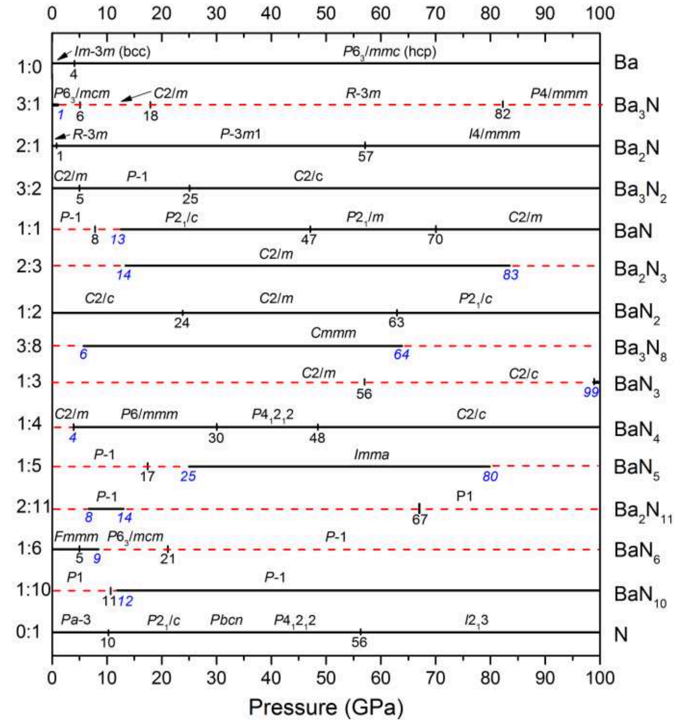

Figure 3.21 Pressure-composition phase diagram of Ba-N system from 0 to 100 GPa. The stable phases are indicated by bold lines, and metastable phases are depicted by thin, red, dashed lines. The blue numbers represent the thermodynamic stability ranges, while black, italic numbers denote phase transition pressures.

According to the structural arrangement and dimensionality of the covalent nitrogen network, the great variety of crystal structures are classified into four different categories (see *Tables 3.3* and *3.4*): structures with (1) isolated nitrogen atoms, as found in Ba_3N, Ba_2N, and Ba_3N_2; (2) encapsulated molecule-like covalent anionic units, such as N_2 dumbbells, linear triatomic N_3 units, bent N_4 finite chain, five-membered rings N_5 and N_5-N, six-membered rings N_6 as found in Ba_3N_2, BaN, BaN_2, Ba_2N_{11}, Ba_5N_7, BaN_5, or BaN_6 or BaN_{10}; (3) 1D infinite nitrogen chains (BaN_3, BaN_4 and BaN_5); and finally (4) 2D covalent nitrogen layers alternating with barium sheets (BaN_3). This structural classification can be applied to other alkaline and alkaline earth nitrides A_xN_y compounds, such as N_2 dumbbells, linear N_3 units, five-membered N_5 rings, cyclic N_6 rings, and 1D linear N_x.

Table 3.3 Structural nitrogen nets in stable Barium-Nitrogen Ba_xN_y phases.

Structure information	Nitrogen network	Ba:N compounds, VEC[a], space group and associated pressure stability range[b]
Isolated nuclei		Ba_3N [11]: $P6_3/mcm$, 0-1 Ba_2N [9]: *R*-3*m*, 0-1; *P*-3*m*1, 1-57; *I4/mmm*, >57 Ba_3N_2 [8]: *P*-1, 5-25; *C2/c*, >25
Isolated nuclei and N_2 dumbells	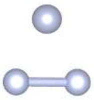	Ba_3N_2 [8]: *C2/m*, 0-5 Ba_4N_3 [7.7]: *P*1, 6-23; *C2/m*, >64
N_2 dumbbells		BaN [7]: $P2_1/c$, 13-47; $P2_1/m$, 47-70; *C2/m*, >70 Ba_2N_3 [6.3]: *C2/m*, 14-83 BaN_2 [6]: *C2/c*, 0-24; *C2/m*, 24-63; $P2_1/c$, >63 Ba_3N_8 [5.8]: *Cmmm*, 6-64 BaN_4 [5.5]: *P6/mmm*, 4-30
N_2 dumbbells and linear N_3 azides	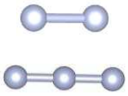	Ba_2N_{11} [5.4]: *P*-1, 6-14
Finite N_4 chains	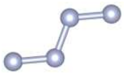	BaN_2 [6]: $P2_1/c$, >63
5-membered rings	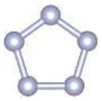	BaN_5 [5.4]: *Imma*, 25-80 BaN_{10} [5.2]: *P*-1, >12
1D armchair chains 2-coordinated N	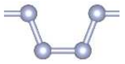	BaN_4 [5.5]: $P4_12_12$, 30-48

[a] Valence electron concentration of Ba_xN_y is given in brakets ; VEC = (2x+5y)/(y).

[b] Pressure in GPa. Pressure range in this work: [0, 100 GPa]

Table 3.4 Structural nitrogen nets in metastable Barium-Nitrogen Ba_xN_y phases.

Structure information	Nitrogen network	Ba:N compounds VEC[a], space group and associated pressure stability range[b]
Isolated nuclei and N_2 dumbells	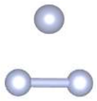	Ba_4N_3 [7.7]: *P*1, 6-23; *C*2/*m*, >64
5-membered ring with terminal N	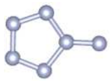	BaN_6 [5.3]: *P*-1*(I)*, >21
6-membered ring	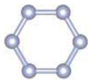	BaN_6 [5.3]: *P*-1*(II)*
1D armchair chains 2-coordinated N	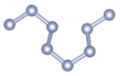	BaN_3 [5.7]: *C*2/*c*, >56
1 D infinite twist chains 2-coordinated N	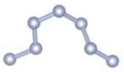	BaN_5 [5.4]: *P*1
2D nitrogen network	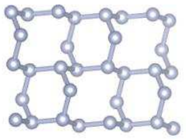	BaN_6 [5.3]: *C*2/*m*

[a]Valence electron concentration of Ba_xN_y is given in brakets ; VEC = (2x+5y)/(y).

[b]Pressure in GPa. Pressure range in this work: [0, 100 GPa]

The electronic and geometric structures of the Ba_xN_y phases were examined to understand their chemical bonding better. Throughout this article, electron transfer is considered to occur from electropositive barium atoms into the polynitrogen sublattice. Thus a N_y network bears 2x valence electrons (ve) per formula unit. Nevertheless, under pressure, the 6s orbital, as well as low-lying 5d levels of barium, may notably participate in bonding crystal orbitals, therefore a deep understanding of the Ba_xN_y electronic properties is required by a careful analysis of their computed DOS, COHP, ELF plots, charge density, and Bader charges, as well as through a molecular orbital approach.

As a first guide, a useful parameter to rationalize the structural properties is the valence electron concentration (VEC) defined for Ba_xN_y compounds as VEC = (2x+5y)/y. For VEC = 8, the octet rule is verified for each nitrogen, *i.e.,* N^{3-}, as in the charge-balanced Ae_3N_2 compound. Thus, in barium-rich phases, in which VEC > 8, the N ions remain isolated. In nitrogen-rich phases (VEC < 8), the nitrogen anions can be viewed as nuclei with unpaired electrons. Therefore, nitrogen-nitrogen bonds are expected to fulfill the octet; molecular or extended covalent nitrogen networks are encountered. This is what we see and detail after that. Nevertheless, remember that the formal charge distribution does not reflect the real charge transfer.

We recall that the lengths of N-N bonds are roughly 1.10 Å for the triple bond, 1.25 Å for the double bond and 1.45 Å for the single bond at ambient conditions. For calibration, the N-N single bond distance in three-dimensional covalent high-pressure *cg*-N ($I2_13$) phase is 1.37, and 1.34 Å at 50 and 100 GPa. These values help us to guide assignment of nitrogen-nitrogen bonds with the help of Lewis rules to rationalize the local structural environments in nitrogen motifs using VSEPR theory.

3.4.2 Ba-rich electrides: Ba_3N and Ba_2N

Two stable Ba-rich compositions are proposed at ambient pressure, namely, Ba_3N and Ba_2N, but only Ba_2N is thermodynamically stable (see *Figure 3.21*) up to 100 GPa. One of their common features is the presence of isolated nitrogen nuclei trapped inside barium sublattice cavities, as depicted in *Figure 3.22*. Ba_3N and Ba_2N have VEC values of 11 and 9, respectively, higher than that of 8 (octet rule). Therefore, extra electron e^- is expected over the whole structure.

a. Ba_3N

At 1 atm, the *anti*-TlI_3-type structure (space group $P6_3/mcm$) is the most stable, enthalpically, which is in good agreement with the experimental findings.[183] The calculated lattice constants are consistent with the experimental data (See *Table 3.5*). Ba and N atoms arrange themselves in an infinite chain of faced sharing barium octahedra, centered with nitrogen atoms, as shown in

Figure 3.22. *P*6$_3$*/mcm* structure presents a hexagonal close packing of [$Ba_{6/2}N$] chains. Within the chains, the calculated Ba-N distance is 2.75 Å, which is slightly lower than the sum of the ionic radii of 2.9 (Ba^{2+} N^{3-}).[187] The closest N-N separation is 3.55 Å. Such distances are explained by assuming strong ionic interactions within the chain according to $[(Ba^{2+})_3(N^{3-})]^{3+}$. This electron repartition leaves an excess of 3 electrons for metallic bonding between the chains; or for ionic interstitial electrons with $(Ba_3N)^{3+}$ chain interactions. The latter bonding mode explains the long inter-chain Ba-Ba separations of 4.9-5.0 Å, to be compared with a calculated Ba-Ba distance of 4.3 Å in Ba bcc metal. An ELF analysis in *Figure 3.23* confirms the existence of interstitial electrons.

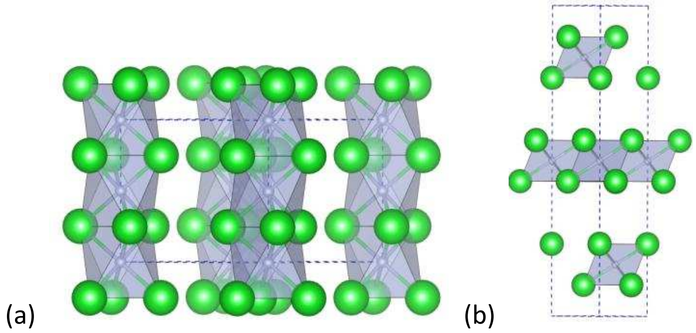

Figure 3.22 Crystal structure of (a) Ba_3N *P*6$_3$*/mcm* and (b) Ba_2N *R-3m* at 0 GPa.

To summarize, the cationic $(Ba_3N)^{3+}$ chains/rods interact with interstitial electrons localized in the one-dimensional void of *P*6$_3$*/mcm* structure. Also, Ba_3N is a 1D electride at 1 atm. Above 1 GPa, Ba_3N is unstable, concerning disproportionation to Ba + Ba_2N.

Table 3.5 Crystal structures of *P*6$_3$*/mcm* Ba_3N phases.

***P*6$_3$*/mcm* Ba_3N**	**Lattice parameters**
Experimental ambient condition[183]	a=7.642, b=7.642, c=7.050 α=90.0, β=90.0, γ=120.0
Present work 0 GPa / 0 K	a=7.728, b=7.728, c=7.096 α=90.0, β=90.0, γ=120.0

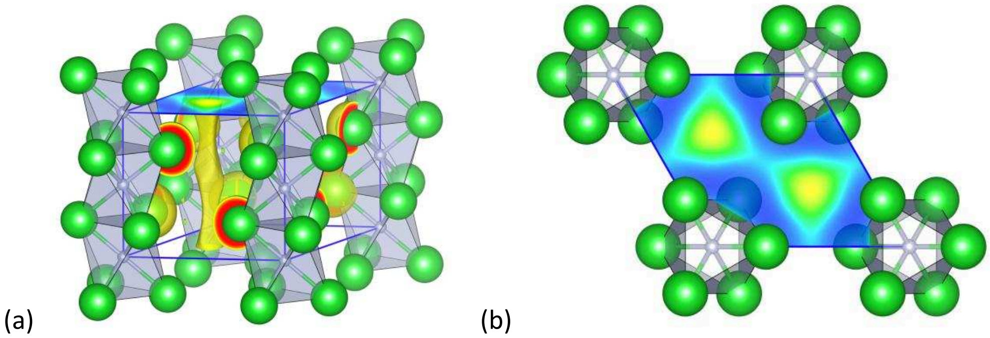

Figure 3.23 *P*6_3*/mcm* Ba_3N structure at 1 atm; (a) Isosurface of ELF with the value of 0.6. Faced sharing Ba_6 octahedra centered with N atoms are enlightened. (b) ELF contours in the (001) plane; hexagonal close-packed $[Ba_{6/2}N]$ chains are shown. Bonds between Ba (large green) and N (small grey) are outlined.

b. Ba_2N

Our structure search correctly identifies the experimental *R*-3*m* structure as the global minimum at 1 atm.[184] At 1 GPa, a new phase of *P*-3*m*1 symmetry becomes the most stable phase. The calculated transition pressure is in perfect agreement with the experimental value of 2 GPa.[188] *P*-3*m*1 phase remains the minimum enthalpy structure up to 57 GPa, where another phase of *I*4*/mmm* symmetry emerges as the ground-state (see *Figure 3.21*).

Atmospheric *R*-3*m* Ba_2N has an *anti*-$CdCl_2$-type structure. The hexagonal layered unit is composed of $Ba_{6/3}$ edge-sharing octahedra centered by a nitrogen atom, with a Ba-N distance of 2.79 Å typical of ionic bonding. In this phase nitrogen exists as N^{3-}: the closest N-N separation is 4.06 Å, much longer than a 1.45 Å N-N bond length, as in $H_2N\text{-}NH_2$ hydrazine.[189] Thus, each Ba_2N unit can be regarded as a positively charged ionic slab, $[(Ba^{2+})_2(N^{3-})]^+$. These cationic $[Ba_2N]^+$ layers are separated by a vacuum of 4.60 Å, and stacked in an ABC fashion along the [001] direction, as shown in *Figure 3.22*. To balance the cationic charge of $[Ba_2N]^+$ layer, the interlayer spacing should work as a confinement space of the extra electrons, resulting in a $[Ba_2N]^+$ plus e^- configuration. This assumption is in work in isoelectronic and isostructural Ca_2N.[190] *Figure 3.24a* and *Figure 3.25a* display the ELF profile and the DOS of *R*-3*m* Ba_2N, which illustrate the unshared electron interaction between interstitial electrons X^- (X is a void), and Ba_2N^+ layers and reflect ionic bonding property.

Looking at its DOS in *Figure 3.25a*, Ba_2N is a metal. The broad density of states peak around E_F is mainly composed of a non-atom centered orbital located at X (voids) with small contributions from Ba and N, as shown in the total and projected DOS displayed in *Figure 3.25a*. The integrated electron density of the conduction band from -2 eV to 0 eV is equal to 0.45 e/f.u. This result is consistent with the chemical view of the $[(Ba^{2+})_2(N^{3-})]^+e^-$ electride.

To summarize, *R*-3*m* dibarium nitride crystal may be view as cationic Ba_2N^+ layer alternating with confined anionic electrons, the signature of a two-dimensional conducting electride.

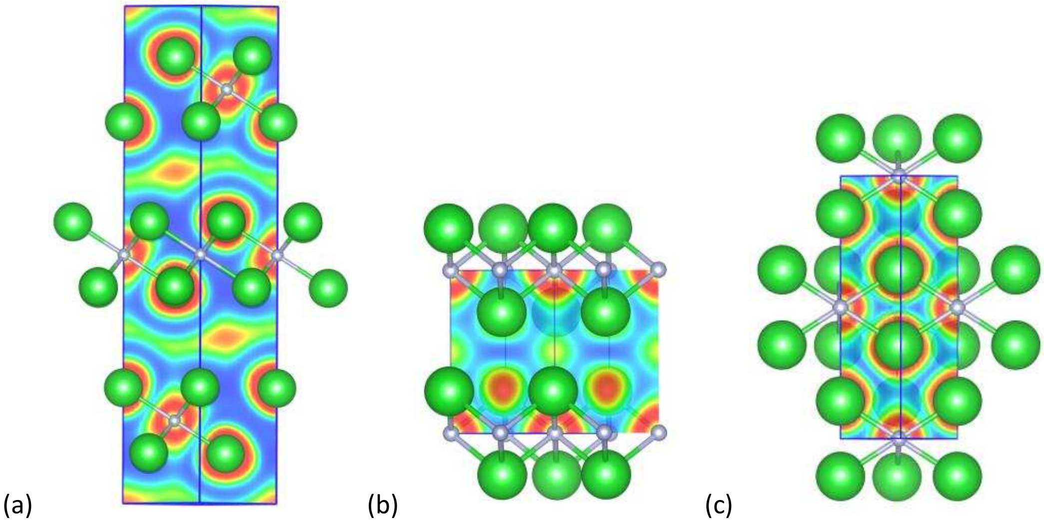

Figure 3.24 Crystal structures of Ba_2N, associated ELF contours (Isosurface value = 0.8). (a) *R*-3*m* phase at 0 GPa; (b) *P*-3*m*1 phase at 10 GPa; (c) *I4/mmm* phase at 100 GPa.

A *R*-3*m* → *P*-3*m*1 phase transition occurs at 1 GPa. This *anti*-CdI_2-*type* structure is computed to be the most stable phase up to 57 GPa. The *P*-3*m*1 Ba_2N crystal structure is closely related to that of the atmospheric phase. It presents an /AA/ stacking of Ba_2N layers based on of $Ba_{6/3}$ edge-sharing octahedra centered by a nitrogen atom. At 10 GPa, The Ba-N distance is 2.62 Å, reflecting an ionic bonding character, while the interlayer Ba-Ba separation is computed at 3.57 Å, analog that in BaO (Ba^{2+}-Ba^{2+}=3.83 Å at 10 GPa). *P*-3*m*1 Ba_2N maintains the 2D electride property; see its ELF plot in *Figure 3.24b*.

Above 57 GPa, a tetragonal phase becomes the ground-state structure (space group *I*4/*mmm*, $MoSi_2$-type), in which the coordination number of nitrogen increases from six to eight. Ba_2N structure presents a bcc-substructure character as displayed in *Figure 3.24c*. Alternatively, this phase may be described as AB-staked Ba_2N layers, made of fused distorted $Ba_{8/4}$ cubes, centered by N atoms. In a distorted NBa_8 cube, Ba-Ba is 2.72 Å, and 3.00 Å and Ba-N are 2.52 Å at 100 GPa. The interspacing slab is computed at 2.94 Å. As displayed in *Figure 3.24c*, no localized electrons are seated in the void layer. Moreover, a s → d transition has been identified in *I*4/*mmm* Ba_2N by a DOS analysis, a well-characterized feature in solid alkaline and earth alkaline metals under high pressure. A metallic bond character is present in high-pressure *I*4/*mmm* Ba_2N.

To summarize, the 2D electride property of Ba_2N is not maintained in high-pressure metallic *I*4/*mmm* phase, although its Ca_2N analog has been claimed to be a 2D electride from 0 to 100 GPa with a predicted *R*-3m → *Fm*-3*m* → *I*4/*mmm* sequence.[164]

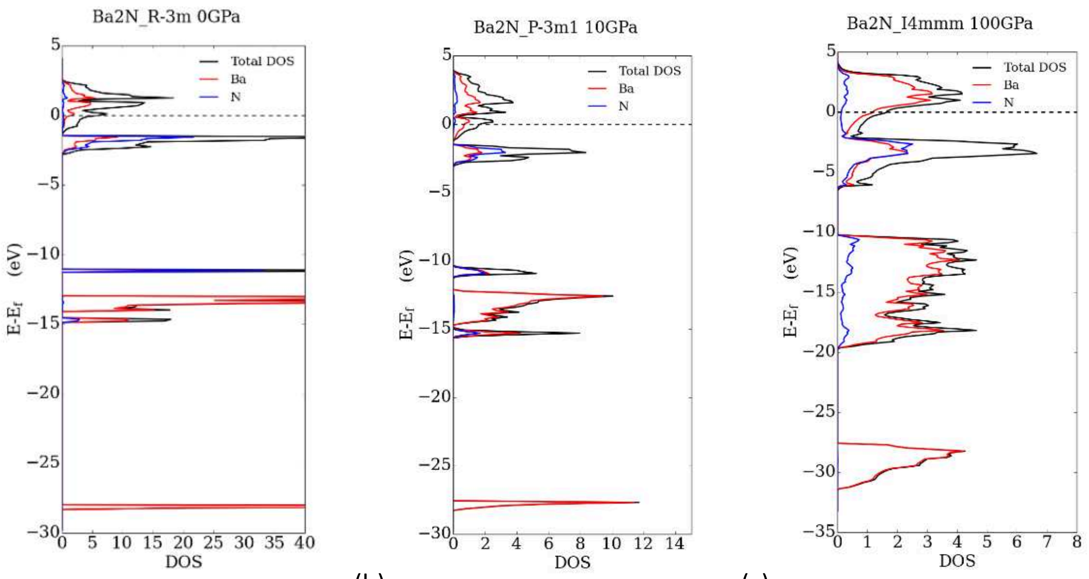

(a) (b) (c)

Figure 3.25 Total and projected DOS of Ba_2N phases. (a) *R-3m* phase at 0 GPa; (b) *P*-3*m*1 phase at 10 GPa; (c) *I*4/*mmm* phase at 100 GPa.

3.4.3 A pressure-induced conducting electride-insulator transition in Ba_3N_2

Ba_3N_2 is an apparently "charge-balanced" compound with unexpected properties, however, there is no evidence to date for experimental 3:2 composition in the barium-nitrogen binary phase diagram. Our theoretical investigation shows that the Ba_3N_2 compound is thermodynamically stable from ambient pressure to 100 GPa. This finding invites experimentalists to quest for this 3:2 composition, which is experimentally known in isoelectronic Ae_3N_2 (Ae=Be, Mg, Ca).[89,159,164] According to our calculations, *C2/m* Ba_3N_2 is the lowest structure between 0 to 4.3 GPa. Above 4.3 GPa, a *P*-1 high-pressure phase becomes lower in enthalpy than *C2/m*, easily accessible in today's high-pressure experimental setups. *P*-1 remains thermodynamically stable up to 25.2 GPa when *C2/c* comes into existence (see *Figure 3.26*).

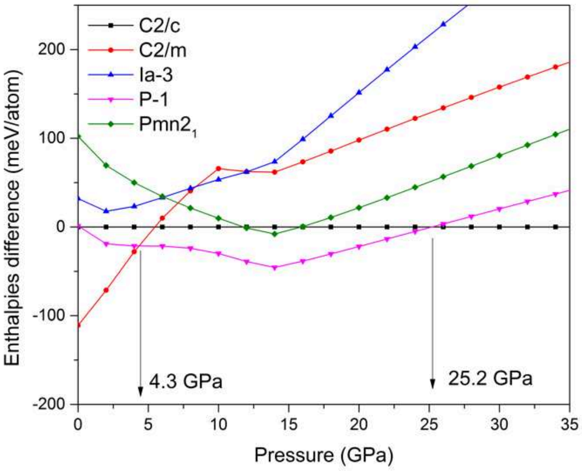

Figure 3.26 The calculated enthalpy differences of various Ba_3N_2 structures relative to the *C2/c* structure as a function of pressure.

Remarkably, the atmospheric *C2/m* phase contains encapsulated N_2 dumbbells and isolated N in distorted Ba_6 octahedral sites, as shown in *Figure 3.27*, while the experimentally known Ae_3N_2 phases present only N^{3-} anions surrounded by six metals. The *C2/m* structure presents stacked hexagonal layers of Ba_3N_2, which are separated by an interlayer region of 3.85 Å. Within the Ba_3N_2 slab, the shortest Ba-Ba separations are computed at 3.71-3.99 Å, to be compared with the Ba-Ba nearest neighbor distances of 3.92 Å in ionic solid BaO.[191] Thus, Ba_3N_2 can be regarded as to contain divalent barium, $(Ba^{2+})_6(2N, N_2)^{6-}$. The Ba-N separations are 2.67-2.91 Å and 2.51-2.84 Å for NBa_6 and N_2Ba_6, respectively. Encapsulated nitrogen ions are N^{3-} nitrides stabilized by Ba^{2+} cations through ionic bonds.

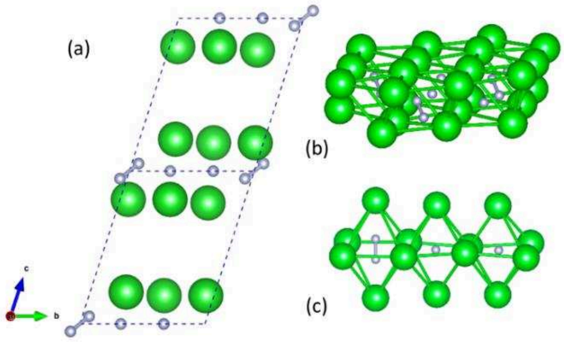

Figure 3.27 Calculated structures of Ba_3N_2. (a) *C2/m* Ba_3N_2 at 1 atm (b) looking at Ba_3N_2 slab based on two hexagonal Ba monolayers with (c) encapsulated N_2 units and N atoms in octahedral sites.

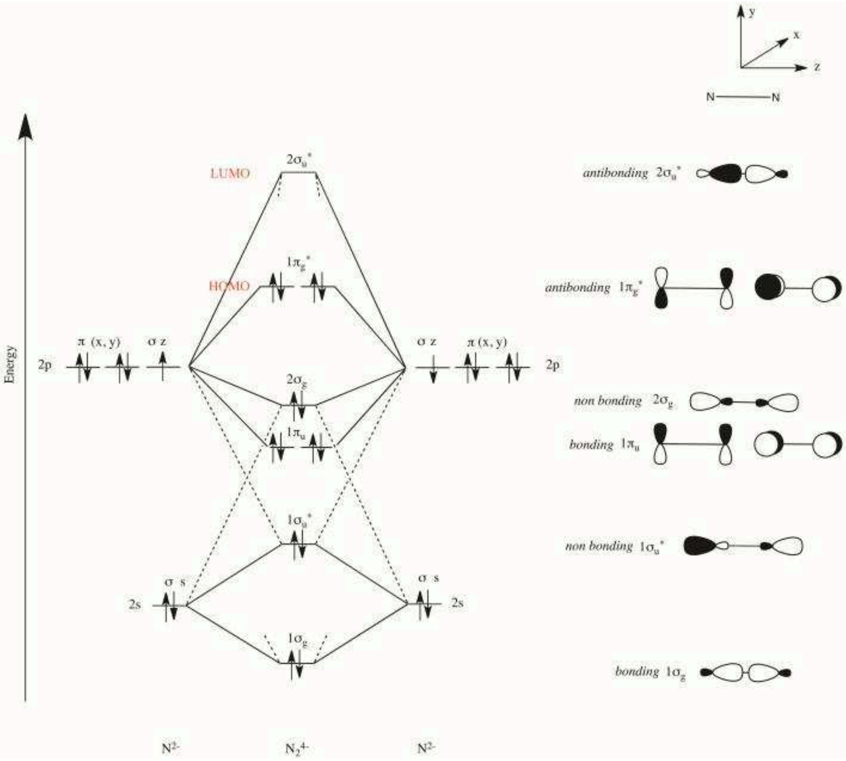

Figure 3.28 Schematic molecular orbital diagram of N_2^{4-}. The solid and dashed lines indicate the primary and secondary parentage of the orbitals, respectively ($2s$-$2p_z$ mixing). Only the valence orbitals are shown.

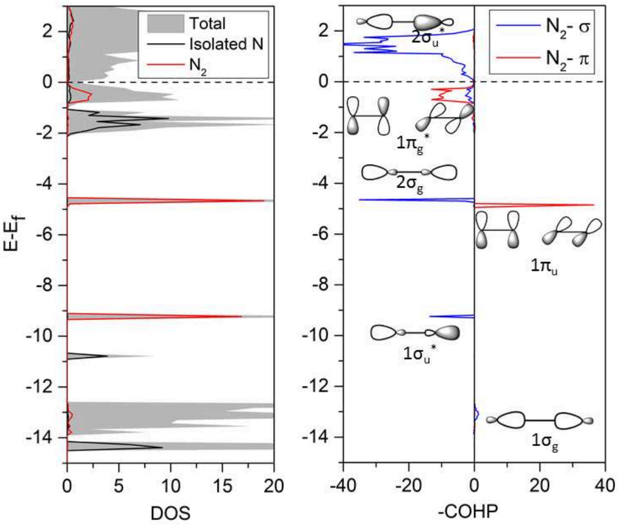

Figure 3.29 (a) Total and projected DOS, and (b) -COHP of *C2/m* Ba_3N_2 at 0 GPa.

What about the charge of diatomic N_2? The crystallographic independent N_2 unit presents an N-N bond length of 1.35 Å. This distance is close to those in experimentally reported diazenide BaN_2, having a distance of 1.24 Å (1.25 Å in HHN=NH), and to pernitride $[N_2]^{4-}$ ions, with N-N bond lengths of about 1.40 Å (1.45 Å in hydrazine H_2N-NH_2).[185] A COHP analysis for the N_2 unit allows us to assign a formal charge of -4 per N_2 (see *Figure 3.28* and *Figure 3.29*); the filling of the two antibonding π^* orbitals of N_2 is computed at 100%, resembling an expected value of 100% for pernitride.

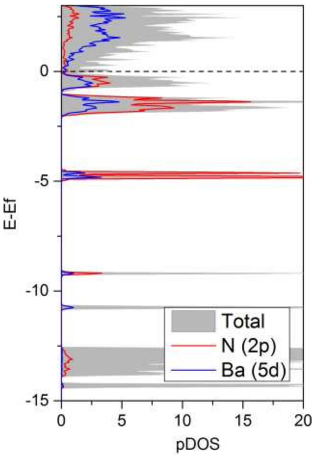

Figure 3.30 Total and projected DOS of *C2/m* Ba_3N_2 at 0 GPa

The shortened single bond observed in $[N_2]^{4-}$ is due to a nitrogen 2p orbital and barium 5d orbital overlap, as displayed in *Figure 3.30*. Less than 4 electrons are transferred from barium to nitrogen. Therefore, the following formulation is proposed for atmospheric stable *C2/m* Ba_3N_2 phase, namely $(Ba^{2+})_6(N_2^{4-})(N^{3-})_2(2e^-)$, an electron-rich structure. To trace these "free" electrons in layered Ba_3N_2 structure, we computed the partial electron charge density of this phase, and looked for high values the plots displayed in *Figure 3.31*.

The contour map of the partial electron density, just below the Fermi level, is very informative; we can see electron density maxima in the interlayer space, located between the cationic $(Ba_3N_2)^+$ slabs. Within -2 and -1 eV energy range, the electrons are localized at the isolated nitrogen. High electron density is found in the interstitial regions and N_2 units in the energy window of -0.5 eV, up to Fermi level, a typical signature of an electride.

Combining the DOS and partial charge density analysis, we conclude that Ba_3N_2 is a conducting 2D electride. Here, non-atom-centered electrons act as intercalated anions, holding the cationic Ba_3N_2 layers together through coulomb attraction. Unexpectedly, at ambient pressure, Ba_3N_2 belongs to the layered subnitride family, such as Ba_2N, and not to the charge-balanced Zintl Ae_3N_2 compounds (Ae=Be, Mg, Ca).

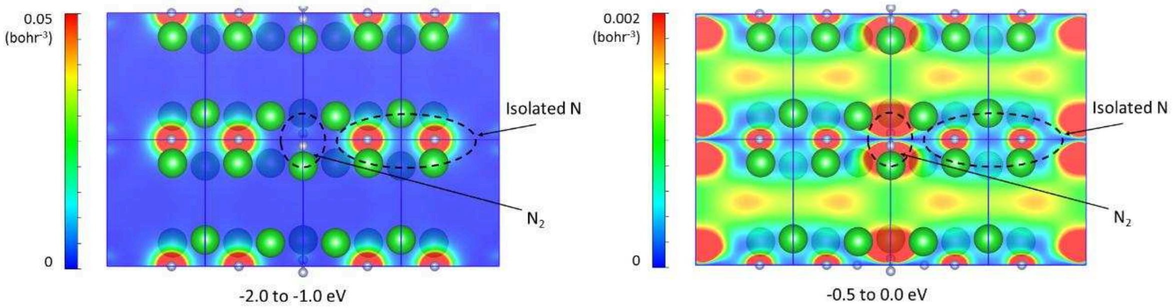

Figure 3.31 (a) The partial charge density maps for the (010) plane of *C2/m* Ba_3N_2 calculated using the energy ranges of -2.0 eV ≤ E ≤ -1.0 eV (b) and -0.5 eV ≤ E ≤ 0.0 eV. The Fermi level is located at E = 0.0 eV.

Finally, we hypothesized that a layer of $[Ba_3N_2]^+(e^-)$ could be separated from the bulk material. Our DFT calculations predict an exfoliation energy of 125 meV/atom for Ba_3N_2, to be compared with 264 meV/atom for $[Ca_2N]^+(e^-)$.[192] Nevertheless, a more profound theoretical investigation is on-going to conclude on the stability of this proposed, two-dimensional, electride Ba_3N_2 material, and to evaluate its electronic properties and superconductivity.

Above 5.5 GPa, a *P*-1 polymorph appears as the lowest structure, and is thermodynamically stable. This phase features isolated nitrogen nuclei which occupy cavities inside barium sublattice, as depicted in *Figure 3.32a*. N atoms have 5 nearest Ba^{2+} neighbors located at a distance lower than 2.76 Å, while Ba is 3- and 4-coordinated to nitrogen.

Interestingly, Ba cages present empty sites in the *P*-1 structure, and 1D tunnels are formed, running along (100) direction. High ELF values correspond to well-localized electrons, and are found around the region of nitrogens, here N^{3-} nitride ions. Zintl phases, such as $(Ba^{2+})_3(N^{3-})_2$, would be expected to be semiconducting or insulator. As PBE functional is known to underestimate band gaps, we employed the HSE06 calculation, which indicated a band gap of 1.8 eV between the valence and conduction band. This *C*2/*m* → *P*-1 phase transition establishes a novel example of the pressure-induced metallic 2D electride-insulating/semiconducting transition.

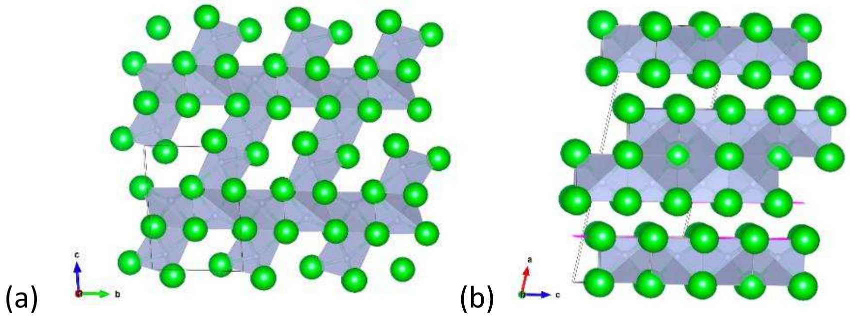

Figure 3.32 Calculated structures of Ba_3N_2. (a) *P*-1 Ba_3N_2 at 10 GPa, (b) *C2/c* Ba_3N_2 at 50 GPa.

The ultimate high-pressure phase, found for Ba_3N_2, adopts a *C2/c* structure (Z=4) above 25 GPa (*Figure 3.32b*). In the *C2/c* layered structure, each slab consists of two condensed layers of face-sharing NBa_8 polyhedra. A separation of 2.24 Å is calculated between two stacked Ba_3N_2 slabs (shortest Ba-Ba distances of ~3.06 Å). The *C2/c* Ba_3N_2 undergoes pressure-induced band gap closure around 40 GPa. When pressure increases, the Ba 5d bands broaden and mix with Ba 6s bands, comparable to the observed s→d transition in elemental alkaline earth metals.[193] These Ba s-d hybridized states overlap with occupied N 2p states of isolated N^{3-} anions enabling the conductivity of *C2/c* Ba_3N_2 at high pressure, nevertheless, the weak density of states at the Fermi level. To summarize, we predict that the Ba_3N_2 compound goes from:

Conducting electride → Insulator/Semiconductor → Metal

in the 0-25 GPa range, an interesting feature for experimentalists.

3.4.4 Molecular-like units and extended nets in nitrogen-rich Ba_xN_y compounds

a. BaN

Above 13 GPa and up to 100 GPa, the 1:1 stoichiometry is computed to be a stable system thermodynamically (see *Figure 3.21*). As the pressure rises, phase transitions appear *P*-1 (metastable) → $P2_1/c$ → $P2_1/m$ → $C2/m$. In BaN, each N is formally N^{2-}, leaving one unpaired electron, thus capable of forming one bond. This structural requirement is observed in all stable phases; their respective structures contain encapsulated N_2 dumbbells with a N-N separation of 1.41 Å ($P2_1/c$, 10 GPa), 1.41 Å ($P2_1/m$, 50 GPa) and 1.38 Å ($C2/m$, 100 GPa). These values indicate an N-N single bond character, as expected for a 14-ve diatomic A_2. N_2^{4-} dumbbell is a solid-state equivalent of molecular F_2, with fully occupied π_g^* levels (See Molecular orbital diagram in *Figure 3.28*). All atoms are obeying the octet rule in $(Ba^{2+})_2(N_2^{4-})$, these Zintl phases would be expected to be semiconducting. However, except for $P2_1/c$ phase at 10 Gpa, the calculated DOS in shows that ZKC does not work in this case.

A close inspection of the DOS shows that 6s/5d Ba orbitals have a significant contribution to the occupied nitrogen levels, the signature of a partial covalent Ba-N character in BaN. A back-donation is in work, from the occupied N_2 π^* levels to the empty Ba ones, and this explains the metallic character of BaN. This finding illustrates the limitation of the Zintl rule in Ba-N system under pressure; not all valence electrons of electropositive alkaline earth metal are localized in nitrogen networks, but may participate in covalent cation-anion bonds, and metallic cation-cation ones, as found in metallic CaSi[194] or K_5Sb_3[195]. We will see that such Zintl violation is a consistent feature of the behavior of several Ba/N phases under pressure.

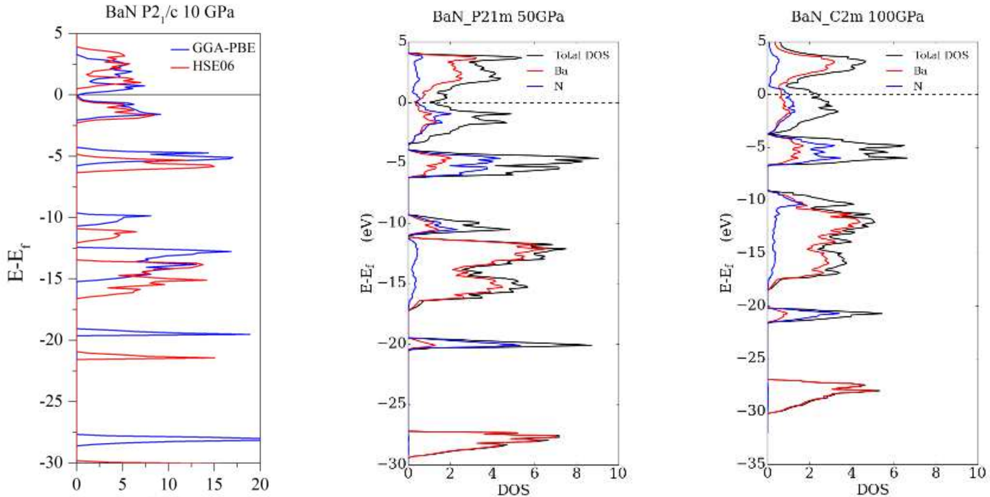

(a) (b) (c)

Figure 3.33 BaN structures and associated total and projected DOS. (a) *P2₁/c* at 0 GPa (b) *P2₁/m* at 50 GPa (c) *C2/m* at 100 GPa.

b. Ba_2N_3

From 14 to 83 GPa, the *C2/m* phase is the thermodynamic ground state phase. Its structure is displayed in *Figure 3.34a,* and can be thought of as being composed of isolated N_2 units embedded in the barium framework. Two non-equivalent N_2 dumbbells are observed in Ba_2N_3. At 50 GPa, the shortest interatomic N-N distance is 1.25 Å, indicating a double bond character. Thus a formal charge of -2 may be attributed. The other non-equivalent N_2 dimer has N-N separation of 1.34 Å, between that of single (1.41 Å) and double (1.25 Å) bonds. Thus, one may attribute a formal charge of -3 to this dimer, which is isoelectronic to the superoxide O_2^- species encountered in the experimental paramagnetic KO_2 salt (O-O distance of 1.28 Å). To explain the bonding mode in Ba_2N_3, this compound could be assigned as $(Ba^{2+})_4(N_2^{2-})(N_2^{3-})_2$. With a charge of -2/-3 per N_2 unit, the two antibonding π_g^* orbitals of $N_2^{2-/3-}$ are partially filled (*Figure 3.34b*). Thus, a bond order of 2 is expected in N_2^{2-} and of 1.5 in N_2^{3-}, which correlates well with the structural properties of N_2 units. In addition, the Ba_2N_3 compound is a metal in the 0-100 GPa range.

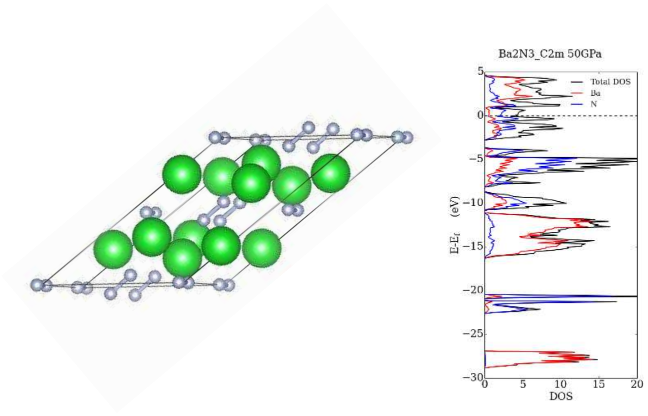

Figure 3.34 (a) *C2/m* Ba_2N_3 structure at 50 GPa, (b) the pDOS.

c. BaN_2

The 1:2 stoichiometry is stable over the whole pressure range. This 1:2 composition presents a phase sequence of *C2/c* (24 GPa) → *C2/m* (63GPa) → $P2_1/c$. The *C2/c* and *C2/m* structures consist of N_2 dimers sitting in the four-fold channels of a 3D barium network (*Figure 3.35*). Up to 63 GPa, the shortest N-N separation is lower than 1.24 Å, indicating N-N double bond character. According to the Zintl-Klemm concept, BaN_2 can be described as $Ba^{2+}N_2^{2-}$, and contains 12-electron N_2 dimers isovalent to paramagnetic O_2. The calculated DOS also corroborates our findings (*Figure 3.35*): the Fermi level crosses a region mainly based on nitrogen π antibonding states, *i.e.,* the π_x^* of N_2^{2-}. Half of the π_x^* band is filled. Up to 63 GPa, *C2/c* and *C2/m* BaN_2 are metallic.

Above 63 GPa, the stoichiometry of BaN_2 stabilizes into the $P2_1/c$ structure, shown in *Figure 3.35c.* There are planar zigzag N_4 units (with two outer N-N distances of 1.30 Å, and a central one of 1.32 Å at 100 GPa) along the *a* direction and contained in the *bc* plane. These finite chains are separated by isolated Ba^{2+} atoms. Following ZKC, one may assign a formal charge of -4 to the N_4 group, leading to the 24 ve tetra-atomic species isoelectronic to solid-state Bi_4^{4-} unit in $CaBi_2$.[196] Molecular orbital analysis of zigzag N_4 species revealed that a substantial energy gap separates the bonding π_x^* level (HOMO) and antibonding π_x^* level (LUMO), thus one may expect that $P2_1/c$ BaN_2 is a semiconductor. Our assumption is verified at ambient pressure (band gap of 0.7 eV) and up to ~20 GPa, but metallic above. When pressure rises, the involvement of the Ba 6d states in the Ba-N bonding interaction is observed, a d(Ba) - p(N) bands mixing occurs around the Fermi level (see *Figure 3.35f*).

In BaN_2, a pressure-induced cross-linking of N_2 may be evocated: two open-shell N_2^{2-} bond to give a closed-shell N_4^{4-} unit. Note that $P2_1/c$ BaN_2 is quenchable to ambient pressure.

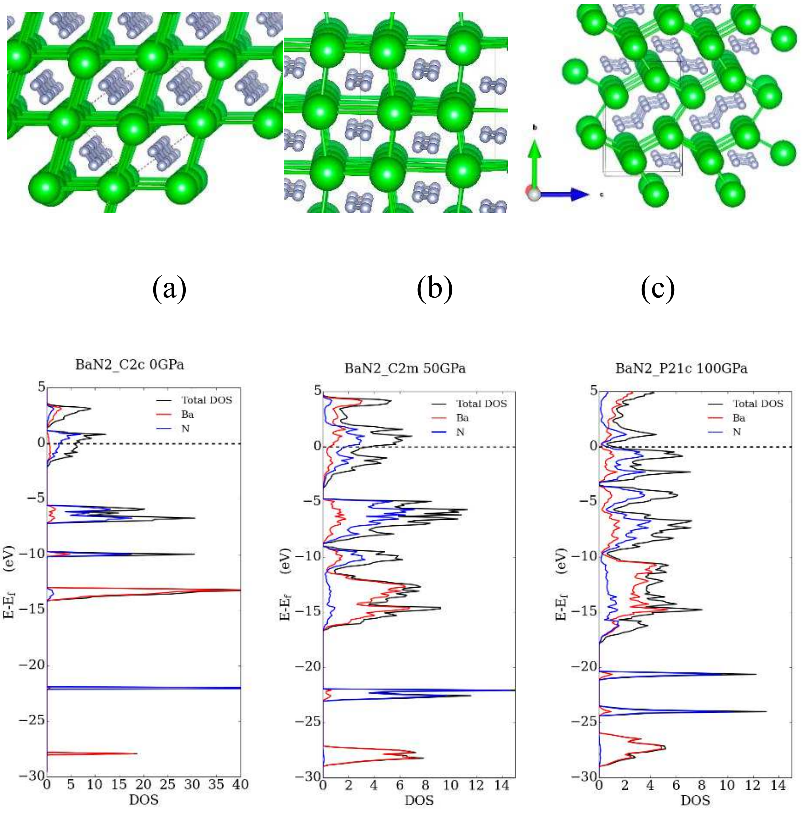

(a) (b) (c)

(d) (e) (f)

Figure 3.35 BaN_2 phases: (a,d) *C2/c* at 0 GPa and DOS, (b,e) *C2/m* at 50 GPa and DOS, (c,f) *$P2_1/c$* at 100 GPa and DOS.

d. Ba_3N_8

Our evolutionary searches uncovered N-rich Mg_3N_8 stoichiometry as a thermodynamic ground state at a pressure as low as 6 GPa, easily achievable in high-pressure synthesis. This phase is stable thermodynamically from 6 to 64 GPa (*Cmmm* space group, Z=2). This aesthetic structure may be viewed as follows: a hexagonal layer of barium atoms (4 Ba/unit cell), a N_2 dumbbell seating in the hole of each Ba_6 hexagon (2 N_2/unit cell), one Ba filling the sixfold channel perpendicular to 2D Ba layers (2 Ba/unit cell), and 6 N_2 surrounding each isolated Ba (6 N_2/unit cell). NN distance is 1.22 (N_2 in ab plane) and 1.16 (N_2 along 100 direction). Thus, a formal electron attribution leads to a layer of $[Ba_2(N_2)]^{2+}$ and two Ba and six neutral N_2.

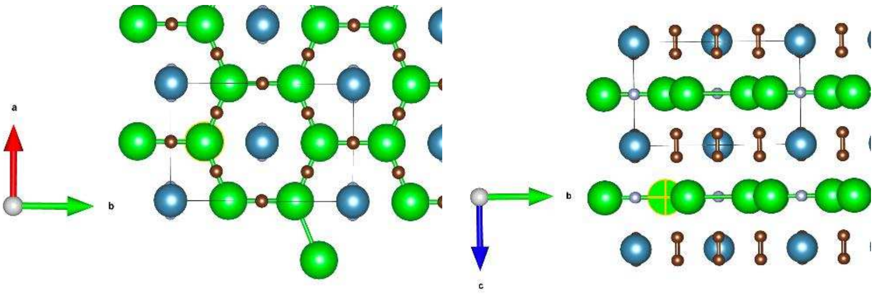

Figure 3.36 Cmmm Ba_3N_8 phase at 50 GPa. Large spheres are barium atoms, and small spheres are nitrogen atoms. Green and blue spheres lie in the ab planes, while N_2 units (in brown) are along c direction. Green contacts are drawn as an eye-guide.

e. BaN_4

BaN_4 is thermodynamically stable above 4 GPa, and exhibits three phase transitions up to 100 GPa, the first phase occurring at 4 GPa (*P6/mmm*), the second one at 30 GPa ($P4_12_12$), and the last at 48 GPa (*C2/c)*. The stable *P6*/*mmm* structure contains N_2 dumbbells in prismatic sites of hexagonal barium network. At 10 GPa, Ba-Ba separations are longer than 4.1 Å, and the shortest Ba-N contact is at 2.91 Å, typical of ionic bonds. Thus, N_2 dimer has formally a minus charge, $(Ba^{2+})(N_2^-)_2$. From this assumption, the N_2^- MO diagram presents a singly occupied antibonding π_g^*. Therefore an elongation of the N-N bond is expected in respect to neutral N_2.

This is what we observed; at 10 GPa, NN separation of 1.174 Å in *P6/mmm* and 1.108 Å in neutral N_2. N_2^- is a radical such as its isovalent nitric oxide NO. Our assumption is validated by the computed electrical conducting property of *P6/mmm* BaN_4; it is a metal (See *Figure 3.37*).

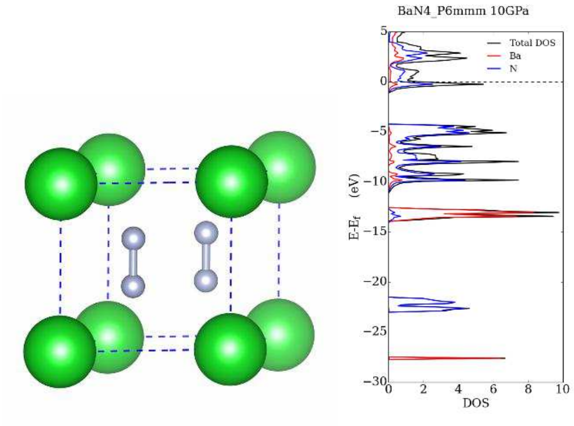

Figure 3.37 (a) Crystal structure of *P6/mmm* BaN_4, and (b) its DOS.

At 30 GPa, a phase transition occurs. $P4_12_12$ becomes the lowest structure in the 30-48 pressure range. Its structure features infinite planar 1D armchair-shaped nitrogen chains, intercalated by barium atoms. Such polymeric chains have been recently proposed in CaN_4,[164] MgN_4,[89] at high pressure. The N-N bond lengths, along the nitrogen chain, are around 1.33 Å, which is greater than a double bond (1.25 Å), but shorter than a single bond. This intermediate distance is consistent with the bonding picture, in which six π electrons are distributed along the polymeric -$(N_4^{2-})_x$- chain, (see the discussion in the previous section on *Cmmm* MgN_4 structure). Standard application of the VSEPR theory to this planar chain enabled rationalization of the structural and bonding properties of poly-N_4^{2-} chains: each nitrogen atom is bent. The planarity of the whole armchair chain is the result of delocalization, but also of the strong ionic interactions between Ba^{2+} ions and poly-N_4^{2-} chains. The densities of states (DOS) of $P4_12_12$ BaN_4 were computed and indicated a metallic character.

A *C2/c* phase shows up above 48 GPa, and also presents one-dimensional nitrogen chains running in Ba channels. Each chain is non-planar and may be viewed as two linked non-planar *cis*-bent N_4 units with a torsional angle of 28.3° at 100 GPa (See *Figure 3.38*). Along the chain, the NN bond lengths are between a double and a single bond (1.28-1.37 Å), and the valence angles are 106.2°-111.2°, typical for bent nitrogen (See *Figure 3.38c*). A small band gap is calculated using HSE06 method which indicates a semiconductor property.

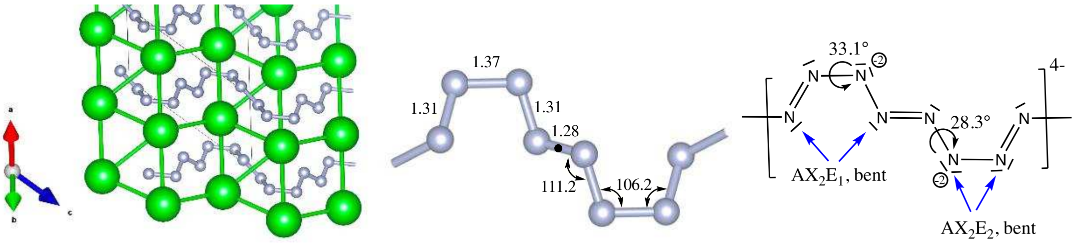

(a) (b) (c)

Figure 3.38 *C2/c* BaN_4 structure at 100 GPa. (a) view of the infinite nitrogen chain in Ba channels, (b) selected structural parameters and (c) Lewis structure of poly-N_4^{4-} chain (distances in Å, angles in °; VSEPR AX_nE_n notation).

f. BaN_5

The stability range of BaN_5 is 25-80 GPa (space group *Imma*). Its structure is displayed in *Figure 3.39*. This phase is built from hcp Ba layers, in between which there are five-membered N_5 rings. Such pentazole rings have been predicted in alkaline and alkaline earth metals MN_5 (M=Ca,[164] Li,[151] Cs,[145] Na,[152] etc), but have also been observed recently in an experimentally high-pressure phase, CsN_5.[144] At 50 GPa, N-N distances are ranging from 1.30 Å to 1.35 Å in planar pentazolate unit, signalling a delocalized system. The averaged N-N bond length in pentazolate N_5^- is 1.301 Å in LiN_5 (40 GPa), 1.30 Å in NaN_5 (20 GPa), 1.328 Å in CsN_5 (1 atm), 1.329 Å in the gas phase. Therefore, it is tempting to assign a formal charge of one minus per N_5 ring. This N_5^- ring, isoelectronic to $C_5H_5^-$ cyclopentadienyl, has delocalized 6 electrons, and follows the Hückel aromaticity (4n+2), and octet rules. Nevertheless, following the ZKC, Ba should give two electrons to each N_5. This is what conclude Zhu *et al.*[164] in their study of electronic properties of predicted CaN_5 structure. Note that, with a 2- charge, N_5^{2-} is a radical species. A close look at the bonding is needed.

In *Imma* BaN_5, inspection of the density of states shows a high participation of barium 5d orbitals in the filled levels of the system (See *Figure 3.39*). A significant d-orbital population of approximatively 0.55 at the barium atom is computed at 50 GPa. Moreover, a -ICOHP of 0.218 eV/pair is computed for Ba-N contacts. Therefore, the cation-anion interactions cannot be described as purely ionic, but also have a partially covalent character. We propose that the extra electron is delocalized over the Ba-(N_5^-)-Ba network, which explains the relatively short cation-anion separation of 2.59 Å at 50 GPa.

To summarize, Ba gives one electron to a N_5 ring, following the Hückel and octet rules, while the remaining electron is delocalized over the whole Ba net through partially covalent Ba-N interactions. This simple but founded picture explains well the metallic property of *Imma* BaN_5:

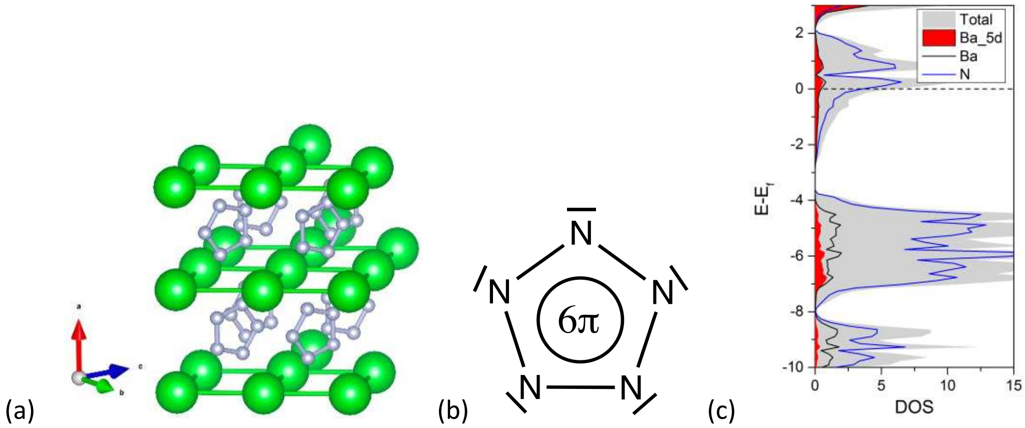

Figure 3.39 (a) *Imma* BaN_5 structure. Ba-Ba green lines are drawn as an eye-guide. (b) Lewis structure of N_5^- pentazolate. (c) Projected DOS.

g. Ba_2N_{11}

From 8 to 14 GPa, the *P*-1 phase of Ba_2N_{11} is stable. As shown in *Figure 3.40*, one linear N_3 and four N_2 motifs per formula unit fill the void between two Ba layers. Ba-Ba and Ba-N separation are longer than 4.03 Å and 2.69 Å, respectively, at 10 GPa. The calculated NN separation is 1.18 Å in centrosymmetric N_3, a value typical of a double bond observed in azide N_3^- structures[169,171]. Thus, it remains formally three electrons to four N_2, $(Ba^{2+})_2(N_3^-)(N_2)^{3-}_4$. A distance of 1.15-1.16 Å is found in N_2 units, a slightly elongated triple bond provoked by the partial occupation of antibonding nitrogen π^* bands. Ba_2N_{11} is a metal.

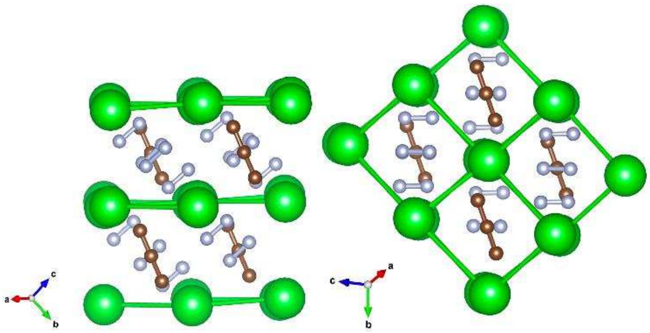

Figure 3.40 Ba_2N_{11} structures with highlighted isolated N_3 and N_2 units. Ba-Ba green lines are drawn as an eye-guide.

h. BaN$_6$, a stable azide crystal and metastable 5- and 6-membered nitrogen ring structure

This 1:6 stoichiometry has a concise range of thermodynamic stability, from 5 to 9 GPa (See *Figure 3.41*). The stable $P2_1/m$ phase presents azide N_3^- units, with NN distances ranging from 1.17 Å to 1.20 Å (double bonds). Beside this well-known phase, our CSP searches found two dynamically stable phases, *P*-1 space group, which do not lie on the convex hull - metastable thermodynamically. In the BaN_6 compound, a *P*-1 structure is the lowest phase above 21 GPa, as shown in *Figure 3.21*. Isolated planar N_5-N units are filling the space between two corrugated barium layers. To the best of our knowledge, such an N_6 motif presents a new topology in nitrogen-based compounds. If one assigns a -2 charge to N_6 (see Lewis structures in *Figure 3.42c*), $(N_5\text{-}N)^{2-}$ is reminiscent to an isoelectronic closed-shell pentazole N_5-F molecule. Eight π electrons are delocalized over the planar N_5-N ring, explaining the double/single bond character (NN=1.24-1.37 Å). At 50 GPa, the second lowest metastable phase of BaN_6 contains six-membered nitrogen rings (See *Figure 3.42b*). This *P*-1 (II) structure lies 115 meV/atom above ground-state N_5-N BaN_6 phase.

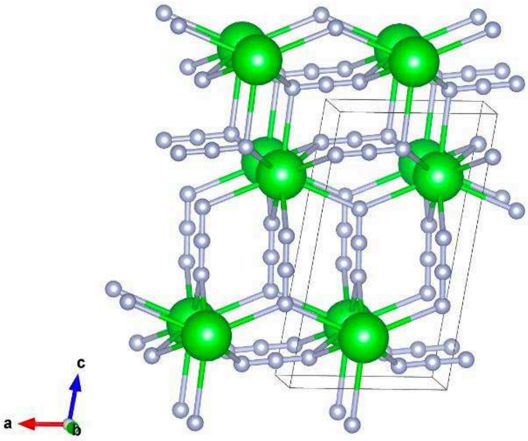

Figure 3.41 $Ba(N_3)_2$ phase at 1 atm. Nine N_3^- ligands are coordinated to a Ba^{2+} cation.

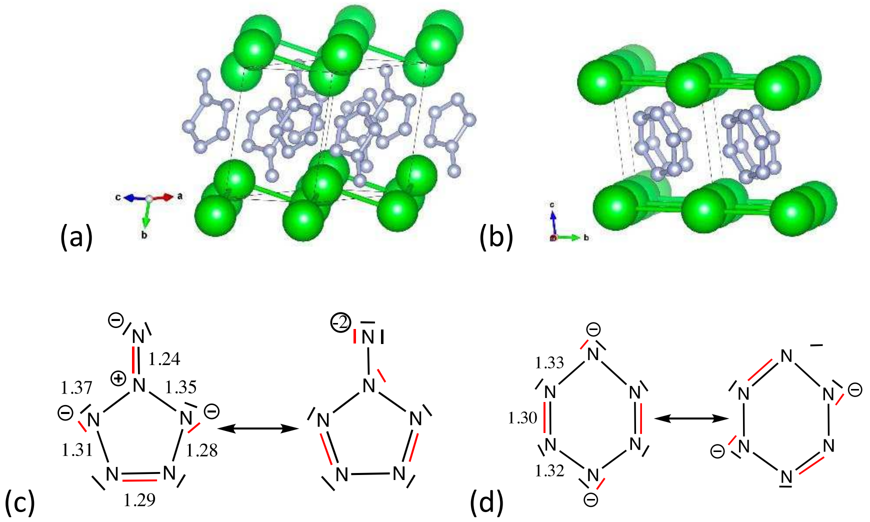

Figure 3.42 (a), (b) Metastable *P*-1 BaN_6 phases at 50 GPa. Selected Lewis structures of (c) $(N_5\text{-}N)^{2-}$ and (d) N_6^{2-} rings (distances in Å).

i. BaN_{10}, a nitrogen-rich phase with two pentazolate rings

Above 12 GPa, a thermodynamically stable BaN_{10} phase emerges (space group *P*-1, Z = 2). This phase has the highest nitrogen content in our explored binary Ba-N phase diagram, but also, to the best of our knowledge, in other s-block element nitrides. Two N_5 rings per barium cation are stacked along the [001] direction, as displayed in *Figure 3.43*. At 50 GPa, NN distances of 1.28-1.31 Å are calculated within the 5-membered ring, typical values for six π electron 5-

membered ring N_5^- (delocalized single/double bonds). A large HOMO (π_3)-LUMO(π_4) gap of 3.37 eV is calculated in isolated pentazolate. In solid-state P-1 BaN_{10}, a large gap separates the valence from the conduction bands, as expected for such a Zintl compound. Owing to the potential application of such a predicted $Ba(N_5)_2$ phase in a high-energy-density material, we explored the quenchability of P-1 BaN_{10}, and found that this phase remains dynamically stable at ambient pressure. Nevertheless, a lower pentazolate-containing structure (space group I-42d, Z=4) is located on the PES by our molecular evolutionary search technics[197] and lies 57 meV/atom below the P-1 phase at 1 atm. The I-42d → P-1 phase transition is computed at 8 GPa. Ambient pressure I-42d structure is displayed in *Figure 3.47*. Each N_5 ring is bounded to four Ba^{2+} through ionic Ba-N bonds of ~3.01 Å, leaving a free lone-pair per N5, thus each Ba^{2+} is coordinated to eight pentazolate units. Usual N-N bond lengths in pentazolate are calculated (~1.32 Å). We checked the thermal stability of I-42d $Ba(N_5)_2$ by running AIMD simulations up to 1000 K during ten ps (see the discussion in the next section). Its structure presents persistent five-membered N_5^- ring motif up to 1000 K.

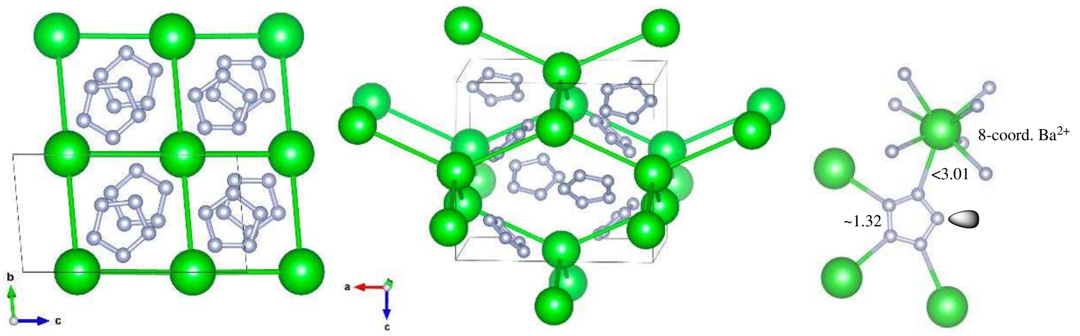

(a) (b) (c)

Figure 3.43 BaN_{10} phases. (a) P-1 at 50 GPa and (b) I-42d at 1 atm. (c) local geometry in I-42d phase (distance in Å).

3.4.5 Conclusion

In this study, we carried out crystal structure prediction to investigate the ground stable states of barium nitrides at ambient, and up to 100 GPa. Along with the experimental reported Ba_3N, BaN_2, BaN_2, and BaN_6, we predicted eight new stoichiometries, namely, Ba_3N_2, BaN, Ba_2N_3, Ba_3N_8, BaN_4, BaN_5, Ba_2N_{11} and BaN_{10}, to become stable at specific range of pressure. Interestingly, Ba_3N and Ba_2N are predicted to have electride properties. Interstitial electrons have been found existing in channel and layer forms. By adjustment of the ratio of barium in the Ba_xN_y phase diagram, a series of polynitrogen forms were achieved in the crystalline, including small molecular units made of a few atoms (N_2, N_4, N_5, and N_6) to1-dimensional chains.

3.5 Pentazolate alkaline-earth metal salts

3.5.1 Motivations

Pentazolate ions in materials have been notoriously elusive for the last hundred years, despite enormous efforts to make these compounds in a condensed state. Recently, researchers have synthesized solid-state compounds consisting of isolated pentazolate anions N_5 and alkaline metal elements, *i.e.,* NaN_5[152] and CsN_5.[144,145] To gain access to the *cyclo*-pentazole ring, they have compressed metastable sodium, or cesium azide (A^+, N_3^-) mixed with the N_2 cryogenic liquid, in a diamond anvil cell together with laser heating. In the previous barium nitrides section, we mentioned that we had predicted a nitrogen-rich phase (*P*-1 BaN_{10}) containing pentazolate anions. Based on our current knowledge, this is the first time that the BaN_{10} with N_5^- motif is proposed. Our calculation predicts that *P*-1 BaN_{10} is thermodynamically stable above 12 GPa.

Motivated by this novel experimental and theoretical discovery, we explored the MN_{10} stoichiometry, where M represents alkaline earth metal elements, *i.e.,* Be, Mg, Ca, Sr and Ba at ambient pressure and 50 GPa. We aim to see if solid-state M(*cyclo*-N_5)$_2$ is stable thermodynamically, dynamically and kinetically. Moreover, we will analyze the cation size effect on the structural, energetic and electronic properties, both at ambient and high pressure (here, 50 GPa, a pressure accessible in high-pressure physics).

3.5.2 Methods

The general methodology is presented in the first chapter. DFT PAW GGA PBE calculations are carried out. Therefore, we will describe only the specific methodological details here. First of all, we carried out molecular crystal searches, using the technics implemented in USPEX code[8,13,30] to make sure we located the most stable pentazolate phase at 0 GPa. Thus, the N_5 pentazolate unit was treated as an integral unit in the molecular crystal. Then we conducted a standard fixed-composition crystal structure prediction at 50 GPa. Up to 44 atoms per primitive cell were used. The phonon dispersion curves are calculated for all of the structures, and show the absence of any imaginary frequencies in the entire Brillouin zone. All of the discussed MN_{10} structures are local (global) minima on the PES.

3.5.3 Results and discussion

Remarkably, a series of pentazolate phases have been predicted as the ground stable, or metastable phase. Remember that all are dynamically stable. The predicted phases are listed in *Table 3.6*.

Table 3.6 Predicted space group of solid-state MN_{10} compounds at 0 and 50 GPa.

Pressure	**BeN_{10}**	**MgN_{10}**	**CaN_{10}**	**SrN_{10}**	**BaN_{10}**
0 GPa	*I*-42*d* (I) meta[a]	$P4_32_12$ meta	*I*-42*d* (II) meta	*I*-42*d* (II) ?[b]	*I*-42*d* (II) meta
50 GPa	*Fdd*2 stable[c]	*I*-42*d* (II) stable	*Ibam* stable	*Ibam* ?	*P*-1 stable

a. thermodynamical metastable; b. absent of data; c. thermodynamical stable

To compare the relative enthalpy stability of MN_{10} polymorphs, *Figure 3.44* represents the enthalpy difference of each phase, relative to *I*-42*d* (II) phase at 0 GPa, and *Ibam* phase at 50 GPa. At 0 GPa, BeN_{10} adopts *I*-42*d* (I) symmetry, and MgN_{10} has a $P4_32_12$ space group, while CaN_{10}, SrN_{10}, and BaN_{10} share the identical space group of *I*-42*d* (II). Notice that the *I*-42*d* (I) become energetically unfavorable when the atomic number increases.

At a pressure of 50 GPa, BeN_{10} adopts *Fdd*2 space group, but very close in energy to *I*-42*d* (II) (6 meV/atm), the lowest phase for MgN_{10}. For the heavier Ca and Sr elements, the *Ibam* phase becomes the lowest enthalpy phase. Finally, BaN_{10} has *P*-1 space group.

Before the discussion of the electronic properties analysis, a question was raised: Are these MN_{10} pentazolate phases ground stable concerning other M_xN_y nitrides? Fortunately, Be-N,[156] Mg-N,[89,159] Ca-N,[164] and Ba-N binary phase diagrams have been explored by us and other researchers, which makes it possible to compare our MN_{10} compounds with other ground stable phases.

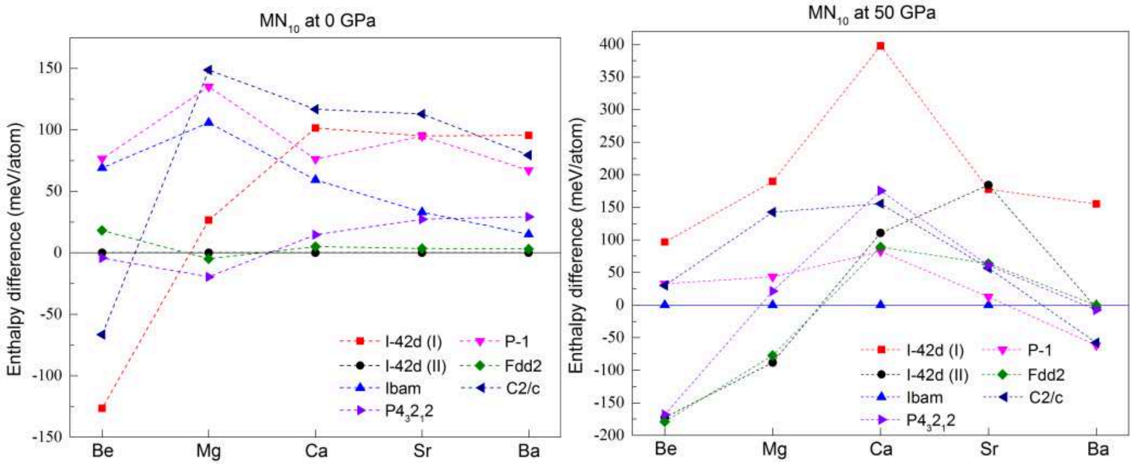

Figure 3.44 (a). Enthalpy difference of each predicted phase relates to *I*-42*d* (II) at 0 GPa; (b). Enthalpy difference of each predicted phase relates to *Ibam* at 50 GPa.

Firstly, 3:2 is the only stoichiometry that locates as ground stable state at ambient pressure in Be-N and Mg-N systems. Therefore, their stability criterion is based on the reaction between MN_{10} and M_3N_2 plus N_2. We calculated the reaction enthalpy as:

$$\Delta H_r=(3MN_{10}-(M_3N_2+14N_2))/33$$

$\Delta H_r > 0$ means MN_{10} is a metastable phase and will decompose to M_3N_2 plus N_2, *vice versa*. Among the two reactions, $\Delta H_{Be}= 0.371$ eV/atom and $\Delta H_{Mg}= 0.274$ eV/atom. Thus, *I*-42*d* (I) BeN_{10} and *P*4_32_12 MgN_{10} are metastable phases at 0 GPa.

For Ca-N and Ba-N systems, CaN_2 and BaN_6 stabilized at 0 GPa, and emerged as the nearest stoichiometries to the 1:10 ratio. The enthalpies of reaction calculated from these phases shows that CaN_{10} and BaN_{10} are metastable phases at ambient pressure as well ($\Delta H > 0$). Besides, we are not able to calculate the thermodynamic stability of SrN_{10} due to the absent information of Sr-N binary phase diagram.

At 50 GPa, the phases that have 1:4 stoichiometry become the ground stable in Be-N and Mg-N systems. The enthalpy of reaction shows that BeN_{10} is 0.109 eV/atom and MgN_{10} 0.164 eV/atom lower than BeN_4/MgN_4 + $3N_2$. Meanwhile, CaN_5/BaN_5 replaces CaN_2/BaN_6 as the nearest stable phase to MN_{10}. The calculation of reaction enthalpy indicates the value of -0.185 eV/atom and -0.150 eV/atom for CaN_{10} and BaN_{10}, respectively. All the negative reaction enthalpies illustrate that BeN_{10}, MgN_{10}, CaN_{10} and BaN_{10} are energetically favorable, and are the ground stable phases at 50 GPa. Although so far there is no available data for SrN_{10}, we hypothesize that SrN_{10} is a thermodynamically stable phase, according to the regular pattern of the periodic table.

Figure 3.45 displayed the *I*-42*d* (I) BeN_{10} phase. The Be-N separation is computed at 1.72, larger than the sum of the Be^{2+} and covalent N one (0.59+0.66, respectively). Thus, as expected for an ionic salt, this phase consists of isolated Be^+ cations and N_5^-. At 0 GPa, the N-N distances are 1.300 Å, 1.313 Å, 1.346 Å, with a ratio of 1:2:2. Be forms a tetrahedron with 4 N_5^- rings. Moreover, beryllium forms also a tetrahedron with the four surrounded beryllium atoms located at 5.29 Å. The sublattice of Be has an *I*4$_1$*/amd* space group which can be found in many crystals, *e.g.,* Sn and Ge. Particularly, the $Be(N_5)_2$ structure presents large vacuums around the atoms, characteristic of a metal-organic framework. These voids might be stabilized molecular N_2 or other species, $Be(N_5)_2$ potentially acting like a sieve. At 7 GPa, *I*-42*d* (I) BeN_{10} undergoes a phase transition to a high symmetric *Fdd*2 phase which contains four formula units per unit cell, and a higher density packing. In *Fdd*2 phase, beryllium atoms lie in the center of a slightly compressed octahedron formed by six N_5 rings (See *Figure 3.45*).

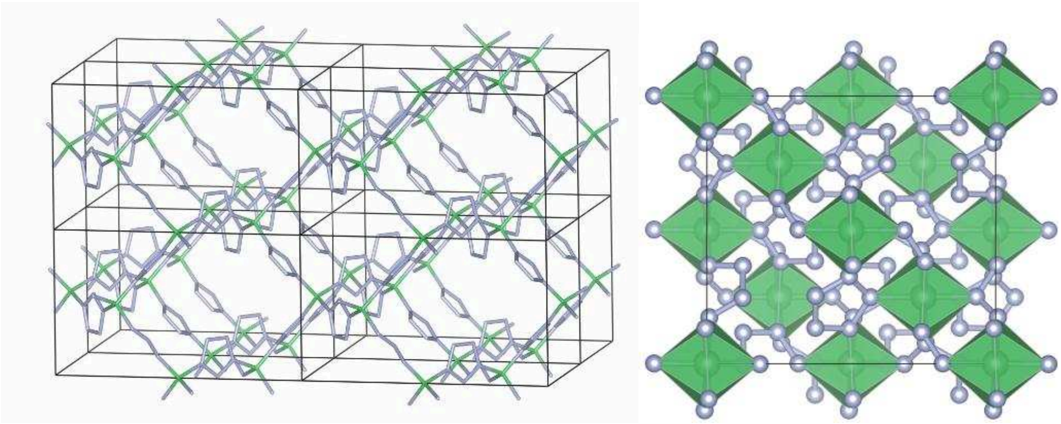

(a) (b)

Figure 3.45 Crystal structure of Be(N_5)$_2$: (a) *I*-42*d* (I) at 0GPa and (b) *Fdd*2 at 50 GPa.

Figure 3.46 displays the *P*4$_3$2$_1$2 and *I*-42*d* (II) MgN_{10} structures at ambient pressure and 50 GPa, respectively. In *P*4$_3$2$_1$2, Mg forms an octahedron with 6 N_5 rings, and Mg-N distance varies from 2.215 Å to 2.270 Å, typical ionic bonds. Interestingly, the sublattice of Mg has the same *I*4$_1$/*amd* space group found in BeN_{10} *I*-42*d* (I). Above 7 GPa, *I*-42*d* (II) phase becomes the lowest phase. The *I*-42*d* (II) contains 8-fold coordinated Mg^{2+} cation with eight different N_5 rings at the corners. The Mg-N distance varies from 1.969 to 2.230 A.

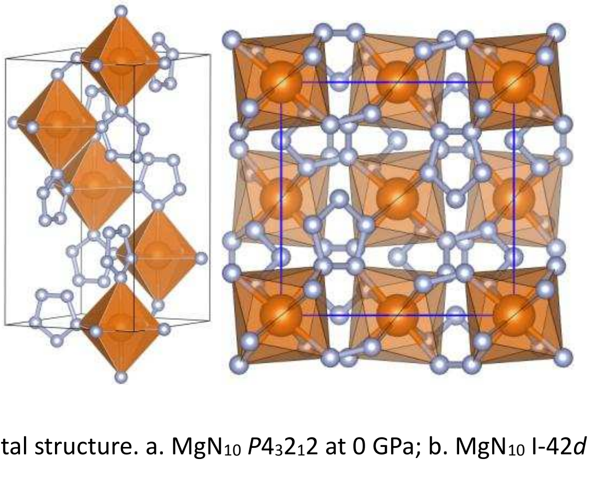

Figure 3.46 Crystal structure. a. MgN_{10} *P*4$_3$2$_1$2 at 0 GPa; b. MgN_{10} I-42*d* (II) at 50 GPa.

CaN_{10}, SrN_{10} and BaN_{10} adopt the *I*-42*d* (II) phase at 0 GPa, which is also identical with MgN_{10} phase at 50 GPa (See *Figure 3.47*). Although the *I*-42*d* (II) share the same symmetry with the *I*-42*d* (I) BeN_{10} phase, the *I*-42*d* (II) has more condensed packing and a different N_5 arrangement. The cation atom formed eight bonds with eight surrounding N_5 rings. Moreover, cation formed a tetrahedron with other cations and had the $I4_1/amd$ sublattice. As the pressure increased, the CaN_{10} and SrN_{10} *I*-42*d* (II) phases transform into the high-pressure *Ibam* phase (See *Figure 3.47b*) at the 18 GPa and 9 GPa, respectively.

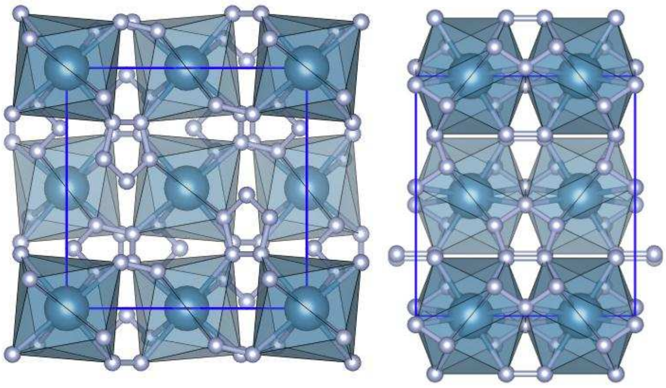
(a) (b)

Figure 3.47 Crystal structures of (a) CaN_{10} *I*-42*d* (II) at 0GPa, SrN_{10} and BaN_{10} adopt the same phase at 0 GPa; (b) CaN_{10} *Ibam* at 50 GPa SrN_{10} adopts the same phase at 50 GPa.

In BaN_{10}, a phase transition from *I*-42*d* (II) to *P*-1 happens at 8 GPa. Note that the *P*-1 barium pentazolate salt lies on the convex hull at a surprisingly low pressure of 12 GPa (*Figure 3.21*). The *P*-1 structures consist of layers of barium atoms sandwiched between layers of pentazolate N_5^- anions, oriented differently to one another in the unit cell (*Figure 3.48*). Because of the aromatic nature of the bond in the pentazolate N_5 ring, the bond lengths for both phases are between those of the double-bond (1.25 Å as in trans-diimine) and the single bond (1.45 Å as in hydrazine). Also, we discovered another metastable *C*2/*c* BaN_{10} phase which is only 4 meV/atom higher in energy than *P*-1 phase at 50 GPa.

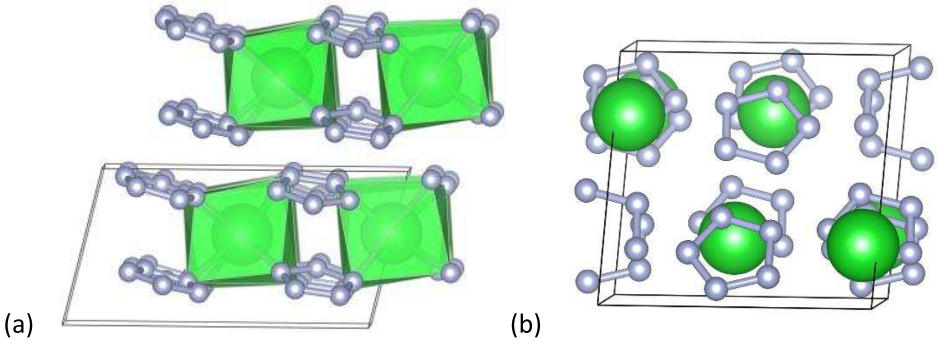

Figure 3.48 (a) *P*-1 and (b) *C2/c* BaN_{10} at 50GPa.

The calculated density of states shows that all predicted stable and metastable compounds are insulators with a wide band gap at ambient pressure and 50 GPa. The band gap energies are listed in *Table 3.7.* Hence, they would be optically transparent, if observed. For example, the calculated band structure of the *P*-1 phase of CsN_5 confirms an optically transparent insulator in experiments.[153,145]

Table 3.7 Band gap (eV) within PBE-GGA level

Band Gap (eV)	BeN_{10}	MgN_{10}	CaN_{10}	SrN_{10}	BaN_{10}
0 GPa	5.0	4.6	5.1	5.2	5.3
50 GPa	3.3	4.4	3.0	2.9	3.7

Notice: GGA-PBE underestimate the band gap.

Dynamical stability

In order to examine the dynamical stability of the MN_{10} phases at 0 GPa, *ab initio* molecular dynamics (AIMD) simulations based on DFT are carried out by using supercells at 1000 K within each time step of 1 fs, and the total simulation time up to 10 ps. In the simulations, the canonical NVT (N - constant number of particles, V - constant volume, and T - constant temperature) ensemble is adopted as implemented in VASP code. During the entire 10 ps AIMD simulations, the covalent N-N bonds in N_5 nets are not broken at least at 1000 K; only small atomic vibrations were observed (*Figure 3.49*). However, several N_5 rings decompose to N_2 and bent N_3 units in BeN_{10} phase, which implies it can only exist at a relatively lower temperature (< 1000 K).

N_2 storage in Metal-Inorganic-Framework (MIF) pentazolate beryllium

The *I*-42*d* (I) $Be(N_5)_2$ structure presents an open framework, a characteristic of MIF materials. Thus, it’s useful to study the capacity of this phase to store molecular species. As a preliminary result, we filled the MIF with N_2 molecules. Our modelling searches lead to at least 1.5 N_2 per formula unit. The thermostability of this extremely nitrogen righ compound has been confirmed using AIMD simulation at room temperature; Be-N covalent net is not destroyed (See *Figure 3.50*).

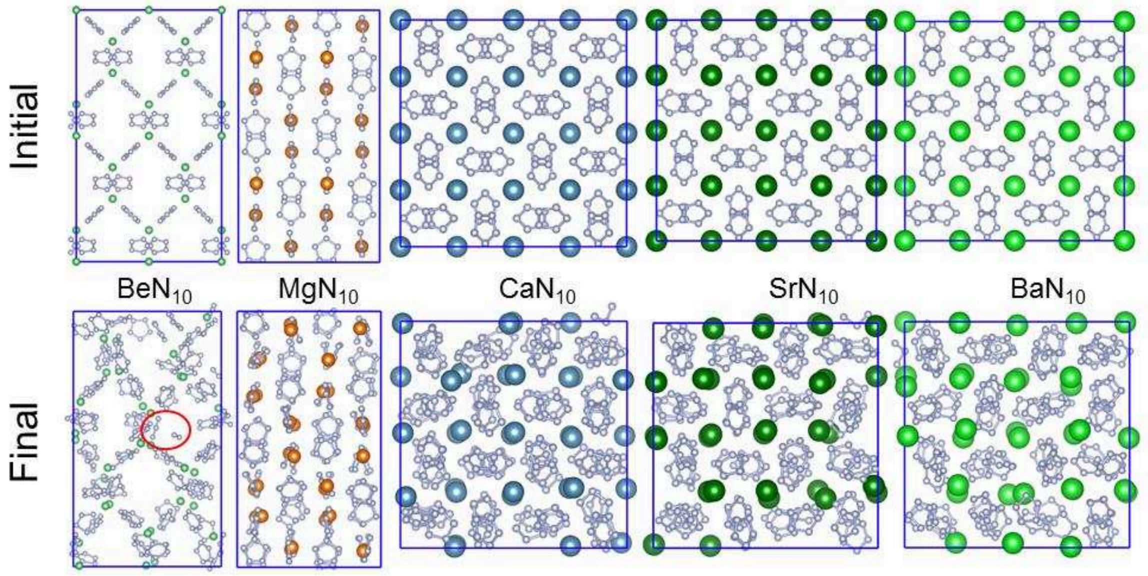

Figure 3.49 Snapshot of AIMD calculations at 0 GPa and 1000 K, the above figures represent the static structures before the AIMD calculation starts; the figures below are captured at 10 ps, and all of the structures achieved the equilibrium states.

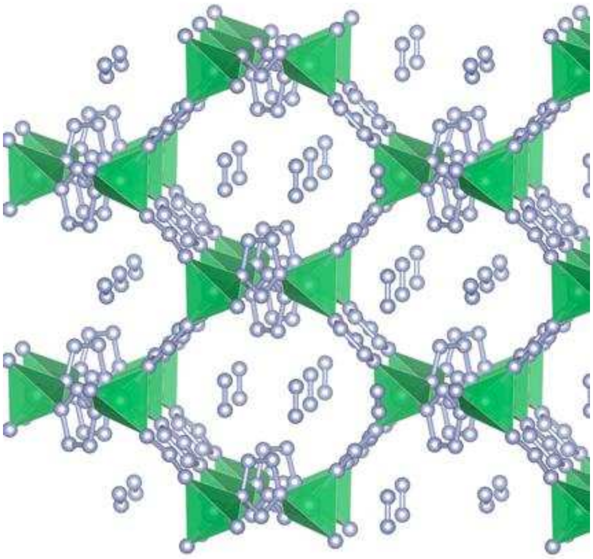

Figure 3.50 Be$(N_5)_2(N_2)_{1.5}$ phase.

3.5.4 Conclusion

We performed the first-principles evolutionary structure search of nitrogen-rich compounds, consisting of alkaline earth metal elements and nitrogen, with 1:10 stoichiometry at ambient condition and 50 GPa. Several new high-nitrogen content materials, containing pentazolate units, have been uncovered. Most of the MN_{10} compounds, featuring pentazolate anions in the crystalline state, are thermodynamically stable at high pressures. However, the zero pressure phases are metastable at ambient conditions. The temperature sustainability of zero pressure phases has been proved by using AIMD at a temperature up to 1000 K. Further thorough experimental validation is feasible and will help us to develop a novel HEDM.

4. Transition metal nitrides

4.1 Introduction

Nearly a century since the pioneering works in the 1920s-1930s by G. Hägg in crystal structure determination of transition metal nitrides M_xN_y (M, transition metal), the elucidation of the atomic arrangement in binary metal-nitrogen phases is still a delicate task.[198,199] Many MN_{1-z} in the literature are possibly oxynitrides, imides, or amides; thus, efforts have to be made to assign a valid crystal structure for a given stoichiometry.[200] A number of studies in the Zr-N,[201] Hf-N,[202] Ta-N,[203,204] and W-N[205] systems have demonstrated the power of high-pressure synthesis in the search for new nitrogen-rich nitrides. The entire field of synthesis and study of the high oxidation state of transition metal nitrides has been reviewed recently by Salamat *et al.*[205]

The understanding of their peculiar mechanical and chemical properties, such as high stiffness, high hardness, high thermal conductivity, high melting point, and good catalytic performance, needs a characterization of materials from a crystallographic point of view. Their fascinating properties stimulate the development of new synthetic routes leading to new well-defined nitride materials.

On the one hand, Molybdenum dinitride (MoN_2) was recently synthesized at a moderate pressure of 3.5 GPa, and a layered MoS_2-type structure has been proposed.[1] However, our first-principles calculations of thermodynamic, mechanical and dynamical properties suggest that this layered $R3m$ structure is unstable. We find that the ground state of the MoN_2 system is a pernitride structure with space group $P6_3/mmc$ which transforms to a $P4/mbm$ phase above 82 GPa. Chemical bonding analysis shows that one could assign MoN_2 as $Mo^{4+}(N_2^{4-})$; *i.e.,* Mo is formally a d^2 metal, in agreement with the experimental results of Wang *et al.*[1] The presence of covalent N_2 dumbbells and strong bonding between Mo^{4+} and N_2^{4-} is the source of the superior mechanical properties of these predicted ultra-incompressible MoN_2 pernitrides.

On the other hand, zirconium nitrides represent a rich family of phases where the stability and microstructures are still not completely understood.[201,206–210] In addition to the known ZrN and Zr_3N_4, new candidate structures with Zr:N ratios of 2:1, 4:3, 6:5, 8:7, 15:16, 7:8 and 4:5 are found to be ground-state configurations, while Zr_3N_2 has a very slightly higher energy. Except for Zr_2N, the newly discovered Zr_xN_y compounds adopt rocksalt structures with ordered nitrogen or zirconium vacancies. The electronic and mechanical properties of the zirconium nitrides are further studied to understand their composition-structure-property relationships.

In this chapter, to address these issues, the crystal structures of MoN_2 and Zr_xN_y were explored by the *ab initio* evolutionary crystal structure prediction method (USPEX). Our work should guide experimental groups aiming to synthesize these new technologically useful materials.

4.2 Computational details

The crystal structure prediction for thermodynamically stable structures was performed using the evolutionary algorithm, as implemented in the USPEX code.[8,13,30] The lowest-energy structures were determined at 0, 10, 20, 40, and 100 GPa with systems containing up to 30 atoms in the simulation cell. The first generation of 80-100 structures was produced randomly; all subsequent generations contained 60-80 structures and were produced using variation operators such as heredity (60%), softmutation (15%), lattice mutation (15%), and 10% of each new generation was produced randomly.

Each structure was fully relaxed to an energy minimum at different pressures within the framework of density functional theory by using the VASP package.[48] We employed the all-electron projector-augmented wave (PAW) method and the Perdew-Burke-Ernzerhof (PBE) version of the generalized gradient approximation (GGA) functional.[41,42] The PAW potentials have [Kr], [Kr] and [He] cores with radii of 2.75, 3.00 and 1.50 a.u. for Mo, Zr and N atoms, respectively. A plane-wave basis set with a kinetic energy cutoff of 600 eV was employed. We used uniform Γ-centered k-point meshes with a reciprocal space resolution of $2\pi \times 0.03$ Å^{-1} for Brillouin zone sampling. These settings enable excellent convergence of total energies, forces, and stress tensors.

Theoretical phonon spectra were calculated by the supercell approach by using the PHONOPY package[97] to probe the dynamical stability of the structures. All discussed energies are zero-point energy (ZPE) corrected. Note that, if any phonons of a given structure exhibit imaginary frequencies, the studied structure is dynamically unstable and should transform under lattice relaxation into a more stable ground state structure. The elastic tensors were further calculated for all dynamically stable structures, and the mechanical stabilities were determined by Born-Huang criteria.[211] Chemical bonding analyses were carried out using the crystal orbital Hamilton population (COHP) method by using the LOBSTER code.[51,53,54]

4.3 Molybdenum nitrides

In 2015, a nitrogen-rich molybdenum-based compound, MoN_2, was proposed[1], extending the well-known binary Mo-N compositions. This newly discovered nitride, *3R*-MoN_2, adopts a rhombohedral *R*3*m* structure and was proposed to be isotypical with MoS_2. This structure is a bulk layered material in which the layers interact via van der Waals forces (*Figure 4.1a*). Mo is located in a trigonal prismatic atomic arrangement and sandwiched between N atoms. The "determined valence state for Mo is +3.5 in both *3R*-MoN_2 and MoS_2" claimed by Wang *et al.*, to our astonishment as MoN_2 has two valence electrons less per formula unit than in MoS_2. Therefore, nitrogen atoms do not fulfill the octet rule in the proposed *R3m* MoN_2, as sulfur does in MoS_2 (*Figure 4.1a*, see the formal electron attribution on tricoordinated X atoms in MoX_2 (X = S, N; Mo^{4+}, d^2)). We hypothesized that this electronic situation should be very unstable from thermodynamic and mechanical points of view and that adjacent MoN_2 layers must be connected through N-N covalent bonding, leading to the well-known pernitride situation (diatomic N_2 units in Mo network).

There are at least two questions that needed to be answered: first, what is the ground-state structure of MoN_2? Knowledge of solid-state MoN_2 geometrical and electronic properties is crucial for understanding the catalytic properties of such a nitrogen-rich molybdenum phase. Second, as the synthesis of MN_2 is done under moderate or high pressure, what is the effect of pressure on solid-state MoN_2? In this work, new ground states and metastable MoN_2 structures at both ambient and high pressures are proposed and established. The previously proposed R3m MoN_2 is found to be thermodynamically, dynamically, and mechanically unstable, while a pernitride phase (*P*6_3*/mmc*) emerges as the ground-state structure.

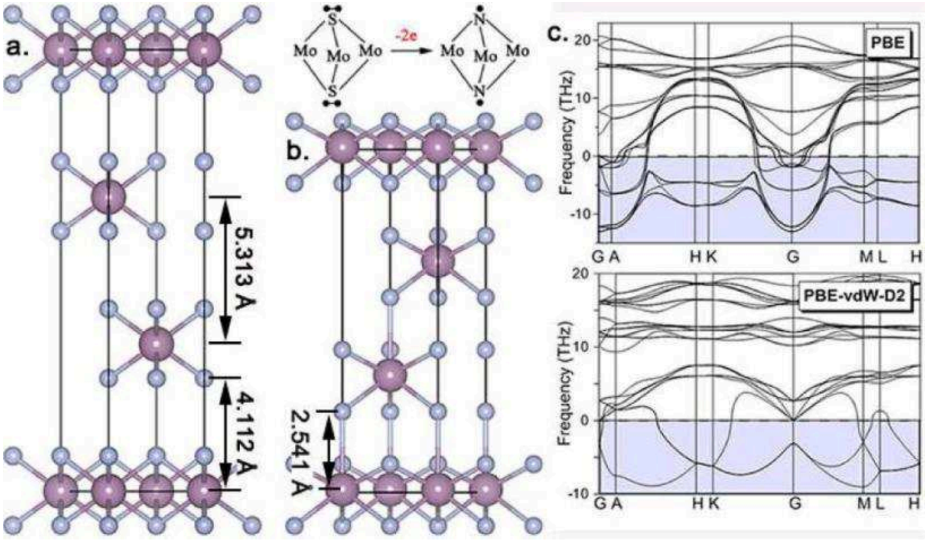

Figure 4.1 (a) Experimental claimed MoS_2-type $R3m$ MoN_2 and formal electron attribution on tricoordinated X atoms in MoX_2 (X = S, N; Mo^{4+}, d^2). (b) Fully optimized $R3m$ crystal structure at the PBE vdW-D2 level. (c) The associated phonon dispersion curves of the fully relaxed $R3m$ structure with/without van der Waals correction.

4.3.1 Experimental layered *R*3*m* MoN_2 structure

In the experimentally claimed layered *3R*-MoN_2 structure displayed in *Figure 4.1a*, each MoN_2 sheet consists of a hexagonally packed molybdenum layer sandwiched between two nitrogen layers. The optimized crystallographic parameters are given in *Table 4.1*. The calculated Mo-Mo bond length is 3.012 Å, slightly longer than that found in bulk fcc Mo (2.729 Å) at ambient pressure. Mo atoms are positioned in a trigonal prismatic coordination concerning the two nitrogen layers. Each Mo atom is coordinated by six N atoms at distances of 2.044/2.062 Å (exp. 1.976/2.037 Å). Moreover, within the *R*3*m* space group, the fully optimized structure—both lattice and atomic positions-presents a dramatic decrease of the van der Waals region. The c lattice parameter goes from 15.939 (exp. value, magnetic phase) to 13.869 Å (opt. value, nonmagnetic phase), reducing the interlayer Mo-N separation down to 3.256 Å.

Table 4.1 Calculated structural parameters for MoN_2 phase at selected Pressure (Å, GPa)

Phase	P	Lattice parameters	Atomic position
$R3m$ unrelaxed	0	a = 2.854 c = 15.938	Mo (0, 0, 0) N (0, 0, 0.258), (0, 0, 0.402)
$R3m$ PBE relaxed	0	a = 3.012 c = 13.869	Mo (0, 0, 0) N (0, 0, 0.253), (0, 0, 0.411)
$R3m$ vdW-D2 relaxed	0	a = 3.119 c = 11.214	Mo (0, 0, 0) N (0, 0, 0.235), (0, 0, 0.416)
$P6_3/mmc$ PBE relaxed	0	a = 2.927 c = 7.762	Mo (0.333, 0.667, 0.75) N (0, 0, 0.089)
$P4/mbm$ PBE relaxed	100	a = 4.007 c = 2.597	Mo (0.5, 0.5, 0.5) N (0.385, 0.885, 0)

While the 2D MoS_2-like MoN_2 layer is magnetic as expected,[212] the coupling of unpaired electrons localized on two adjacent layers is responsible for the ferromagnetic to nonmagnetic phase transition. However, the state-of-the-art DFT is not a suitable method for studying interactions in loosely packed systems (such as soft matter, van der Waals complexes, and biomolecules), as this method fails to adequately describe the long-ranged dispersion interactions.[213,214] Therefore, we performed a full structural optimization by using the PBE-GGA DFT level and vdW-D2 method of Grimme for van der Waals correction (*Table 4.1*).[215] The structural parameters within the covalent 2D MoN_2 sheet are very similar, while the lattice constant c decreased from 13.869 Å (PBE without vdW correction) to 11.214 Å (PBE with vdW-D2 correction). Therefore, short interlayer Mo-N contacts appear (Mo-N = 2.541 Å) and $R3m$ is no more a MoS_2-like layered structure (*Figure 4.1b*). This phenomenon illustrates the strong structural instability of the claimed layered MoS_2-type $R3m$ MoN_2 structure.

To ensure whether such a MoS_2-type structure is a stable local minimum on the MoN_2 potential energy surface, we have examined its mechanical and dynamical stabilities by calculating the elastic constants and phonon spectrum. $R3m$ is found to be mechanically unstable due to the negative C_{44} value of -222 GPa, and large imaginary frequencies are found over the entire Brillouin zone (*Figure 4.1c*). When van der Waals correction is taken into account, the fully relaxed $R3m$ structure is also found to be dynamically unstable with very large imaginary frequencies (*Figure 4.1c*). One may conclude that atomic displacements in *R*3*m* shall lower its enthalpy by transforming barrierlessly to a metastable state which will have another space group. Moreover, the *R*3*m* structure has a very high positive formation enthalpy of 0.819 eV/atom (endothermic $Mo(s) + N_2(g) = MoN_2(s)$ reaction), while, in other transition metal nitrides, the ground-state structures usually have negative formation enthalpies, and even for high-pressure pernitrides the positive formation enthalpies at zero pressure are much lower ($\Delta H_f < 0.64$ eV/atom). The thermodynamic, dynamical, and mechanical instabilities of layered *R*3*m* MoN_2 motivated us to search for other possible ground-state structures at both atmospheric and high pressures. While the use of vdW-D2 correction is shown to be crucial to describe the structural properties of layered compounds, we show that the experimental bond lengths in bulk Mo_2N and MoN are well reproduced at the GGA-PBE level of theory; therefore, we still used the GGA-PBE level of theory for all bulk Mo-N based structures.

4.3.2 NiAs-type MoN_2 pernitride and other metastable structures at ambient pressure

We started to perform fixed-composition structure searches at ambient pressure. The 12 predicted structures with lowest energies are shown in *Figure 4.2*. Almost all of the pernitride structures which contain discrete N_2 units (1-6) lie lower in energy than the structures with isolated nitrogen anions (7-8) and the ones with layered structures (10-12). The lowest pernitride (N_2^{x-}, x = 2-4) is more stable by at least 0.34 eV/atom than the dinitrides ($2N^{3-}$). The energetic preference of the pernitride over the dinitride could be related to (i) covalent N-N bonds being more energetic than Mo-Mo and Mo-N ones and (ii) the high Mo oxidation state (VI) in the latter, as proposed for other transition metal MN_2 phases (FeN_2[216], ReN_2[217]). Mo (VI) can only be found in solid-state extended structures under extremely oxidizing conditions such as in MoO_3 and polymolybdates.[218] In addition, the three van der Waals-type structures, *Cm*, *P*6$_3$*/mmc*, and *R*3*m* (10-12), are by far the less stable ones in our predicted MoN_2 structures ($\Delta H > 0.6$ eV/atom). This result confirms that *R*3*m* MoN_2 is definitively not a viable structure. Recently, Wu *et al.*[219]

proposed a nonmagnetic 2D T-type MoN_2 structure which contains octahedral Mo atoms. Our evolutionary searches locate the corresponding 3D T-type phase (space group *C2/m*) at 0.701 eV/atom higher in energy than the ground-state one. Moreover, its phonon dispersion curves present strong imaginary frequencies; thus, this octahedral Mo-containing layered structure is dynamically unstable.

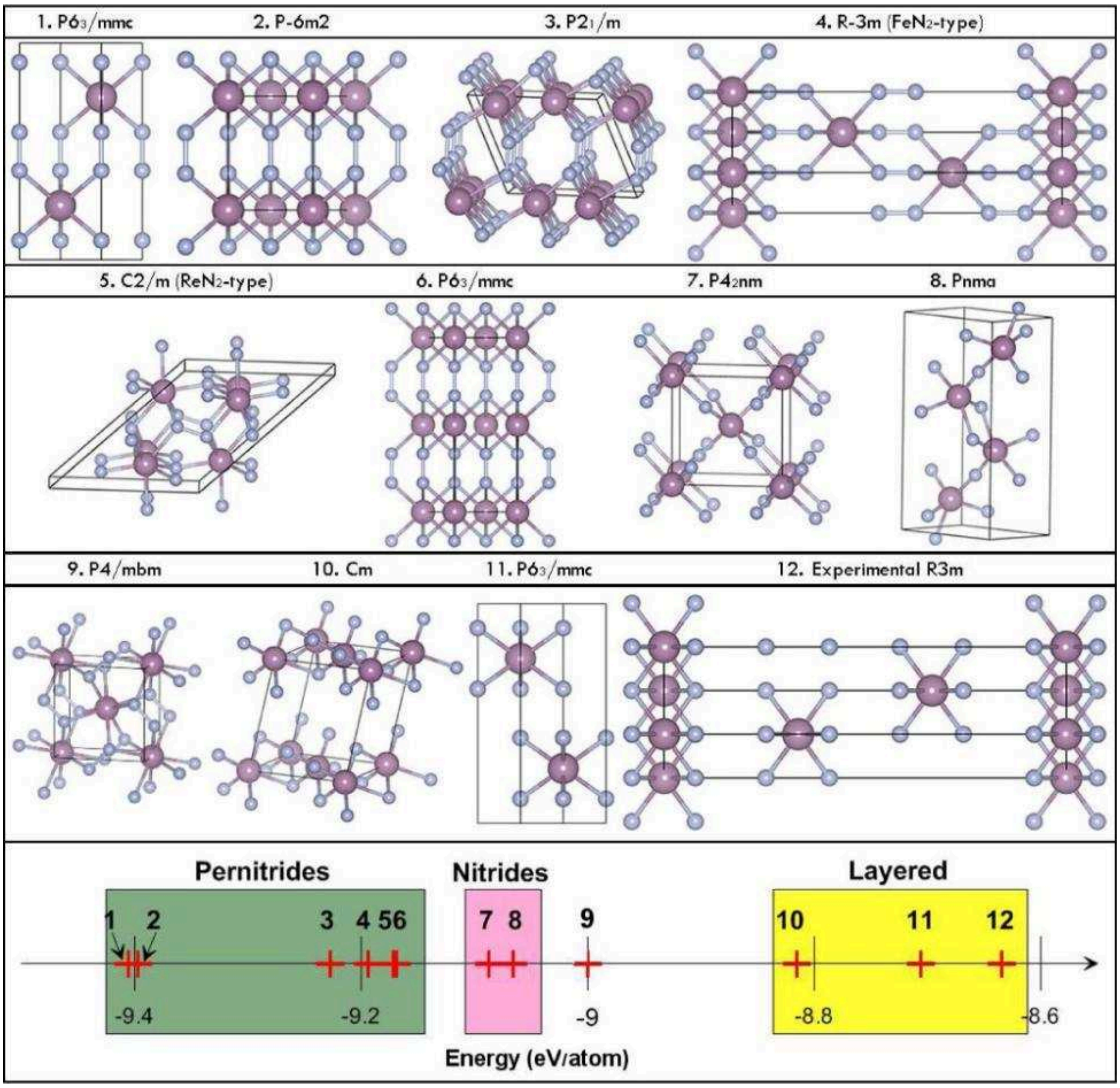

Figure 4.2 Predicted stable and metastable MoN_2 structures and their corresponding energies.

At atmospheric pressure, the lowest-energy MoN_2 phase adopts a NiAs-type hexagonal structure (*P6₃/mmc*, if one considers N_2 groups as a single entity, *Figure 4.3a*). Its calculated phonon spectrum indicates no imaginary phonon frequencies in the whole Brillion zone, which confirms its dynamical stability. This hexagonal *P6*$_3$*/mmc* structure may also be described as stacking of the MoS_2-type MoN_2 sheets formed by N-Mo-N sandwiches (Mo-N = 2.103 Å; Mo-Mo = 2.927 Å). These MoN_2 sheets exhibit an AB stacking sequence but layers are bound not by weak van der Waals interactions as found in MoS_2-type structures. They are linked to each other through covalent N-N bonds. Thus, *P6*$_3$*/mmc* MoN_2 contains discrete N_2 units, and is a transition metal pernitride. The molecular axis of N_2 is oriented parallel to the c axis, and the shortest N_2-N_2 separation is 2.504 Å.

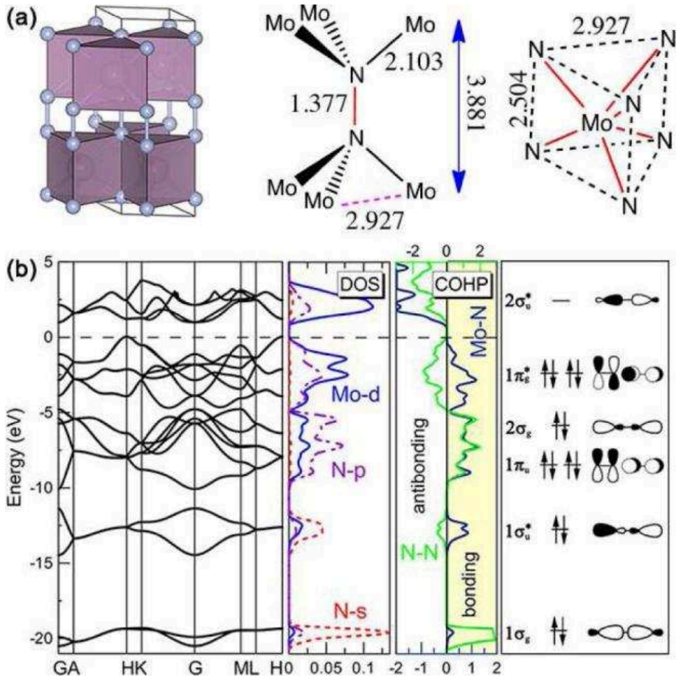

Figure 4.3 (a) Crystal structures of the ground-state *P6*$_3$*/mmc* MoN_2. (b) The corresponding band structure, DOS, and -COHP plots computed at 0 GPa. The right part shows a schematic molecular orbital energy level diagram of N_2^{4-} unit.

The calculated N-N distance of 1.377 Å is close to the value found in N_2H_4 (1.45 Å) and PtN_2 (1.41 Å) but much longer than that in N_2F_2 (1.21 Å) and BaN_2 (1.23 Å) where a formal N═N double bond is assigned. Therefore, one may assign to the dinitrogen unit a formal charge of -4 leading to the singly bonded N_2^{4-} diatomic species. With fourteen valence electrons N_2^{4-}

would be isoelectronic with F_2 (1.412 Å) and disulfide anion (S_2^{2-}), which is found in pyrite FeS_2 with four electrons in the antibonding $1\pi_g^*$ orbitals. Formally, one could assign MoN_2 as $Mo^{4+}(N_2^{4-})$, *i.e.*, Mo is a d^2 metal, in agreement with the experimental results of Wang *et al.*[1] They noticed "the determined valence state for Mo is +3.5..., inferring a peculiar $4d^{2.5}$ electronic structure."

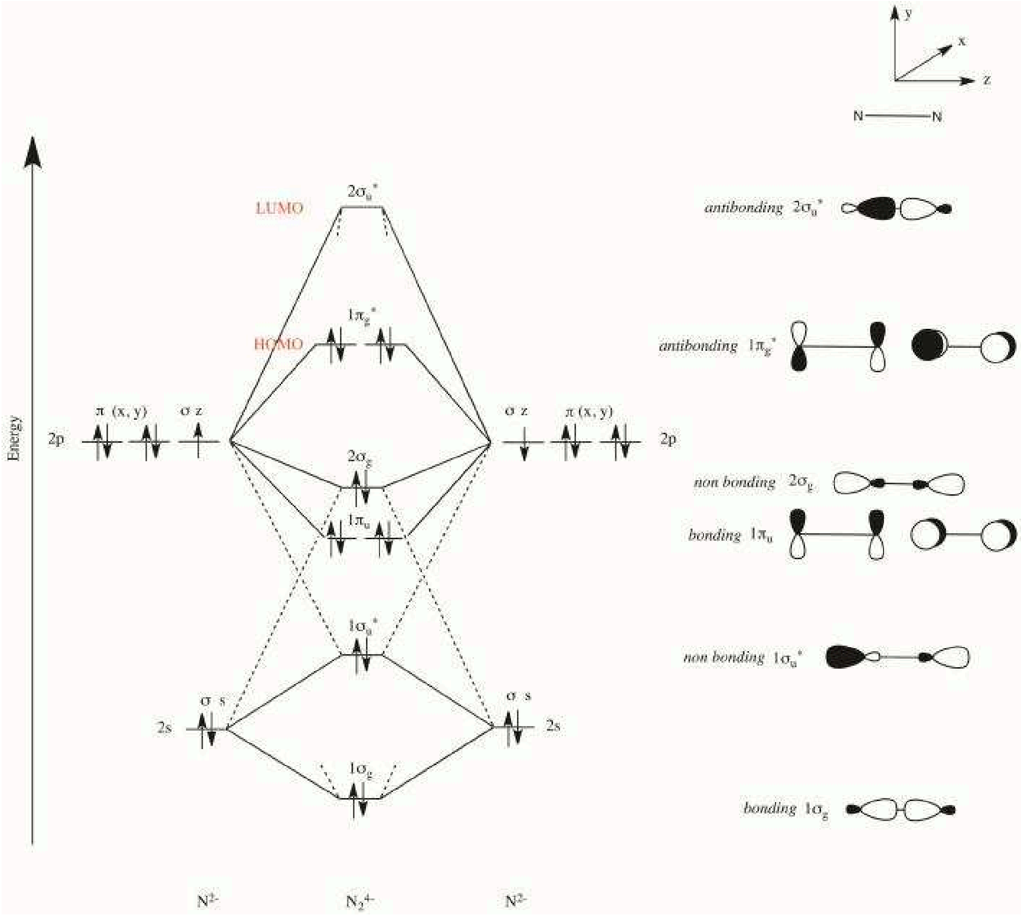

Figure 4.4 Schematic molecular orbital diagram of N_2^{4-}. The solid and dashed lines indicate the primary and secondary parentage of the orbitals, respectively (2s-2p$_z$ mixing). Only the valence orbitals are shown. N_2^{4-} anion has 14 valence electrons and the bond order is one.

To confirm these electron counting and oxidation state assignments, the electronic properties of *P*6$_3$*/mmc* MoN_2 were analyzed (*Figure 4.3*). Band structure and the density of states (DOS) show that the *P*6$_3$*/mmc* phase is a semiconductor. Around -20 eV, the lowest states are dominated by N-2s states and correspond mainly to the bonding $1\sigma_g$ orbitals of diatomic N_2 units (see the molecular orbital interaction diagram of N_2^{4-} in *Figure 4.4*). Between -12 and -14 eV, the states are the nonbonding out-of-phase $1\sigma_u$ orbitals, which interact strongly with d orbitals. Below the Fermi level, the states are dominated by strong orbital mixing between 4d Mo and 2p N orbitals. Notice that the 2p N states located between -5 eV and the Fermi level are occupied and the associated crystal orbitals possess N-N antibonding character. They correspond to the occupied $1\pi_g^*$ levels of the 14 electrons diatomic N_2^{4-} species.

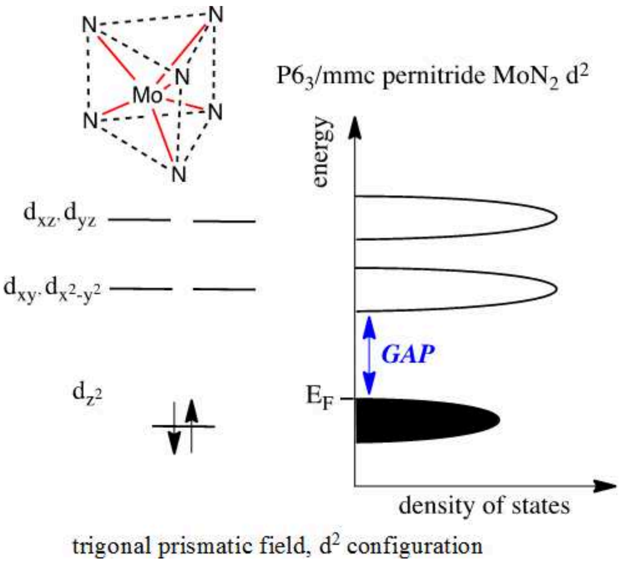

Figure 4.5 Crystal field splitting of the d levels of the Mo atoms (d^2 configuration) in a trigonal prismatic MoN_6 environment of the *P6₃/mmc* MoN_2. Each Mo atom is coordinated to six N atoms, forming a trigonal prismatic MoN_6 environment.

As mentioned previously, the formulation of $Mo^{4+}N_2^{4-}$ refers to a d^2 electron count for molybdenum atoms located in a trigonal prismatic coordination environment. According to crystal field theory, in a low-spin configuration -strong field ligands- these two d electrons occupy the d_z^2 orbital while the four remaining d orbitals must be empty and higher in energy (*Figure 4.5*). Because pernitride *P6₃/mmc* MoN_2 has a filled d_z^2 band and unfilled d_{xy}/d_x^2-$_y^2$ bands, MoN_2 should be a semiconductor, consistent with an energy gap found at the Fermi level (DOS, indirect gap, *Figure 4.3*). Moreover, an analysis of the chemical bonding between Mo and N in the crystal orbital Hamilton population (COHP) plots displayed in *Figure 4.3* shows that all bonding levels have been filled with electrons, and all Mo-N antibonding states show up in the unoccupied crystal orbitals, well above the Fermi level. With respect to Mo-N bonding and the octet rule for N_2^{4-}, *P6₃/mmc* pernitride structure is ideal.

Even though the formation enthalpy of *$P6_3/mmc$* MoN_2 is negative at 0 K and ambient pressure (ΔH_f = -0.297 eV/atom), this criterion is not sufficient to claim that the *$P6_3/mmc$* pernitride phase is thermodynamically stable. In fact, a thermodynamically stable compound must be more stable than any isochemical mixture of the elements or other Mo_xN_y stoichiometries at a given pressure. A truly stable structure must lie on the convex hull constructed on the plot of the formation enthalpy versus composition x = N/(N + Mo). For all possible phases of the Mo-N system, we generated the Mo-N convex hulls by using the variable-composition evolutionary algorithm combined with first-principles calculations and the results are shown in *Figure 4.6.* Formation enthalpies per atom of the Mo_xN_y phass.

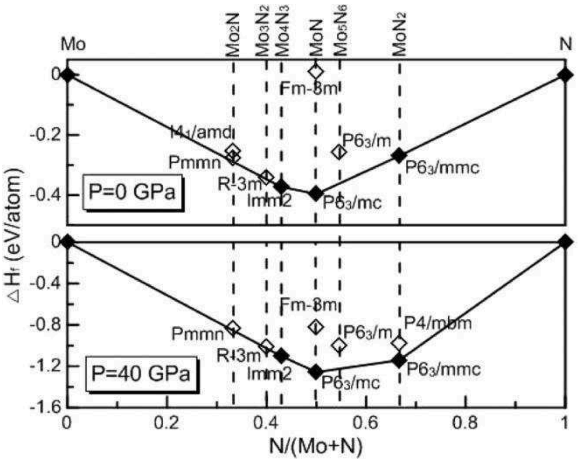

Figure 4.6 Convex hull diagrams of the Mo-N system at 0 and 40 GPa considering zero-point energy correction (solid squares, stable; open squares, metastable).

One may clearly see that, at both atmospheric pressure and 40 GPa, *$P6_3/mmc$* MoN_2 lies on the convex hull. Therefore, pernitride MoN_2 is a truly stable structure, stable against decomposition into its elements and other Mo_xN_y phases at both ambient and high-pressure conditions. Our predicted pernitride phase should stimulate experimentalists to look for its synthesis and characterization. Besides MoN_2 and the experimentally well-known *$P6_3/mc$*-MoN, we also found a stable compound Mo_4N_3 which crystallizes in the *Imm*2 symmetry, while Mo_2N, Mo_3N_2, and Mo_5N_6 are metastable in the whole studied pressure range (*Figure 4.7*).

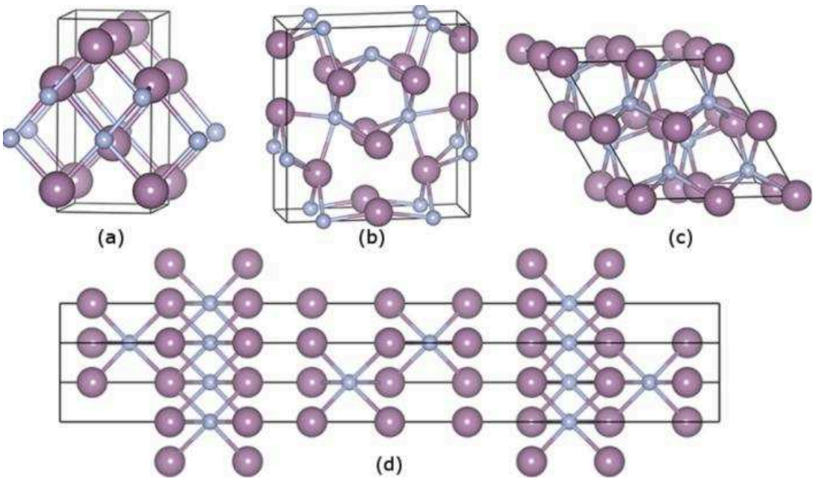

Figure 4.7 Crystal structures of the Mo_xN_y. (a) *Pmmn*-Mo_2N, (b) *Imm*2-Mo_4N_3, (c) $P6_3/mc$-MoN and (d) *R*3*m*-Mo_3N_2. The large purple and small blue spheres represent Mo and N atoms, respectively.

4.3.3 Pressure effect on MoN_2

As transition metal nitrides are usually experimentally obtained under high pressure, we studied the relative enthalpies of different MoN_2 structures compared with the experimental claimed *R*3*m* structure as a function of pressure. For comparison, the structures discussed in MoS_2-type ($P6_3/mmc$), OsN_2-type (*P6/mmm*),[220] *Cm*, and ReN_2-type (*C*2/*m*)[217] were considered in our study. The thermodynamic stability of MoN_2 with respect to decomposition into elemental Mo + N_2 and reactants MoN + 1/2N_2 was also discussed. The body-centered-cubic Mo (*Im*-3*m*), hexagonal MoN ($P6_3/mc$),[221] and depending on the applied pressures, α, $P4_12_12$, *cg* phases of N were chosen as reference states.[8,222]

It is seen from *Figure 4.8* that $P6_3/mmc$ pernitride is thermodynamically stable against decomposition into the mixture of Mo + N_2 or MoN + 1/2N_2 over the whole pressure range. The experimental *R*3*m* MoN_2 is thermodynamically unstable with respect to decomposition into Mo + N_2 below roughly 20 GPa. Moreover, it is seen that, for all phases with layered structures

($P6/mmm$, MoS_2-type $P6_3/mmc$, Cm, and $R3m$), their formation enthalpies are positive below 10 GPa and become negative under high pressure. However, they all have much higher enthalpies than our $P6_3/mmc$ pernitride phase and the MoN + $1/2N_2$ reactants over the whole pressure range, indicating their chemical instability. It is noteworthy that we also found a WN_2-type ($P6$-$m2$)[221] structure with enthalpy only 9 meV/atom higher at ambient pressure and 13 meV/atom at 100 GPa than the $P6_3/mmc$ MoN_2. Also, our calculations show that the fully optimized $R3m$ MoN_2 structure is nonmagnetic, thus considering the magnetic corrections will not affect the relative stability of MoN_2.

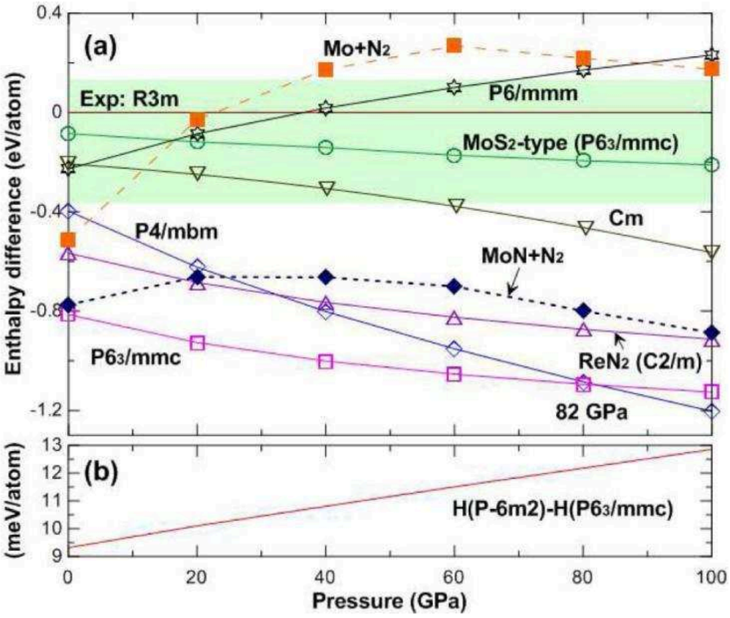

Figure 4.8 (a) The calculated enthalpy differences of various MoN_2 structures relative to the claimed $R3m$ structure as a function of pressure together with decomposition into the mixture of Mo+N_2 and MoN+$1/2N_2$. (b) Energy difference of P-6m2 and $P6_3/mmc$ structures as a function of pressure.

Previous studies proposed that the $P6/mmm$ structure is a universal ground-state structure for all MN_2 compounds at low pressures (M = Os, Ir, Ru, and Rh),[220] a statement that could not be applied for the MoN_2 system. Nevertheless, MoN_2 adopts the same tetragonal $P4/mbm$ structure proposed for these nitrides at high pressures, and it can be obtained through the phase transformation via the marcasite structure. Starting from ambient pressure, the NiAs-type $P6_3/mmc$ structure remains competitive up to 82 GPa. Above, we found the tetragonal $P4/mbm$

structure as a ground state (*Figure 4.8*). The calculated phonon spectrum of the predicted *P4/mbm* MoN$_2$ confirms its dynamical stability. The crystal structure of *P4/mbm* MoN$_2$ is shown in *Figure 4.9*. The *P4/mbm* phase contains MoN$_8$ edge-sharing cuboids stacking along the c axis with a Mo-N bond length of 2.091 Å at 100 GPa. Here we have N$_2$ dumbbells encapsulated in the slightly elongated Mo$_8$ cube. The N-N bond length is calculated at 1.324 Å at 100 GPa and 1.369 Å at atmospheric pressure, a value close to the one discovered in the *P6$_3$/mmc* structure (1.377 Å at 0 GPa). Thus, the singly bonded N$_2$ unit remains and the *P4/mbm* phase is also a pernitride structure.

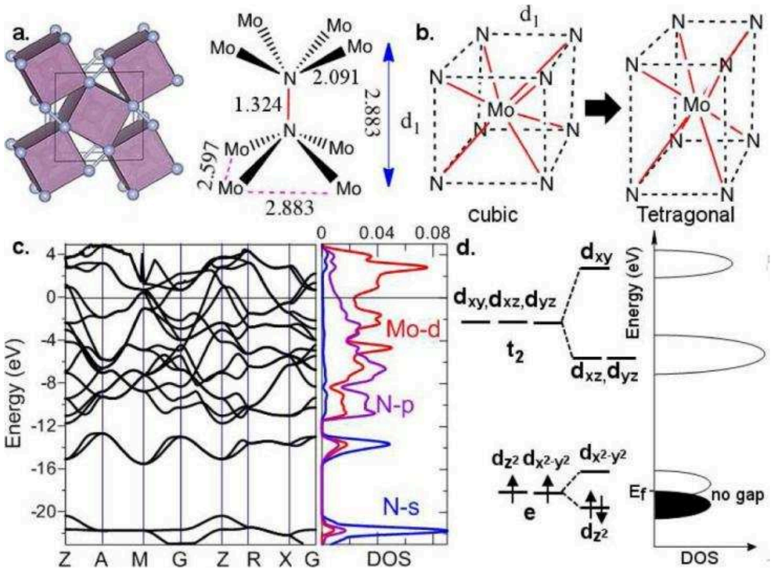

Figure 4.9 (a) Crystal structure of *P4/mbm* MoN$_2$ at 100 GPa. (b) Jahn-Teller elongation of the MoN$_8$ cuboids. (c) Band structure and DOS of *P4/mbm* MoN$_2$ at 100 GPa. (d) A schematic explanation of the crystal field splitting of the d$_{Mo}$ orbital.

The structural features of the *P4/mbm* MoN$_2$ are mirrored in the electronic properties, shown in *Figure 4.9*. As DOS in the pernitride *P6$_3$/mmc* phase, N$_2$ states are clearly identified in *P4/mbm* DOS: $1\sigma_g$ around -22 eV, $1\sigma_u^*$ at -14 eV, $1\pi_u$ levels between -7 and -11 eV, $2\sigma_g$ between -5 and -7 eV, and the fully occupied $1\pi_g^*$ located above the Fermi level. Consequently, for electron counting purposes, the dinitrogen unit should be formally considered as N_2^{4-}, a pernitride unit isoelectronic to F$_2$ molecules. Its electronic ground-state configuration is

$(1\sigma_g)2(1\sigma_u^*)2(1\pi_u)4(2\sigma_g)2(1\pi_g^*)4$ for 14 valence electrons, and its bond order is one (*Figure 4.4*). Note that the discrete N_2 units point directly toward the square faces of the eight-coordinate polyhedra of the molybdenum atoms (Mo-N bonding length is 2.091 Å at 100 GPa) and are perpendicular to each other in order to minimize the steric repulsion between the nitrogen σ-lone pairs (Pauli repulsions). Formally, this leaves the molybdenum atoms of MoN_2 in a d^2 configuration (Mo^{4+}). In a cubic crystal field, the five d orbitals split into doubly degenerate levels, $e(d_{z^2}, d_{x^2-y^2})$ and triply degenerate ones, $t_2(d_{xy}, d_{xz}, d_{yz})$, leading to half-filled e levels.

This degenerate electronic configuration e^2 is Jahn-Teller unstable: the cubic MoN_8 complexes should undergo a geometric distortion to remove this degeneracy. Effectively, a weak Jahn-Teller effect is observed in the *P*4*/mbm* phase (*Figure 4.9b*) with the N-N distances in tetragonal MoN_8 units 2.330 and 2.597 Å at 100 GPa. As the Jahn-Teller effect is very weak for a low-spin d^2 configuration, a small $d_{z^2}/d_{x^2-y^2}$ splitting occurs (*Figure 4.9d*). Nevertheless, the tetragonal *P*4*/mbm* phase is expected to be a metal due to the overlap of the filled d_{z^2} and unfilled $d_{x^2-y^2}$ bands, as confirmed by the calculated DOS (*Figure 4.9c*). Moreover, the covalent nature of the bonding is manifested by the significant penetration of the metal d levels into the nitrogen p block, and the Mo-N bonding states are all fully occupied while the antibonding ones are unoccupied. This electronic situation explains well the stability of ground-state *P*4*/mbm* under high pressure.

4.3.4 Mechanical properties

The mechanical properties of the MoN_2 structures were further studied. The elastic constants C_{ij}, bulk modulus B, shear modulus G, and Young's modulus E were calculated. We noticed that the calculated elastic constants of *P*6*3/mmc* and *P*4*/mbm* structures satisfy the mechanical stability criteria.[223] Furthermore, *P*6*3/mmc* MoN_2 possesses a remarkably high C_{33} value (952 GPa) which is comparable to diamond (C_{33} = 1079 GPa),[224] revealing its extremely high stiffness along the c axis, which could be well understood by the strong directional Mo-N and N-N covalent bonds along the c axis. On the basis of the Voigt-Reuss-Hill (VRH) approximation,[225,226] the calculated B and G of *P*6*3/mmc* MoN_2 are 338 and 206 GPa, respectively, comparable to OsN_2

(B = 353 GPa and G = 222 GPa) and IrN_2 (B = 333 GPa and G = 205 GPa).[217] The high-pressure *P4/mbm* structure has a comparable bulk modulus (B = 345 GPa) but exhibits a much larger shear modulus (G = 251 GPa) than OsN_2 and IrN_2.

Figure 4.10 illustrates the directional dependence of Young's modulus for the two novel MoN_2 structures. The degree of deviation of its shape from spherical indicates the degree of anisotropy. From *Figure 4.10*, one can find that the $P6_3/mmc$ structure is much more anisotropic than the *P4/mbm* structure, due to the N-Mo-N sandwich stacking and strong directional Mo-N and N-N covalent bonds along the c direction (large C_{33}). For tetragonal *P4/mbm* MoN_2, the comparable C_{11}, C_{22}, and C_{33} make Young's modulus more isotropic, consistent with the atomic arrangements in the two novel structures. Moreover, the Poisson's ratios υ for $P6_3/mmc$ and *P4/mbm* structures are 0.247 and 0.207, respectively, close to 0.2. A low Poisson's ratio results from directional bonds, which increases the shear modulus and limits the motion of dislocations, thereby increasing the material's hardness. The theoretical Vickers hardness H_v was estimated by using Chen's model,[227] $H_v = 2(\kappa^2 G)^{0.585} - 3$. The estimated hardness values for $P6_3/mmc$ and *P4/mbm* structures are 22.3 and 32 GPa, respectively, making them potentially interesting for applications as hard coating materials.

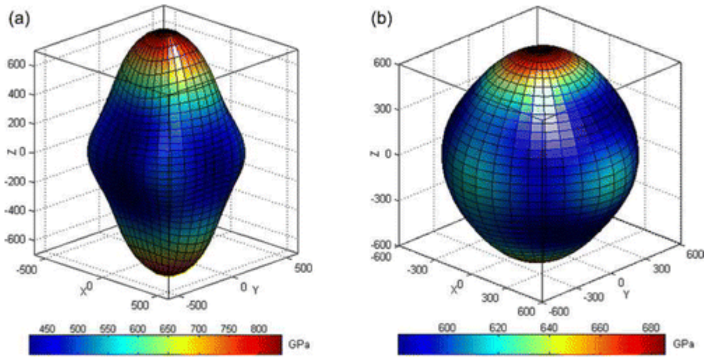

Figure 4.10 Directional dependence of Young's modulus for MoN_2 at ambient pressure: (a) $P6_3/mmc$; (b) *P4/mbm*.

4.3.5 Conclusion

In summary, we have found that the experimentally proposed MoS_2-type MoN_2 structure is unstable, as indicated by the negative C_{44} value, imaginary phonon frequencies, and positive enthalpy of formation based on first-principles calculations. By using the evolutionary methodology USPEX for crystal structure prediction, we have extensively explored the potentially stable structures of MoN_2 in the pressure range 0-100 GPa. Two energetically more stable pernitride phases were discovered. Enthalpy calculations demonstrate that the hexagonal $P6_3/mmc$ MoN_2 will transform into a tetragonal $P4/mbm$ structure above 82 GPa. The $P6_3/mmc$ phase is a narrow-gap semiconductor, while the high-pressure $P4/mbm$ structure is metallic. Both pernitride MoN_2 structures are mechanically and dynamically stable. The atmospheric ground-state structure has a high bulk modulus (B = 338 GPa) and shear modulus (G = 206 GPa), and is predicted to be a hard material. Further chemical bonding analyses reveal that the two MoN_2 structures incorporate a tetravalent metal (Mo^{4+}, d^2) and a N_2^{4-} species with a covalent N-N single bond.

4.4 Zr-N compounds

According to the phase diagram provided by Gribaudo *et al.*[210], ZrN and Zr_3N_4 can be stable at ambient conditions. In 2003, c-Zr_3N_4 with a Th_3P_4 structure was synthesized by Zerr *et al.*[201] using diamond-anvil cell experiments at 16 GPa and 2500 K. This compound was expected to exhibit a very high Vickers hardness around 30 GPa, similar to that of γ-Si_3N_4. However, Kroll showed that hardness is just slightly harder than 14 GPa.[209] Besides c-Zr_3N_4, an orthorhombic *Pnma* modification of Zr_3N_4 has been proposed. First-principles calculations show that *o*-Zr_3N_4 are energetically more stable than c-Zr_3N_4. However, both structures are metastable considering decomposition into ZrN and N_2. Besides, two nitrogen-rich phases ZrN_x ($1.06 < x < 1.23$) with NaCl-type structures was claimed by Juza *et al.*[206] in 1964. However, precise stoichiometries and crystal structures are not known for their synthesized samples. Here, we apply recently developed evolutionary algorithm USPEX to extensively explore the crystal structures and stoichiometries in the Zr-N system at ambient conditions, and then their phase stability at finite temperatures are evaluated.

4.4.1 Phase stability of the Zr-N system at finite temperatures

Thermodynamic stability of zirconium nitrides in the temperature range of 0-2000 K was quantified by constructing the thermodynamic convex hull, which is defined as the Gibbs free energy of formation of the most stable phases at each composition:

$$\Delta G(Zr_xN_y) = [G(Zr_xN_y) - xG(Zr) - yG(N)]/(x + y)$$

Any phase located on the convex hull is considered to be thermodynamically stable (at $T = 0$ K, $G = H$) and at least in principle synthesizable.[210] In the case of zirconium nitrides, a series of stable compounds at various Zr:N ratios, *i.e.,* 2:1, 4:3, 6:5, 8:7, 1:1, 15:16, 7:8, 4:5 have been discovered by our evolutionary searches at 0 K, shown in *Figure 4.11.* The rocksalt ZrN with space group (SG) *Fm*-3*m* was found to have the lowest enthalpy of formation. Besides ZrN, substoichiometric Zr_2N (SG: $P4_2/mnm$), Zr_4N_3 (SG: *C*2/*m*), Zr_6N_5 (SG: *C*2/*m*) and Zr_8N_7 (SG: *C*2/*m*) have also been found to be thermodynamically stable. For the missing composition Zr_3N_2, the lowest-energy structure is *Immm* with the enthalpy of formation lying very close to the convex hull at only 0.005 eV per atom, *i.e.,* Zr_3N_2 is a metastable phase at 0 K.

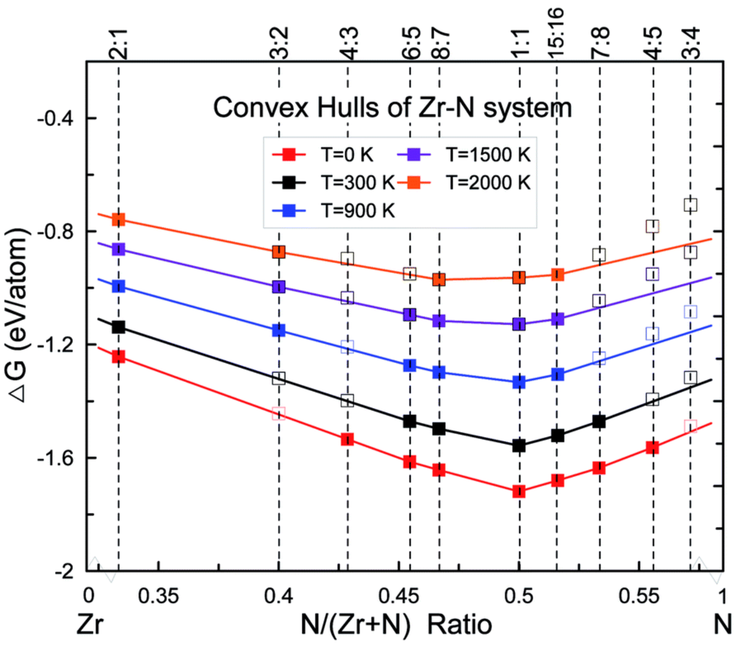

Figure 4.11 Convex hulls of the Zr-N system in the temperature range of 0-2000 K at ambient pressure. The solid squares represent stable structures, while open ones denote metastable structures. The solid *P6₃/mmc* phase of Zr, α-N_2 (T = 0 K) and N_2 gas (T ≥ 300 K) were adopted as reference states.

Additionally, Juza *et al.* in 1964 have discovered two nitrogen-rich phases with rocksalt structures. Unfortunately, detailed stoichiometries and crystallographic information were not determined. From our evolutionary searches, we found these two compounds could be $Zr_{15}N_{16}$ (x = 1.07, SG: *P*-1) and Zr_4N_5 (x = 1.25, SG: *C2/m*). Their structures are composed of edge-sharing ZrN_6 and $□N_6$ (□ means Zr vacancy) octahedra, similar to the rocksalt ZrN structure. To the best of our knowledge, such nitrogen-rich nitrides have never been reported in other TM-N systems. For Zr_3N_4, the most stable structure has the orthorhombic *Pnma* symmetry,[228] which is energetically more favorable than the Th_3P_4-type structure by 0.019 eV per atom at 0 GPa and 0 K. We found it is thermodynamically metastable considering decomposition into ZrN and N_2 at ambient conditions. First-principles calculation shows that *o*-Zr_3N_4 will transform into *c*-Zr_3N_4 at 2 GPa.

We have carefully calculated the temperature contribution to the phase stability of the new discovered zirconium nitrides from 0 K to 2000 K within the quasiharmonic approximation, as shown in *Figure 4.11*. Note that for each stoichiometry, the space group/structure found at 0 K is kept at higher temperatures. The free energies of formation increase with increasing temperatures for all phases but at different rates, yielding a convex hull which changes with temperature. Our results show that Zr_2N, Zr_8N_7, ZrN and $Zr_{15}N_{16}$ will not lose their stability in the whole studied temperature range. The unstable Zr_3N_2 at 0 K will become stable at temperatures higher than 900 K, while for Zr_4N_3, Zr_6N_5, Zr_7N_8 and Zr_4N_5, the temperature contributions have a negative effect on their structural stability. For example, the formation enthalpy of reaction

$$2Zr_4N_5\ (s) = 8ZrN\ (s) + N_2\ (g)$$

will become negative above 300 K, which means Zr_4N_5 should decompose into ZrN and N_2 gas at roughly room temperature if associated kinetic barrier allows this process, perfectly consistent with the results of Juza *et al.*[206]

Crystal structures of the representative zirconium-rich Zr_6N_5 and nitrogen-rich Zr_4N_5 are schematically shown in *Figure 4.12*. No imaginary phonon frequencies are found, indicating their dynamical stability. The computed lattice parameters for ZrN and Zr_3N_4 are in good agreement with those obtained from other theoretical and experimental investigations, which confirms the accuracy of our calculations. From the structural point of view, ZrN has the ideal cubic rocksalt structure, while $Zr_{n+1}N_n$ (n = 2, 3, 5, 7) and Zr_mN_{m+1} (m = 4, 7, 15) are versions of the rocksalt structure with ordered nitrogen or zirconium vacancies (Zr_2N has rutile-type structure).

In the structures of Zr-rich phases, the metal atoms form hexagonal close-packed (hcp) sublattices with N atoms filled in the octahedral voids, thus each N atom is coordinated by six Zr atoms, forming NZr_6 octahedra. However, the concentration of filled octahedral voids in various $Zr_{n+1}N_n$ structures is different. Two thirds of them are filled in Zr_3N_2; while seven eighths in Zr_8N_7. Similar nitrogen vacancy-ordered structures were also reported earlier to be stable for transition metal carbides $M_{n+1}C_n$ (M = Hf and n = 2, 5;[229] M = Zr and n = 1, 2, 3, 6;[229] M = Ti and n = 1, 2, 5)[230] and nitrides $M_{n+1}N_n$ (M = Ti and n = 1, 2, 3, 5).[231] For N-rich phases, one eighth of the metal atoms are replaced with vacancies in Zr_7N_8, while one fifth in Zr_4N_5.

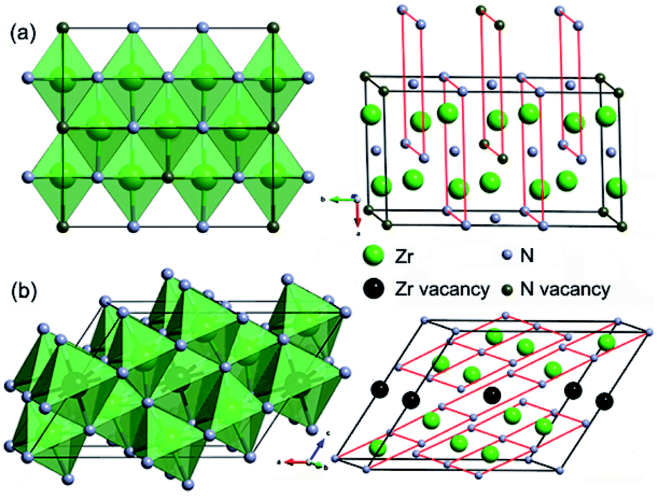

Figure 4.12 Crystal structures of the representative (a) Zr_6N_5 and (b) Zr_4N_5 compounds.

The formation of such N-rich phases could be attributed to the enhanced stability of the +4 oxidation state of Zr and Hf compared to Ti due to the relativistic effects, leading to the coexistence of +3 in MN and +4 in M_3N_4, while in the Ti-N system, TiN has the highest nitrogen content under normal conditions. In the structures of Zr_3N_4, the hcp metal framework of the rocksalt structure is significantly distorted. For o-Zr_3N_4, there are three nonequivalent types of Zr atoms, one of them is octahedrally coordinated to six N atoms, one resides at the center of a trigonal prism, and the last one is located inside of a heavily distorted octahedron. Thus, the second and third nonequivalent Zr atoms are sevenfold coordinated, while in *c*-Zr_3N_4, each Zr atom is coordinated to eight N atoms.

4.4.2 Electronic properties and chemical bonding

We calculated the electronic properties (density of states, DOS, See *Figure 4.13*) of zirconium nitrides at ambient conditions in order to study their chemical bonding. Let us start first with Zr_3N_4 and then discuss the effect of zirconium or nitrogen vacancies on the electronic properties of rocksalt based-structures. In DOS of *o*-Zr_3N_4 displayed in *Figure 4.13a*, three main regions may be described with three kinds of molecular orbital overlaps: nonbonding, bonding and antibonding.[231] Firstly, a rather sharp peak at roughly -13 eV appears and it is mainly of N(2s) character although with some Zr(4d) character. This sharp peak reflects the localized character of the nonbonding N(2s)-based levels; secondly, from -6 eV to 4 eV, a very broad structure with two well-defined main peaks originates from mixing of Zr(4d) and N(2p) orbitals. The lower peak corresponds to the bonding states, and the antibonding counterparts appear just above the Fermi level. These bonding and antibonding peaks exhibit a clear mixing of metal 4d and nitrogen 2p states, although the latter has a stronger Zr(4d) character. In o-Zr_3N_4, the gap separates bonding and antibonding states, thus Zr_3N_4 is a semiconductor and possesses a remarkable stability. Its calculated band gap (0.68 eV) is consistent with previous theoretical results.[209,232] These findings are understandable if one considers the following Zintl picture: Zr is in a formal oxidation state of +4 (Zr^{4+}, d^0), and N^{3-} follows the octet rule.

For the well-known stoichiometric rocksalt Zr_xN_y, we will first briefly discuss their electronic properties, then analyze the electronic perturbation due to the creation of nitrogen or zirconium vacancies - empty octahedral sites in the fcc network - leading to symmetry-broken $Zr_{n+1}N_n$ and Zr_mN_{m+1} structures. Similarly to *o*-Zr_3N_4, DOS of Zr_xN_y phases can be decomposed into three well-separated energy regions as shown in *Figure 4.13*, but here no gap separates the valence and conducting bands: (1) a deep lowest valence band, s_N; (2) hybridized Zr(4d)/N(2p) band, d_Mp_N; (3) a partially filled higher-energy Zr(4d) band, d_M. The s_N band is dominated by the 2s orbitals of the nitrogen atoms and is nonbonding. The next group of valence bands, d_Mp_N, results from strong hybridization of the 4d states of zirconium atoms with 2p states of nitrogen atoms. Also, one may see that for Zr_xN_y the bottom of the d_M band, dominated by 4d orbitals of zirconium atoms, responsible for metallicity.

When nitrogen vacancies are created in substoichiometric $Zr_{n+1}N_n$ (n = 1, 2, 3, 5 and 7), notice that obviously the formal oxidation state of Zr decreases as the number of nitrogen vacancies increases, going from Zr^{3+} d^1 in ZrN to $Zr^{1.5+}$ $d^{2.5}$ in Zr_2N. Therefore, one may expect the occupation of the Zr 4d levels in substoichiometric $Zr_{n+1}N_n$ compounds. This is what happens: Zr-Zr bonding and nonbonding (slightly antibonding) Zr-N levels appear just below the Fermi level, mainly metal 4d in character (See *Figure 4.13d*). In $Zr_{n+1}N_n$, Zr atoms are no longer all in the MN_6 octahedral environment; some of them are in MN_5 square pyramidal configurations.

Therefore, one may expect the stabilization of antibonding Zr-N levels when going from formally octahedral ZrN_6 to square pyramidal ZrN_5 environment due to the lack of a Zr(4d)-N(2p) antibonding component. The occupation of these Zr-N nonbonding levels may explain the mechanical properties of these substoichiometric $Zr_{n+1}N_n$ compounds.

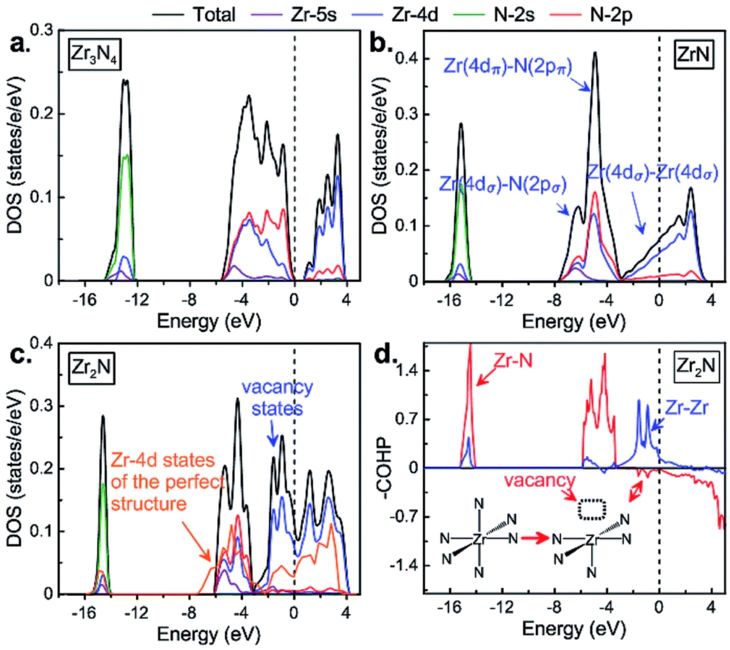

Figure 4.13 The calculated electronic density of states of (a) o-Zr_3N_4, (b) ZrN and (c) Zr_2N. (d) Crystal orbital Hamilton population (-COHP) curves of Zr_2N.

Figure 4.13c displays the total and projected DOS of Zr_2N, but also the projected d states of a hypothetical ZrN structure within the Zr_2N structure (all N vacancies are filled in the so-called perfect structure). One can see that nitrogen vacancies give rise to additional states just below the Fermi level compared to its corresponding perfect structure, which originates from the Zr-Zr bonds passing through a nitrogen vacancy site. Such “vacancy states” usually lead to a drastic increase in the density of states at the Fermi level (0.076 in ZrN; 0.090 in Zr_6N_5; 0.112 in Zr_2N, states per eV per electron). The increasing density of the d state at the Fermi level can be interpreted as an increase in the $Zr(4d_\sigma)$-$Zr(4d_\sigma)$ bonding or metallic bonds between the zirconium atoms.

4.4.3 Conclusion

By using the variable-composition *ab initio* evolutionary algorithm USPEX, we explored stable and metastable compounds in the Zr-N system at ambient pressure. Our calculations revealed that ZrN, Zr_2N, Zr_4N_3, Zr_6N_5, Zr_8N_7, $Zr_{15}N_{16}$, Zr_7N_8 and Zr_4N_5 are thermodynamically stable compounds at low temperatures, while Zr_3N_2 is marginally metastable and could be stable at high temperatures. Particularly, we found the two controversial compounds discovered by Juza *et al*. could be $Zr_{15}N_{16}$ and Zr_4N_5. The newly discovered compounds have defective rocksalt structures with ordered nitrogen or zirconium vacancies. Besides, we found hardness of bulk Zr_3N_4 is below 15 GPa.

5. Silica-like compounds under pressure: $GaPO_4$ and SiS_2

5.1 Pressure-induced transitions in $GaPO_4$

The discovery of the pressure-induced amorphization of α-quartz at pressures above 15 GPa[233] generated a great deal of interest in the origin of this phenomenon, which has been the subject of numerous experimental and theoretical studies. Amorphous material has also been reported to be present in addition to high-pressure crystalline phases,[234] which highlights the competition between transitions to crystalline and amorphous forms[235] and the different transition pathways available at high pressure, many involving metastable states. α-quartz homeotypes (GeO_2, BeF_2, PON, ABO_4: A = B, Al, Ga, Fe; B = P, As) provide models for the high-pressure behavior of silica and are also potential new materials with improved properties (*e.g.*, piezoelectrics).[236] Starting from the α-quartz- or α-berlinite-type structure (space group $P3_121$, Z = 3) for AO_2 or ABO_4 compounds, respectively, transitions to amorphous and/or crystalline phases have been reported for various α-quartz homeotypes.[236,237] In the case of $FePO_4$,[238] for example, simultaneous transitions to a $CrVO_4$ structure and an amorphous form were observed at 2.5 GPa. This $CrVO_4$ structure with mixed 6:4 cation coordination is also the stable high-pressure form for $AlPO_4$ and $GaPO_4$;[238–240] however, thermal activation is often necessary to obtain this form. The $CrVO_4$-type form is also obtained at room temperature from α-cristobalite-type $GaPO_4$;[241] however, the behavior at ambient temperature starting with the α-berlinite-type form is less clear with the materials obtained at high pressure not always being well crystallized.[242–245] Several solid solutions exist between α-quartz homeotypes. In the case of the $AlPO_4$-$GaPO_4$, an x-ray diffraction study indicated that there is complete static Al/Ga disorder, which may open the way to design materials with tunable piezoelectric properties.[246–248] Up to the present, it is not known what influence preexistent static disorder has on the competition between transitions to crystalline or amorphous high-pressure phases.

Therefore, in this work, we cooperated with the experimental group and indicated, in addition to the presence of a $CrVO_4$-type phase, the formation of a new, unidentified, poorly crystallized phase in the Ga-rich region of the $AlPO_4$-$GaPO_4$ solid solution.[249] The combined use of x-ray absorption spectroscopy (XAS) and x-ray diffraction (XRD) as a function of pressure and temperature along with Raman scattering and first-principles calculations in the present study has enabled us to better understand the competition between this new phase and other crystalline or amorphous forms. The detail of experiments can be found in the appendix.

5.1.1 Computational details

To identify the (meta)stable structures in the $GaPO_4$ system, we have employed the first-principles evolutionary structure prediction method USPEX. [8,13,30] It searches for the global minimum of free energy of the crystal concerning its structural parameters. At a given pressure ($P = 5$ and 20 GPa), a fixed stoichiometry crystal structure search is performed using up to 4 formula units per primitive unit cell. The first generation had 80 randomly produced candidate structures; all subsequent generations contained 60 structures. Evolutionary variation operators were applied to search for the global energy minimum; 50% of the new structures were produced by heredity, with the remaining structures were produced by atomic mutation (10%), lattice mutation (10%), permutation (10%), and random generator (20%). Density functional total energy calculations and geometry optimizations were performed using the VASP program[48] with the Perdew-Burke-Ernzerhof parametrization of the generalized gradient approximation (GGA/PBE).[41] We used projector-augmented wave (PAW) potentials[49] for Ga (Ga_d), P, and O with radii 2.3 a.u. for Ga ([Ar] core), 1.9 a.u. for P ([Ne] core), and 1.52 a.u. for O ([He] core). A plane-wave basis set with a kinetic energy cutoff of 520 eV was employed. We used uniform Γ-centered meshes with a reciprocal space resolution of $2\pi \times 0.06$ Å^{-1} for Brillouin zone sampling to ensure the error bars of the total energies were less than 1 meV/atom. Structure relaxations proceeded until all forces on atoms were less than 1meV/Å and the total stress tensor had deviations from target pressure within 0.01 GPa.

5.1.2 Results and discussions

5.1.2.1 Compression of the α-berlinite-type phase and high-pressure phase transition

From the experiment of view, the initial compression behavior of the α-berlinite-type phase ($P3_121$) was in good agreement with previous work.[249] Beginning at between 9 and 12 GPa, new diffraction features were observed (*Figure 5.1*). A new crystalline phase was obtained, which was characterized by broad diffraction lines with a highly inhomogeneous intensity distribution in the 2D diffraction images indicating poor crystallinity and strongly preferred orientation effects. This renders structural determination difficult. The most prominent diffraction lines of this phase at 21 GPa and are distinct from those expected for an orthorhombic $CrVO_4$-type structure. However, above 20 GPa, some very weak diffraction lines at positions where those of an orthorhombic $CrVO_4$-type form could be expected were observed. This phase remained at an impurity level concerning the new unidentified phase even after heating to 340 ℃ at 25 GPa. Upon pressure release, the sample retransformed to the α-berlinite-type phase. To determine the effect of temperature on the competition between these two structures $GaPO_4$ was studied isothermally at 320 ℃ up to 32 GPa. New diffraction features appeared beginning near 9 GPa, which is slightly lower than in previous ambient-temperature studies. Again, the data exhibited poor crystallinity and strong preferred orientation. However, in contrast to $Al_{0.3}Ga_{0.7}PO_4$, strong diffraction features corresponding to the orthorhombic $CrVO_4$-type form were observed in addition to the principal lines of the new unidentified phase observed for the solid solution. The unit cell of the $CrVO_4$-type form at 32GPa and 320 ℃ was refined, and the following values obtained: space group *Cmcm*, a = 5.157(17) Å, b = 7.030(14) Å, c = 5.680(12) Å. This is consistent with previous measurements on this phase.[240,241,250] The pressure was decreased to 15 GPa at 320 ℃ and then final decompression was performed at ambient temperature. On pressure release, a mixture of the berlinite-type and these two high-pressure phases was retained.

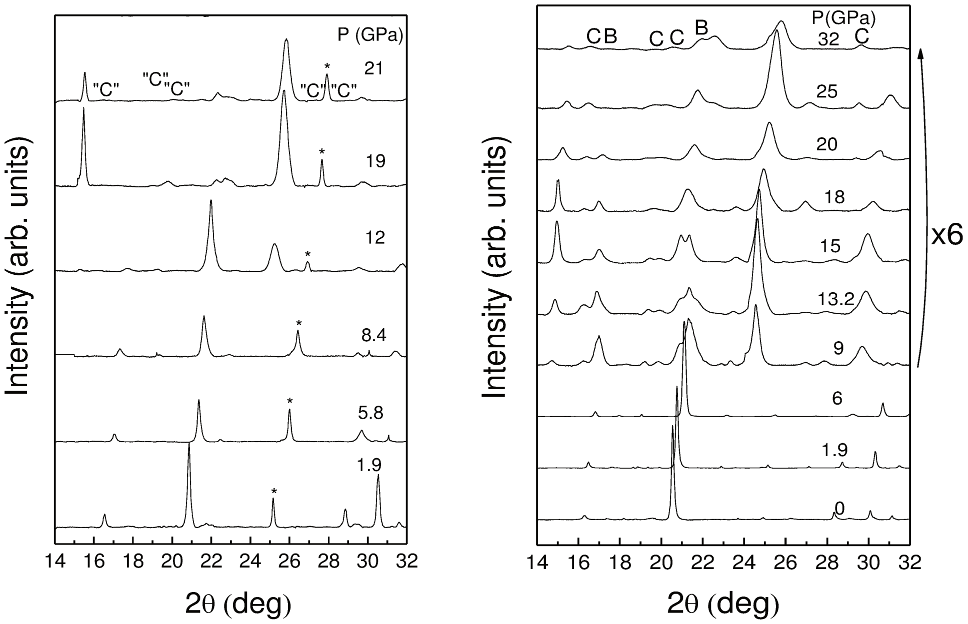

Figure 5.1 (a) X-ray diffraction patterns of $Al_{0.3}Ga_{0.7}PO_4$ at 25 °C (left), (b) $GaPO_4$ at 320 °C (right) as a function of pressure on compression. (* = NaCl pressure calibrant, B = remaining berlinite-type $GaPO_4$, C = $CrVO_4$-type $GaPO_4$, "C" = expected positions for $CrVO_4$-type $Al_{0.3}Ga_{0.7}PO_4$).

The XAS spectra of $Al_{0.3}Ga_{0.7}PO_4$ and $GaPO_4$ obtained at ambient pressure are in good agreement with spectra of α-berlinite-type $GaPO_4$ reported in the literature.[251] At high pressure, the spectra bear some resemblance to those of α-Ga_2O_3, in which Ga is in 6-fold coordination, thereby providing evidence for an increase in the coordination number of gallium from 4 to 6 as has been reported previously.[244] More quantitative information confirming this increase in coordination number can be obtained by analysis of the EXAFS data. As expected, the Ga-O bond distance in $GaPO_4$ undergoes initial compression prior to the phase transition. Fitting the data for $GaPO_4$ above the phase transition at 11.4 GPa was possible taking into account two contributions corresponding to 4 oxygen atoms at 1.759 Å and 6 at 1.883 Å in a 45:55 ratio. The ratio was calculated based on the amplitudes arising from the two different coordination environments normalized by the number of atoms in the first shell. The corresponding fit at 30 GPa gives 4 oxygen atoms at 1.73 Å and 6 at 1.866 Å in a 30:70 ratio. Based on the diffraction data, the contribution corresponding to 4-fold coordination can be assigned to remaining α-berlinite-type material, whereas the 6-fold coordination contribution is due to the high-pressure phases. The increase in Ga-O bond length, by about 7% due to the increase in coordination number of gallium from 4 to 6 is consistent with previous work on $GaAsO_4$ at high pressure.[237,244]

5.1.2.2 First-principles evolutionary crystal structure prediction

We used the evolutionary algorithm USPEX to investigate candidates for high-pressure (meta)stable structures of gallium orthophosphate ($GaPO_4$). We performed fully unconstrained variable-cell USPEX simulations at 5 and 20 GPa, using no experimental information such as lattice parameters, space group symmetry, etc. Among the predicted structures at 5 and 20 GPa, the structures with the lowest enthalpies are used to investigate their relative stability as a function of pressure (See *Figure 5.2*). Lattice constants and structural parameters of the most interesting candidate structures are given in the *Appendix*.

Table 5.1 Lattice parameters of *Cmcm* phase at 32 GPa.

Pressure	Source	Lattice parameters
32 GPa	USPEX	a =5.104, b = 7.132, c = 5.792 α = β = γ = 90°
32 GPa	Experiment	a =5.157, b = 7.030, c = 5.680 α = β = γ = 90°

Note that the calculated lattice constant of the $CrVO_4$-type Cmcm phase at 32 GPa (T = 0 K) is in excellent agreement with the experimental value (T = 593 K), which gives a benchmark of the typical accuracy to expect of density functional theory (DFT) simulations for this system (See Table 5.1).

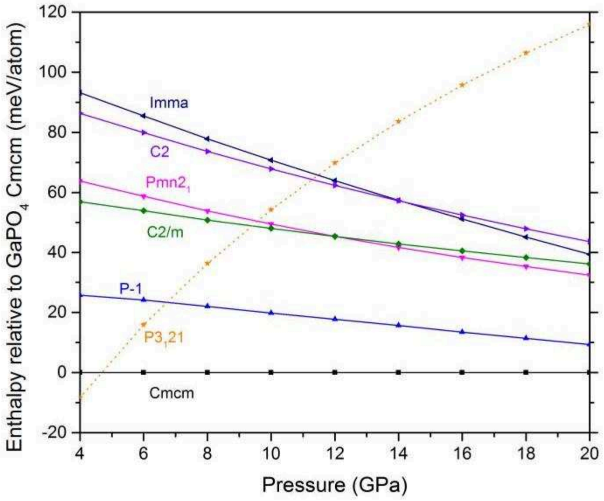

Figure 5.2 Static ground-state enthalpies (per atom) of various $GaPO_4$ structures relative to the $CrVO_4$-type *Cmcm* phase as a function of pressure. Structures contain 4-coordinated (dashed line) or 6-coordinated Ga atoms (solid lines).

Our theoretical study indicates that the $CrVO_4$-type form of $GaPO_4$ (space group *Cmcm*) has the lowest enthalpy (G = H at T = 0 K) from roughly 5 to at least 20 GPa. At 5 GPa, we note a tiny enthalpy difference between orthorhombic *Cmcm* and *α*-berlinite-type $P3_121$ phases. Our calculated phase transition pressure from $P3_121$ to *Cmcm* is 4.7 GPa at T = 0 K, but one has to be reminded that the possibility of a large kinetic barrier for the *α*-berlinite-type $P3_121$ phase to *Cmcm* phase transformation has to be considered. Even if the *Cmcm* phase is calculated to be ground state at 5 GPa, higher pressure and/or thermal activation may be needed to reach it. As shown in *Figure 5.2*, the *α*-berlinite-type phase $P3_121$ becomes thermodynamically unstable relative to all proposed low-enthalpy structures when external pressure is higher than roughly 12 GPa. Recall that the $P3_121$ phase contains 4-fold coordinated Ga atoms (GaO_4 units) while the other predicted structures possess octahedral GaO_6 units. The PO_4 tetrahedra remain unaltered from 4 to 20 GPa, in agreement with the well-known rigidity of these PO_4 units. As we are looking for metastable phases at high pressure, we focus our attention on the low-enthalpy structures located on the potential energy surface of $GaPO_4$ at 20 GPa. At 20 GPa, the second lowest structure is *P*-1, located at +9 meV/atom (+20 meV/atom at 10 GPa) from *Cmcm*. This phase becomes lower in energy than *Cmcm* above 30 GPa. This *P*-1 structure consists of stacked infinite chains of edge-sharing distorted GaO_6 octahedra and the linkage between GaO_6-based chains is made by PO_4 tetrahedra (See Figure 5.3).

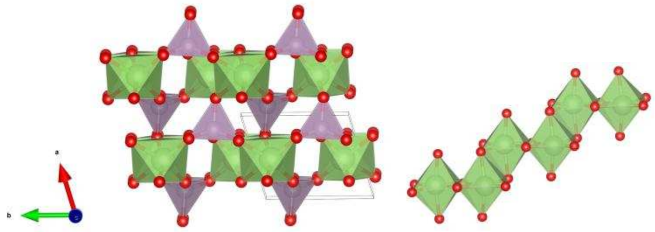

Figure 5.3 *P*-1 $GaPO_4$ crystal structure and GaO_6-based chains in *P*-1 phase at 20 GPa.

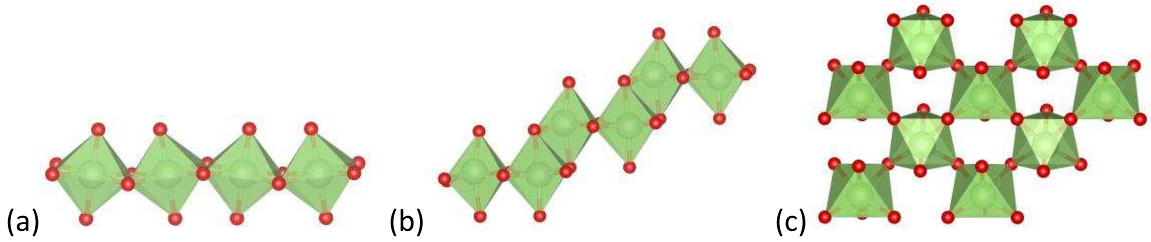

Figure 5.4 GaO_6 based motifs encountered in computed low-enthalpy structures of $GaPO_4$ at 20 GPa. (a) edge-sharing, (b) linked pairs of edge-sharing, and (c) layer of corner-sharing GaO_6 octahedra.

At 20 GPa, four other low-enthalpy structures are located in the energy range from +32 to +43 meV/atom to the ground state *Cmcm*, namely *Pmn*2_1, *C2/m*, *Imma*, and *C*2 structures. As previously mentioned, all of them contain 6-fold coordinated gallium and 4-fold coordinated phosphorus atoms. These structures mainly differ by the connectivity of the GaO_6 octahedral building units (See *Figure 5.4*). *Cmcm*, *C*2/*m*, and *Imma* structures are built up of chains of edge-sharing GaO_6 octahedra. *P*-1 and *C*2 Ga-O networks contain linked pairs of edge-sharing GaO_6 octahedra which form infinite chains. Finally, layers of corner-sharing GaO_6 octahedra are present in *Pmn*2_1 structure. Our evolutionary crystal structure searches lead to four competitive metastable structures for $GaPO_4$ at 20 GPa. In the next section, we will turn our discussion to the comparison of theoretical x-ray diffraction patterns obtained from our *in silica* high-pressure metastable crystal structures with experimental XRD results.

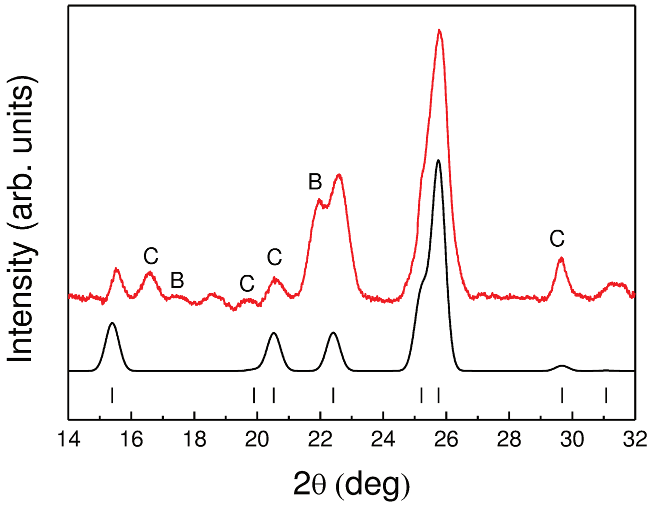

Figure 5.5 Experimental (above) X-ray diffraction pattern of $GaPO_4$ at 32 GPa and 320°C and calculated pattern using the refined experimental unit cell parameters and the fractional atomic coordinates of the *Pmn*2_1 structure from first-principles calculations (below). Vertical bars indicate the refined positions of the Bragg reflections. (B = remaining berlinite-type $GaPO_4$, C = $CrVO_4$-type $GaPO_4$).

5.1.2.3. Nature of the metastable high-pressure phase

In addition to the stable $CrVO_4$-type phase, which was already identified by x-ray diffraction, the five higher enthalpy structures built up from GaO_6 octahedra and PO_4 tetrahedra obtained in the USPEX search at 20 GPa were considered as potential candidates for the new metastable phase of $GaPO_4$. The diffraction patterns of all these structures were calculated. Only one structure gave rise to a diffraction pattern that bore any similarity to the experimental data (See *Figure 5.5*).

This was the orthorhombic *Pmn*2_1 structure with calculated lattice parameters of a = 5.479 Å, b = 4.529 Å, and c = 4.408 Å at 20 GPa. Using this structural model, the experimental data could be readily indexed, and the unit cell refined giving a = 5.507(13) Å, b = 4.487(19) Å, and c = 4.268(21) Å at 32 GPa and 320 °C. The $CrVO_4$ and some of the initial berlinite-type form were present as secondary phases. The unit cell volume is 105.5(7) Å^3, which indicated that this structure is about 3% less dense than the stable $CrVO_4$ form under the same P-T conditions. The data obtained for the $Al_{0.3}Ga_{0.7}PO_4$ solid solution at 21 GPa could also be indexed with this model.

As the data are of relatively better quality for this material, in particular due to the higher purity of this phase with only some remaining berlinite-type form as the principal secondary phase, it was possible to perform a fit by the Le Bail method to obtain the unit cell parameters giving a = 5.52(6) Å, b = 4.446(3) Å, c = 4.27(3) Å. These results indicate that this *Pmn*2₁ structure is a very reasonable model for this new metastable phase for which the diffraction data are of modest quality due to the presence of secondary phases, preferred orientation, and line broadening.

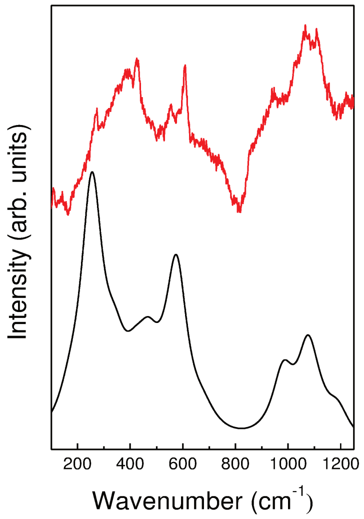

Figure 5.6 Experimental (above) Raman spectrum of $GaPO_4$ at 19 GPa on decompression and the spectrum from DFT using the *Pmn*2₁ structure (below). The calculated FWHM is arbitrary.

To further test this hypothesis, the Raman spectrum of this phase was simulated in *Figure 5.6*. The obtained spectrum can be compared to the experimental data, which are characterized by a relatively weak signal. The difference between the calculated and experimental Raman shifts varies between 0 and 6%, which is very similar to the differences observed for the starting berlinite-type phase.[252] Nevertheless, the observed differences in Raman shift and intensity remain satisfactory considering this type of calculation and approach. In addition, no soft modes are calculated at the *Γ* point. Although the present results cannot definitely be used to determine the structure of this phase, the *Pmn*2₁ structure is by far the best model available. The *Pmn*2₁ structure is built up of layers of corner-sharing GaO_6 octahedra in the *yz* plane linked by PO_4 tetrahedra with one shared edge between tetrahedra and octahedra in the a direction. This is very different from the *Cmcm* structure, which is built up of chains of edge-sharing GaO_6 octahedra in the c direction linked by corner-sharing by PO_4 tetrahedra in the other directions. It can be noted that in the low-pressure α-berlinite-type structure all tetrahedra share corners. The stable high-pressure phase with the $CrVO_4$ structure is obtained on heating at high pressure from berlinite-type $GaPO_4$. In contrast, α-cristobalite $GaPO_4$, which is based on a cubic close-packed oxygen sublattice, can transform to the $CrVO_4$ phase at ambient temperature via a displacive mechanism. The present results show that starting from the berlinite-type phase, a new orthorhombic $Pmn2_1$ structure is obtained at high pressure and ambient temperature or with moderate heating. This transition can be expected to be less reconstructive than the berlinite-$CrVO_4$ transition. This is similar to what occurs in α-quartz, where at ambient temperature transitions occur to metastable monoclinic $P2_1/c$ and $P2/c$ phases via diffusion less pathways. As the phase is metastable, its presence in a given experiment will depend on time (transition kinetics), temperature (in the absence of enough thermal activation to obtain the stable high-pressure form), and nonhydrostatic stress, which could favor certain energetic pathways.

5.1.3 Conclusion

A combination of experiment and first-principles calculations was used to investigate the high-pressure phase transitions in $GaPO_4$ and the $AlPO_4$-$GaPO_4$ solid solution. X-ray absorption and Raman spectroscopy are consistent with an increase in the coordination number of Ga to 6 with the phosphorus remaining in 4-fold coordination. Raman spectroscopy and x-ray diffraction provide evidence for a new metastable high-pressure phase in addition to the stable $CrVO_4$-type form. In the case of the solid solution, the sample consisted essentially of the new metastable phase, indicating that cation disorder or the smaller cation size of aluminum are favorable factors for its metastability. First-principles calculations and the evolutionary algorithm USPEX were used to predict possible high-pressure structures in this system. The experimental data were consistent with one predicted metastable orthorhombic structure, space group $Pmn2_1$. This structure is found to be present at ambient temperature and after heating at moderate temperatures up to 320-340 °C indicating the presence of a non-negligible activation energy for a reconstructive phase transition to the stable $CrVO_4$-type form. This can be understood by the major difference between the structures of the $CrVO_4$-type form based on chains of edge-sharing GaO_6 octahedra and the orthorhombic $Pmn2_1$ structure built up of layers of corner-sharing GaO_6 octahedra.

5.2 From 4- to 8-coordinated silicon atoms in solid-state SiS_2 under pressure

At ambiant conditions, the 16-valence electron triatomic species have different ground-state covalent structures. Examples are given in *Scheme 5.1*.

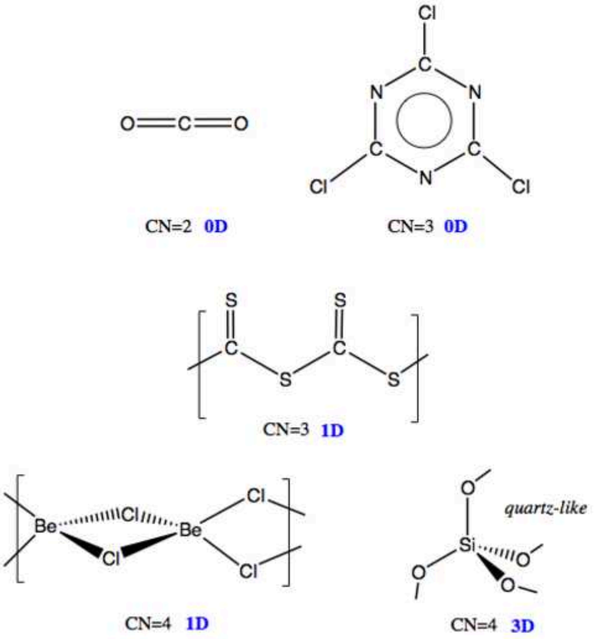

Scheme 5.1 16 valence electron triatomic AB_2 systems. CN, coordination number ; 0D, molecular; 1D polymeric; and 3D extended systems.

CO_2 is a molecular (0 D) linear structure with 2-coordinated C atoms, while SiO_2 is a solid-state compound with an extended three-dimensional Si-O net containing four-coordinated silicon centers. Besides these two compounds, others structural properties have been experimentally observed and predicted in 16-ve AB_2. In 2000, Frapper and Saillard proposed a polymeric form of CO_2, isostructural to 1D CS_2 as well as other molecular and extended polymorphs of carbon dioxide and carbon disulfide.[64] Following this work, and others, we studied silicon disulfide SiS_2 under high pressure. We expect that such a compound may have new and original structures under pressure, with high Si and S coordination numbers, due to their atomic size (CN > 4).

In autumn 2015, we started to develop the CSP of SiS_2 under pressure using evolutionary technics and DFT calculations. A Northwestern Polytechnical University (NPU) exchange program student has been trained in this research field under the direction of G. Frapper and under my supervision. Mr. Shipeng Gong wrote a training research report in April 2016 on our preliminary results. Then, in November 2016, while we were writing our SiS_2 manuscrit, Plašienka, Mortonak and Tosatti[259] published an article entitled "*Creating new layered structures at high pressures: SiS₂*". They presented predictive *ab initio* calculations combined with an evolutionary structure search (UPSEX code) of SiS_2 up to 100 GPa. And, of course, all of their predicted phases are identical with ours. Thus, we decided here to focus our discussion on results of high pressure SiS_2 phases from 100 to 500 GPa.

In 1935, the ambient pressure (NP) phase of silicon disulfide had been reported by Zintl and Loosen and Büssem *et al.*[253,254] NP-SiS_2 structure presents 1-dimensional infinite chains which interact via weak van der Waals forces (orthorhombic *Ibam* space group, Z=4).[255,256] Each extended SiS_2 chain consists of distorted, edge-sharing SiS_4 tetrahedra that run in the same direction, as displayed in *Figure 5.8*. This "covalent" topology is encountered in isoelectronic $BeCl_2$ phase shown in *Scheme 5.1*.

In 1965, Silverman *et al.*[257] reported the first high pressure phase HP3 at 6.0-6.5 GPa and 1148-1573 K (tetragonal space group *I*-42*d* , Z = 4). This experimental crystal structure is shown in *Figure 5.8*. It consists of distorted, corner-sharing SiS_4 tetrahedra. This HP polypmorph is similar to that of silica-like 3D phases with a silicon coordination number of 4 and is quenchable at ambient conditions.

Forty years later, two novel high-pressure phases have been characterized by Evers, Schnöckel and co-workers.[258] These structures are claimed to be the "*missing links between the extremes of only edge-sharing and only corner-sharing tetrahedra*". A monoclinic $P2_1/c$-I phase emerges at 2.8 GPa as the ground state phase. This structure may be viewed as the interconnection of polymeric tetrahedral $SiS_{4/2}$ chains through Si-S bonds. Here, a 2D layer is formed and silicon is four-coordinated. At slightly elevated pressure (3.5 GPa), a phase transition occurs, again with $P2_1/c$ space group. $P2_1/c$–II has a covalent Si-S net with edge- and corner-sharing tetrahedral, as found in $P2_1/c$–I, however, with a 3D connectivity net with voids.

Finally, in September 2016, Evers, Schnöckel, Medvedev *et al* submitted an article in Inorganic Chemistry entitled "*More Than 50 Years After Its Discovery in SiO_2, Octahedral Coordination Has Also Been Established in SiS_2 at High Pressure*".[260] Their high-pressure phase is one that we predicted a few weeks before (space group *P*-3*m*1, Z=1, CdI_2 type), among others [259]. Then, at 27.5 GPa, a CdI_2-type structure is characterized by X-ray powder diffraction as well as by Raman spectroscopy. This structure features octahedral SiS_6 coordination. Note that these authors claimed that the "*NP-SiS_2 phase remains stable up to approximately 7 GPa, at which pressure, the appearance of the new diffraction peaks indicates the onset of the structural phase transition*". Moreover, in their conclusion, they wrote: "*a SiS_2 polymorph with FeS_2 structure (CN 6 + 2) could probably be synthesized in a diamond anvil at less rigorous experimental conditions than for SiO_2*". The authors proposed this phase by making an analogy with post-stishovite SiO_2 phase proposed by Oganov *et al.*[261] in February 2005, and characterized above 268 GPa and 1800 K by Kuwayama *et al.*[262] a few months later (August 2005). Let's say right now that our CSP searches did not confirm their hypothesis; no FeS_2 pyrite-like phase has been located on the SiS_2 PES as a global minimum. Above ~45 GPa, the phase diagram of SiS_2 has not been explored experimentally.

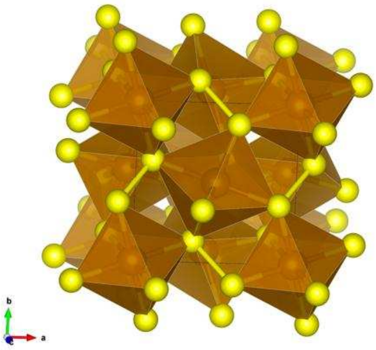

Figure 5.7 *Pa*-3 pyrite FeS_2 phase. Coordination polyhedra of S atoms around Fe atoms are shown as octahedral, while S_2 dumbbells are in yellow.

To summarize the experimental SiS_2 phases, the claimed transition phase sequence is:

$$\mathit{Ibam}\ NP \xrightarrow{} P2_1/c\text{-I HP1} \xrightarrow{} P2_1/c\text{-II HP2} \xrightarrow{} P\text{-}3m1\text{ HP4}$$

2.8 GPa 3.5 GPa 4 GPa

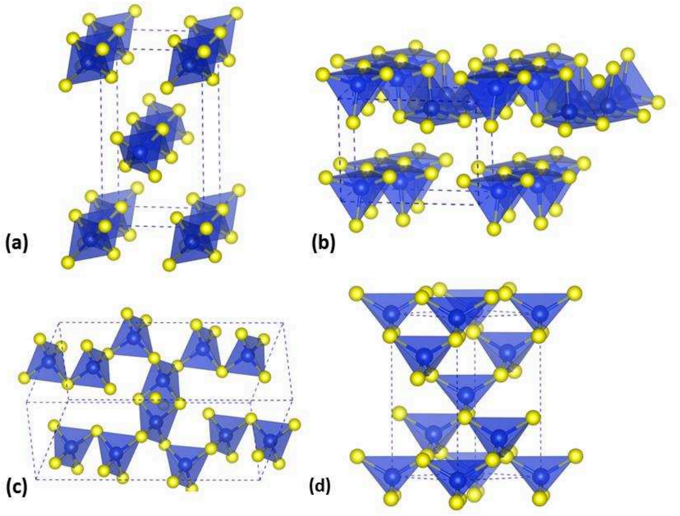

Figure 5.8 Crystalline structures of the experimental SiS_2 phases. (a) *Ibam* (NP), (b) *P*2_1*/c*-I (HP1), (c) *P*2_1*/c-II* (HP2). (d) *I*-42*d* (HP3).

In Autumn 2015, we hypothesized that a 6-fold coordinated phase, and even an 8-fold coordinated phase, may dominate the higher-pressure range. Since, this "*6-fold*" hypothesis has been double-checked by both numerical simulations and experimental data,[259,260] let's see if our 8-fold hypothesis is valid by scrutinizing the 40-500 GPa pressure range. In this study, we used *ab initio* electronic structure calculations, combined with an evolutionary search for crystal structure prediction, to explore the high-pressure phases of SiS_2 up to 500 GPa. In addition to the presence of the known low-pressure phases, we predicted several structures with 6-fold coordination and 8-fold coordination at higher pressures. In the following, we will detail our results obtained in the 100-500 GPa pressure range, as previous theoretical work has been published recently which looksat the 0-100 GPa region.

5.2.1 Computational details

The search for ground stable SiS_2 structures was performed using the evolutionary algorithm, as implemented in the USPEX code. [8,13,30] The lowest-energy structures were determined at 0, 20, 50, 100, 150, 250, 300, 400, and 500 GPa with systems containing up to 12 formula units (f.u.), thus up to 36 atoms per primitive unit cell. The first generation of 80 structures was produced randomly; all subsequent generations contained 60 structures and were produced using variation operators such as heredity (50%), softmutation (15%), lattice mutation (15%), 20% of each new generation was produced randomly.

Each structure was fully relaxed to an energy minimum within the framework of DFT embedded in the VASP package. [48] We employed the all-electron PAW method[49] and the PBE version of the GGA functional. [41,42] A plane-wave basis set, with a kinetic energy cutoff of 600 eV, was employed. We used uniform Γ-centered k-points meshes with a reciprocal space resolution of $2\pi \times 0.04$ Å^{-1} for Brillouin zone sampling. These settings enable the great convergence of total energies, forces, and stress tensors.

The dynamical stability of the statically relaxed structures was established by the absence of imaginary phonon frequencies, which were computed using the finite-displacement approach, as implemented in the PHONOPY code[97].

5.2.2 Results and discussions

First of all, the experimentally known NP-SiS_2 *Ibam* phase was successfully found as a ground-state at 1 atm in our CSP searches, which validated the reliability of our methodology. Above 0 GPa, the $P2_1/c$-I HP1 phase was the lowest phase thermodymically, and contains both edge- and corner-sharing SiS_4 tetrahedra. At 4 GPa, 4-fold $P2_1/c$-II HP2 transforms to a 2-dimensional layered P-3m1 phase (See *Figure 5.9*). However, the previous found HP3 phase was never a ground stable phase in our calculation. The P-3m1 exhibits an excellent pressure stability up to 171 GPa. The dynamic stability of this structure at 20 and 100 GPa has been verified by phonon calculations, which showed no imaginary frequency in the entire Brillouin zone (see in Appendix). P-3m1 SiS_2 is a layered structure, formed by separate sheets of edge-sharing SiS_6 octahedra (Si-S bond lengths of 2.24 and 2.02 Å, at 20 GPa and 180 GPa, respectively). Note that this CdI_2-type structure has already been reported in isovalent SnS_2 and $SnTe_2$ systems. This layered character is of potential interest given the possible facile frictional sliding under high-pressure shear. The stacking pattern within each SiS_2 slab is /AbC/ (A, C: sulfur atoms; b, hexagonally packed silicon atoms), and is illustrated in *Figure 5.9*.

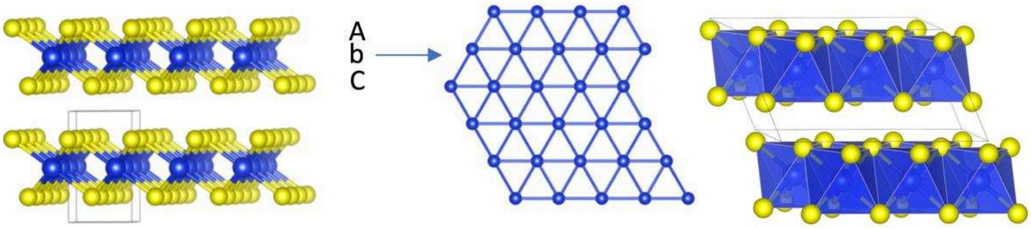

(a) (b) (c)

Figure 5.9 Crystal structure of *P*-3*m*1 SiS_2. (a) stacked SiS_2 slabs; (b) hexagonally packed silicon layer (blue sticks: Si-Si separation of 2.88 Å at 100 GPa), and (c) *CdI*$_2$-type structure. Coordination polyhedra of S atoms around Si atoms are shown as octahedral (blue).

The interlayer separation is calculated at 5.04 Å (20 GPa) and 4.15 Å (180 GPa). The DOS of *P*-3*m*1 SiS_2 at 20 GPa is displayed in *Figure 5.10*. This phase is semiconducting, with a calculated PBE band gap of 0.48 eV at 20 GPa. This electrical property is understandable if one considers the Lewis structure of $SiS_{6/3}$ building blocks, shown in *Scheme 5.2*. Here, we deliberately chose to display one Lewis formula, whereas several resonant structures exist. A precise electron count is observed, where each interatomic contact is associated to a localized 2electron-2 center bond. The local structural environment around each atom may be rationalized by looking at Lewis structures and using simple VSEPR rules. The formal $(Si^{2-})(-S)_{6/3}$ unit is reminiscent to classical stable octahedral SF_6 species, whereas the $(S^+)(-Si)_3$ unit is isovalent and isotructural to NH_3. As expected, when pressure increases, a band gap closure is observed; the valence and conduction bands overlap. The interlayer spacing decreases, thus lone pairs of sulfur atoms interact (4 electrons/2 center interaction = destabilizing interaction); this contributes to the destabilization of the valence band (the occupied out-of-phase pz - pz orbital is destabilized when pressure increases).[264] Moreover, the conduction band is decreasing (Si in character) = band gap closure. A weak density of states is computed around the Fermi level, characteristic of a poor metal (See *Figure 5.10*, DOS of SiS_2 at 50 GPa). Note that PBE DFT levels underestimate the band gap, therefore this band gap closure may have appeared at higher pressure.

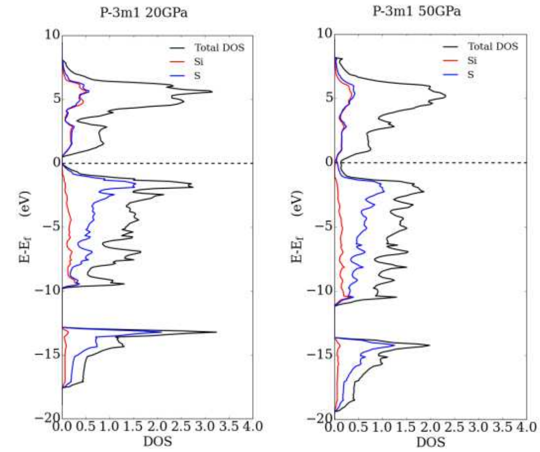

Figure 5.10 Densities of states (DOS) for the 6-fold coordinated *P*-3*m*1 phase at 20 GPa and 50 GPa.

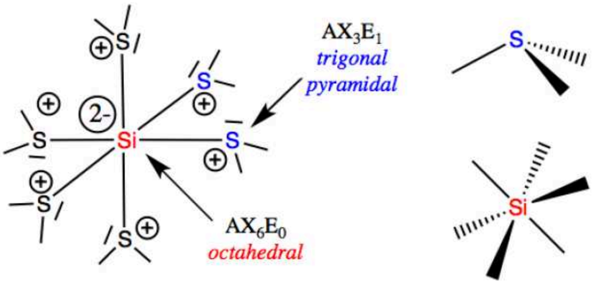

Scheme 5.2 Lewis structure of $SiS_{6/3}$ unit in solid-state HP4 *P*-3*m*1 SiS_2. The VSEPR AX_nE_m notation is indicated, as well as the local structural environment of Si and S.

Moreover, our CSP searches determined several low-energy metastable phases in 20-100 GPa pressure range, all of them present layered */AbC/* SiS_2 slabs, but with different packing. Therefore, a van de Waals correction was introduced to consider the long-term interactions between these slabs. Thus, we performed a full structural optimization by using the vdW-D2 method of Grimme.[215] Taking into account such vdW correction, the enthalpy difference between *P*-3*m*1 and low enthalpy metastable phases is reduced by roughly 50 %, but the *P*-3*m*1 phase still remains the ground stable phase. As we mentioned previously, both experimental and theoretical results by Plašienka *et al.*[259] and Evers *et al.*[260] were published in late 2016, while we were writing down our own results. These authors reported the *P*-3*m*1 phase, both predicted and experimentally characterized. Our predicted phase and transition pressure is in very good agreement with their results.

Let's now focus on the SiS_2 phase diagram above 100 GPa (and T=0K). Our predicted lowest-enthalpy phases are displayed in *Figure 5.11*, where the enthalpy-pressure curve of each selected phase is plotted. *Figure 5.12* shows the evolution of the unit cell volume of solid SiS_2 upon pressure. The dynamic stability of each structure is verified by phonon calculations (see Appendix).

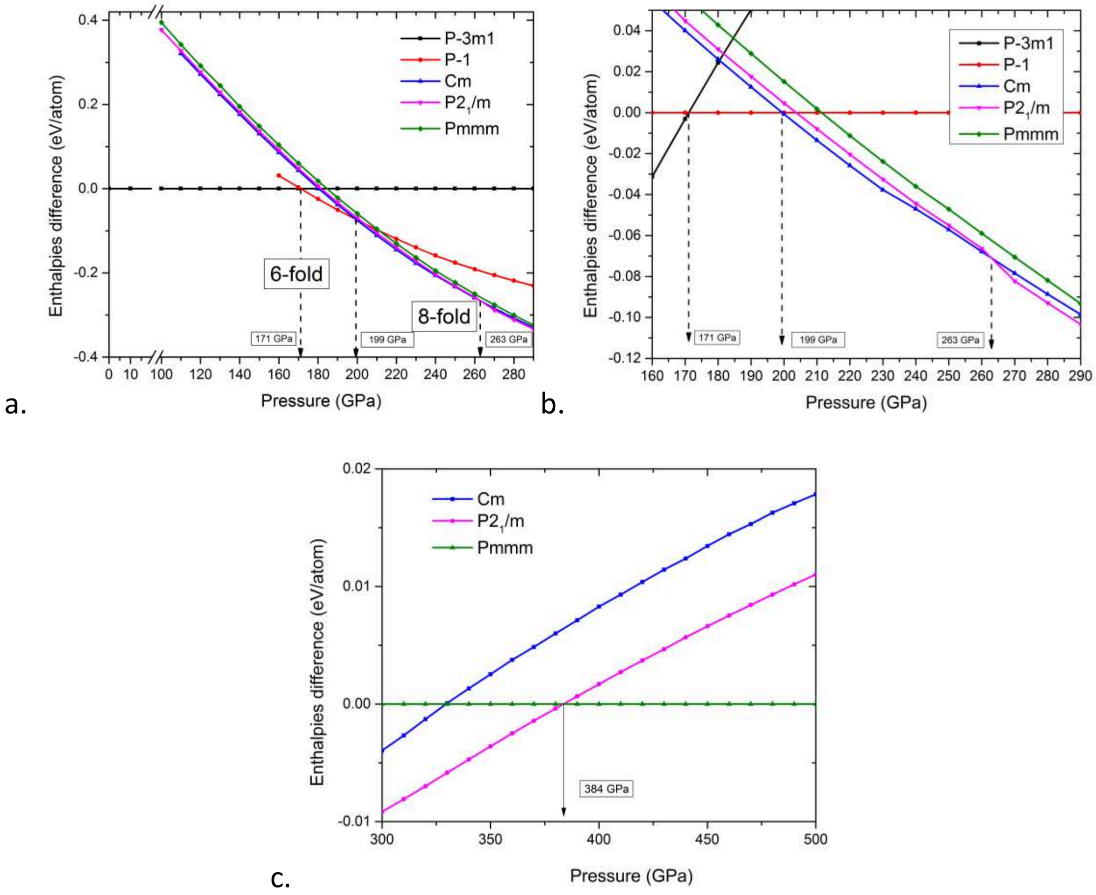

Figure 5.11 Enthalpy-pressure relations for solid SiS_2: (a) 0-285 GPa range; enthalpies are shown per atom and relative to the 6-fold coordinated *P*-3*m*1 phase; (b) 160-290 GPa range ; enthalpies are shown per atom and relative to the 6-fold coordinated *P*-1 phase; (c) focus of the 300-500 GPa range; enthalpies are shown per atom and relative to the 8-fold coordinated *Pmmm* phase.

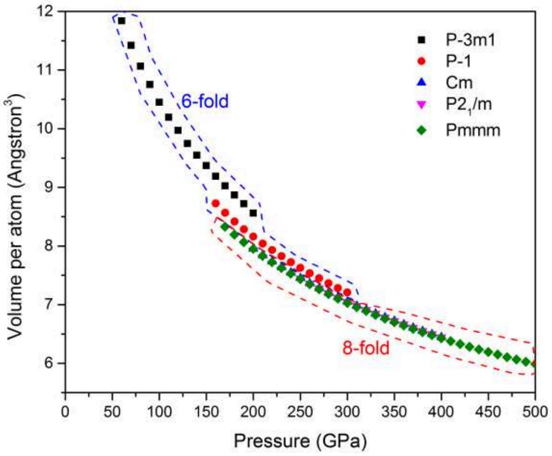

Figure 5.12 Volume evolution upon pressure for predicted solid-sate SiS_2 phases from 100 to 500 GPa: The volume difference (ΔV) of *Cm*, *P*2$_1$*/m* and *Pmmm* is slightly lower than our accuracy ($\Delta V < 0.02$ Å^3). Volume is given in Å^3 and pressure in GPa.

From 0 to 500 GPa, the following transition phase sequence is computed for silicon disulfide (transition pressure in GPa):

$$Ibam\ (\mathrm{NP}) \xrightarrow[2.5]{} P2_1/c\text{-I}\ (\mathrm{HP1}) \xrightarrow[3.5]{} P2_1/c\text{-II}\ (\mathrm{HP2}) \xrightarrow[4]{} P\text{-}3m1\ (\mathrm{HP4}) \xrightarrow[171]{} P\text{-}1 \xrightarrow[199]{} Cm \xrightarrow[263]{} P2_1/m \xrightarrow[384]{} Pmmm$$

4-fold to 8-fold Si coordinated structures are observed. Note that three high-density phases compete in energy between 200 and 400 GPa within an energy window of only ~20 meV/atom (See *Figure 5.11b*), namely *Cm*, *P*2$_1$*/m* and *Pmmm*.

P-3*m*1 SiS_2 transforms to *P*-1 phase at 171 GPa (Z=8). *Figure 5.11* shows that this *P*-1 phase stabilized as ground state in a concise pressure range (171-199 GPa). *P*-1 structure is based on separate sheets of edge-sharing SiS_6 octahedra (See *Figure 5.13a*). Meanwhile, due to the compression at high pressure, the inter-layer distance is reduced to 1.30 Å, and silicon-sulfur single bonds are present (2.22 Å at 200 GPa). In *P*-1, 7-fold silicon atoms are observed, leading to a 3-dimensional network. Therefore, we propose that this *P*-1 SiS_2 phase is the transition phase that connects the "*6-fold*" and "*8-fold*" phases. Further works are needed to support our hypothesis, such as the exploration of the transition phase pathways using Variable-Cell Nudged-Elastic-Band (VCNEB) method, implemented in USPEX.[263]

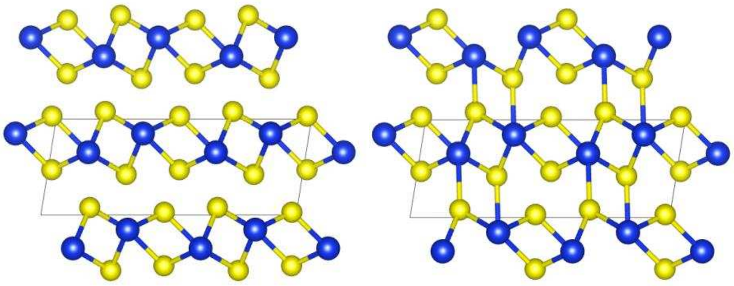

Figure 5.13 Crystal structure of SiS_2 *P*-1 structure at 200 GPa. (a) net without interlayer Si-S bond (Si-S< 2.22 Å); (b) net with the Si-S interlayer bonds (Si-S < 2.23 Å).

At 199 GPa, the *P*-1 structure undergoes a transition into a *Cm* phase where Si and S atoms form SiS_8 decahedral units linked by S atoms at the corners (*Figure 5.14*). The Si-S bond distance is 2.17 Å at 200 GPa. In this case, silicon atoms, located at the cubic center, and sulfur atoms at the corners, and the bcc like SiS_8 unit, connected with each other according to face sharing. However, there is one remaining sulfur atom per SiS_2 formula. Hence, these extra sulfur atoms form bonds with other sulfur atoms to have a SS_8 bcc like unit (see the red distorted cubic in *Figure 5.14c*). As a consequence, the *Cm* SiS_2 phase consists of two type of bcc nets. Unlike the previous 6-fold structures, it is composed of a three-dimensional network of decahedral units with high-density packing.

A distorted cubic unit, where silicon or sulfur atoms are coordinated with 8 sulfur atoms, is pressure favorable stacking than octahedrons. This indicates that the higher densities achieved in *Cm* arise from the higher coordination and denser polyhedral packings. Volume compression curves (*Figure 5.12*) show that the *Cm* unit cell volume is smaller than the *P*-1 phase volume across all pressures studied. However, there are so far, no experimental and theoretical reports available. Between 263 and 384 GPa, a ground stable phase with space group $P2_1/m$ is the lowest structure (See *Figure 5.15*). The $P2_1/m$ phase has similar sublattice to that found in *Cm* phase, thus 8-fold Si atoms are observed. Interestingly, the eight coordinated $P2_1/m$ phase will transform into a layered P-3m1 like phase when pressure is released.

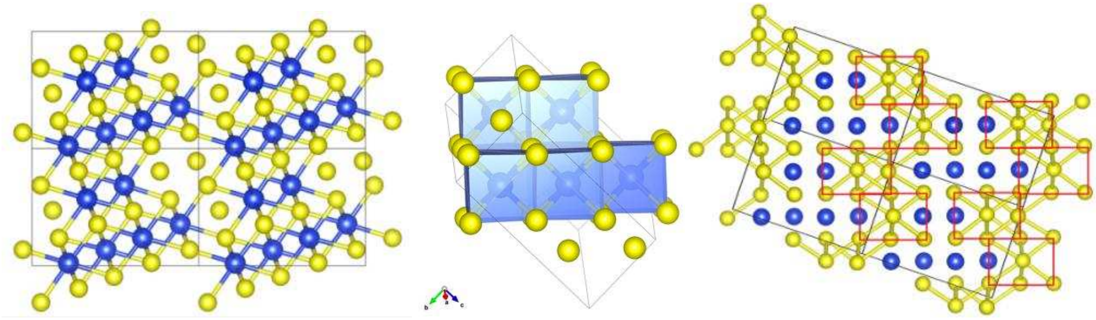
(a) (b) (c)

Figure 5.14 Crystal structure of *Cm* SiS_2 phase at 250 GPa. (a) ball&stick view, (b) coordination polyhedra of S atoms around Si atoms are shown as distorted S_8 cubes (blue), and (c) the red line indicates the SS_8 cubes.

At 384 GPa, an even higher density structure with space group *Pmmm* becomes the most stable phase. The crystal structures of the *Pmmm* are shown in *Figure 5.15b*. Each unit shares its face with others. Unlike the other high-pressure phases, *i.e., Cm* and $P2_1/m$, there is no SS_8 and SiS_8 unit overlapping. Each single unit packed analog to bcc stacking, and all of the atoms occupied an equivalent position. The volume compression curves show that the *Pmmm* unit cell volume is smaller than the *Cm* and $P2_1/m$ volume across all pressures studied. The more significant density of *Pmmm* leads directly to higher stability than *Cm* and $P2_1/m$ at sufficiently high pressures.

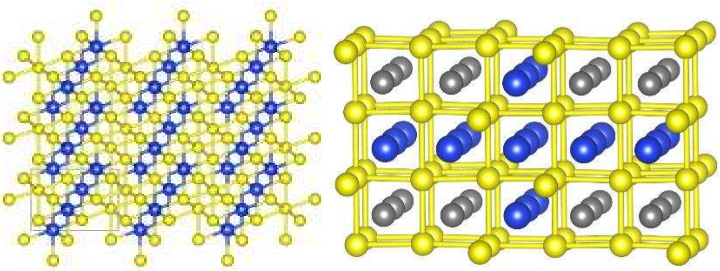

(a) (b)

Figure 5.15 Crystal structures of SiS_2: (a) $P2_1/m$ at 300 GPa and (b) *Pmmm* at 500 GPa (Yellow and gray represent S atoms and blue represents Si atoms.

The calculated DOS, *P*-1, *Cm* and *Pmmm*, are displayed in *Figure 5.16*. All high-pressure phases with decahedral units (*P*-1, *Cm* and *Pmmm*) are metallic.

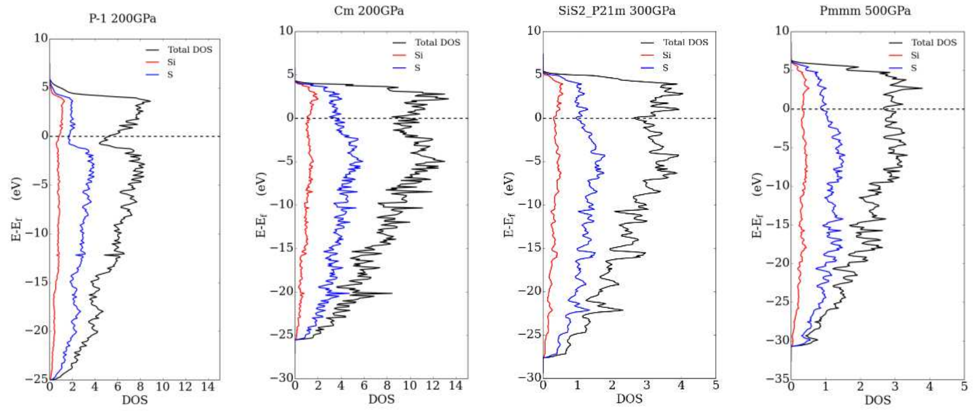

Figure 5.16 Densities of states (DOS) for the *P*-1, *Cm* $P2_1/m$ and *Pmmm* phase at 200 GPa, 200 GPa, and 500 GPa, respectively.

5.2.3 Conclusion

In summary, a high-pressure *P*-3*m*1 phase has been predicted as the stable phase thermodynamically above 4 GPa and up to 171 GPa. As was experimentally characterized before the publication of this USPEX CSP result. Its structure presents hypercoordinated silicon atoms (6-fold) and a layered character of CdI_2-type. Between 171 and 199 GPa, a *P*-1 phase is the stable form and has 7-coordinated silicon atoms. *P*-1 topology links the 6-fold and 8-fold coordinated

Si atom families in SiS_2. Finally, above 199 GPa, three stable structures are based on compact SiS_8 and SS_8 cubic units. These phases are metallic.

With the increase of pressure, SiS_2 undergoes an interesting evolution. The *covalent* dimensionality changes from 1D to 2D to 3D. The associated high barriers, and the substantial reorganization demanded by the transformation, suggests that the P-3m1 phase may recover back to ambient conditions as a metastable phase, in contradiction with experiments. However, all of the other predicted phases have been proved to be unstable at ambient pressure. Also, the P-3m1 phase is a semiconductor with a band gap of 0.48 eV at 20 GPa. It metallized around 50 GPa and remains a relatively poor metal up to the 100 GPa.

Finally, according to current knowledge, high-pressure phases of SiS_2 do not present a thermodynamically stable pyrite-like structure.[260] Further investigations are underway to complete the following results – including a comparison with SiO_2. Our aim is to present a definitive and clearer picture of SiS_2 structural evolution upon pressure.

General conclusion

The discovery of novel crystalline compounds by numerical simulation is a major challenge in Materials Science. Three families have been studied: compounds consisting of lithium and carbon dioxide; the M_xN_y nitride phases with M = Mg, Ba, Mo and Zr; the $GaPO_4$ and SiS_2 systems. The crystallographic structures are determined *in silico* using the evolutionary algorithm USPEX coupled with DFT calculations (VASP). The study of polymorphism as a function of pressure has been carried out, whereas the analysis of structural and electronic properties constitutes the heart of this thesis. Our work clearly presents the effect of pressure on the emergence of unexpected stoichiometries, such as $Li_2(CO_2)$, MgN_4, and BaN_{10}. Some of these hypothetical materials remain stable at atmospheric pressure. It has been shown that the addition of the s-block element allows the "polymerization" of the unsaturated molecules CO_2 and N_2 to be carried out at lower pressures. Thus, oxalate $C_2O_4^{2-}$ polymerizes in an infinite poly-dioxane chain in $LiCO_2$ at 33 GPa; the new Li_2CO_2 composition presents the ethene like $(-O)_2C=C(O^-)_2$ motif; N_2, N_3 and N_4 finite chains, N_5-pentazolate anions, and N_6 rings are identified in the Ae_xN_y phases, as well as, infinite covalent (1D) chains stabilized by the alkaline earth cations (Ae); the Ba_3N_2 compound is a conductive electride at ambient pressure and an insulator above 5 GPa; the ground stable structure of MoN_2 has encapsulated N_2 units, and is not the MoS_2 type arrangement proposed by experimentalists; our predictions coupled with the XRD data allow the elucidation of the $GaPO_4$ structure at 20 GPa.

References

(1) Wang, S.; Ge, H.; Sun, S.; Zhang, J.; Liu, F.; Wen, X.; Yu, X.; Wang, L.; Zhang, Y.; Xu, H.; Neuefeind, J. C.; Qin, Z.; Chen, C.; Jin, C.; Li, Y.; He, D.; Zhao, Y. *J. Am. Chem. Soc.* **2015**, *137* (14), 4815.

(2) Francis, C; What Mad Pursuit: A Personal View of Scientific Discovery. Basic Books: New York, 1988.

(3) Maddox, J. *Nature* **1988**, *335* (6187), 201.

(4) Gavezzotti, A. *Acc. Chem. Res* **1994**, *27* (8), 309.

(5) Dunitz, J. D. *Chem. Commun.* **2003**, *0* (5), 545.

(6) Pulido, A.; Chen, L.; Kaczorowski, T.; Holden, D.; Little, M. A.; Chong, S. Y.; Slater, B. J.; McMahon, D. P.; Bonillo, B.; Stackhouse, C. J.; Stephenson, A.; Kane, C. M.; Clowes, R.; Hasell, T.; Cooper, A. I.; Day, G. M. *Nature* **2017**, *543* (7647), 657.

(7) Wang, Y.; Lv, J.; Zhu, L.; Ma, Y. *Phys. Rev. B - Condens. Matter Mater. Phys.* **2010**, *82* (9), 1.

(8) Oganov, A. R.; Glass, C. W. *J. Chem. Phys.* **2006**, *124* (24), 244704.

(9) Pannetier, J.; Bassas-Alsina, J.; Rodriguez-Carvajal, J.; Caignaert, V. *Nature* **1990**, *346* (6282), 343.

(10) Schön, J. C.; Jansen, M. *Angew. Chemie Int. Ed. English* **1996**, *35* (12), 1286.

(11) Martoňák, R.; Laio, A.; Parrinello, M. *Phys. Rev. Lett.* **2003**, *90* (7), 75503.

(12) Woodley, S. M.; Battle, P. D.; Gale, J. D.; Richard A. Catlow, C. *Phys. Chem. Chem. Phys.* **1999**, *1* (10), 2535.

(13) Oganov, A. R.; Lyakhov, A. O.; Valle, M. *Acc. Chem. Res.* **2011**, *44* (3), 227.

(14) Spall, J. C. *Introduction to stochastic search and optimization : estimation, simulation, and control*; Wiley-Interscience, 2003.

(15) Pickard, C. J.; Needs, R. J. *J. Phys. Condens. Matter* **2011**, *23* (5), 53201.

(16) Pickard, C. J.; Needs, R. J. *Phys. Rev. B* **2015**, *91* (10), 104101.

(17) Deem, M. W.; Newsam, J. M. *Nature* **1989**, *342* (6247), 260.

(18) Boisen, M. B.; Gibbs, G. V.; Bukowinski, M. S. T. *Phys. Chem. Miner.* **1994**, *21* (5), 269.

(19) Mellot Draznieks, C.; Newsam, J. M.; Gorman, A. M.; Freeman, C. M.; Férey, G. *Angew. Chemie Int. Ed.* **2000**, *39* (13), 2270.

(20) Goedecker, S. *J. Chem. Phys.* **2004**, *120* (21), 9911.

(21) Roy, S.; Goedecker, S.; Hellmann, V. *Phys. Rev. E* **2008**, *77* (5), 56707.

(22) Goedecker, S.; Hellmann, W.; Lenosky, T. *Phys. Rev. Lett.* **2005**, *95* (5), 55501.

(23) Willand, A.; Gramzow, M.; Alireza Ghasemi, S.; Genovese, L.; Deutsch, T.; Reuter, K.; Goedecker, S. *Phys. Rev. B* **2010**, *81* (20), 201405.

(24) Bao, K.; Goedecker, S.; Koga, K.; Lançon, F.; Neelov, A. *Phys. Rev. B* **2009**, *79* (4), 41405.

(25) Bush, T. S.; Catlow, C. R. A.; Battle, P. D. *J. Mater. Chem.* **1995**, *5* (8), 1269.

(26) Avery, P.; Falls, Z.; Zurek, E. *Comput. Phys. Commun.* **2017**, *217*, 210.

(27) Wang, Y.; Lv, J.; Zhu, L.; Ma, Y. *Comput. Phys. Commun.* **2012**, *183* (10), 2063.

(28) Oganov, A. R.; Glass, C. W. *J. Chem. Phys.* **2006**, *124*, 244704.

(29) Glass, C. W.; Oganov, A. R.; Hansen, N. *Comput. Phys. Commun.* **2006**, *175* (11–12), 713.

(30) Lyakhov, A. O.; Oganov, A. R.; Stokes, H. T.; Zhu, Q. *Comput. Phys. Commun.* **2013**, *184* (4), 1172.

(31) Woodley, S. M. *Phys. Chem. Chem. Phys.* **2004**, *6* (8), 1823.

(32) Woodley, S. M.; Battle, P. D.; Gale, J. D.; Richard A. Catlow, C. *Phys. Chem. Chem. Phys.* **2004**, *6* (8), 1815.

(33) Woodley, S. M.; Catlow, C. R. A.; Battle, P. D.;

Gale, J. D. *Chem. Commun.* **2004**, *0* (1), 22.

(34) Born, M.; Huang, K. *Dynamical Theory of Crystal LatticesMax Born and Kun Huang*; Clarendon P, 1954.

(35) Li, K.; Wang, X.; Zhang, F.; Xue, D. *Phys. Rev. Lett.* **2008**, *100* (23), 235504.

(36) Jóhannesson, G. H.; Bligaard, T.; Ruban, A. V.; Skriver, H. L.; Jacobsen, K. W.; Nørskov, J. K. *Phys. Rev. Lett.* **2002**, *88* (25), 255506.

(37) Born, M.; Oppenheimer, R. *Ann. Phys.* **1927**, *389* (20), 457.

(38) Dirac, P. A. M. In *Mathematical Proceedings of the Cambridge Philosophical Society*; 1930; Vol. 26, pp 376–385.

(39) Hohenberg, P.; Kohn, W. *Phys. Rev.* **1964**, *136* (3B), B864.

(40) Kohn, W.; Sham, L. J. *Phys. Rev.* **1965**, *140* (4A), A1133.

(41) Perdew, J. P.; Burke, K.; Ernzerhof, M. *Phys. Rev. Lett.* **1998**, *80* (4), 891.

(42) Perdew, J. P.; Burke, K.; Ernzerhof, M. *Phys. Rev. Lett.* **1996**, *77* (18), 3865.

(43) Catlow, C. R. A. *Interdiscip. Sci. Rev.* **2015**, *40* (3), 294.

(44) Heyd, J.; Scuseria, G. E.; Ernzerhof, M. *J. Chem. Phys.* **2003**, *118* (18), 8207.

(45) Heyd, J.; Scuseria, G. E.; Ernzerhof, M. *J. Chem. Phys.* **2006**, *124* (21), 219906.

(46) Rappe, A. M.; Rabe, K. M.; Kaxiras, E.; Joannopoulos, J. D. *Phys. Rev. B* **1990**, *41* (2), 1227.

(47) Troullier, N.; Martins, J. L. *Phys. Rev. B* **1991**, *43* (3), 1993.

(48) Kresse, G.; Furthmüller, J. *Phys. Rev. B* **1996**, *54* (16), 11169.

(49) Blöchl, P. E. *Phys. Rev. B* **1994**, *50* (24), 17953.

(50) Monkhorst, H. J.; Pack, J. D. *Phys. Rev. B* **1976**, *13* (12), 5188.

(51) Dronskowski, R.; Bloechl, P. E. *J. Phys. Chem.* **1993**, *97* (33), 8617.

(52) Hoffmann, R. *J. Chem. Phys.* **1963**, *39*, 1397.

(53) Deringer, V. L.; Tchougréeff, A. L.; Dronskowski, R. *J. Phys. Chem. A* **2011**, *115* (21), 5461.

(54) Maintz, S.; Deringer, V. L.; Tchougréeff, A. L.; Dronskowski, R. *J. Comput. Chem.* **2013**, *34* (29), 2557.

(55) Bader, R. F. W.; Molecules, A. I. *Clarendon Oxford, UK* **1990**.

(56) Tang, W.; Sanville, E.; Henkelman, G. *J. Phys. Condens. Matter* **2009**, *21* (8), 84204.

(57) Sanville, E.; Kenny, S. D.; Smith, R.; Henkelman, G. *J. Comput. Chem.* **2007**, *28* (5), 899.

(58) Henkelman, G.; Arnaldsson, A.; Jónsson, H. *Comput. Mater. Sci.* **2006**, *36* (3), 354.

(59) Yu, M.; Trinkle, D. R. *J. Chem. Phys.* **2011**, *134* (6), 64111.

(60) Becke, A. D.; Edgecombe, K. E. *J. Chem. Phys.* **1990**, *92* (1990), 5397.

(61) Savin, A.; Nesper, R.; Wengert, S.; Fässler, T. F. *Angew. Chemie Int. Ed. English* **1997**, *36* (17), 1808.

(62) Landrum, G. A. Viewkel (ver 3.0). Viewkel is distributed as part of the YAeHMOP extended Hückel molecular orbital package and is freely available at: http://yaehmop.sourceforge.net

(63) Lewars, E. *Journal of molecular structure: THEOCHEM.*; Elsevier B.V, 1996; Vol. 1.

(64) Frapper, G.; Saillard, J.-Y. *J. Am. Chem. Soc.* **2000**, *122* (22), 5367.

(65) Yong, X.; Liu, H.; Wu, M.; Yao, Y.; Tse, J. S.; Dias, R.; Yoo, C.-S. *Proc. Natl. Acad. Sci.* **2016**, *113* (40), 11110.

(66) Lu, C.; Miao, M.; Ma, Y. *J. Am. Chem. Soc.* **2013**, *135* (38), 14167.

(67) Sun, J.; Klug, D. D.; Martonák, R.; Montoya, J. A.; Lee, M.-S. M.-S.; Scandolo, S.; Tosatti, E.; Martonak, R.; Montoya, J. A.; Lee, M.-S. M.-S.; Scandolo, S.; Tosatti, E. *Proc. Natl. Acad. Sci. U. S. A.* **2009**, *106* (15), 6077.

(68) Iota, V.; Yoo, C. S.; Cynn, H. *Science* **1999**, *283* (5407), 1510.

(69) Serra, S.; Cavazzoni, C.; Chiarotti, G. L.; Scandolo, S.; Tosatti, E. *Science* **1999**, *284* (5415), 788.

(70) Yoo, C. S.; Cynn, H.; Gygi, F.; Galli, G.; Iota, V.; Nicol, M.; Carlson, S.; Häusermann, D.;

Mailhiot, C. *Phys. Rev. Lett.* **1999**, *83* (26), 5527.

(71) Oganov, A. R.; Ono, S.; Ma, Y.; Glass, C. W.; Garcia, A. *Earth Planet. Sci. Lett.* **2008**, *273* (1–2), 38.

(72) Liu, L. *Earth Planet. Sci. Lett.* **1984**, *71* (1), 104.

(73) Olinger, B. *J. Chem. Phys.* **1982**, *77* (12), 6255.

(74) Giordano, V. M.; Datchi, F. *Europhys. Lett.* **2007**, *77* (4), 46002.

(75) Aoki, K.; Yamawaki, H.; Sakashita, M.; Gotoh, Y.; Takemura, K. *Science (80-.).* **1994**, *263* (5145), 356.

(76) Yoo, C. S.; Kohlmann, H.; Cynn, H.; Nicol, M. F.; Iota, V.; LeBihan, T. *Phys. Rev. B* **2002**, *65* (10), 104103.

(77) Bouibes, A; Zaoui, A. *Sci. Rep.* **2014**, *4*, 5172.

(78) Čančarevič, Ž.; Schön, J. C.; Jansen, M. *Zeitschrift für Anorg. und Allg. Chemie* **2006**, *632* (8–9), 1437.

(79) Boulard, E.; Pan, D.; Galli, G.; Liu, Z.; Mao, W. L. *Nat. Commun.* **2015**, *6*, 6311.

(80) Zumdahl, S. S. *Chemical principles*; Houghton Mifflin, 2009.

(81) Suito, K.; Namba, J.; Horikawa, T.; Taniguchi, Y.; Sakurai, N.; Kobayashi, M.; Onodera, A.; Shimomura, O.; Kikegawa, T. *Am. Mineral.* **2001**, *86* (9).

(82) Boldyreva, E. V.; Ahsbahs, H.; Chernyshev, V. V.; Ivashevskaya, S. N.; Oganov, A. R. *Zeitschrift für Krist. - Cryst. Mater.* **2006**, *221* (3), 186.

(83) Beagley, B.; Small, R. W. H. *Acta Crystallogr.* **1964**, *17* (6), 783.

(84) Dinnebier, R. E.; Vensky, S.; Panthöfer, M.; Jansen, M. *Inorg. Chem.* **2003**, *42* (5), 1499.

(85) Mailhiot, C.; Yang, L. H.; McMahan, A. K. *Phys. Rev. B* **1992**, *46* (22), 14419.

(86) Lipp, M.; Evans, W. J.; Garcia-Baonza, V.; Lorenzana, H. E. *J. Low Temp. Phys.* **1998**, *111* (3/4), 247.

(87) Bernard, S.; Chiarotti, G.; Scandolo, S.; Tosatti, E. *Phys. Rev. Lett.* **1998**, *81* (10), 2092.

(88) Eremets, M. I.; Popov, M. Y.; Trojan, I. A.; Denisov, V. N.; Boehler, R.; Hemley, R. J. *J. Chem. Phys.* **2004**, *120* (22), 10618.

(89) Yu, S.; Huang, B.; Zeng, Q.; Oganov, A. R.; Zhang, L.; Frapper, G. *J. Phys. Chem. C* **2017**, *121* (21), 11037.

(90) Ravishankara, A. R.; Daniel, J. S.; Portmann, R. W. *Science (80-.).* **2009**, *326* (5949), 123.

(91) Liu, J.; Kopold, P.; van Aken, P. A.; Maier, J.; Yu, Y. *Angew. Chemie Int. Ed.* **2015**, *54* (33), 9632.

(92) Chen, H.; Armand, M.; Demailly, G.; Dolhem, F.; Poizot, P.; Tarascon, J.-M. *ChemSusChem* **2008**, *1* (4), 348.

(93) Wang, Y.; Ding, Y.; Pan, L.; Shi, Y. Y.; Yue, Z.; Shi, Y. Y.; Yu, G. *Nano Lett.* **2016**, *16* (5), 3329.

(94) Zhao, Q.; Wang, J.; Lu, Y.; Li, Y.; Liang, G.; Chen, J. *Angew. Chemie Int. Ed.* **2016**, *55* (40), 12528.

(95) Gavryushkin, P. N.; Behtenova, A.; Popov, Z. I.; Bakakin, V. V.; Likhacheva, A. Y.; Litasov, K. D.; Gavryushkin, A. *Cryst. Growth Des.* **2016**, *16* (10), 5612.

(96) Pople, J. A. Rev. Mod. Phys. 1999, 71, 1267.

(97) Togo, A.; Oba, F.; Tanaka, I. *Phys. Rev. B* **2008**, *78* (13), 134106.

(98) Momma, K.; Izumi, F. *J. App. Cryst.* **2011**, *44*(6), 1272

(99) Dinnebier, R. E.; Nuss, H.; Jansen, M. *Zeitschrift für Krist. - Cryst. Mater.* **2005**, *220* (11), 954.

(100) Bundy, F. P.; Kasper, J. S. *J. Chem. Phys.* **1967**, *46* (9), 3437.

(101) Tateyama, Y.; Ogitsu, T.; Kusakabe, K.; Tsuneyuki, S.; Tateyama; Ogitsu; Kusakabe, K.; Tsuneyuki. *Phys. Rev. B* **1996**, *54* (21), 14994.

(102) Weck, G.; Desgreniers, S.; Loubeyre, P.; Mezouar, M. *Phys. Rev. Lett.* **2009**, *102* (25), 1.

(103) Katzke, H.; Tolédano, P. *Phys. Rev. B* **2009**, *79* (14), 140101.

(104) Matsuoka, T.; Sakata, M.; Nakamoto, Y.; Takahama, K.; Ichimaru, K.; Mukai, K.; Ohta, K.; Hirao, N.; Ohishi, Y.; Shimizu, K. *Phys. Rev. B* **2014**, *89* (14), 144103.

(105) Marqués, M.; McMahon, M. I.; Gregoryanz, E.; Hanfland, M.; Guillaume, C. L.; Pickard, C. J.; Ackland, G. J.; Nelmes, R. J. *Phys. Rev. Lett.* **2011**, *106* (9), 95502.

(106) Koleżyński, A.; Małecki, A. *J. Therm. Anal. Calorim.* **2013**, *114* (3), 1391.

(107) Dean, P. A. W. *J. Chem. Educ.* **2012**, *89* (3), 417.

(108) Islam, M. S.; Fisher, C. A. J. *Chem. Soc. Rev.* **2014**, *43* (1), 185.

(109) Schon, T. B.; McAllister, B. T.; Li, P.-F.; Seferos, D. S. *Chem. Soc. Rev.* **2016**, *45* (22), 6345.

(110) McDaniel, M. P. Academic Press, 2010; Vol. 53, pp 123–606.

(111) Dobbin, L. *J. Chem. Educ.* **1935**, *12* (8), 370.

(112) Greenwood, N. N. (Norman N.; Earnshaw, A. (Alan). *Chemistry of the elements*; Butterworth-Heinemann, 1997.

(113) Klapötke, T. M. M. *High energy density materials*; Springer, 2007.

(114) Singh, R. P. P.; Verma, R. D. D.; Meshri, D. T. T.; Shreeve, J. M. M. *Angew. Chemie Int. Ed.* **2006**, *45* (22), 3584.

(115) Brinck, T. *Green energetic materials*.

(116) Jursic, B. S. *J. Mol. Struct. THEOCHEM* **2001**, *536* (2–3), 143.

(117) Eremets, M. I.; Hemley, R. J.; Mao, H.; Gregoryanz, E. *Nature* **2001**, *411* (6834), 170.

(118) Eremets, M. I.; Gavriliuk, A. G.; Trojan, I. A.; Dzivenko, D. A.; Boehler, R. *Nat. Mater.* **2004**, *3* (8), 558.

(119) Ritter, S. *Chem. Eng. News* **2004**, *82* (31), 10.

(120) McMahan, A. K.; LeSar, R. *Phys. Rev. Lett.* **1985**, *54* (17), 1929.

(121) Eremets, M. I.; Gavriliuk, A. G.; Serebryanaya, N. R.; Trojan, I. A.; Dzivenko, D. A.; Boehler, R.; Mao, H. K.; Hemley, R. J. *J. Chem. Phys.* **2004**, *121* (22), 11296.

(122) Zahariev, F.; Hooper, J.; Alavi, S.; Zhang, F.; Woo, T. K. *Phys. Rev. B* **2007**, *75* (14), 140101.

(123) Alemany, M. M. G.; Martins, J. L. *Phys. Rev. B* **2003**, *68* (2), 24110.

(124) Wang, X.; Wang, Y.; Miao, M.; Zhong, X.; Lv, J.; Cui, T.; Li, J.; Chen, L.; Pickard, C. J.; Ma, Y. *Phys. Rev. Lett.* **2012**, *109* (17), 1.

(125) Bondarchuk, S. V.; Minaev, B. F. *Phys. Chem. Chem. Phys.* **2017**, *19* (9), 6698.

(126) Huynh, M. H. V.; Baker, R. T.; Jameson, D. L.; Labouriau, A.; Meyer, T. J. *J. Am. Chem. Soc.* **2002**, *124* (17), 4580.

(127) Liang, Y. H.; Luo, Q.; Guo, M.; Li, Q. S. *Dalt. Trans.* **2012**, *41* (39), 12075.

(128) Zhou, H.; Wong, N.-B.; Zhou, G.; Tian, A. *J. Phys. Chem. A* **2006**, *110* (10), 3845.

(129) Thompson, M. D.; Bledson, T. M.; Strout, D. L. *J. Phys. Chem. A* **2002**, *106* (29), 6880.

(130) Glukhovtsev, M. N.; Jiao, H.; Schleyer, P. von R. *Inorg. Chem.* **1996**, *35* (24), 7124.

(131) Manaa, M. R. *Chem. Phys. Lett.* **2000**, *331* (2–4), 262.

(132) Moxnes, J. F. *J. Mol. Model.* **2017**, *23* (10), 284.

(133) Cacace, F; de Petris, G; Troiani, A. *Science* **2002**, *295* (5554), 480.

(134) Wang, X.; Tian, F.; Wang, L.; Jin, X.; Duan, D.; Huang, X.; Liu, B.; Cui, T. *New J. Phys.* **2013**, *15*.

(135) Vij, A.; Pavlovich, J. G.; Wilson, W. W.; Vij, V.; Christe, K. O. *Angew. Chemie* **2002**, *114* (16), 3177.

(136) Benin, V.; Kaszynski, P.; Radziszewski, G. *J. Org. Chem.* **2002**, *67* (4), 1354.

(137) Bazanov, B.; Haas, Y. *J. Phys. Chem. A* **2015**, *119* (11), 2661.

(138) Geiger, U.; Haas, Y. *J. Phys. Chem. B* **2015**, *119* (24), 7338.

(139) Bazanov, B.; Geiger, U.; Carmieli, R.; Grinstein, D.; Welner, S.; Haas, Y. *Angew. Chemie* **2016**, *128* (42), 13427.

(140) Portius, P.; Davis, M.; Campbell, R.; Hartl, F.; Zeng, Q.; Meijer, A. J. H. M.; Towrie, M. *J. Phys. Chem. A* **2013**, *117* (48), 12759.

(141) Huisgen, R. *Angew. Chemie Int. Ed. English* **1963**, *2* (10), 565.

(142) Huisgen, R.; Ugi, I. *Chem. Ber.* **1957**, *90* (12), 2914.

(143) Östmark, H.; Wallin, S.; Brinck, T.; Carlqvist, P.; Claridge, R.; Hedlund, E.; Yudina, L. *Chem. Phys. Lett.* **2003**, *379* (5–6), 539.

(144) Steele, B. A.; Stavrous, E.; Prakapenka, V. B.; Radousky, H.; Zaug, J.; Crowhurst, J. C.; Oleynik, I. I. **2017**; Vol. 40016, p 40016.

(145) Peng, F.; Han, Y.; Liu, H.; Yao, Y. *Sci. Rep.* **2015**, *5* (1), 16902.

(146) Zhang, C.; Sun, C.; Hu, B.; Yu, C.; Lu, M. *Science* **2017**, *355* (6323), 374.

(147) Xu, Y.; Wang, Q.; Shen, C.; Lin, Q.; Wang, P.; Lu, M. *Nature* **2017**, *549* (7670), 78.

(148) Xu, Y.; Wang, P.; Lin, Q.; Lu, M. *Dalt. Trans.* **2017**, *46* (41), 14088.

(149) Prasad, D. L. V. K.; Ashcroft, N. W.; Hoffmann, R. *J. Phys. Chem. C* **2013**, *117* (40), 20838.

(150) Peng, F.; Yao, Y.; Liu, H.; Ma, Y. *J. Phys. Chem. Lett.* **2015**, *6* (12), 2363.

(151) Shen, Y.; Oganov, A. R.; Qian, G.; Zhang, J.; Dong, H.; Zhu, Q.; Zhou, Z. *Nat. Publ. Gr.* **2015**, *5*, 1.

(152) Steele, B. A.; Oleynik, I. I. *Chem. Phys. Lett.* **2016**, *643* (4–6), 21.

(153) Steele, B. A.; Stavrou, E.; Crowhurst, J. C.; Zaug, J. M.; Prakapenka, V. B.; Oleynik, I. I. *Chem. Mater.* **2016**, acs. chemmater.6b04538.

(154) Eckerlin, P.; Rabenau, A. *Zeitschrift für Anorg. und Allg. Chemie* **1960**, *304* (3-4), 218.

(155) Chang, J.; Ge, N.; Liu, K. *Philos. Mag.* **2017**, *97* (25), 2182.

(156) Wei, S.; Li, D.; Liu, Z.; Wang, W.; Tian, F.; Bao, K.; Duan, D.; Liu, B.; Cui, T. *J. Phys. Chem. C* **2017**, *121*(18), 9766.

(157) Glasson, D. R.; Jayaweera, S. A. A. *J. Appl. Chem.* **2007**, *18* (3), 77.

(158) Liu, P.-F.; Zhou, L.; Frauenheim, T.; Wu, L.-M. *Phys. Chem. Chem. Phys.* **2016**, *18* (44), 30379.

(159) Wei, S.; Li, D.; Liu, Z.; Li, X.; Tian, F.; Duan, D.; Liu, B.; Cui, T. *Phys. Chem. Chem. Phys.* **2017**, 1.

(160) Hao, J.; Li, Y. W. W.; Wang, J. S. S.; Ma, C. L. L.; Huang, L. Y. Y.; Liu, R.; Cui, Q. L. L.; Zou, G. T. T.; Liu, J.; Li, X. D. D. *J. Phys. Chem. C* **2010**, *114* (39), 16750.

(161) Keve, E. T.; Skapski, A. C. *Inorg. Chem.* **1968**, *7* (9), 1757.

(162) Braun, C.; Börger, S. L. L.; Boyko, T. D. D.; Miehe, G.; Ehrenberg, H.; Höhn, P.; Moewes, A.; Schnick, W. *J. Am. Chem. Soc.* **2011**, *133* (12), 4307.

(163) Schneider, S. B.; Frankovsky, R.; Schnick, W. *Inorg. Chem.* **2012**, *51* (4), 2366.

(164) Zhu, S.; Peng, F.; Liu, H.; Majumdar, A.; Gao, T.; Yao, Y. *Inorg. Chem.* **2016**, *55* (15), 7550.

(165) Maquenne, M.; Hebd, C. R. *Séanc Acad. Sci.* **1892**, *114,* 220.

(166) Künzel, H.-T. *PhD thesis Univ. Stuttgart* **1980**.

(167) Guntz, A.; Benoit, F. *Ann. Cltint* **1923**, *20*, 5.

(168) Antropoff, A. v; Krüger, K. H. *Zeitschrift für Phys. Chemie* **1933**, *167* (1), 49.

(169) Wang, X.; Li, J.; Botana, J.; Zhang, M.; Zhu, H.; Chen, L.; Liu, H.; Cui, T.; Miao, M. *J. Chem. Phys.* **2013**, *139* (16), 1.

(170) Zhang, M.; Yin, K.; Zhang, X.; Wang, H.; Li, Q.; Wu, Z. *Solid State Commun.* **2013**, *161*, 13.

(171) Zhang, M.; Yan, H.; Wei, Q.; Liu, H. *RSC Adv.* **2015**, *5* (16), 11825.

(172) Wang, X.; Li, J.; Xu, N.; Zhu, H.; Hu, Z.; Chen, L. *Sci. Rep.* **2015**, *5*, 16677.

(173) Wang, X.; Li, J.; Zhu, H.; Chen, L.; Lin, H. *J. Chem. Phys.* **2014**, *141* (4), 44717.

(174) Zhang, X.; Zunger, A.; Trimarchi, G. *J. Chem. Phys.* **2010**, *133* (19), 194504.

(175) Xia, Y.; Li, Q.; Ma, Y. *Comput. Mater. Sci.* **2010**, *49* (1), S76.

(176) Ramesh Babu, K.; Vaitheeswaran, G. *Chem. Phys. Lett.* **2013**, *586*, 44.

(177) Zhu, W.; Xu, X.; Xiao, H. *J. Phys. Chem. Solids* **2007**, *68* (9), 1762.

(178) Vajenine, G. V.; Wang, X.; Efthimiopoulos, I.; Karmakar, S.; Syassen, K.; Hanfland, M. *Phys. Rev. B* **2009**, *79* (22), 224107.

(179) Fischer, D.; Jansen, M. *Angew. Chemie Int. Ed.* **2002**, *41* (10), 1755.

(180) Römer, S. R.; Dörfler, T.; Kroll, P.; Schnick, W. *Phys. status solidi* **2009**, *246* (7), 1604.

(181) Bertani, R. *Solids and surfaces. A chemist's view of bonding in extended structures.*; 1990; Vol. 168.

(182) Choi, C. S. *Acta Crystallogr. Sect. B Struct. Crystallogr. Cryst. Chem.* **1969**, *25* (12), 2638.

(183) Steinbrenner, U.; Simon, A. *Zeitschrift für Anorg. und Allg. Chemie* **1998**, *624* (2), 228.

(184) Reckeweg, O.; DiSalvo, F. J. *Zeitschrift für Krist. - New Cryst. Struct.* **2005**, *220* (1–4), 519.

(185) Zhang, L. Q.; Cheng, Y.; Niu, Z. W.; Piao, C. G.; Ji, G. F. *Zeitschrift fur Naturforsch. - Sect. A J. Phys. Sci.* **2014**, *69* (12), 619.

(186) Reckeweg, O.; Simon, A. *Zeitschrift für Naturforsch. B* **2003**, *58* (11), 1097.

(187) Ionic Radii: *http://abulafia.mt.ic.ac.uk/shannon/.*

(188) Vajenine, G. V.; Grzechnik, A.; Syassen, K.; Loa, I.; Hanfland, M.; Simon, A. *Comptes Rendus Chim.* **2005**, *8* (11–12), 1897.

(189) Miessler, G. L.; Tarr, D. A. *Inorganic Chemistry, 2nd ed.*;Prentice-Hall: Upper Saddle River, NJ, 1999; 260

(190) Lee, K.; Kim, S. W.; Toda, Y.; Matsuishi, S.; Hosono, H. *Nature* **2013**, *494* (7437), 336.

(191) Taylor, D. *Trans. J. Br. Ceram. Soc.* **1984**, *83* (1), 5.

(192) Druffel, D. L.; Kuntz, K. L.; Woomer, A. H.; Alcorn, F. M.; Hu, J.; Donley, C. L.; Warren, S. C. *J. Am. Chem. Soc.* **2016**, *138* (49), 16089.

(193) Tal, A. A.; Katsnelson, M. I.; Ekholm, M.; Jönsson, H. J. M.; Dubrovinsky, L.; Dubrovinskaia, N.; Abrikosov, I. A. *Phys. Rev. B* **2016**, *93* (20), 205150.

(194) Kurylyshyn, I. M.; Fässler, T. F.; Fischer, A.; Hauf, C.; Eickerling, G.; Presnitz, M.; Scherer, W. *Angew. Chemie Int. Ed.* **2014**, *53* (11), 3029.

(195) Alemany, P.; Llunell, M.; Canadell, E. *Inorg. Chem.* **2006**, *45* (18), 7235.

(196) Dong, X.; Fan, C. *Sci. Rep.* **2015**, *5*, 9326.

(197) Zhu, Q.; Oganov, A. R.; Glass, C. W.; Stokes, H. T. *Acta Crystallogr. Sect. B Struct. Sci.* **2012**, *68* (3), 215.

(198) Hägg, G. *Z. Phys. Chem. B* **1930**, *7*, 339.

(199) Hägg, G. *Nov. Acta Reg. Soc. Sci. Ups.* **1928**, *4* (7), 1.

(200) Brese, N. E.; O'Keeffe, M. In *Complexes, Clusters and Crystal Chemistry*; Springer-Verlag: Berlin/Heidelberg, 1992; 307–378.

(201) Zerr, A.; Miehe, G.; Riedel, R. *Nat. Mater.* **2003**, *2* (3), 185.

(202) Salamat, A.; Hector, A. L.; Gray, B. M.; Kimber, S. A. J.; Bouvier, P.; McMillan, P. F. *J. Am. Chem. Soc.* **2013**, *135* (25), 9503.

(203) Salamat, A.; Woodhead, K.; Shah, S. I. U.; Hector, A. L.; McMillan, P. F. *Chem. Commun.* **2014**, *50* (70), 10041.

(204) Zerr, A.; Miehe, G.; Li, J.; Dzivenko, D. A.; Bulatov, V. K.; Höfer, H.; Bolfan-Casanova, N.; Fialin, M.; Brey, G.; Watanabe, T.; Yoshimura, M. *Adv. Funct. Mater.* **2009**, *19* (14), 2282.

(205) Salamat, A.; Hector, A. L.; Kroll, P.; McMillan, P. F. *Coord. Chem. Rev.* **2013**, *257* (13–14), 2063.

(206) Juza, R.; Gabel, A.; Rabenau, H.; Klose, W. *Zeitschrift für Anorg. und Allg. Chemie* **1964**, *329* (1), 136.

(207) Baur, W. H.; Lerch, M. *Zeitschrift für Anorg. und Allg. Chemie* **1996**, *622* (10), 1729.

(208) Chhowalla, M.; Unalan, H. E. *Nat. Mater.* **2005**, *4* (4), 317.

(209) Kroll, P. *Phys. Rev. Lett.* **2003**, *90* (12), 125501.

(210) Gribaudo, L.; Arias, D.; Abriata, J. *J. Phase Equilibria* **1994**, *15* (4), 441.

(211) Born, M.; Huang, K. Oxford **1954**,.

(212) Wu, F.; Huang, C.; Wu, H.; Lee, C.; Deng, K.; Kan, E.; Jena, P. *Nano Lett.* **2015**, *15* (12), 8277.

(213) Langreth, D. C.; Dion, M.; Rydberg, H.; Schröder, E.; Hyldgaard, P.; Lundqvist, B. I. *Int. J. Quantum Chem.* **2005**, *101* (5), 599.

(214) van Mourik, T.; Gdanitz, R. J. *J. Chem. Phys.* **2002**, *116* (22), 9620.

(215) Grimme, S. *J. Comput. Chem.* **2006**, *27* (15), 1787.

(216) Wessel, M.; Dronskowski, R. *Chem. - A Eur. J.* **2011**, *17* (9), 2598.

(217) Wang, Y.; Yao, T.; Yao, J.-L.; Zhang, J.; Gou, H. *Phys. Chem. Chem. Phys.* **2013**, *15* (1), 183.

(218) Cotton, F. A.; Wing, R. M. *Inorg. Chem.* **1965**, *4* (6), 867.

(219) Wu, H.; Qian, Y.; Lu, R.; Tan, W. *Phys. Lett. A* **2016**, *380* (5–6), 768.

(220) Li, Y.; Wang, H.; Li, Q.; Ma, Y.; Cui, T.; Zou, G. *Inorg. Chem.* **2009**, *48* (20), 9904.

(221) Belonoshko, A. B.; Burakovsky, L.; Chen, S. P.; Johansson, B.; Mikhaylushkin, A. S.; Preston, D. L.; Simak, S. I.; Swift, D. C. *Phys. Rev. Lett.* **2008**, *100* (13), 135701.

(222) Pickard, C. J.; Needs, R. J. *Phys. Rev. Lett.* **2009**, *102* (12), 125702.

(223) Born, M.; Huang, K.; Lax, M. *Am. J. Phys.* **1955**, *23* (7), 474.

(224) McSkimin, H. J.; Andreatch, P. *J. Appl. Phys.*

1972, *43* (7), 2944.

(225) Chandrasekar, S.; Santhanam, S. *J. Mater. Sci.* **1989**, *24* (12), 4265.

(226) Hill, R. *Proc. Phys. Soc. Sect. A* **1952**, *65* (5), 349.

(227) Chen, X.-Q.; Niu, H.; Li, D.; Li, Y. *Intermetallics* **2011**, *19* (9), 1275.

(228) Lerch, M.; Füglein, E.; Wrba, J. *Zeitschrift für Anorg. und Allg. Chemie* **1996**, *622* (2), 367.

(229) Yu, X.-X.; Weinberger, C. R.; Thompson, G. B. *Comput. Mater. Sci.* **2016**, *112*, 318.

(230) Jiang, C.; Jiang, W. *Phys. status solidi* **2014**, *251* (3), 533.

(231) Yu, S.; Zeng, Q.; Oganov, A. R.; Frapper, G.; Zhang, L. *Phys. Chem. Chem. Phys.* **2015**, *17* (17), 11763.

(232) Bazhanov, D. I.; Knizhnik, A. A.; Safonov, A. A.; Bagatur'yants, A. A.; Stoker, M. W.; Korkin, A. A. *J. Appl. Phys.* **2005**, *97* (4), 44108.

(233) Hemley, R. J.; Jephcoat, A. P.; Mao, H. K.; Ming, L. C.; Manghnani, M. H. *Nature* **1988**, *334* (6177), 52.

(234) Haines, J.; Léger, J. M.; Gorelli, F.; Hanfland, M. *Phys. Rev. Lett.* **2001**, *87* (15), 155503.

(235) Kingma, K. J.; Meade, C.; Hemley, R. J.; Mao, H.-K.; Veblen, D. R. *Science.* **1993**, *259*, 666.

(236) Haines, J.; Cambon, O. *Zeitschrift für Krist. - Cryst. Mater.* **2004**, *219* (6), 314.

(237) Polian, A.; Itie, J.-P.; Grimsditch, M.; Badro, J.; Philippot, E.; Division, M. S.; Curie, U. P. and M.; Curie, U. P. and M.; Terre, L. des S. de la; Bataillon, U. M. I. place E. *Eur. J. Sol. State Inorg. Chem.* **1997**, *34* (1997).

(238) Pasternak, M. P.; Rozenberg, G. K.; Milner, A. P.; Amanowicz, M.; Zhou, T.; Schwarz, U.; Syassen, K.; Dean Taylor, R.; Hanfland, M.; Brister, K. *Phys. Rev. Lett.* **1997**, *79* (22), 4409.

(239) Pellicer-Porres, J.; Saitta, A. M.; Polian, A.; Itié, J. P.; Hanfland, M. *Nat. Mater.* **2007**, *6* (9), 698.

(240) Badro, J.; Itié, J. P.; Polian, A. *Eur. Phys. J. B* **1998**, *1* (3), 265.

(241) Robeson, J. L.; Winters, R. R.; Hammack, W. S. *Phys. Rev. Lett.* **1994**, *73* (12), 1644.

(242) Gillet, P.; Badro, J.; Varrel, B.; McMillan, P. F. *Phys. Rev. B* **1995**, *51* (17), 11262.

(243) Sharma, S. M.; Garg, N.; Sikka, S. K. *Phys. Rev. B* **2000**, *62* (13), 8824.

(244) Itié, J. P.; Tinoco, T.; Polian, A.; Demazeau, G.; Matar, S.; Philippot, E. *High Press. Res.* **1996**, *14* (4–6), 269.

(245) Peters, M. .; Grimsditch, M.; Polian, A. *Solid State Commun.* **2000**, *114* (6), 335.

(246) Haines, J.; Cambon, O.; Cachau-Herreillat, D.; Fraysse, G.; Mallassagne, F. . *Solid State Sci.* **2004**, *6* (9), 995.

(247) Haines, J.; Cambon, O.; Fraysse, G.; Lee, A. van der. *J. Phys. Condens. Matter* **2005**, *17* (28), 4463.

(248) Angot, E.; Parc, R. Le; Levelut, C.; Beaurain, M.; Armand, P.; Cambon, O.; Haines, J. *J. Phys. Condens. Matter* **2006**, *18* (17), 4315.

(249) Haines, J.; Cambon, O.; Le Parc, R.; Levelut, C. *Phase Transitions* **2007**, *80* (10–12), 1039.

(250) Ming, L. C.; Nakamoto, Y.; Endo, S.; Chio, C. H.; Sharma, S. K. *J. Phys. Condens. Matter* **2007**, *19* (42), 425202.

(251) Charton, P.; Armand, P. *J. Non. Cryst. Solids* **2004**, *333* (3), 307.

(252) Souleiman, M.; Hermet, P.; Haidoux, A.; Levelut, C.; Haines, J.; Cambon, O. *RSC Adv.* **2013**, *3* (44), 22078.

(253) Büssem, W.; Fischer, H.; Gruner, E. *Naturwissenschaften* **1935**, *23* (43), 740.

(254) Zintl, G.; Loosen, K. *Zeitschrift für Phys. Chemie* **1935**, *174* (1), 301.

(255) Peters, J.; Krebs, B. *Acta Crystallogr. Sect. B Struct. Crystallogr. Cryst. Chem.* **1982**, *38* (4), 1270.

(256) Troyanov, S. I. *Zhurnal Neorg. Khimii* **2000**, *45* (10), 1619.

(257) Silverman, M. S.; Soulen, J. R. *Inorg. Chem.* **1965**, *4* (1), 129.

(258) Evers, J.; Mayer, P.; Möckl, L.; Oehlinger, G.; Köppe, R.; Schnöckel, H. *Inorg. Chem.* **2015**, *54* (4), 1240.

(259) Plašienka, D.; Martoňák, R.; Tosatti, E. *Sci. Rep.* **2016**, *6* (1), 37694.

(260) Evers, J.; Möckl, L.; Oehlinger, G.; Köppe, R.;

Schnöckel, H.; Barkalov, O.; Medvedev, S.; Naumov, P. *Inorg. Chem.* **2017**, *56* (1), 372.

(261) Oganov, A. R.; Gillan, M. J.; Price, G. D. *Phys. Rev. B* **2005**, *71* (6), 64104.

(262) Kuwayama, Y. *Science (80-.).* **2005**, *309* (5736), 923.

(263) Qian, G. R.; Dong, X.; Zhou, X. F.; Tian, Y.; Oganov, A. R.; Wang, H. T. *Comput. Phys. Commun.* **2013**, *184* (9), 2111.

(264) Filsø, M. Ø.; Eikeland, E.; Zhang, J.; Madsen, S. R.; Iversen, B. B. *Dalt. Trans.* **2016**, *45* (9), 3798.

(265) Oganov, A. R.; Ma, Y.; Lyakhov, A. O.; Valle, M.; Gatti, C. *Rev. Mineral. Geochemistry* **2010**, *71* (1), 271.

(266) Hellmann, H. *J. Chem. Phys.* **1935**, *3* (1), 61.

(267) Hamann, D. R.; Schlüter, M.; Chiang, C. *Phys. Rev. Lett.* **1979**, *43* (20), 1494.

(268) Dong, J.; Tomfohr, J. K.; Sankey, O. F.; Leinenweber, K.; Somayazulu, M.; McMillan, P. F. *Phys. Rev. B* **2000**, *62* (22), 14685.

(269) Parker, V. B. *Thermal properties of aqueous uni-univalent electrolytes*; US Government Printing Office Washington, DC, USA, 1965; Vol. 2.

(270) Huheey, J. E.; Cottrell, T. L. *Butterworths, London* **1958**.

Appendixes

Appendix 1. VASP input files & Constraints

1.1 INCAR for USPEX

To have accurate relaxation and low computational costs, I adopted the 5 steps of relaxation for each structure, *i.e.*, five INCAR files. The initial steps only relax atoms and cell shape at constant volume. I then performed full optimization with very accurate criterions. Below, I provide an example of INCAR files for Ba-N systems.

```
SYSTEM = INCAR_1
PREC = LOW
EDIFF = 1e-2
IBRION = 2
ISIF = 4
NSW = 100
ISMEAR = 1 ; SIGMA = 0.10
ISTART = 0
#Crude optimisation
LCHARG = FALSE
LWAVE = FALSE
NCORE = 4
```

```
SYSTEM = INCAR_2
PREC = Normal
EDIFF = 1e-3
IBRION = 1
ISIF = 4
NSW = 100
ISMEAR = 1 ; SIGMA = 0.08
POTIM = 0.30
LCHARG = FALSE
LWAVE = FALSE
#Crude optimisation
NCORE = 4
```

```
SYSTEM = INCAR_3
PREC = Normal
EDIFF = 1e-3
IBRION = 2
ISIF = 3
NSW = 100
ISMEAR = 1 ; SIGMA = 0.07
POTIM = 0.20
ISTART = 0
LCHARG = FALSE
LWAVE = FALSE
NCORE = 4
```

```
SYSTEM = INCAR_4
PREC = Normal
ENCUT = 500.00
EDIFF = 1e-4
IBRION = 2
ISIF = 3
NSW = 100
ISMEAR = 1 ; SIGMA = 0.06
POTIM = 0.10
ISTART = 0
LCHARG = FALSE
LWAVE = FALSE
NCORE = 4
```

```
SYSTEM = INCAR_5
PREC = Accurate
ENCUT = 550.00
EDIFF = 1e-4
IBRION = 2
ISIF = 3
NSW = 100
ISMEAR = 1 ; SIGMA = 0.05
POTIM = 0.05
ISTART = 0
LCHARG = FALSE
LWAVE = FALSE
NCORE = 4
```

1.2 INCAR and POSCAR for projected DOS of empty sphere (Chapter 3.2)

To plot the projected DOS in a vacuum sphese, the INCAR and POSCAR are provided below. The projected vacuum DOS is in the last column of DOSCAR. You may use *split_dos.py* from http://theory.cm.utexas.edu/vtsttools/ to get the split DOS.

```
SYSTEM = Ba3N2
PREC = Accurate
ENCUT = 600.00
EDIFF = 1e-5
IBRION = -1
ISIF = 3
NSW = 0
ISMEAR = 1
SIGMA = 0.05
ISTART = 0
PSTRESS = 0
NCORE = 4
LORBIT = 1
# The 1st, 2nd represent the RWIGS of
elements and 3rd one is for empty
sphere (unit = Angstrom)
RWIGS = 1.8405 1.20 1.6
NEDOS = 801
```

```
POSCAR
1.0000
7.0198     0.0112     0.3044
3.0815     6.3131     0.1416
-1.8921     2.4820     7.6276
Ba     N
6      4
Direct
0.3991   0.9342   0.1854 Ba
0.6008   0.0657   0.8145 Ba
0.9341   0.3990   0.8145 Ba
0.0658   0.6009   0.1854 Ba
0.7121   0.2878   0.2083 Ba
0.2878   0.7121   0.7916 Ba
0.0550   0.9449   0.9504 N
0.9449   0.0550   0.0495 N
0.3282   0.3282   0.0000 N
0.6717   0.6717   0.9999 N
Empty (vacuum sphere position)
3
0.5000     0.5000    0.5000
0.1899     0.1899    0.5000
0.8000     0.8000    0.5000
```

1.3 INCAR for phonopy

In this work, first principles phonon calculations with a finite displacement method at quasi-harmonic level were performed, using the open source package Phonopy. Supercell structures with displacements are created from a unit cell fully considering crystal symmetry. Force constants are calculated using the structure files POSCAR (VASP code). The INCAR files to calculate the phonon frequency are shown below. The first step is to get a highly optimized structure. People should use force, not energy, as the converge criterion. Once the structural optimization is completed, copy the CONTCAR to POSCAR into a new folder, and use (phonopy -d –dim= “a b c”, where a, b and c represent the number of supercells in each direction). Normally, the lattice parameter of the supercell around 10 Å is large enough. Then Phonopy will generate numerous supercells with different displacements. Now use the second INCAR and Gamma point only to calculate these supercells.

```
SYSTEM = Phonon_opt
PREC = Accurate
ENCUT = 600.00
EDIFF = 1e-8
EDIFFG = -1e-8
IBRION = 2
ISIF = 3
NSW = 200
ISMEAR = -5 ; SIGMA = 0.05
ISTART = 0
LCHARG = FALSE
LWAVE = FALSE
NCORE = 4
PSTRESS= 0
KSPACING = 0.2
```

```
SYSTEM = Phonon
PREC = Accurate
ENCUT = 600.00
EDIFF = 1e-8
IBRION = -1
NSW = 0
ISMEAR = 1 ; SIGMA = 0.05
ISTART = 0
LCHARG = FALSE
LWAVE = FALSE
PSTRESS= 0
IALGO = 38
LREAL = .FALSE.
ADDGRID = .TRUE.
NCORE = 4
KSPACING = 1
```

1.4 INCAR for projected DOS

The calculation can be divided into two steps. First, perform a static, selfconsistent calculation. Note that the ICHARG option should be true. In the second step, a non-selfconsistent calculation can be performed by using the precalculated CHGCAR file from the selfconsistent..

```
SYSTEM = DOS_self
PREC = Accurate
ENCUT = 600.00
EDIFF = 1e-5
IBRION = -1
NSW = 0
ISMEAR = -5 ; SIGMA = 0.05
ISTART = 0
NCORE = 4
PSTRESS=0
LORBIT = 11
#ICHARG = 11
LCHARG = TRUE
LWAVE = TRUE
```

```
SYSTEM = DOS_self
PREC = Accurate
ENCUT = 600.00
EDIFF = 1e-5
IBRION = -1
NSW = 0
ISMEAR = -5 ; SIGMA = 0.05
ISTART = 1
NCORE = 4
PSTRESS=0
LORBIT = 11
ICHARG = 11
LCHARG = TRUE
LWAVE = TRUE
```

1.5 INCAR file for Lobster

In this case, the calculation is similar, with a single point calculation. The difference is that the number of bands has to be set up (NBANDS). It’s meaningless if the number of bands is too low. And the symmetry has to be turned off completely, *i.e.*, ISYM=-1.

1.6 INCAR file for HSE06 calculation

Normally, I perform a static standard DFT calculation first, then start Hartree-Fock type calculations from a preconverged WAVECAR file.

```
SYSTEM = HSE06
PREC = Accurate
ENCUT = 600.00
EDIFF = 1e-4
IBRION = -1
ISIF = 3
NSW = 0
ISMEAR = -5
SIGMA = 0.05
ISTART = 1
LCHARG = TRUE
LWAVE = TRUE
PSTRESS = 100
NPAR = 4
LHFCALC = TRUE
HFSCREEN = 0.2
ALGO = Damped
IALGO = 53
TIME = 0.4
```

1.7 Structural constraint in Li-CO_2 (Chapter 2)

```
# Ovito 2.5.1 (https://ovito.org/)
from ovito.io import import_file
from ovito.data import CutoffNeighborFinder
import os

# Load input simulation file.
node = import_file('CONTCAR')
data = node.source
num_particles = data.position.size
# Initialize neighbor finder object:
cutoff = 3
dis_AX = 1.2
dis_BB = 1.5
dis_CC = 1.4
dis_BC = 1.5
finder = CutoffNeighborFinder(cutoff, data)
# Iterate over all input particles:
raw_list = list()
for index in range(num_particles):
# Iterate over the neighbors of the current particle:
for neigh in finder.find(index):
rawline = '%02d          %02d          %.5f          %s\n'%(index,neigh[0],neigh[1],neigh[3])
raw_list.append(rawline)
# Read the POSCAR to Get the number of each element
#This step is only for Na-C-O system
poscar = open('CONTCAR', 'r')
pos_cont = poscar.readlines()
line_num = pos_cont[6]
elem_num = line_num.split()
if len(elem_num) == 3:
A = int(elem_num[0])- 1
B = int(elem_num[1])+ A
C = int(elem_num[2])+ B
else:
A = -10
B = -10
C = -10
poscar.close()
#Final OUTPUT
```

```
output = open('OUTPUT.txt','w')
#for bondlist in indivi:
#       output.write(bondlist)
#Calculate the bonds of each atom
TF = 0
TF1 = 0
TF2 = 0
TF3 = 0
TF4 = 0
for atom_id in range(num_particles):
bond_BB = 0
bond_CC = 0
bond_AX = 0
bond_BC = 0
Criterion = 0
for elem in raw_list:
elem_1 = int(elem.split()[0])
elem_2 = int(elem.split()[1])
distance = float(elem.split()[2])
# For atom_id(i), if there is no bond with atom_id(i), continue
if atom_id != elem_1:
continue
# I don't care the pure A or pure BC.
elif A == -10 and B == -10 and C == -10:
continue
else:
# number of Li--X bond
if elem_1 <= A and distance < dis_AX:
bond_AX = bond_AX + 1
output.write(elem)
# number of O--O bond
elif elem_1 > B and elem_2 > B and distance < dis_CC:
bond_CC = bond_CC + 1
output.write(elem)
# number of C--C bond
elif elem_1 <= B and elem_1 > A and elem_2 <= B and elem_2 > A and distance < dis_BB:
bond_BB = bond_BB + 1
output.write(elem)
# number of C--O bond
elif elem_1 <= B and elem_1 > A and elem_2 > B and distance < dis_BC:
bond_BC = bond_BC + 1
```

```
output.write(elem)
elif elem_1 > B and elem_2 <= B and elem_2 > A and distance < dis_BC:
bond_BC = bond_BC + 1
output.write(elem)
else:
continue
if bond_AX > 0:
Criterion = 1
TF1 = Criterion + TF1
if bond_CC > 0:
Criterion = 1
TF2 = Criterion + TF2
if bond_BB > 3:
Criterion = 1
TF3 = Criterion + TF3
if bond_BB == 3 and bond_BC == 0:
Criterion = 1
TF4 = Criterion + TF4
TF = TF1 + TF2 + TF3 + TF4
if bond_BB != 0 or bond_CC != 0 or bond_AX != 0 or bond_BC != 0:
output.write('Atom ID:|%02d|    O-O:|%02d|    C-C:|%02d|    C-O:|%02d| Li-X|%02d|
\n'%(atom_id,bond_CC,bond_BB,bond_BC,bond_AX))
output.close()
feedback = open('distNum','w')
if TF > 0 :
feedback.write('False')
else:
feedback.close()
```

Appendix 2. Crystal structures information

Table A1. Structural parameters of the predicted $Li_x(CO_2)_y$ compounds at selected pressures (Chapter 2) (distances in Å, angles in °, pressure in GPa).

Phase	Z	P	Space Group	Lattice Parameters	Atomic coordinates (fractional)
Li_2CO_2	4	0	*C2/m*	a=4.261, b=9.269, c=4.097 α=90.0, β=86.9, γ=90.0	Li (0.209, 0.158, 0.240); C (0.618, 0.000, 0.375); O (0.740, 0.873, 0.253)
$Li_3(CO_2)_2$	2	0	*P*-1	a=5.101, b=6.519, c=5.273 α=90.9, β=104.2, γ=108.8	Li (0.245, 0.044, 0.946), (0.252, 0.559, 0.883), (0.997, 0.800, 0.493); C (0.469, 0.103, 0.421), (0.574, 0.292, 0.645); O (0.159, 0.602, 0.273), (0.391, 0.328, 0.755), (0.361, 0.843, 0.755), (0.823, 0.948, 0.700)
$LiCO_2$	4	0	$P2_1/c$ *(I)*	a=4.202, b=4.651, c=10.044 α=90.0, β=115.5, γ=90.0	Li (0.786, 0.997, 0.787); C (0.623, 0.873, 0.500); O (0.833, 0.777, 0.626), (0.591, 0.785, 0.376)
$LiCO_2$	4	10	$P2_1/c$ *(II)*	a=5.566, b=5.833, c=4.948 α=90.0, β=125.4, γ=90.0	Li (0.022, 0.130, 0.260); C (0.498, 0.433, 0.634); O (0.246, 0.389, 0.567), (0.742, 0.380, 0.895)
Li_2CO_2	4	50	*Pnma*	a=5.380, b=2.581, c=8.301 α=90.0, β=90.0, γ=90.0	Li (0.887, 0.250, 0.894), (0.784, 0.250, 0.200); C (0.950, 0.250, 0.540); O (0.524, 0.250, 0.801), (0.802, 0.750, 0.025)
$Li_3(CO_2)_2$	2	50	*P*-1	a=4.790, b=5.305, c=4.790 α=76.5, β=105.9, γ=112.0	Li (0.218, 0.993, 0.952), (0.239, 0.450, 0.995), (0.989, 0.757, 0.512); C (0.478, 0.134, 0.400), (0.583, 0.306, 0.633); O (0.134, 0.620, 0.253), (0.387, 0.344, 0.735), (0.339, 0.797, 0.790), (0.824, 0.892, 0.730)
$LiCO_2$	4	50	*P2/c*	a=6.207, b=4.939, c=4.070 α=90.0, β=131.9, γ=90.0	Li (0.000, 0.114, 0.250), (0.500, 0.121, 0.750); C (0.163, 0.627, 0.424); O (0.261, 0.391, 0.695), (0.750, 0.149, 0.354)
$Li_3(CO_2)_4$	4	50	*C2*	a=8.949, b=9.767, c=6.209 α=90.0, β=136.8, γ=90.0	Li (0.717, 0.222, 0.434), (0.794, 0.282, 0.008), (0.000, 0.309, 0.500), (0.500, 0.312, 0.500); C (0.400, 0.436, 0.960), (0.103, 0.442, 0.176), (0.959, 0.059, 0.570), (0.616, 0.064, 0.773); O (0.281, 0.058, 0.712), (0.227, 0.059, 0.205), (0.462, 0.439, 0.247), (0.971, 0.448, 0.258), (0.294, 0.326, 0.807), (0.203, 0.329, 0.266), (0.453, 0.177, 0.249), (1.000, 0.172, 0.291)

$Li(CO_2)_2$	4	50	*P*1	a=4.410, b=7.965, c=5.121 α=81.0, β=90.0, γ=102.6	Li (0.756, 0.514, 0.061), (0.743, 0.488, 0.569), (0.244, 0.507, 0.875), (0.254, 0.494, 0.383); C (0.953, 0.200, 0.297), (0.546, 0.805, 0.647), (0.955, 0.203, 0.804), (0.542, 0.795, 0.154), (0.040, 0.787, 0.630), (0.460, 0.217, 0.270), (0.036, 0.777, 0.320), (0.461, 0.223, 0.957); O (0.010, 0.342, 0.146), (0.490, 0.662, 0.568), (0.011, 0.341, 0.650), (0.485, 0.657, 0.069), (0.979, 0.639, 0.776), (0.520, 0.366, 0.341), (0.978, 0.620, 0.292), (0.520, 0.379, 0.849), (0.675, 0.117, 0.379), (0.825, 0.889, 0.687), (0.167, 0.117, 0.890), (0.331, 0.882, 0.196), (0.335, 0.890, 0.686), (0.165, 0.115, 0.379), (0.824, 0.878, 0.198), (0.674, 0.119, 0.889)
$Li_3(CO_2)_2$	2	100	*C2/m*	a=8.756, b=2.328, c=7.591 α=90.0, β=143.3, γ=90.0	Li (0.144, 0.000, 0.028), (0.000, 0.500, 0.500); C (0.179, 0.500, 0.388); O (0.055, 0.500, 0.781), (0.731, 0.000, 0.270)
$Li_3(CO_2)_4$	2	100	*P*1	a=4.352, b=7.850, c=4.688 α=89.5, β=90.4, γ=89.9	Li (0.420, 0.244, 0.364), (0.921, 0.234, 0.380), (0.415, 0.750, 0.355), (0.416, 0.995, 0.591), (0.420, 0.494, 0.588), (0.919, 0.497, 0.590); C (0.753, 0.986, 0.129), (0.085, 0.003, 0.104), (0.086, 0.502, 0.113), (0.753, 0.488, 0.104), (0.248, 0.248, 0.851), (0.583, 0.233, 0.852), (0.668, 0.744, 0.851), (0.160, 0.755, 0.839); O (0.185, 0.069, 0.328), (0.172, 0.333, 0.100), (0.665, 0.419, 0.334), (0.665, 0.157, 0.105), (0.658, 0.662, 0.092), (0.178, 0.828, 0.082), (0.174, 0.576, 0.335), (0.675, 0.913, 0.351), (0.150, 0.824, 0.609), (0.656, 0.906, 0.863), (0.674, 0.163, 0.628), (0.149, 0.081, 0.851), (0.175, 0.587, 0.855), (0.671, 0.409, 0.859), (0.164, 0.325, 0.622), (0.665, 0.672, 0.622)
$Li(CO_2)_2$	4	100	*P*-1	a=4.314, b=7.542, c=4.582 α=81.3, β=89.9, γ=98.2	Li (0.498, 0.505, 0.248), (0.995, 0.495, 0.751); C (0.177, 0.210, 0.575), (0.822, 0.791, 0.929), (0.321, 0.783, 0.845), (0.679, 0.218, 0.486); O (0.206, 0.322, 0.295), (0.205, 0.322, 0.795), (0.278, 0.616, 0.972), (0.720, 0.385, 0.529), (0.900, 0.113, 0.601), (0.099, 0.888, 0.906), (0.406, 0.113, 0.093), (0.595, 0.887, 0.400)
Li_2CO_2	4	0 Quench	*Pnma*	a=5.896, b=2.813, c=8.833 α=90.0, β=90.0, γ=90.0	Li (0.892, 0.250, 0.901), (0.794, 0.250, 0.205); C (0.950, 0.250, 0.540); O (0.510, 0.250, 0.805), (0.789, 0.750, 0.023)
$LiCO_2$	4	0 Quench	*P2/c*	a=7.298, b=5.559, c=4.257 α=90.0, β=131.9, γ=90.0	Li (0.000, 0.102, 0.750), (0.500, 0.205, 0.250); C (0.143, 0.623, 0.923); O (0.233, 0.409, 0.204), (0.775, 0.172, 0.866)

Table A2. Structural parameters of lithium, carbon, oxygen, carbon dioxide, lithium oxide Li_2O, lithium carbonate $Li_2(CO_3)$ compounds at selected pressures. (distances in Å, angles in °, pressure in GPa) (Chapter 2)

Phase	Z	P	Space Group	Lattice Parameters	Atomic coordinates (fractional)
C	4	0	$P6_3/mmc$	a=2.467, b=2.467, c=7.806 α=90.0, β=90.0, γ=120.0	C (0.000, 0.000, 0.250), (0.333, 0.667, 0.250)
C	8	10	*Fd*-3*m*	a=3.546, b=3.546, c=3.546 α=90.0, β=90.0, γ=90.0	C (0.000, 0.500, 0.500)
CO_2	4	0	*Pa*-3	a=5.858, b=5.858, c=5.858 α=90.0, β=90.0, γ=90.0	C (0.000, 0.000, 0.000); O (0.116, 0.116, 0.116)
CO_2	4	50	*I*-42*d*	a=3.532, b=3.532, c=3.532 α=90.0, β=90.0, γ=90.0	C (0.500, 0.500, 0.000); O (0.705, 0.750, 0.125)
Li_2O	4	0	*Fm*-3*m*	a=4.619, b=4.619, c=4.619 α=90.0, β=90.0, γ=90.0	Li (0.250, 0.750, 0.750); O (0.000, 0.000, 0.000)
Li_2O	4	50	*Pnma*	a=4.551, b=2.796, c=5.309 α=90.0, β=90.0, γ=90.0	Li (-0.978, 0.750, 0.177), (-0.850, 0.750, 0.575); O (-0.755, 0.250, 0.393)
Li_2CO_3	4	0	*C2/c*	a=8.364, b=5.009, c=6.312 α=90.0, β=114.2, γ=90.0	Li (0.699, 0.051, 0.839); C (0.000, 0.935, 0.250); O (0.148, 0.065, 0.315), (0.000, 0.678, 0.250)
Li_2CO_3	2	10	$P6_3/mcm$	a=4.494, b=4.494, c=5.129 α=90.0, β=90.0, γ=120.0	Li (0.333, 0.667, 0.500); C (0.000, 0.000, 1.250); O (0.712, 0.712, 0.750)
Li	2	0	*Im*-3*m*	a=3.427, b=3.427, c=3.427 α=90.0, β=90.0, γ=90.0	Li (0.000, 0.000, 0.000)
Li	4	10	*Fm*-3*m*	a=3.799, b=3.799, c=3.799 α=90.0, β=90.0, γ=90.0	Li (0.000, 0.000, 0.000)
Li	16	50	*I*-43*d*	a=5.105, b=5.105, c=5.105 α=90.0, β=90.0, γ=90.0	Li (0.307, 0.193, 0.807)
Li	24	100	*Cmca*	a=7.825, b=4.297, c=4.297 α=90.0, β=90.0, γ=90.0	Li (0.334, 0.891, 0.657), (0.500, 0.674, 0.562)
O	4	0	*C2/m*	a=8.186, b=3.677, c=5.452 α=90.0, β=,148.6 γ=90.0	O (1.000, 0.089, 0.000)
O	16	10	*C2/m*	a=7.741, b=5.630, c=3.849 α=90.0, β=114.8, γ=90.0	O (0.034, 0.263, 0.175), (0.231, 0.000, 0.187), (0.161, 0.000, 0.836)

Table A3. Structural parameters of the barium and nitrogen ground stable compounds at selected pressures (distances in Å, angles in °, pressure in GPa). (Chapter 3.3 and 3.4)

Phase	P	Space Group	Lattice Parameters	Atomic coordinates (fractional)
Mg	0	$P6_3/mmc$	a=3.203, b=3.203, c=5.105 α=90.0, β=90.0, γ=120.0	Mg(0.333, 0.667, 0.250), (0.667, 0.333, 0.750)
Mg	100	*Im*-3*m*	a=2.827, b=2.827, c=2.827 α=90.0, β=90.0, γ=90.0	Mg(0.000, 0.000, 0.000), (0.500, 0.500, 0.500)
Ba	0	*Im*-3*m*	a=5.041, b=5.041, c=5.041 α=90.0, β=90.0, γ=90.0	Ba(0.000, 0.000, 0.000)
Ba	10	$P6_3/mmc$	a=3.779, b=3.779, c=5.728 α=90.0, β=90.0, γ=120.0	Ba(0.333, 0.667, 0.750)
N	0	*Pa*-3	a=5.856, b=5.856, c=5.856 α=90.0, β=90.0, γ=90.0	N (0.055, 0.055, 0.055)
N	10	$P2_1/c$	a=3.283, b=3.256, c=5.266 α=90.0, β=117.6, γ=90.0	N (0.855, 0.611, 0.458)
N	10	$P4_12_12$	a=3.267, b=3.267, c=9.328 α=90.0, β=90.0, γ=90.0	N (0.458, 0.317, 0.729)
N	10	*Pbcn*	a=3.248, b=5.242, c=5.793 α=90.0, β=90.0, γ=90.0	N (0.112, 0.857, 0.823)
N	100	$I2_13$	a=3.513, b=3.513, c=3.513 α=90.0, β=90.0, γ=90.0	N (0.676, 0.324, 0.824)
N	250	*Pba*2	a=4.178, b=4.164, c=3.970 α=90.0, β=90.0, γ=90.0	N (0.293, 0.217, 0.661) (0.785, 0.217, 0.340), (0.021, 0.336, 0.177), (0.838, 0.017, 0.822)
N	300	*I*-43*m*	a=4.287, b=4.287, c=4.287 α=90.0, β=90.0, γ=90.0	N (0.353, 0.000, 0.000), (0.675, 0.675, 0.675)

Table A4. Calculated enthalpies of the Mg, Ba and N at different pressure. (Chapter 3.3 and 3.4)

Phase	P	Space Group	Enthalpy (eV/atom)
Mg	0	$P6_3/mmc$	-1.542
Mg	100	*Im*-3*m*	7.544
Ba	0	*Im*-3*m*	-1.924
Ba	10	$P6_3/mmc$	0.920
N	0	*Pa*-3	-8.320
N	10	$P2_1/c$	-7.341
N	10	$P4_12_12$	
N	10	*Pbcn*	
N	100	$I2_13$	-3.067
N	250	*Pba*2	1.457
N	300	*I*-43*m*	2.727

Table A5. Structural parameters of the predicted Mg_xN_y compounds at selected pressures (Chapter 3.3) (distances in Å, angles in °, pressure in GPa).

Phase	Z	P	Space Group	Lattice parameters	Atomic coordinates (fractional)
Stable compounds					
Mg_5N_3	2	150	$P6_3/mcm$	a=5.472, c=4.246	Mg (0, 0.749, 0.75) (0.333, 0.667, 1); N (0, 0.388, 0.75)
Mg_3N_2	16	0	*Ia*-3	a=9.992	Mg (0.118, 0.389, 0.847); N (0.25, 0.25, 0.75) (0.031, 0.5, 0.25)
Mg_3N_2	4	30	*Pbcn*	a=7.353, b=5.141 c=5.242	Mg (0.152, 0.106, 0.607) (0, 0.547, 0.750); N (0.615, 0.753, 0.532)
Mg_3N_2	6	50	*C2/m*	a=11.931,b=3.074, c=7.485, β=99.1	Mg (0.130, 0.5, 0.288) (0.797, 0.5, 0.369) (0.828, 0.5, 0.03) (0.971, 0, 0.34) (0, 0, 0) N (0.033, 0.5, 0.814) (0.863, 0, 0.515) (0.815, 0, 0.863)
Mg_3N_2	4	40	*Pnma*	a=5.280, b=2.967 c=11.427	Mg (0.361, 0.250, 0.561) (0.525, 0.250, 0.106) (0.636, 0.250, 0.718); N (0.168, 0.250, 0.197) (0.238, 0.750, 0.452)
Mg_4N_3	4	100	*I*-43*d*	a=5.873	Mg (0.321, 0.179, 0.821) N (0.625, 0, 0.75)
Mg_5N_4	4	200	*Cmca*	a=9.487, b=4.793 c=4.811	Mg (0.147, 0.324, 0.671) (0, 0.5, 1) N (0, 0.11, 0.889) (0.2, 0.5, 1)
Mg_5N_7	2	250	*C2*	a=5.67, b=4.517 c=5.005, β=98.6	Mg (0.739, 0, 0.213) (0.323, 0.502, 0.79) (0, 0.363, 0.5);N (0.561, 0.22, 0.906) (0.812, 0.731, 0.501) (0.556, 0.785, 0.894) (0, 0.917, 0.5)
Mg_2N_3	2	50	*Pmmn*	a=9.104,b=2.728 c=3.071	Mg (0.147, 0, 0.726) N (0.868, 0.5, 0.213) (0, 0.5, 0.428)
MgN_2	4	40	*Cmcm*	a=3.805,b=7.777,c=3.192	Mg (0, 0.363, 0.75) N (0.664, 0.603, 0.75)
MgN_2	4	100	$P6_3/mcm$	a=4.387, c=4.782	Mg (0.667, 0.333, 0) N (0, 0, 0.25) (0, 0.292, 0.25)
MgN_3	2	200	*P*-1 (II)	a=3.574, b=3.551 c=3.598, α=101 β=69.4, γ=105	Mg (0.122, 0.824, 0.135); N (0.335, 0.373, 0.11) (0.314, 0.515, 0.487) (0.306, 0.895, 0.58)
MgN_3	2	50	*P*-1 (I)	a=4.866, b=4.830 c=2.768, α=78.7 β=78.7, γ=61.2	Mg (0.667, 0.671, 0.478) N (0.796, 0.306, 0.054) (0.692, 0.106, 0.981) (0.903, 0.814, 0.856)
MgN_4	2	100	*Cmmm*	a=3.521, b=7.312 c=2.393	Mg (0.667, 0, 0) N (0.684, 0.166, 0.5)
MgN_4	1	10	*P*-1	a=3.059, b=3.812 c=4.075, α=101.7 β=86.2, γ=69.4	Mg (0, 0,0.5); N (0.578, 0.516, 0.852) (0.443, 0.126, 0.159)
Metastable compounds					
Mg_5N_3	4	0	*Cmcm*	a=4.113, b=10.414, c=10.558	Mg (1, 0.191, 0.575) (1, 0.259, 0.25) (1, 0.548, 0.116); N (1, 0.306, 0.75) (1, 0.356, 0.437)
Mg_3N_2	1	100	*P*-3*m*1	a=3.14, c=4.528 a=3.177, c=4.784	Mg (0.333, 0.667, 0.665) (0, 0, 0) N (0.333, 0.667, 0.227)
Mg_4N_3	4	0	*C2*	a=9.937, b=5.502 c=13.599,	Mg (0, 0.162, 1) (0.115, 0.314, 0.861) (0.266, 0.105, 0.773) (0.360, 0.265, 0.605) (0, 0.6,

				β=154.1	0.5); N (0.254, 0.958, 0.917) (0.105, 0.454, 0.704) (0.148, 0.952, 0.556)
Mg_5N_4	3	0	*R*3*m*	a=3.420 c=31.208	Mg (0, 0, 0.611) (0, 0, 0.340) (0, 0, 0.477) (0, 0, 0.076) (0, 0, 0.881); N (0, 0, 0.541) (0, 0, 0.970) (0, 0, 0.778) (0, 0, 0.721)
Mg_5N_7	2	0	*Imm*2	a=22.821 b=3.389, c=4.133	Mg (0.132, 0.5, 0.199) (0.558, 0.5, 0.210) (0.5, 0, 0.711); N (0.218, 0.5, 0.561) (0.190, 0.5, 0.790) (0.414, 0.5, 0.712) (0.5, 0, 0.211)
Mg_2N_3	2	0	*C2/m*	a=5.631, b=3.131 c=7.310, β=113.7	Mg (0.089, 0.5, 0.846); N (0.956, 0, 0.412) (0.5, 0.5, 0)
MgN_2	4	0	*Cm*	a=5.686, b=3.274 c=10.026, β=128.2	Mg (0.735, 0, 0.442) (0.180, 0.5, 0.699); N (0.465, 0.5, 0.965) (0.220, 0, 0.582) (0.186, 0, 0.257) (0.071, 0, 0.109)
MgN_3	4	0	*C2/m*	a=9.285, b=3.104 c=6.229, β=100.3	Mg (0.379, 0.5, 0.755); N (0.282, 0.5, 0.212) (0.382, 0.5, 0.116) (0.451, 0, 0.551)
MgN_4	1	0	*P2/m*	a=5.484, b=3.097 c=4.199, β=94.4	Mg (0, 0, 0); N (0.999, 0.5, 0.644) (0.397, 0, 0.014)
MgN_4	4	205	*C2/c*	a=5.912, b=3.678 c=4.697, β=97.6	Mg (0, 0.047, 0.75); N (0.079, 0.597, 0.956) (0.246, 0.392, 0.914)

Table A6. Structural parameters of the predicted Ba_xN_y compounds at selected pressures (Chapter 3.4) (distances in Å, angles in °, pressure in GPa).

Phase	P	Z	Space Group	Lattice Parameters	Atomic coordinates (fractional)
Ground stable phase					
Ba_3N	0	2	$P6_3/mcm$	a=7.728, b=7.728, c=7.096 α=90.0, β=90.0, γ=120.0	Ba (0.000, 0.273, 0.250); N (0.000, 0.000, 0.500)
Ba_2N	0	3	*R*-3*m*	a=4.059, b=4.059, c=22.854 α=90.0, β=90.0, γ=120.0	Ba (0.667, 0.333, 0.101); N (0.333, 0.667, 0.167)
Ba_2N	10	1	*P*-3*m*1	a=3.724, b=3.724, c=5.837 α=90.0, β=90.0, γ=120.0	Ba (0.667, 0.333, 0.256); N (0.000, 0.000, 0.000)
Ba_2N	100	2	*I4/mmm*	a=2.996, b=2.996, c=9.514 α=90.0, β=90.0, γ=90.0	Ba (0.000, 0.000, 0.857); N (0.500, 0.500, 0.000)
Ba_3N_2	10	2	*P*-1	a=3.837, b=6.607, c=9.018 α=96.0, β=98.9, γ=80.1	Ba (0.668, 0.231, 0.952), (0.770, 0.052, 0.344), (0.138, 0.499, 0.331); N (0.249, 0.165, 0.124), (0.418, 0.265, 0.557)
Ba_3N_2	50	4	*C2/c*	a=16.240, b=3.204, c=6.227 α=90.0, β=78.5, γ=90.0	Ba (0.180, 0.545, 0.166), (0.500, 0.153, 0.750); N (0.608, 0.496, 0.947)
BaN	10	4	$P2_1/c$	a=6.883, b=4.688, c=7.029 α=90.0, β=136.2, γ=90.0	Ba (0.241, 0.422, 0.994); N (0.399, 0.598, 0.459)
BaN	50	4	$P2_1/m$	a=3.295, b=5.512, c=6.449 α=90.0, β=76.3, γ=90.0	Ba (0.300, 0.250, 0.511), (0.397, 0.750, 0.072); N (0.944, 0.122, 0.227)
BaN	100	4	*C2/m*	a=8.827, b=3.181, c=3.491 α=90.0, β=98.2, γ=90.0	Ba (0.351, 0.500, 0.787); N (0.445, 0.000, 0.338)
Ba_2N_3	50	4	*C2/m*	a=10.807, b=5.806, c=6.795 α=90.0, β=142.7, γ=90.0	Ba (0.751, 0.000, 0.953), (0.680, 0.000, 0.376),(0.000, 0.885, 0.000); N (0.937, 0.199, 0.491)
BaN_2	0	4	*C2/c*	a=7.227, b=4.485, c=8.879 α=90.0, β=126.9, γ=90.0	N (0.499, 0.102, 0.546); Ba (0.000, 0.037, 0.750)
BaN_2	50	4	*C2/m*	a=6.953, b=6.102, c=3.470 α=90.0, β=105.2, γ=90.0	Ba (0.223, 0.000, 0.469); N (0.444, 0.202, 0.112)
BaN_2	100	4	$P2_1/c$	a=2.945, b=7.859, c=5.251 α=90.0, β=87.9, γ=90.0	Ba (0.982, 0.842, 0.657); N (0.488, 0.403, 0.213), (0.553, 0.424, 0.454)
Ba_3N_8	50	2	*Cmmm*	a=5.486, b=8.557, c=5.328 α=90.0, β=90.0, γ=90.0	Ba (0.000, 0.683, 0.500), (0.500, 0.500, 0.000); N (0.000, 0.500, 0.891), (0.250, 0.250, 0.111), (0.388, 0.500, 0.500)
BaN_4	10	1	*P6/mmm*	a=4.326, b=4.326, c=4.145 α=90.0, β=90.0, γ=120.0	Ba (0.000, 0.000, 0.000); N (0.333, 0.667, 0.358)
BaN_4	50	4	$P4_12_12$	a=3.660, b=3.660, c=15.173 α=90.0, β=90.0, γ=90.0	Ba (0.844, 0.844, 0.000); N (0.639, 0.831, 0.594), (0.970, 0.860, 0.344)
BaN_4	100	4	*C2/c*	a=4.719, b=5.934, c=8.488 α=90.0, β=134.8, γ=90.0	Ba (0.500, 0.886, 0.250); N (0.243, 0.283, 0.069), (0.382, 0.490, 0.138)
BaN_5	50	4	*Imma*	a=8.897, b=4.557, c=5.622 α=90.0, β=90.0, γ=90.0	Ba (0.750, 0.250, 0.750); N (0.881, 0.750, 0.654), (0.925, 0.750, 0.883), (0.500, 0.250, 0.019)
Ba_2N_{11}	10	1	*P*-1	a=5.339, b=5.627, c=6.649 α=96.6, β=98.4, γ=118.1	Ba (0.063, 0.784, 0.266); N (0.563, 0.276, 0.955), (0.464, 0.252, 0.098), (0.082, 0.777, 0.695),(0.453, 0.286, 0.540), (0.019, 0.764, 0.855),(0.500, 0.500, 0.500)

BaN_6	0	2	*P*2$_1$*/m*	a=5.527, b=4.442, c=9.806 α=90.0, β=99.1, γ=90.0	Ba (0.671, 0.750, 0.219); N (0.208, 0.750, 0.338), (0.359, 0.250, 0.096), (0.149, 0.250, 0.110), (0.940, 0.250, 0.122), (0.721, 0.250, 0.417), (0.756, 0.250, 0.539)
BaN_{10}	50	2	*P*-1	a=4.822, b=4.656, c=8.817 α=91.7, β=77.0, γ=76.2	Ba (0.510, 0.002, 0.243); N (0.811, 0.142, 0.454),(0.830, 0.225, 0.019),(0.861, 0.287, 0.330),(0.869, 0.227, 0.868),(0.731, 0.495, 0.082),(0.803, 0.568, 0.378),(0.786, 0.502, 0.839),(0.727, 0.594, 0.529),(0.707, 0.669, 0.969),(0.265, 0.669, 0.424)
Metastable phase					
Ba_4N_3	10	2	*P*1	a=6.934, b=7.080, c=7.384 α=107.6, β=71.0, γ=74.6	Ba (0.332, 0.473, 0.424),(0.782, 0.128, 0.493), (0.966, 0.088, 0.945),(0.338, 0.606, 0.925),(0.318, 0.962, 0.398),(0.469, 0.077, 0.929),(0.825, 0.606, 0.354),(0.883, 0.534, 0.814); N (0.230, 0.263, 0.719),(0.105, 0.262, 0.315),(0.594, 0.392, 0.037),(0.710, 0.910, 0.175),(0.9290, 0.808, 0.107),(0.949, 0.827, 0.613)
Ba_4N_3	100	2	*C2/m*	a=10.272, b=3.082, c=9.257 α=90.0, β=141.5, γ=90.0	Ba (0.627, 0.000, 0.290),(0.179, 0.000, 0.807); N (0.585, 0.000, 0.527),(0.500, 0.500, 0.000)
BaN_3	100	4	*C2/c*	a=5.027, b=7.821, c=4.164 α=90.0, β=60.0, γ=90.0	Ba (0.50000, 0.36117, 0.75000); N (0.09127, 0.42754, 0.45047); N (0.00000, 0.32891, 0.75000)
BaN_5	100	2	*P*1	a=4.634, b=5.446, c=4.175 α=71.3, β=107.7, γ=94.3	Ba (0.373, 0.839, 0.917), (0.887, 0.477, 0.085); N (0.065, 0.946, 0.265),(0.361, 0.524, 0.599),(0.449, 0.200, 0.469),(0.505, 0.433, 0.438),(0.618, 0.106, 0.328),(0.017, 0.222, 0.720),(0.695, 0.873, 0.520),(0.904, 0.773, 0.453),(0.259, 0.348, 0.843),(0.898, 0.058, 0.940)
BaN_6 (Lowest)	50	2	*P*-1(I)	a=5.274, b=6.068, c=4.664 α=99.5, β=102.7, γ=115.4	Ba (0.220, 0.886, 0.153); N (0.287, 0.654, 0.665), (0.740, 0.708, 0.350), (0.220, 0.319, 0.359), (0.758, 0.459, 0.616), (0.293, 0.505, 0.838), (0.263, 0.106, 0.721)
BaN_6 (Second lowest)	50	1	*P*-1(II)	a=3.606, b=3.654, c=4.94 α=97.2, β=88.6, γ=77.1	Ba (0.000, 0.000, 0.000); N (0.377, 0.445, 0.254), (0.745, 0.717, 0.547), (0.388, 0.326, 0.694)
BaN_6	100	2	*C2/m*	a=4.311, b=4.578, c=6.100 α=90.0, β=121.1, γ=90.0	Ba (0.500, 0.000, 0.500), (0.307, 0.500, 0.232); N (0.817, 0.259, 0.917)

Table A7. Structural parameters of the predicted alkaline earth metal - pentazolate compounds at selected pressures (distances in Å, angles in °, pressure in GPa). (Chapter 3.5)

Phase	P	Z	Space Group	Lattice Parameters	Atomic coordinates (fractional)
BeN_{10}	0	4	*I*-42*d*	a=8.034, b=8.034, c=13.774 α=90.0, β=90.0, γ=90.0	Be (0.500, 0.500, 0.000); N (0.750, 0.524, 0.875), (0.655, 1.424, 0.927), (0.691, 1.264, 0.907)
BeN_{10}	50	4	*Fdd*2	a=9.498, b=8.822, c=7.058 α=90.0, β=90.0, γ=90.0	Be (0.250, -0.750, 0.219) ; N (0.317, -0.499, -0.028), (0.244, -0.382, -0.076), (0.126, -0.384, 0.016), (0.126, -0.504, 0.119), (0.242, -0.576, 0.090)
MgN_{10}	0	4	$P4_{3}2_{1}2$	a=6.662, b=6.662, c=11.881 α=90.0, β=90.0, γ=90.0	Mg (0.244, 0.245, 0.000); N (0.414, 0.760, 0.497), (0.352, 0.781, 0.391), (0.094, 0.761, 0.498), (0.255, 0.748, -0.436), (0.155, 0.781, 0.392)
MgN_{10}	50	4	*I*-42*d*	a=6.909, b=6.909, c=6.821 α=90.0, β=90.0, γ=90.0	Mg (-0.000, 0.500, 1.250); N (0.180, 0.288, 1.313), (0.135, 0.111, 1.274), (0.250, 0.000, 1.375)
CaN_{10}	0	4	*I*-42*d*	a=8.307, b=8.307, c=7.966 α=90.0, β=90.0, γ=90.0	Ca (1.000, -0.500, 0.250) ; N (0.774, -0.309, 0.180), (1.122, 0.154, 0.715), (1.028, 0.250, 0.625)
CaN_{10}	50	4	*Ibam*	a=5.573, b=8.141, c=7.453 α=90.0, β=90.0, γ=90.0	Ca (0.500, 0.500, 0.750) ; N (0.838, 0.377, 1.141), (0.429, 0.741, 1.412), (0.280, 0.963, 0.500)
SrN_{10}	0	4	*I*-42*d*	a=8.665, b= 8.665, c= 8.093 α=90.0, β=90.0, γ=90.0	Sr (0.500, 0.000, 0.750); N (0.264, 0.193, 0.679), (0.618, 0.658, 1.213), (0.528, 0.750, 1.125)
SrN_{10}	50	4	*Ibam*	a=8.222, b=5.731, c=7.641 α=90.0, β=90.0, γ=90.0	Sr (0.500, -0.500, 0.250) ; N (1.118, -0.348, 0.862), (1.247, -0.452, 0.914), (0.536, 0.217, 0.500)
BaN_{10}	0	4	*I*-42*d*	a=9.107, b= 9.107, c=8.296 α=90.0, β=90.0, γ=90.0	Ba (0.500, 0.500, 1.000) ; N (0.663, 0.116, 0.961), (0.696, 0.255, 0.928), (0.750, 0.031, 0.875)
BaN_{10}	50	2	*P*-1	a=4.822, b=4.656, c=8.817 α=91.7, β=77.0, γ=76.2	Ba (0.510, 0.002, 0.243); N (0.811, 0.142, 0.454),(0.830, 0.225, 0.019),(0.861, 0.287, 0.330),(0.869, 0.227, 0.868),(0.731, 0.495, 0.082),(0.803, 0.568, 0.378),(0.786, 0.502, 0.839),(0.727, 0.594, 0.529),(0.707, 0.669, 0.969),(0.265, 0.669, 0.424)

Table A8. Structural parameters of the predicted molybdenum dinitrides at 0 GPa (Chapter 4.3) (distances in Å, angles in °, pressure in GPa).

Phase	Z	Lattice parameters	Atomic coordinates (fractional)
$P6_3/mmc$ *(I)*	2	a=b=2.927, c=7.762	Mo (0.333, 0.667, 0.75) ; N (0, 0, 0.089)
P-6*m*2	2	a=b=2.92, c=3.901	Mo (0, 0, 0) ; N (0.333, 0.667, 0.678)
$P2_1/m$	2	a=4.252, b=2.89, c=5.212, β=113.9	Mo (0.011, 0.25, 0.717); N (0.363, 0.75, 0.705), (0.706, 0.75, 0.827)
R-3*m*	3	a=b=2.904, c=11.892	Mo (0, 0, 0) ;N (0, 0, 0.556)
*C*2/*m*	4	a=6.739, b=3.083, c=8.110, β=137.0	Mo (0.941, 0.5, 0.776); N (0.211, 0, 0.85), (0.129, 0.5, 0.536)
$P6_3/mmc$ *(II)*	2	a=b=2.887, c=8.004	Mo (0, 0, 0); N (0.333, 0.667, 0.833)
$P4_2nm$	2	a=b=4.882, c=3.044	Mo (0, 0, 0); N (0.296, 0.704, 0.881)
Pnma	4	a=5.797, b=3.628, c=9.731	Mo (0.542, 0.75, 0.373); N (0.625, 0.25, 0.437), (0.68, 0.25, 0.75)
*P*4/*mbm*	2	a=b=4.343, c=2.752	Mo (0, 0, 0); N (0.111, 0.611, 0.5)
*P*6/*mmm*	1	a=b=2.85, c=5.156	Mo (0, 0, 0); N (0, 0, 0.388)
Cm	2	a=5.521, b=3.014, c=5.822, β=111.5	Mo (0, 0, 0); N (0.154, 0.5, 0.202), (0.709, 0.5, 0.812)
$P6_3/mmc$ *(III)*	2	a=b=3.052, c=7.806	Mo (0.667, 0.333, 0.75); N (0.333, 0.667, 0.889)
*R*3*m*	3	a=b=3.012, c=13.869	Mo (0, 0, 0); N (0, 0, 0.253), (0, 0, 0.411)

Table A9. Structural parameters of the predicted Zr_xN_y at 0 GPa (Chapter 4.4)

(distances in Å, angles in °, pressure in GPa).

Phase	Space group	Lattice parameter	Position
Zr_2N	$P4_2/mnm$	a=5.426, c=3.319	Zr (0.704, 0.296, 1) N (0.5, 0.5, 0.5)
Zr_3N_2	*Immm*	a=9.921, b=3.292, c=4.542	Zr (0.319, 0, 1); (0, 0, 1) N (0.337, 0, 0.5)
Zr_4N_3	*C2/m*	a=10.836,b=3.267 c=5.645, β=100.7	Zr (0.127, 0, 0.883); (0.132, 0.5, 0.368) N (0.751, 0.5, 0.249); (0, 0.5, 0)
Zr_6N_5	*C2/m*	a=5.659, b=9.763 c=5.654, β=109.5	Zr (0.756, 0.673, 0.253); (0.759, 0.5, 0.742) N (0.5, 0.165, 0); (0.5, 0.334, 0.5); (0, 0.5, 0.5)
Zr_8N_7	*C2/m*	a=11.302,b=6.534 c=5.639, β=109.8	Zr (0.372, 0.256, 0.243); (0.628, 0, 0.241); (0.875, 0, 0.751) N (0.249, 0, 0.999); (0.25, 0.25, 0.5); (0, 0, 0.5); (0, 0.249, 1)
ZrN	*Fm*-3*m*	a=4.608	Zr (0, 0, 0) N (0.5, 0.5, 0.5)
$Zr_{15}N_{16}$	*P*-1	a=5.640,b=8.590,c=8.584, α=106.3,β=90.0, γ=77.3	Zr (0.189, 0.439, 0.126);(0.685, 0.938, 0.133); (0.622, 0.635, 0.257); (0.144, 0.124, 0.256); (0.569, 0.306, 0.378); (0.06, 0.82, 0.378); (0, 0.5, 0.5); (0.246, 0.749, 0.994); N (0.370, 0.871, 0.241); (0.442, 0.188, 0.123); (0.311, 0.563, 0.375); (0.174, 0.935, 0.63); (0.246, 0.254, 0.5); (0, 1, 0);(0.5, 0.5, 0); (0.062, 0.312, 0.874); (0.122, 0.624, 0.747)
Zr_7N_8	*P*-1	a=6.499, b=5.617,c=5.601, α=80.3,β=73.1, γ=90.0	Zr (0.867, 0.749, 0.520); (0.258, 0.999, 0.996); (0.377, 0.736, 0.507); (0, 0.5, 0) N (0.065, 0.877, 0.751); (0.563, 0.891, 0.742); (0.305, 0.365, 0.741); (0.174, 0.630, 0.262)
Zr_4N_5	*C2/m*	a=10.820, b=3.239,c=8.158, β=122.2	Zr (0.771, 0, 0.684); (0.913, 0.5, 0.115) N (0.121, 0.5, 0.379); (0.302, 0.5, 0.189); (0, 0, 0)
Zr_3N_4	*Pnma*	a=9.875, b=3.297,c=10.904	Zr (0.772, 0.75, 0.648); (0.892, 0.75, 0.907); (0.930, 0.75, 0.377) N (0.103, 0.75, 0.970); (0.494, 0.75, 0.775); (0.643, 0.75, 0.018); (0.764, 0.25, 0.787)
Zr_3N_4	*I*-43*d*	a=6.784	Zr (0.375, 0, 0.25) N (0.063, 0.063, 0.063)

Table A10. Structural parameters of the predicted $GaPO_4$ at selected pressures (Chapter 5.1) (distances in Å, angles in °, pressure in GPa).

Phase	P	Lattice parameters	Atomic coordinates (fractional)
Cmcm	20	a =5.317, b = 7.360, c = 5.927 α = β =γ= 90	Ga (0.5 0.5 0.5); P (0.5 0.142 0.75); O (0.245 0.517 0.75), (0.5 0.246 0.469)
Cmcm	32	a =5.104, b = 7.132, c = 5.792 α=β=γ=90	Ga (0.5 0.5 0.5); P (0.5 0.135 0.75); O (0.246 0.508 0.75), (0.5 0.240 0.475)
P-1	20	a=4.468, b=5.397, c=4.822 α=90, β=79.8, γ=73.9	Ga (0.510 -0.169 0.745); P (0.868 0.279 0.696); O (0.263 -0.077 0.123), (0.236 0.171 0.635), (0.764 0.308 0.413), (0.233 0.467 0.135)
*Pmn*2$_1$	20	a=5.479, b=4.529, c=4.408 α=β=γ=90	Ga (0. 0.448 0.246); P (0.5 0.138 0.184); O (0.782 0.687 0.539), (0. 0.173 0.572), (0. 0.819 0.024)
*C*2/*m*	20	a=8.826, b=5.974, c=4.374 α=γ=90, β=107.4	Ga (0. 0.248 0.0); P (-0.310 0.5 0.633); O (-0.134 0.218 0.263), (0.123 0.5 0.239), (0.139 0. 0.260)
Imma	20	a=6.248, b=5.024, c=6.556 α=β=γ=90	Ga (0. 0.003 -0.5), (0.5 0.159 0.0); P (0.692 -0.032 -0.360); O (0.374 0.208 -0.748), (0.368 -0.259 -0.761), (0.359 -0.034 -0.303), (0.125 -0.039 -0.762)
*C*2	20	a=9.095, b=5.304, c=4.779 α=γ=90, β=110.6	Ga (0. 0.003 -0.5), (0.5 0.159 0.0); P (0.692 -0.032 -0.359); O (0.374 0.208 -0.748), (0.368 -0.259 -0.761), (0.359 -0.039 -0.762), (0.125 -0.039 -0.762)

Table A11. Structural parameters of the predicted SiS_2 at selected pressures (Chapter 5.2) (distances in Å, angles in °, pressure in GPa).

Phase	P	Lattice parameters	Atomic coordinates (fractional)
P-3*m*1	20	a= 3.153, b=3.153, c= 5.041 α=90.0, β=90.0, γ=120.0	Si (0.000, 0.000, 0.500); S (0.333, 0.667, 0.240)
P-1	200	a=2.584, b=3.918, c=5.115 α=78.8, β=79.2, γ=77.2	Si (-1.066, -0.902, -1.297); S (0.260, -0.721, -0.032), (0.421, -0.672, -0.621)
Cm	250	a=10.405, b=3.476, c= 12.770 α=90.0, β=144.5, γ=90.0	Si (0.667, -0.000, 0.888), (0.333, -0.000, 0.443), (0.166, -0.500, 0.553), (0.500, -0.500, 0.662), (0.164, -0.500, 0.217), (0.001, -1.000, 0.329); S (0.000, -0.000, 0.161), (0.660, -0.000, 0.715), (0.833, -0.500, 0.944), (-0.166, -0.500, 0.279), (0.501, -0.500, 0.827), (0.496, -0.500, 0.985), (0.174, -0.500, 0.392), (-0.154, -0.500, 0.124), (0.321, -1.000, 0.767), (-0.333, -1.000, 0.052), (0.333, -1.000, 0.608), (-0.006, -1.000, 0.490)
*P*2$_1$/*m*	300	a=4.168, b= 3.442, c=5.894 α=90.0, β=90.0, γ=90.0	Si (0.665, 0.250, 0.582), (0.003, 0.250, 0.250); S (0.844, 0.250, 0.917), (0.501, 0.250, 0.25308), (0.349, 0.250, 0.91291), (0.164, 0.250, 0.581)
Pmmm	500	a=6.877, b=2.283, c= 4.577 α=90.0, β=90.0, γ=90.0	Si (0.337, -0.000, 0.500), (0.000, 0.000, 0.000), (0.000, 0.000, 0.500); S (0.326, -0.000, 0.000), (0.166, 0.500, 0.253), (0.500, 0.500, 0.242)

Appendix 3. Energy information

Table A12. Calculated enthalpies of the predicted $Li_x(CO_2)_y$ compounds at different pressure. (Chapter 2)

Structure	**Space Group**	**Pressure (GPa)**	**Enthalpy (eV/atom)**	**ZPE (eV/atom)**	**Formation Enthalpy[a] (eV/atom)**	**Reaction Enthalpy[b] (eV/atom)**	**Distance to the true convex hull (eV/atom)**
Li_2CO_2	*C2/m*	0	-6.097	0.094	-1.516	-0.724	0.200
$Li_3(CO_2)_2$	*P*-1	0	-6.474	0.101	-1.596	-0.715	0.166
$LiCO_2$	*P2₁/c (I)*	0	-6.894	0.108	-1.644	-0.654	0.049
Li_2CO_2	*C2/m*	10	-5.614	0.103	-1.809	-1.121	0.147
$LiCO_2$	*P2₁/c (II)*	10	-6.310	0.112	-1.777	-0.917	0.027
Li_2CO_2	*Pnma*	50	-4.039	0.125	-2.344	-1.678	0.103
$Li_3(CO_2)_2$	*P*-1	50	-4.300	0.126	-2.228	-1.487	0.152
$LiCO_2$	*P2/c*	50	-4.601	0.136	-2.056	-1.223	0.064
$Li_3(CO_2)_4$	*C2*	50	-4.579	0.136	-1.750	-0.861	0.168
$Li(CO_2)_2$	*P1*	50	-4.725	0.140	-1.573	-0.620	0.115
$Li_3(CO_2)_2$	*C2/m*	100	-2.582	0.141	-2.478	-1.708	0.147
$LiCO_2$	*P2/c*	100	-2.903	0.153	-2.299	-1.431	0.014
$Li_3(CO_2)_4$	*P1*	100	-2.817	0.152	-1.792	-0.867	0.169
$Li(CO_2)_2$	*P*-1	100	-2.992	0.157	-1.744	-0.752	0.074
$LiCO_2$	*P2/c*	0 quench	-6.651	0.107	-1.401	-0.411	
Li_2CO_2	*Pnma*	0 quench	-6.044	0.097	-1.463	-0.671	
[c]Li_2CO_3	*C2/c*	0	-6.567		-1.927	-0.808	
Li_2CO_3	*P6₃/mcm*	10	-5.998		-2.119	-1.105	
Li_2CO_3	*P6₃/mcm*	50	-4.335		-2.549	-1.522	
Li_2CO_3	*P6₃/mcm*	100	-2.586		-2.794	-1.712	
[d]CO_2	*Pa*-3	0	-7.686		-1.320		
CO_2	*Pa*-3	10	-6.893		-1.146		
CO_2	*I*-42*d*	50	-5.074		-1.111		
CO_2	*I*-42*d*	100	-3.264		-1.157		

[a] Formation enthalpy of $xLi+yC+2yO = Li_x(CO_2)_y$

[b] Reaction enthalpy of $xLi+yCO_2 = Li_x(CO_2)_y$

[c] Experimental standard formation enthalpy for Li_2CO_3 solid phase=-12.603 eV/atom

[d] Experimental standard formation enthalpy for CO_2 gas phase=-4.079 eV/atom

Table A13. Calculated enthalpies of lithium, carbon, oxygen, carbon dioxide, lithium oxide Li_2O, lithium carbonate $Li_2(CO_3)$ phases at different pressure. (Chapter 2)

Compounds	Enthalpies (eV/atom)			
	0 GPa	**10 GPa**	**50 GPa**	**100 GPa**
Li	*Im-3m(BCC)*	*Fm-3m(FCC)*	*I*-43*d*	*Cmca*
	-1.904	-0.893	1.708	3.905
C	$P6_3/mmc$	*Fd*-3*m*	*Fd*-3*m*	*Fd*-3*m*
	-9.223	-8.740	-7.399	-5.842
O	*C2/m (O4)*	*C2/m (O8)*	*C2/m (O8)*	*C2/m (O8)*
	-4.937	-4.250	-2.245	-0.240
Li_2O	*Fm*-3*m*	*Fm*-3*m*	*Pnma*	*Pnma*
	-4.783	-4.294	-2.671	-1.048
Li_2CO_3	*C2/c*	$P6_3/mcm$	$P6_3/mcm$	$P6_3/mcm$
	-6.567	-5.998	-4.335	-2.586
CO_2	*Pa*-3	*Pa*-3	*I*-42*d*	*I*-42*d*
	-7.686	-6.893	-5.074	-3.264

Table A14. Gravimetric energy densities for nitrogen-based materials (Chapter 3.3)

Stoichiometry	Space group	Enthalpy (eV/atom)	Energy density	
			(eV/f.u)	**(kJ/g)**
MgN_4	*P2/m*	-7.013	1.065	1.279
MgN_4	*P-1*	-6.879	1.735	2.084
MgN_4	*Cmmm*	-6.820	2.030	2.438
MgN_3	*C2/m*	-6.753	0.798	1.161
MgN_3	*P*-1 *(I)*	-6.459	1.974	2.872
MgN_2	*Cmcm*	-6.224	0.818	1.509
MgN_2	$P6_3/mcm$	-6.144	1.058	1.951
Mg_2N_3	*Pmmm*	-5.776	1.780	1.895
Mg_2N_3	*C2/m*	-6.023	0.545	0.580
Nitrogen	*Pa*-3	-8.320	-	-
Mg_3N_2	*Ia*-3	-5.038	-	-

Table A15. Calculated enthalpies of the predicted Ba_xN_y compounds at different pressure. (Chapter 3.4)

Structure	**Space Group**	**Pressure (GPa)**	**Enthalpy (eV/atom)**	**ZPE (eV/atom)**	**Formation Enthalpy (eV/atom)**
Ground stable phase					
Ba_3N	$P6_3/mcm$	0	-3.829	0.021	-0.306
Ba_2N	R-3m	0	-4.460	0.024	-0.404
Ba_2N	P-3m1	10	-2.611	0.033	-0.777
Ba_2N	$I4/mmm$	100	7.102	0.055	-1.084
Ba3N2	P-1	10	-3.275	0.036	-0.891
Ba_3N_2	$C2/c$	50	1.270	0.050	-1.267
BaN	$P2_1/c$	10	-4.133	0.051	-0.923
BaN	$P2_1/m$	50	-0.107	0.063	-1.400
BaN	$C2/m$	100	3.964	0.073	-1.409
Ba_2N_3	$C2/m$	50	-1.393	0.078	-1.443
BaN_2	$C2/c$	0	-6.710	0.063	-0.522
BaN_2	$C2/m$	50	-2.190	0.082	-1.412
BaN_2	$P2_1/c$	100	1.199	0.099	-1.361
Ba_3N_8	$Cmmm$	50	-2.835	0.094	-1.303
BaN_4	$P6/mmm$	10	-6.372	0.089	-0.683
BaN_4	$P4_12_12$	50	-3.511	0.117	-1.075
BaN_4	$C2/c$	100	-0.704	0.125	-1.013
BaN_5	$Imma$	50	-3.841	0.116	-0.991
Ba_2N_{11}	P-1	10	-6.602	0.094	-0.532
$BaN_6{}^{Exp}$	$P2_1/m$	0	-7.603	0.101	-0.197
BaN_{10}	P-1	50	-4.482	0.136	-0.690
Metastable phase					
Ba_4N_3	$P1$	10	-3.511	0.040	-0.891
Ba_4N_3	$C2/m$	100	5.306	0.067	-1.272
BaN_3	$C2/c$	100	0.009	0.115	-1.144
BaN_5	$P1$	100	-1.067	0.130	-0.814
BaN_6	P-1(I)	50	-3.996	0.127	-0.849
BaN_6	P-1(II)	50	-3.881	0.114	-0.735
BaN_6	$C2/m$	100	-1.390	0.142	-0.735

Appendix 4. DOS and band structure

Figure A1. DOS for Li-CO_2 phases (Chapter 2)

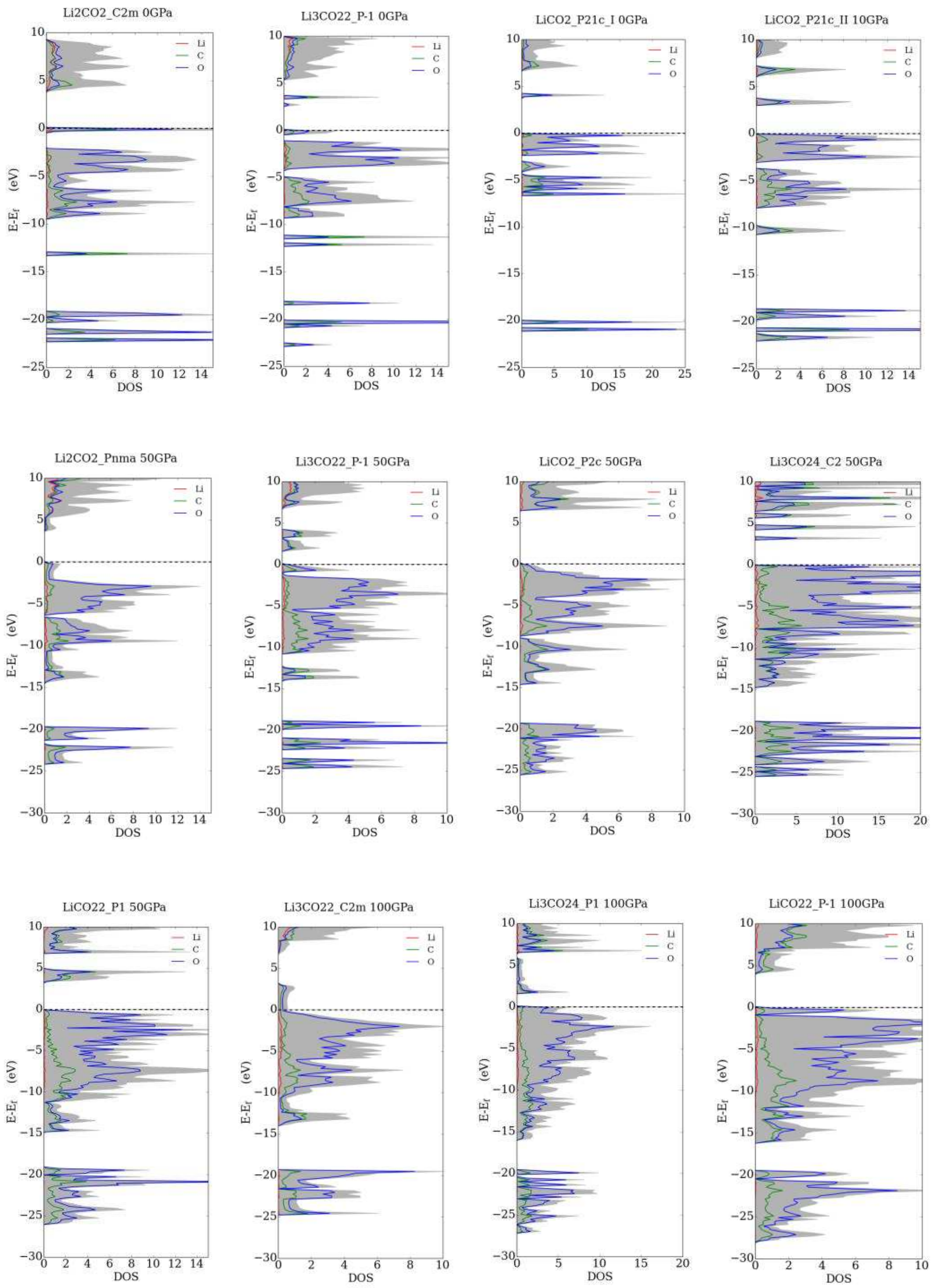

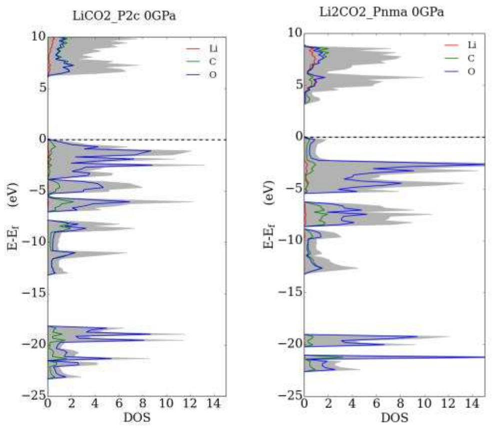

Figure A2. Density of states (DOS) for Ba-N phases (Chapter 3.4)

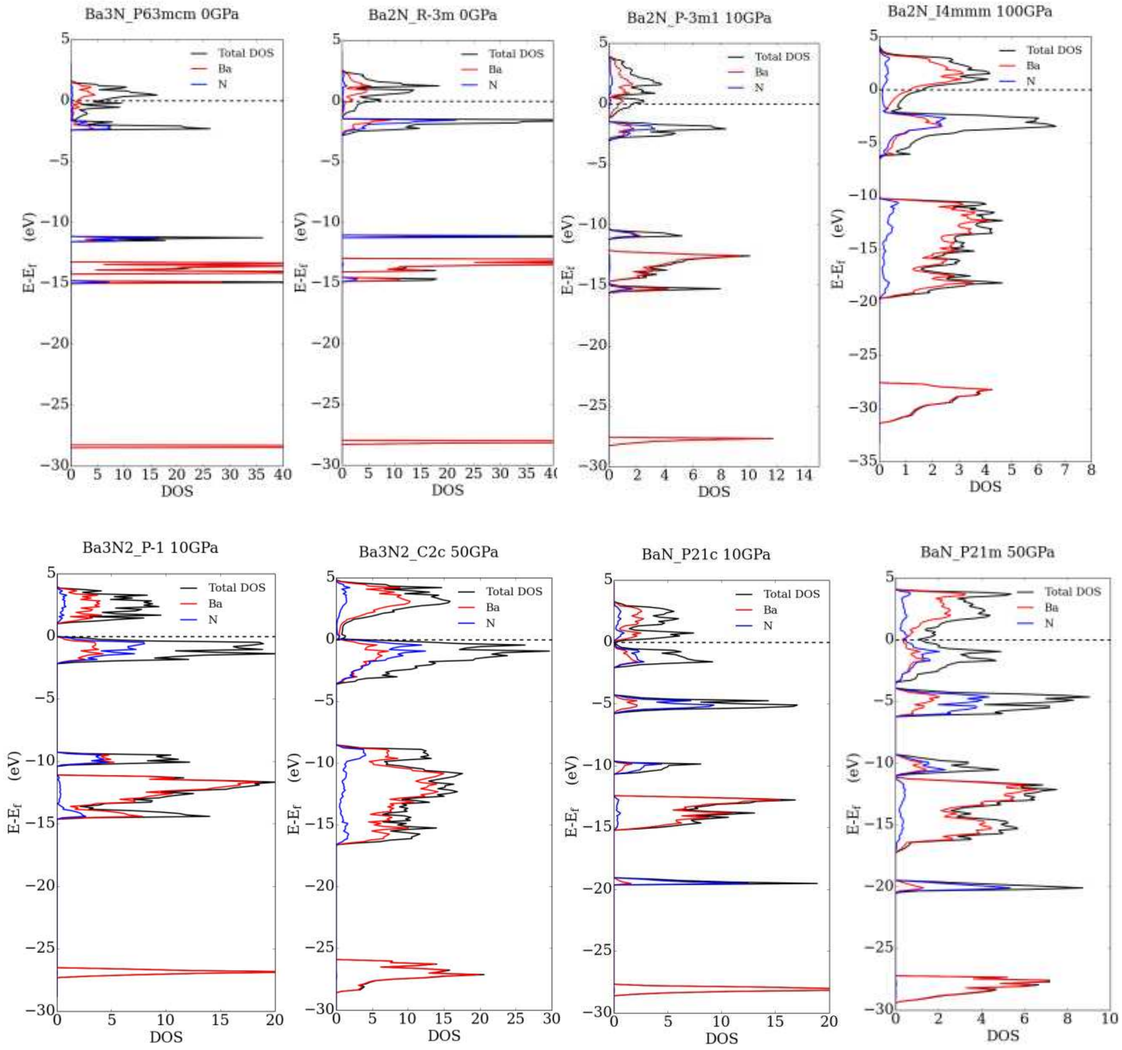

BaN_C2m 100GPa

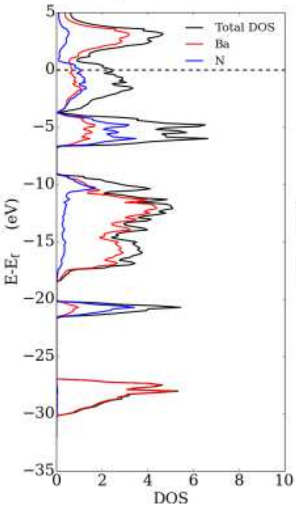

Ba2N3_C2m 50GPa

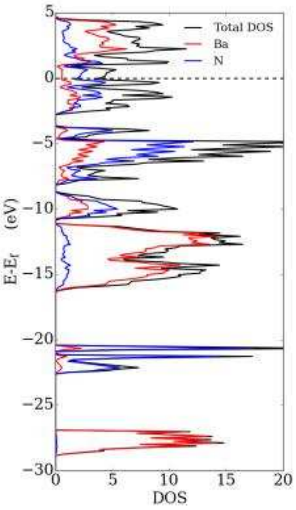

BaN2_C2c 0GPa

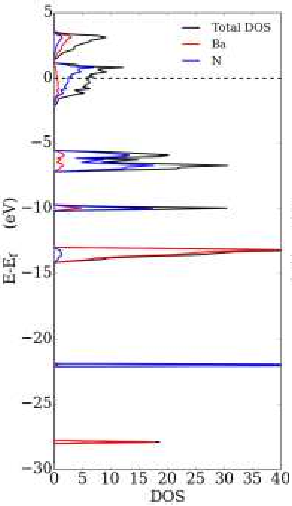

BaN2_C2m 50GPa

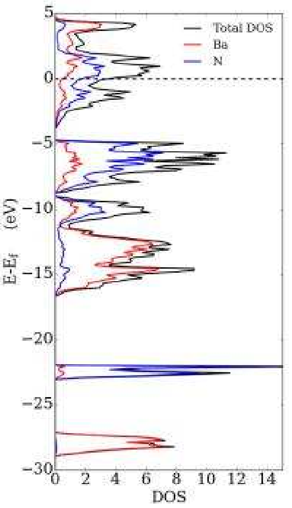

BaN2_P21c 100GPa

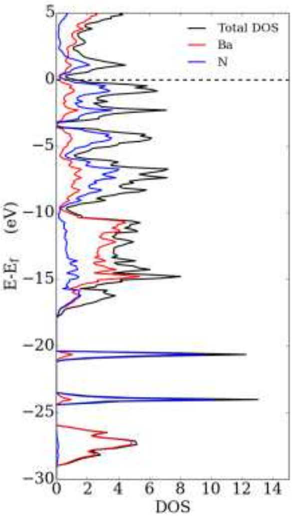

Ba3N8_Cmmm 50GPa

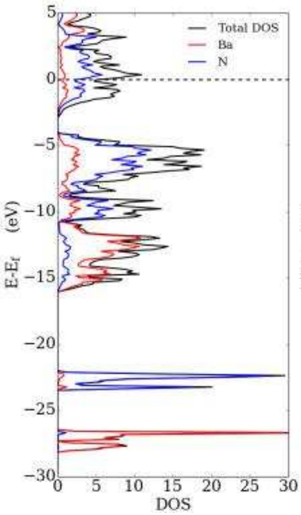

BaN4_P6mmm 10GPa

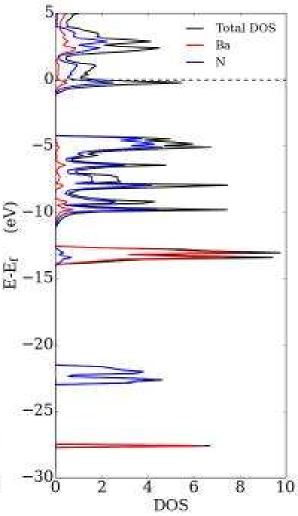

BaN4_P41212 50GPa

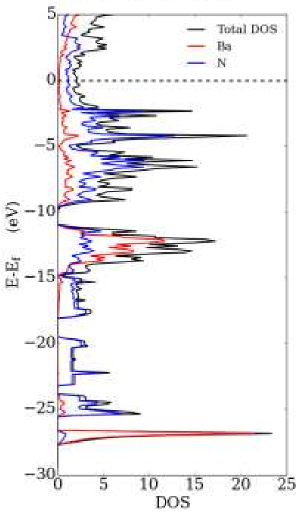

BaN4_C2c 100GPa

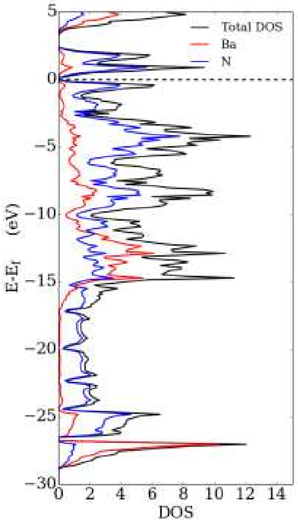

BaN5_Imma 50GPa

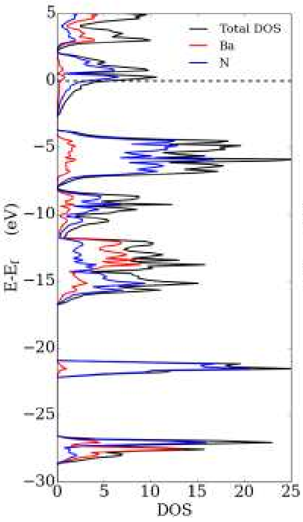

Ba2N11_P-1 10GPa

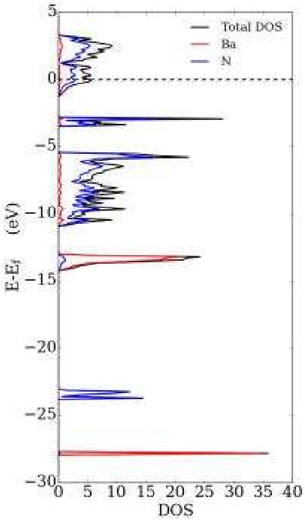

BaN6_P21m 0GPa

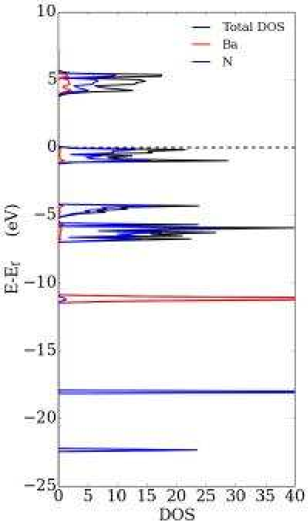

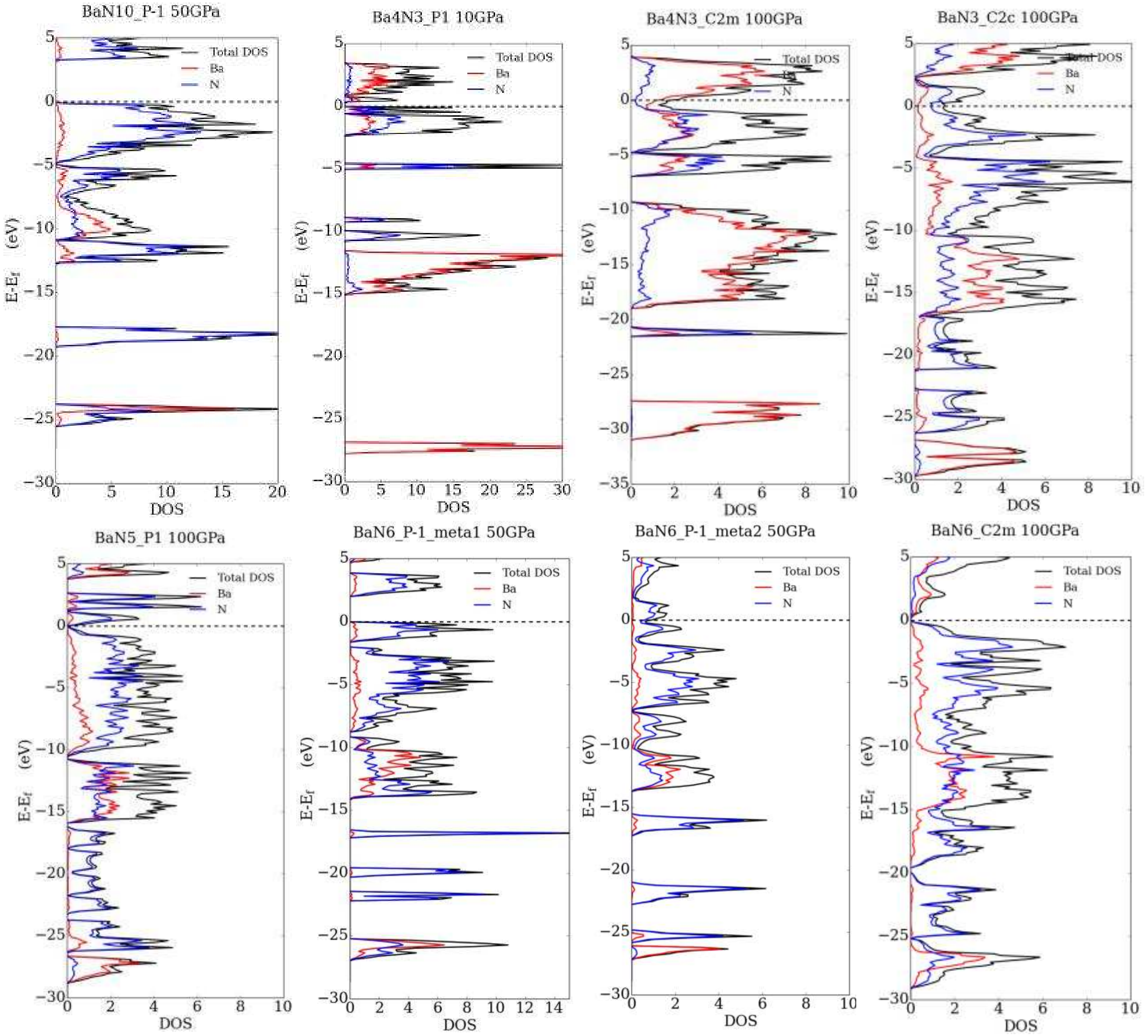

Figure A3. DOS and band structure for Ba_xN_y electride phases calculated by local function method (CRYSTAL 17) (Chapter 3.4)

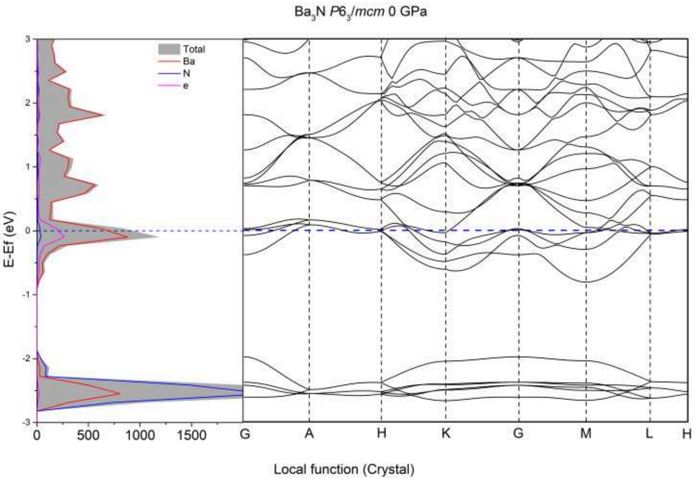

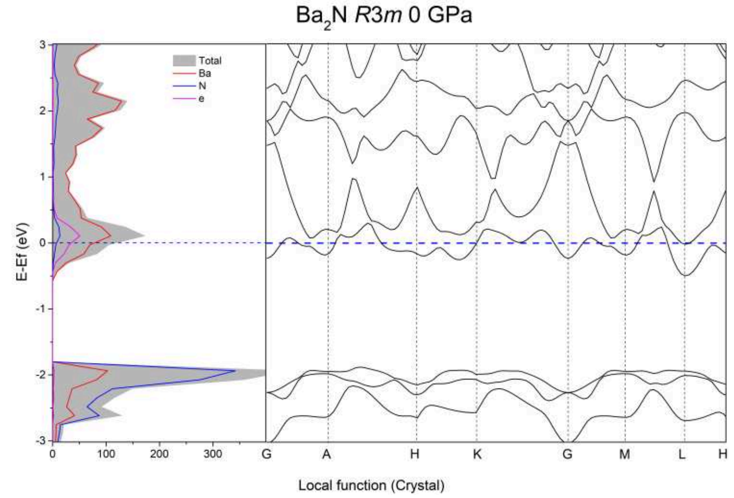

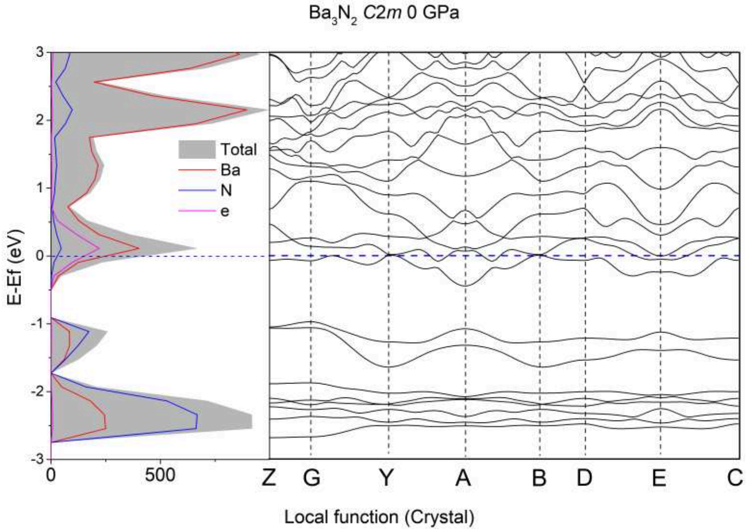

Figure A4. Density of states (DOS) for MN_{10} phases (Chapter 3.5)

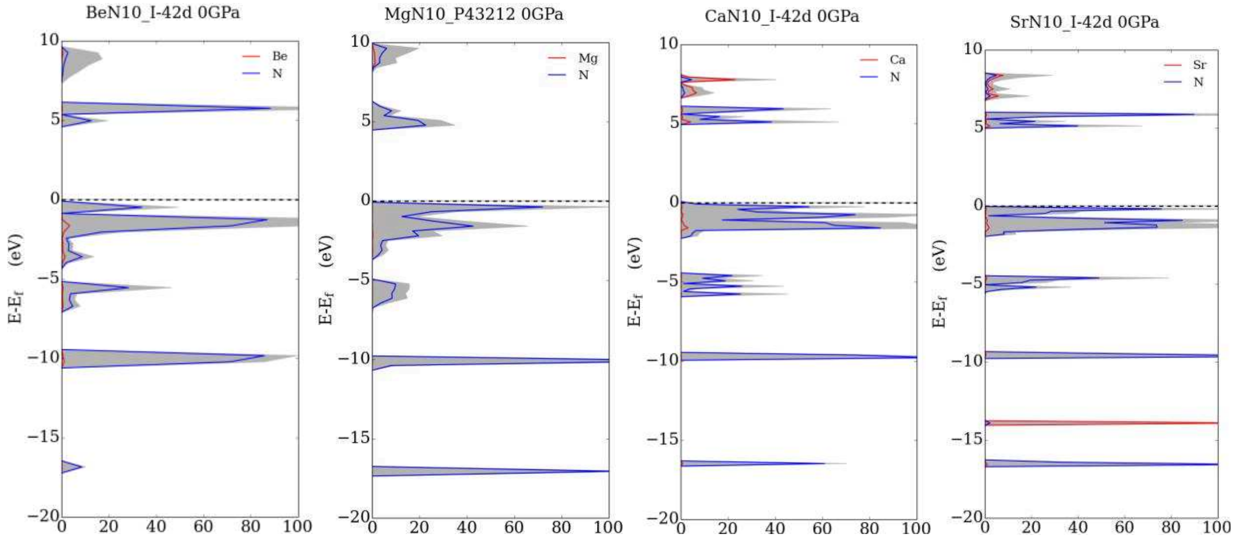

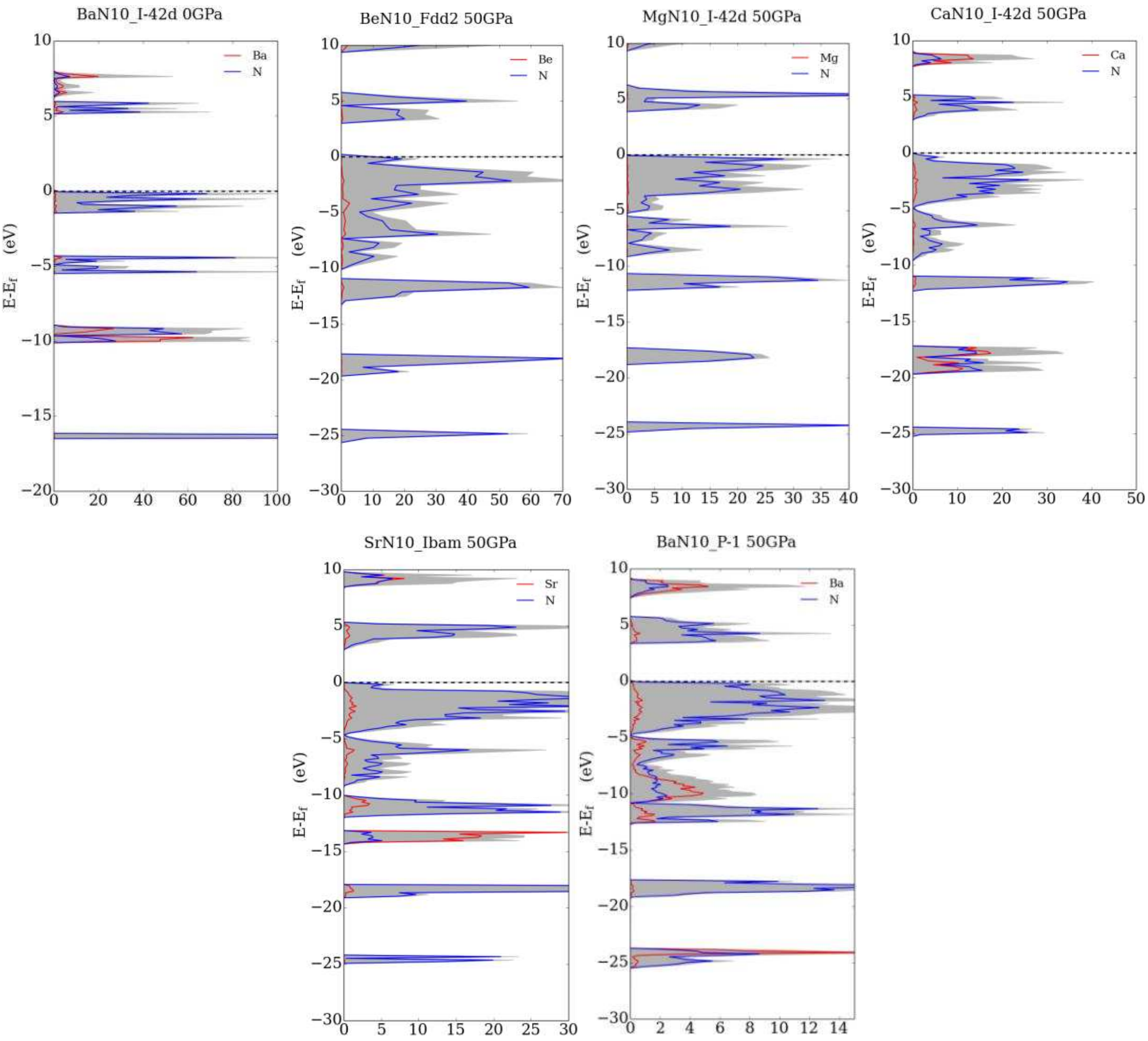
BaN10_I-42d 0GPa
Ba
N
E-E$_f$ (eV)
10
5
0
−5
−10
−15
−20
0
20
40
60
80
100
BeN10_Fdd2 50GPa
Be
N
E-E$_f$ (eV)
10
5
0
−5
−10
−15
−20
−25
−30
0
10
20
30
40
50
60
70
MgN10_I-42d 50GPa
Mg
N
E-E$_f$ (eV)
10
5
0
−5
−10
−15
−20
−25
−30
0
5
10
15
20
25
30
35
40
CaN10_I-42d 50GPa
Ca
N
E-E$_f$ (eV)
10
5
0
−5
−10
−15
−20
−25
−30
0
10
20
30
40
50
SrN10_Ibam 50GPa
Sr
N
E-E$_f$ (eV)
10
5
0
−5
−10
−15
−20
−25
−30
0
5
10
15
20
25
30
BaN10_P-1 50GPa
Ba
N
E-E$_f$ (eV)
10
5
0
−5
−10
−15
−20
−25
−30
0
2
4
6
8
10
12
14

Appendix 5. Phonon frequency

Figure A5. Phonon dispersion curves of the Li$_x$(CO$_2$)$_y$ compounds at selected pressures. No imaginary phonon modes are found in the whole Brillouin zone, which confirms their dynamical stability. (Chapter 2)

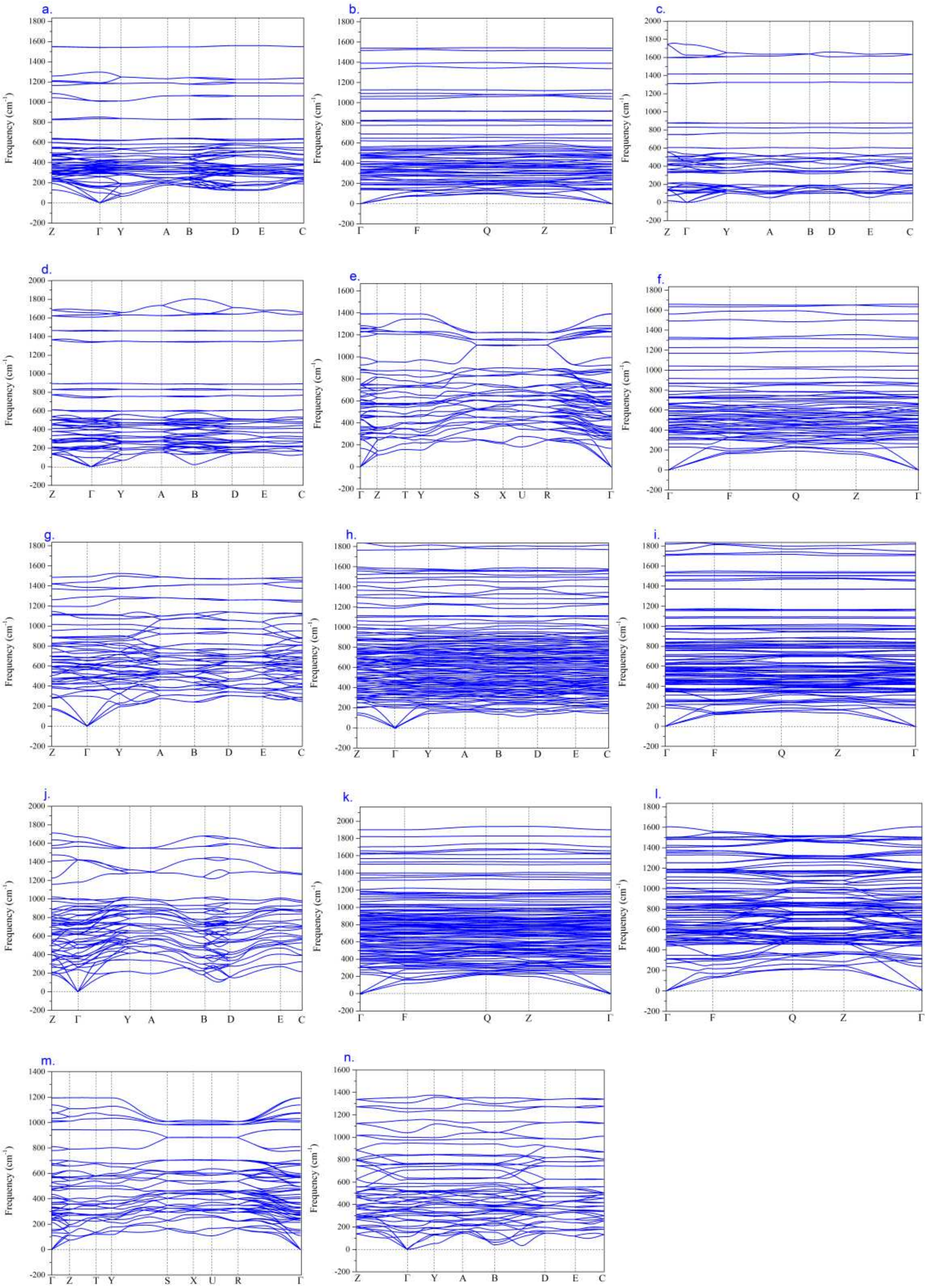

a	b	c	d	e	f	g
Li_2CO_2 *C2/m* 0 GPa	$Li_3(CO_2)_2$ *P*-1 0 GPa	$LiCO_2$ $P2_1/c$-1 0 GPa	$LiCO_2$ $P2_1/c$-2 10 GPa	Li_2CO_2 *Pnma* 50 GPa	$Li_3(CO_2)_2$ *P*-1 50 GPa	$LiCO_2$ *P2/c* 50 GPa
h	i	j	k	l	m	n
$Li_3(CO_2)_4$ *C2* 50 GPa	$Li(CO_2)_2$ *P*1 50 GPa	$Li_3(CO_2)_2$ *C2/m* 100 GPa	$Li_3(CO_2)_4$ *P*1 100 GPa	$Li(CO_2)_2$ *P*-1 100 GPa	Li_2CO_2 *Pnma* Quench(0 GPa)	$LiCO_2$ *P2/c* Quench (0 GPa)

Figure A6. Phonon dispersion curves of the Ba_xN_y compounds at selected pressures. No imaginary phonon modes are found in the whole Brillouin zone, which confirms their dynamical stability. (Chapter 3.4)

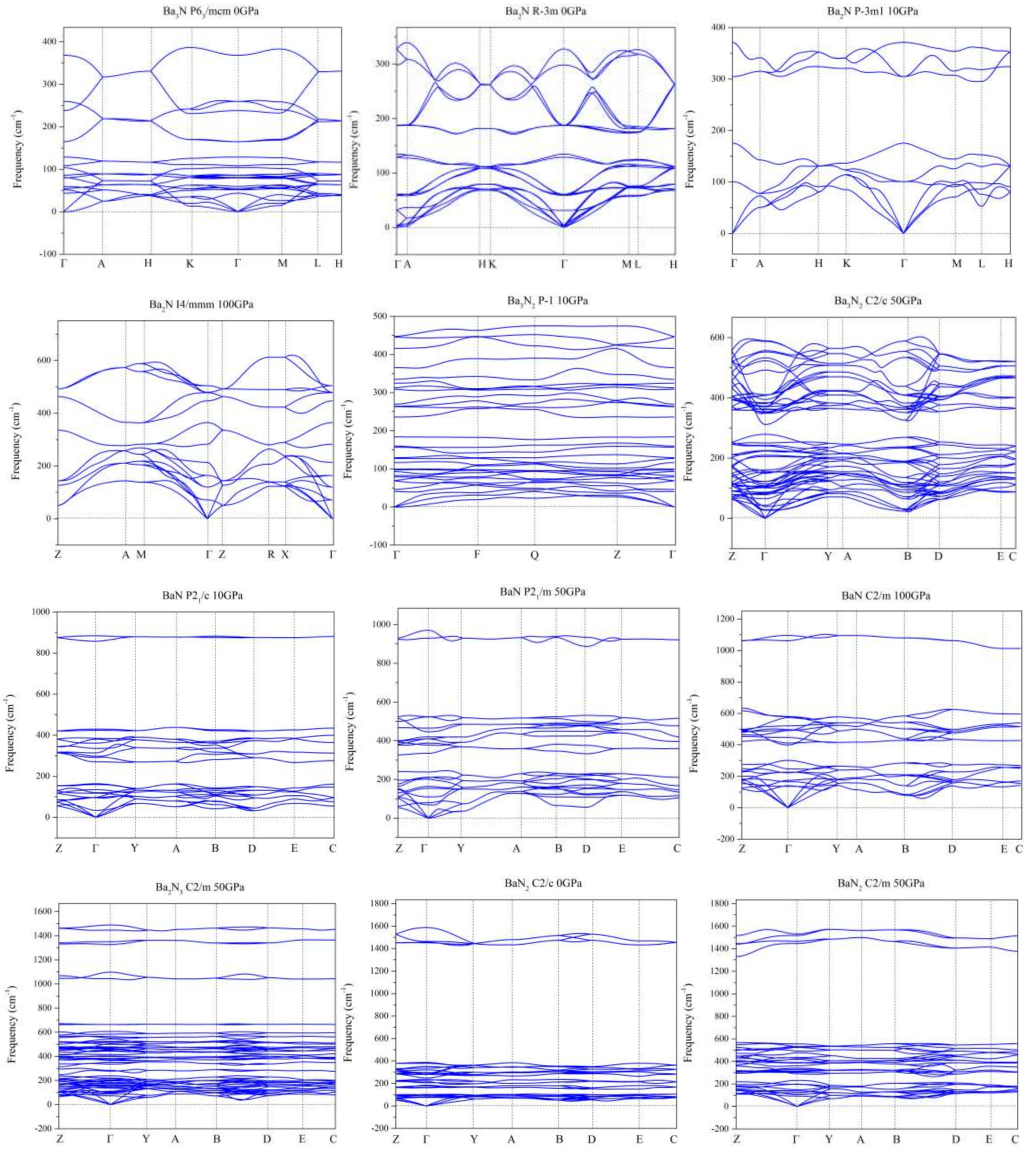

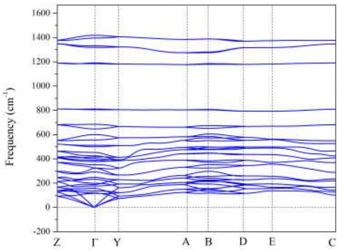
BaN$_2$ P2$_1$/c 100GPa

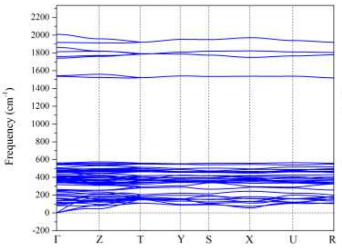
Ba$_3$N$_8$ Cmmm 50GPa

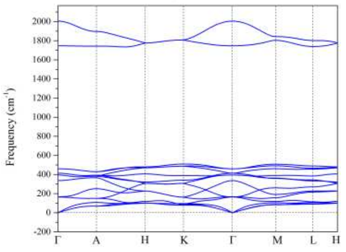
BaN$_4$ P6/mmm 10GPa

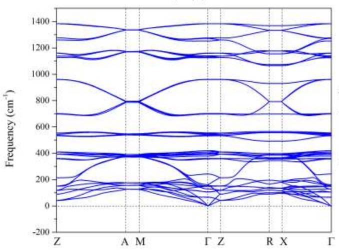
BaN$_4$ P4$_1$2$_1$2 50GPa

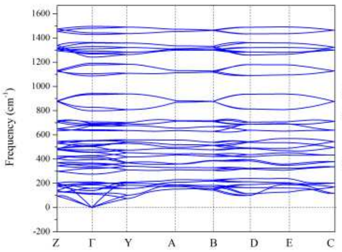
BaN$_4$ C2/c 100GPa

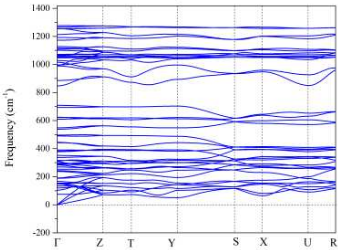
BaN$_5$ Imma 50GPa

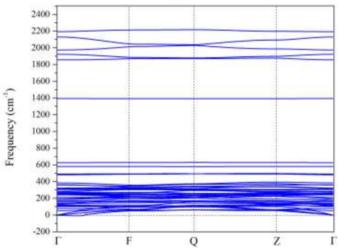
Ba$_2$N$_{11}$ P-1 10GPa

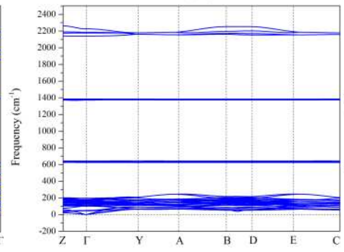
BaN$_6$ P2$_1$/m 0GPa

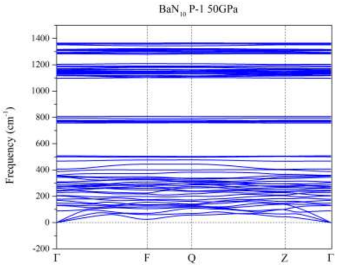
BaN$_{10}$ P-1 50GPa

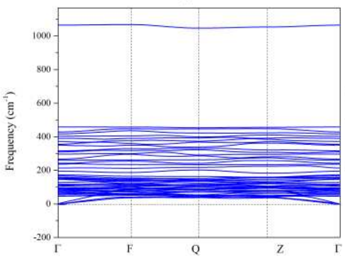
Ba$_4$N$_3$ P1 10GPa

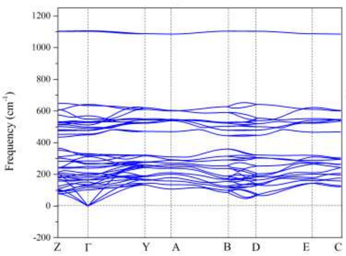
Ba$_4$N$_3$ C2/m 100GPa

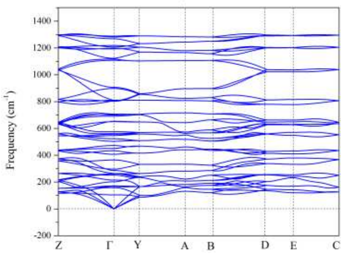
BaN$_3$ C2/c 100GPa

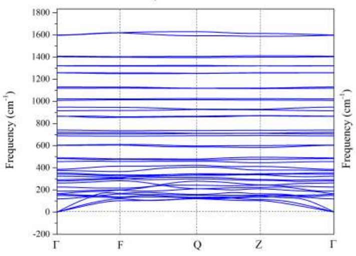
BaN$_6$ P-1 0GPa (1st metastable)

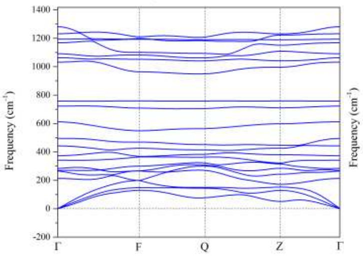
BaN$_6$ P-1 0GPa (2nd metastable)

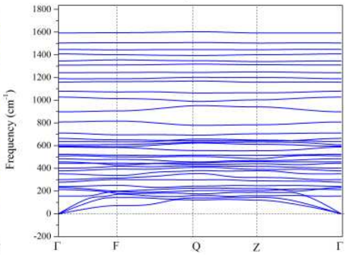
BaN$_5$ P1 100GPa

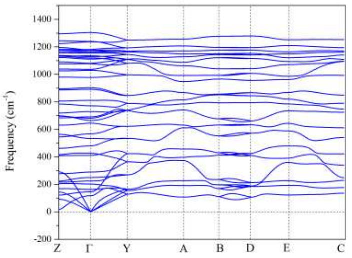
BaN$_6$ C2/m 100GPa

Figure A7. Phonon dispersion curves of the SiS_2 compounds at selected pressures. No imaginary phonon modes are found in the whole Brillouin zone, which confirms their dynamical stability. (Chapter 5.2)

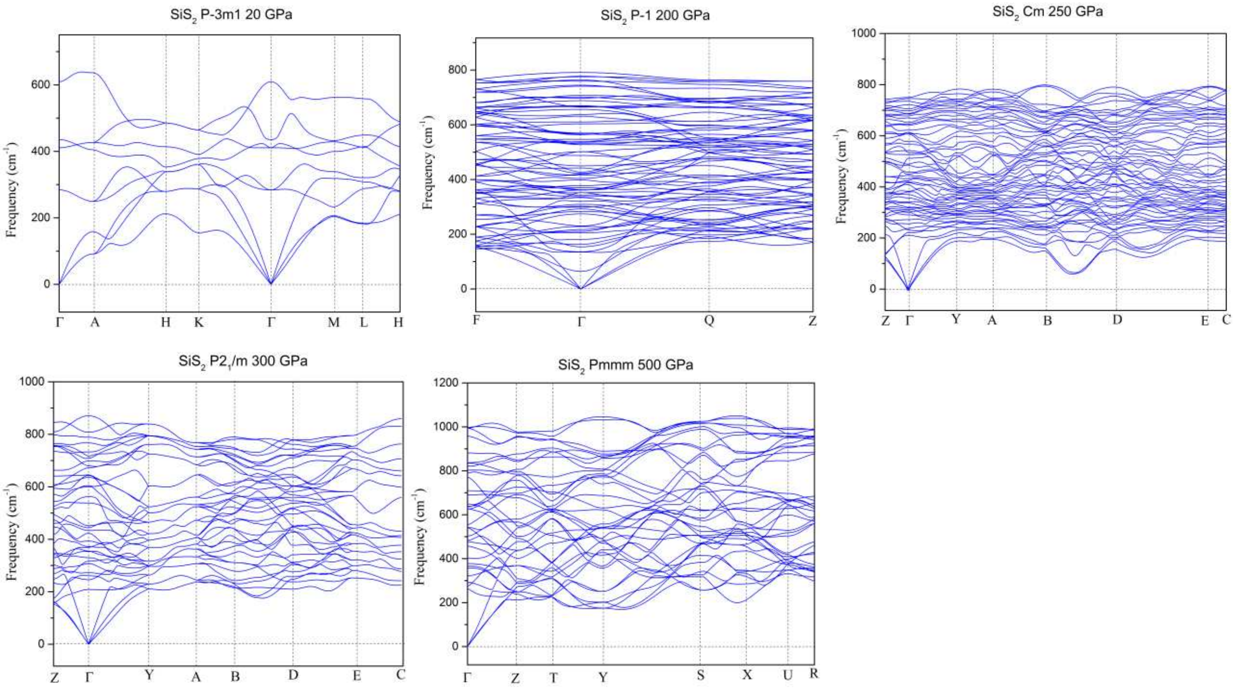

Appendix 6. AIMD simulations (Chapter 3 and 4)

In our DFT calculations on $Li_x(CO_2)_y$ phases, the PBE functional is used throughout this work. The projector-augmented wave (PAW) method was used for the core-electron representation. After preliminary convergence tests, we used a cutoff energy E_{cut}= 550 eV for the valence basis set. *ab initio* (DFT) molecular dynamics simulations were performed with VASP for the periodic supercell of three phases. Starting from each structure at ambient pressure, AIMD calculations were performed at 300 K, 600 K, 900, and 1200 K. The timestep was 1 fs, and the total simulation time was as long as 10 ps. Brillouin zone integration is restricted to the Γ point of the supercell.

Structure	Space Group	Supercell	Number of atoms
$LiCO_2$	P2/c	2*3*3	288
$Li_3(CO_2)_2$	P-1	2*2*2	144
Li_2CO_2	Pnma	2*4*2	320

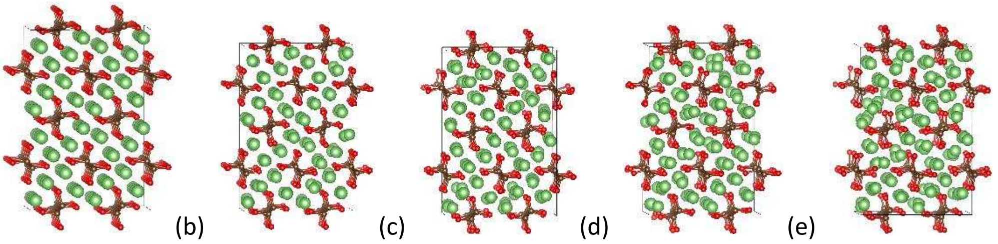

Figure A8. Snapshots of the 2*4*2 supercell at 1 atm (a) before AIMD (Li_2CO_2 *Pnma* phase at 0 K), and at the end of 10 ps AIMD simulations at (b) 300 K, (c) 600 K, (d) 900 K and (e) 1200 K. Large green spheres are lithium atoms, medium brown spheres are carbon atoms and medium red spheres are oxygen atoms.

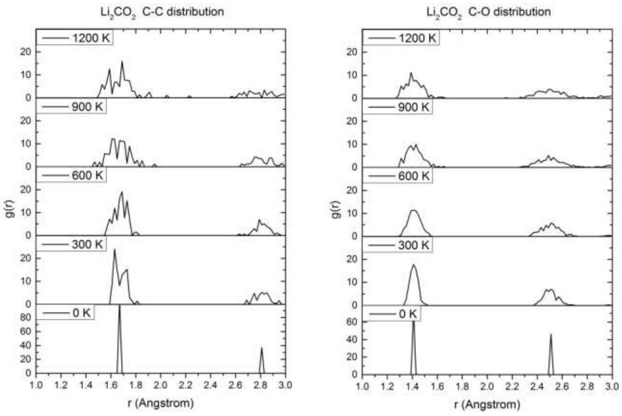

Figure A9. Radial distribution functions (RDF) for the (a) C-C, (b) C-O, and (c) Li-O separations observed during AIMD simulations for 2*4*2-based supercell at ambient pressure and T = 0 K (Li_2CO_2 *Pnma* phase), 300 K, 600 K, 900 K and 1200 K.

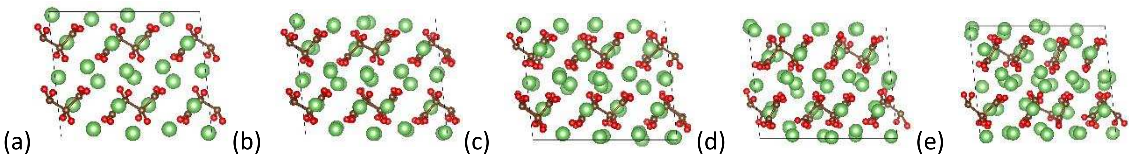
(a) (b) (c) (d) (e)

Figure A10. Snapshots of the 2*2*2 supercell at 1 atm (a) before AIMD ($Li_3(CO_2)_2$ *P-1* phase at 0 K), and at the end of 10 ps AIMD simulations at (b) 300 K, (c) 600 K, (d) 900 K and (e) 1200 K. Large green spheres are lithium atoms, medium brown spheres are carbon atoms and medium red spheres are oxygen atoms.

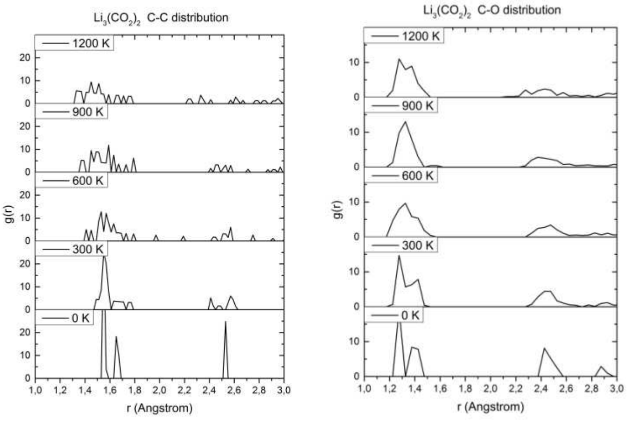

Figure A11. Radial distribution functions (RDF) for the (a) C-C, (b) C-O, and (c) Li-O separations observed during AIMD simulations for 2*2*2-based supercell at ambient pressure and T = 0 K($Li_3(CO_2)_2$ *P-1* phase), 300 K, 600 K, 900 K and 1200 K.

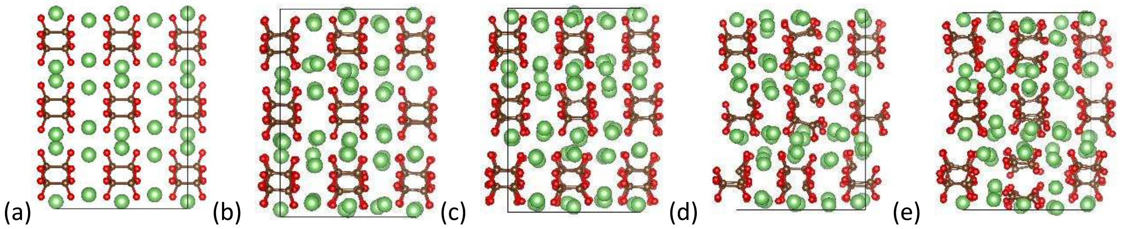

Figure A12. Snapshots of the 2*3*3 supercell at 1 atm (a) before AIMD ($LiCO_2$ *P*2/*c* phase at 0 K), and at the end of 10 ps AIMD simulations at (b) 300 K, (c) 600 K, (d) 900 K and (e) 1200 K. Large green spheres are lithium atoms, medium brown spheres are carbon atoms and medium red spheres are oxygen atoms.

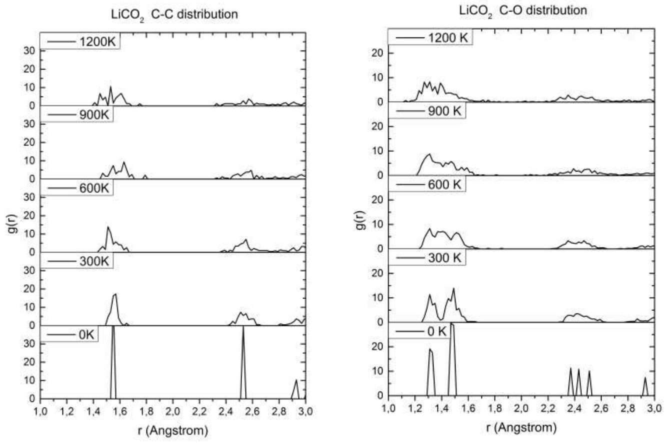

Figure A13. Radial distribution functions (RDF) for the (a) C-C, (b) C-O, and (c) Li-O separations observed during AIMD simulations for 2*3*3-based supercell at ambient pressure and T = 0 K ($LiCO_2$ *P*2/*c* phase), 300 K, 600 K, 900 K and 1200 K.

Ab initio (DFT) molecular dynamics simulations were performed with VASP for the case of a 3×2×4 (48 Mg and 192 N atoms; 240 atoms) *Cmmm* MgN_4-based periodic supercell. Starting from the *Cmmm* MgN_4 structure at ambient pressure, AIMD calculations were performed at 300 K, 600 K and 900 K. The timestep was 1 fs, and the total simulation time was as long as 10 ps. Brillouin zone integration is restricted to the Γ point of the supercell. A canonical NVT (N: constant number of particles, V: constant volume, and T: constant temperature) ensemble was adopted for the AIMD calculations using the algorithm of Nose, as implemented in the VASP code.

In our DFT calculations on Mg_xN_y phases, the PBE functional is used throughout this work. The projector-augmented wave (PAW) method was used for the core−electron representation. After preliminary convergence tests, we used a cutoff energy E_{cut}= 550 eV for the valence basis set.

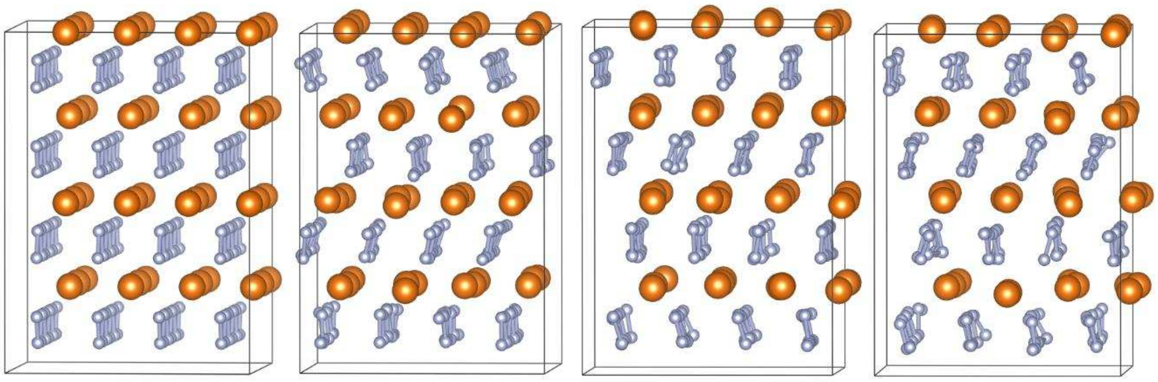

(a) (b) (c) (d)

Figure A14. Snapshots of the MgN_4 supercell at 1 atm (a) before AIMD (*Cmmm* phase at 0 K), and at the end of 10 ps AIMD simulations at (b) 300 K, (c) 600 K, and (d) 900 K. Small grey spheres are nitrogen atoms and large brown spheres are magnesium atoms.

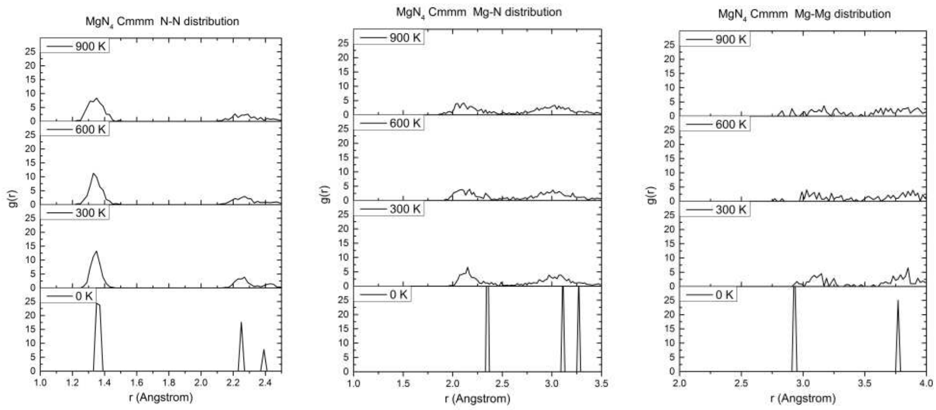

Figure A15. Radial distribution functions (RDF) for the (a) N-N, (b) Mg-N, and (c) Mg-Mg separations observed during AIMD simulations for *Cmmm* MgN_4-based supercell at ambient pressure and T = 0 K, 300 K, 600 K, and 900 K.

Abstract

The discovery of novel crystalline compounds by numerical simulation is a major challenge in Materials Science. Three families have been studied: compounds consisting of lithium and carbon dioxide; the M_xN_y nitride phases with M = Mg, Ba, Mo and Zr; the $GaPO_4$ and SiS_2systems. The crystallographic structures are determined in silico using the evolutionary algorithm USPEX, coupled with DFT calculations (VASP). The study of polymorphism as a function of pressure has been carried out, whereas the analysis of structural and electronic properties constitutes the heart of this thesis.

Our work clearly presents the effect of pressure on the emergence of unexpected stoichiometries, such as $Li_2(CO_2)$, MgN_4, and BaN_{10}. Some of these hypothetical materials remain stable at atmospheric pressure. It is shown that the addition of the s-block element allows the "polymerization" of the unsaturated molecules CO_2 and N_2 to be carried out at lower pressures. Thus, oxalate $C_2O_4^{2-}$ polymerizes in an infinite poly-dioxane chain in $LiCO_2$ at 33 GPa; the new Li_2CO_2 composition presents the ethene like $(-O)_2C=C(O-)_2$ motif; N_2, N_3 and N_4 finite chains, N_5^- pentazolate anions, and N_6 rings are identified in the Ae_xN_y phases, as well as infinite covalent (1D) chains, stabilized by the alkaline earth cations (Ae); the Ba_3N_2 compound is a conductive electride at ambient pressure and an insulator above 5 GPa; the ground stable structure of MoN_2 has encapsulated N_2 units, and is not the MoS_2 type arrangement proposed by experimentalists; our predictions coupled with the XRD data allow the elucidation of the $GaPO_4$ structure at 20 GPa.

Keywords : alkaline earth, evolutionary algorithm, orbital analysis, theoretical calculation, CO_2, DFT, carbon dioxide, $GaPO_4$, high pressure*, in silico*, chemical bond, MoN_2, nitrides, pentazolate, crystalline phase prediction, electronic structure, SiS_2, USPEX, ZrN_2

Résumé

La découverte de nouveaux composés cristallins par simulation numérique est un défi majeur en Science des Matériaux. Aussi, trois familles sont à l'étude : les composés constitués de lithium et de dioxyde de carbone ; les phases nitrures M_xN_y avec M = Mg, Ba, Mo et Zr ; les systèmes $GaPO_4$ et SiS_2. Les structures cristallographiques sont déterminées *in silico* à l'aide de l'algorithme évolutionnaire USPEX couplé à des calculs DFT (VASP). L'étude du polymorphisme en fonction de la pression est conduite tandis que l'analyse des propriétés structurales et électroniques constitue le cœur de cette thèse. Nos travaux mettent clairement en évidence l'effet de la pression dans l'émergence de stoichiométries inhabituelles telles que $Li_2(CO_2)$, MgN_4, et BaN_{10}. Certains de ces matériaux hypothétiques restent stables à pression atmosphérique. Il est montré que l'ajout d'un élément du bloc s autorise la « polymérisation » des molécules insaturées CO_2 et N_2 à des pressions plus basses. Ainsi, l'oxalate $C_2O_4^{2-}$ polymérise en chaine infinie poly-dioxane à 33 GPa dans $LiCO_2$; la nouvelle composition Li_2CO_2 présente des motifs de type éthène $(^{-}O)_2C=C(O^{-})_2$; des chaînons N_2, N_3 et N_4, des anions pentazolates N_5^- et des cycles N_6 sont identifiés dans les phases Ae_xN_y, ainsi que des chaines covalentes infinies (1D) stabilisés par les cations alcalino-terreux Ae ; le composé Ba_3N_2 est un électride conducteur à pression ambiante et un isolant au-dessus de 5 GPa ; la structure stable de MoN_2 a des entités N_2 encapsulées, et non l'arrangement en feuillet de type MoS_2 proposé par des expérimentateurs ; nos prédictions couplées aux données DRX permettent l'élucidation de la structure de $GaPO_4$ à 20 GPa.

Mots-clés : alcalino-terreux, algorithme évolutionnaire, analyse orbitalaire, calculs théoriques, CO_2, DFT, dioxyde de carbone, $GaPO_4$, haute pression, *in silico*, liaison chimique, MoN_2, nitrures, pentazolate, prédiction de phases cristallines, structure électronique, SiS_2, USPEX, ZrN_2

Adresse du Laboratoire :

IC2MP – UMR 7285
Université de Poitiers – SFA
Bâtiments B27, rue Michel Brunet – TSA 51106,
86073 Poitiers cedex 9